Investigation of LIBS and Raman data analysis methods in the context of in-situ planetary exploration

DISSERTATION

zur Erlangung des akademischen Grades
doctor rerum naturalium (Dr. rer. nat.)
im Fach Physik (Spezialisierung Experimentalphysik)

eingereicht an der
Mathematisch-Naturwissenschaftlichen Fakultät
der Humboldt-Universität zu Berlin
von

Kristin Rammelkamp, M.Sc.

Präsidentin der Humboldt-Universität zu Berlin:
Prof. Dr.-Ing. Dr. Sabine Kunst

Dekan der Mathematisch-Naturwissenschaftlichen Fakultät:
Prof. Dr. Elmar Kulke

Gutachter/innen:

1. Prof. Dr. Heinz-Wilhelm Hübers
2. Dr. habil. Cécile Fabre
3. Prof. Dr. Norbert Esser

Tag der mündlichen Prüfung: 23. Oktober 2019

Abstract

The studies presented in this thesis investigate different data analysis approaches for mainly laser-induced breakdown spectroscopy (LIBS) and also Raman data in the context of planetary in-situ exploration. Most studies were motivated by Mars exploration due to the first extraterrestrially employed LIBS instrument ChemCam on NASA's Mars Science Laboratory (MSL) and further planned LIBS and Raman instruments on upcoming missions to Mars. Furthermore, LIBS in vacuum conditions is addressed in one study which is relevant for LIBS space exploration instruments to bodies without an atmosphere. Next to analytical approaches, statistical methods known as multivariate data analysis (MVA) were applied and evaluated.

LIBS is an atomic emission spectroscopy technique from which the elemental composition of a target can be derived qualitatively and quantitatively. A pulsed high energy laser is used to ablate material from the sample surface which evolves into a small plasma of highly excited atoms, ions, and simple molecules. Spectral analysis of the emitted plasma radiation gives spectra with tens to hundreds of characteristic emission lines. The LIBS technique has several advantages for the geochemical analysis of extraterrestrial surfaces: It is fast, needs only optical access to the target, and is sensitive to all elements including hydrogen. With Raman spectroscopy, molecule and lattice vibrations can be derived by means of inelastic scattering.

In this thesis, four studies are presented in which LIBS and Raman data analysis strategies are evaluated. In the first study, LIBS data normalization with plasma parameters, namely the plasma temperature and the electron density, was studied. It was shown that plasma parameters derived with the standard methods are not better suited for LIBS data normalization than the usually used total emission intensity. In the second study, LIBS measurements in vacuum conditions were investigated with a focus on the degree of ionization of the LIBS plasma. Additional ionized emission lines were observed for lower pressures which can be relevant for the selection of useful spectral ranges when designing LIBS instruments for surface analysis of atmosphereless bodies. However, these lines are more affected by changing experimental conditions and might not be suited well for quantification. In the third study, the capability of MVA methods such as principal component analysis (PCA) and partial least squares regression (PLS-R) for the identification and quantification of halogens by means of molecular emissions was tested. The outcomes are promising, as it was possible to distinguish apatites and to quantify chlorine in a particular concentration range. In the fourth and last study, LIBS data was combined with complementary Raman data in a low-level data fusion approach using MVA methods. Also, concepts of high-level data fusion were implemented. The data of salts relevant for Mars was measured with miniaturized instrument components in order to simulate the performance of light weight space mission hardware. Low-level LIBS and Raman data fusion can improve identification capabilities in comparison to the single datasets. However, the improvement is comparatively small regarding the higher amount of information in the low-level fused data and dedicated strategies for the joint analysis of LIBS and Raman data have to be found for particular scientific objectives. These can include high-level data fusion relying on decision tree architectures.

Kurzfassung

Die in dieser Arbeit vorgestellten Studien untersuchen verschiedene Ansätze für die Analyse von spektroskopischen Daten für die Erforschung anderer Himmelskörper. Der Fokus lag hierbei auf der laserinduzierten Plasmaspektroskopie (LIBS, engl. laser-induced breakdown spectroscopy), aber auch Daten der Raman-Spektroskopie wurden analysiert. Das erste extraterrestrisch eingesetzte LIBS Instrument, ChemCam, auf dem Mars Science Laboratory (MSL) der NASA untersucht die Marsoberfläche seit 2012 und weitere Missionen mit LIBS und Raman Instrumenten zum Mars sind geplant. Diese motivierten einen Großteil der Studien in dieser Arbeit. Zusätzlich wird in einer Studie LIBS unter Vakuumbedingungen behandelt, da die meisten Himmelskörper im Gegensatz zum Mars oder der Erde keine Atmosphäre haben. Neben analytischen Ansätzen wurden statistische Methoden, die als multivariate Datenanalysen (MVA) bekannt sind, verwendet und evaluiert.

LIBS ist eine Spektroskopietechnik, mit der die elementare Zusammensetzung einer Probe qualitativ und quantitativ bestimmt werden kann. Ein gepulster Laser mit hoher Energie wird verwendet, um ein kleines Plasma aus angeregten Atomen, Ionen und einfachen Molekülen zu erzeugen. Dieses Plasma emittiert Strahlung, die spektral zerlegt wird und dessen Spektren aus zahlreichen charakteristischen Emissionslinien bestehen. Die LIBS Technik hat mehrere Vorteile für die geochemische Analyse von extraterrestrischen Oberflächen: Sie ist schnell, benötigt keinen direkten Kontakt zu der Probe und kann viele Elemente gleichzeitig detektieren, darunter auch Wasserstoff. Mit Raman Spektroskopie können Molekül- und Gitterschwingungen aufgrund unelastischer Streuprozesse gemessen werden.

In dieser Arbeit werden insgesamt vier Studien vorgestellt. In der ersten Studie wurde die Normalisierung von LIBS Daten mit Plasmaparametern, also der Plasmatemperatur und der Elektronendichte, untersucht. Exemplarisch konnte hierbei gezeigt werden, dass mit den Standardmethoden berechnete Plasmaparameter für die Normalisierung von LIBS Daten nicht besser geeignet sind, als die üblicherweise verwendete Gesamtintensität. In der zweiten Studie wurden LIBS Messungen unter Vakuumbedingungen untersucht, wobei zusätzliche höher ionisierte Emissionslinien für niedrigere Drücke beobachtet wurden. Diese können für die Auswahl nützlicher Spektralbereiche beim Entwurf von LIBS Instrumenten für atmosphärenlose Körper relevant, aber im Hinblick auf robuste Quantifizierung auch kritisch sein. In der dritten Studie wurden MVA Methoden wie die Hauptkomponentenanalyse (PCA) und die partielle Regression kleinster Quadrate (PLS-R) zur Identifizierung und Quantifizierung von Halogenen mittels molekularer Emissionen angewandt. Die Ergebnisse sind vielversprechend, da es möglich war zwischen verschiedenen Apatiten zu unterscheiden und Chlor in einem ausgewählten Konzentrationsbereich zu quantifizieren. In der letzten Studie wurden LIBS-Daten mit komplementären Raman-Daten von Mars relevanten Salzen in einem low-level Datenfusionsansatz kombiniert. Bei diesem Ansatz werden keine Analysen der einzelnen Datensätze vor der Datenfusion durchgeführt. Es wurden MVA Methoden angewandt und auch Konzepte der high-level Datenfusion implementiert. Mit der low-level LIBS und Raman Datenfusion konnten im Vergleich zu den einzelnen Techniken mehr Salze richtig identifiziert werden. Der Gewinn durch die low-level Datenfusion ist jedoch vergleichsweise gering und für konkrete Missionen müssen individuelle und angepasste Strategien für die gemeinsame Analyse von LIBS- und Raman-Daten gefunden werden. Hierbei kann beispielsweise eine auf Entscheidungsbäumen basierende high-level Zusammenführung der Daten eine weitere Option sein.

Contents

List of abbrevations

BU	Body unit
CNES	Centre national d'études spatiales
cw	continuous wave
DLR	Deutsches Zentrum für Luft- und Raumfahrt
ESA	European space agency
FWHM	Full width at half maximum
ICA	Independent component analysis
ICCD	Intensified charge-coupled device
IRAP	Institut de recherche en astrophysique et planétologie
ISRO	Indian space research organisation
JAXA	Japan aerospace exploration agency
LIBS	Laser-induced breakdown spectroscopy
LSC	Laser-supported combustion wave
LSD	Laser-supported detonation wave
LSR	Laser-supported radiation wave
LTB	Laser Technik Berlin
LTE	Local thermodynamic equilibrium
LV	Latent variable
MAVEN	Mars atmosphere and volatile evolution
MMX	Martian moons exploration
MSL	Mars science laboratory
MU	Mast unit
MVA	Multivariate data analysis
NASA	National aeronautics and space administration
Nd:YAG	Neodymium-doped yttrium aluminum garnet
NIPALS	Non-linear iterative partial least squares
NIR	Near-infrared
NN	Nearest neighbor
PC	Principal component
PCA	Principal component analysis
PLS-DA	Partial least squares discriminant analysis
PLS-R	Partial least squares regression
PRESS	Predicted residual sum of squares
RAX	Raman for MMX
RLS	Raman laser spectrometer
RMI	Remote micro imager
RMSE	Root mean square error
RSD	Relative standard deviation
RSL	Recurring slope lineae
SHERLOC	Scanning habitable environments with Raman & luminescence for organics & chemicals
SNR	Signal-to-noise ratio
TGO	Trace gas orbiter
UV	Ultraviolet
VIS	Visible

List of symbols

A_{ij}	Transition probability between state i and j
at %	Atomic percentage
c	Speed of light in vacuum
e	Elementary charge
E_{ion}	Ionization energy
g_i	Degeneracy of state E_i
h	Planck constant
k_B	Boltzmann constant
m	Mass
m_e	Electron rest mass
n_e	Electron density
T	Temperature
U	Partition function
wt %	Weight percentage
Z	Ionization stage

1 Introduction

The Solar System with its variety of different worlds has fascinated people for a long time. Understanding its origin and evolution in combination with the search for extraterrestrial life naturally has a high relevance for humankind. Regarding the different bodies in the Solar System, the gas giants Saturn and Jupiter, for example, are orbited by many moons showing very different environmental conditions each being an individual world on its own. There are icy moons such as Enceladus, Ganymed or Europa. For some of them the existence of oceans below their icy surface layers was proven [Sohl et al., 2010]. Also moons with strong volcanism are known, e.g., Io [McEwen et al., 1998] and there is Saturn's extraordinary moon Titan which has lakes of methane and ethane [Stofan et al., 2007]. Not only Jupiter and Saturn are accompanied by moons, Uranus and Neptune also have many satellites. Until now, more than 170 moons are known in the outer Solar Sytem which vary in size and composition [Jaumann et al., 2018]. Besides these fascinating moon worlds, the inner rocky planets next to Earth are of great interest for humankind. In comparison to Earth, Mercury, Venus, and Mars presumably formed similar but evolved differently resulting in very different environments today. Understanding the processes during their evolution can give further insight into the evolution of life in general and further input to understand Earth better. To conclude, the Solar System offers a variety of worlds to discover and further explore.

Much knowledge about the bodies in the Solar System was obtained from spacecrafts which were sent to orbit particular bodies and which also often passed other bodies during their journey to their final destinations. Further insight was obtained from several in-situ exploration missions with rovers and landers. The footprint of orbital instruments is much larger compared to the area that in-situ missions can probe. On the larger scale of orbital data, the signals are usually mixtures of signals from several components in which detailed variations can not be resolved and features remain undetected [Milliken et al., 2019]. In-situ observations are needed as verification of orbital data and for detailed investigations on a smaller scale. However, these landed missions are rare, since landing on extraterrestrial bodies is usually challenging, expensive, and of high risk. Another important stage in planetary exploration is the sample return, where extraterrestrial material is collected and can be studied in detail with high performance laboratory setups on Earth, e.g. [Tsuda et al., 2013, Witze, 2014]. While sending humans is still in the future, due to the large distances, the mentioned risky landing, and the lack of return possibilities, humans depend on robotic missions for the in-situ exploration of extraterrestrial worlds. The scientific payload of these missions is selected to best suit the mission objectives with typical constraints coming from mass, volume, and energy budget. Due to the effort needed for successfully providing running space exploration instruments, it is important to get the most out of the instruments and to analyze the data in the best ways possible to maximize the scientific return.

One analytic technique with a high potential for the in-situ exploration of surfaces from extraterrestrial bodies is laser-induced breakdown spectroscopy (LIBS), e.g., [Cremers, 2007]. The principle of this technique is to focus high energy laser pulses onto the sample surface

which lead to material ablation and the generation of a luminous micro plasma. The plasma consists of excited atoms, ions, and simple molecules which emit characteristic radiation. Spectral analysis of the plasma light reveals tens to hundreds of unique emission lines from which the elemental composition of the target can be derived. LIBS has many advantages for the application on extraterrestrial bodies. First, it is sensitive to all geological major elements and also to most minor and trace elements including hydrogen. Furthermore, with LIBS, only optical access to the sample is required and acquisition times are short (seconds to a few minutes). These two properties allow for a frequent use of LIBS space exploration instruments in particular missions resulting in a large amount of returned data as seen for the ChemCam instrument [Maurice et al., 2016]. Depending on the mission and the size of the instrument, LIBS can measure samples at close-up distances of several centimeters or remotely at distances up to several meters. Usually, the laser spot has a diameter in the range of tens to hundreds of microns enabling the tracking of changes in elemental composition on a small scale. Also, a layer by layer investigation is possible when one position on the sample is measured by successive laser pulses. Due to these capabilities, the LIBS instrument ChemCam was selected for NASA's Mars Science Laboratory (MSL) and is successfully measuring the surface composition in Gale crater on Mars since landing in 2012 [Maurice et al., 2016].

Besides all these advantages, one drawback of LIBS is its low reproducibility due to the complexity of the laser matter interaction and the interaction of the particles in the plasma. The LIBS plasma and its emission characteristics therefore strongly depend on internal and external experimental conditions. Internal factors are called matrix effects which can be subdivided into physical (surface roughness, opacity, grain sizes, etc.) and chemical (sample composition) matrix effects. In particular, quantitative LIBS analysis of geological samples which are diverse in composition and physical properties suffers from matrix effects. Furthermore, changes in experimental conditions such as the laser irradiances strongly affect the LIBS plasma and complicate quantification, especially, when experimental conditions are less controllable, like on extraterrestrial bodies. Thus, there is a high interest in dedicated data analysis techniques which can reduce or compensate for these influences on LIBS data in particular for LIBS applications with a focus on geological targets. Several approaches were proposed and investigated in the past [Takahashi and Thornton, 2017]. In general, normalization procedures are required prior to the actual data analysis [Zorov et al., 2010]. Also statistical methods such as multivariate data analysis techniques (MVA) have become standard tools in the LIBS community, e.g. [Sirven et al., 2006]. Furthermore, the combination of LIBS with complementary spectroscopic techniques, such as Raman spectroscopy, is a possibility to assist the data analysis and to increase the scientific return [Wiens et al., 2005]. Raman spectroscopy also uses a laser for excitation and can measure molecular as well as lattice vibrations. Therefore, Raman data can deliver complementary information to the elemental information in LIBS data.

This work focuses on data analysis techniques and strategies for LIBS data mainly measured under Martian atmospheric conditions. As pointed out above, optimized data analysis is important for the scientific return of space exploration missions, and especially for LIBS, dedicated methods to overcome signal fluctuations due to changing experimental conditions and sample matrices are essential. For LIBS space exploration studies, Mars is of particular interest because of the ChemCam LIBS instrument on Mars and further planned LIBS instruments for upcoming in-situ exploration missions to Mars. Thus, most of the studies in this work were motivated by the exploration of the surface of Mars. The terrestrial planet

has already been the destination of several missions, however, there are still open questions about Mars' ancient climate and its habitability in the past and present. Nowadays, surface conditions on Mars are not favorable for life due the exposure to high energy radiation, the dry and cold climate, the thin atmosphere, and highly oxidizing conditions. Nevertheless, the search for present or past life on Mars is an important topic for the scientific community. The topography of Mars' surface shows features which can be related to past aqueous activity [Carr, 2012]. There are valley networks, river deltas, and alluvial fans. Furthermore, by spectroscopic analysis of Mars' surface from orbit, minerals were identified which form under the presence of liquid water [Ehlmann and Edwards, 2014]. Besides hydrated minerals, salts can play a key role in the detection of present or past liquid water [Brass, 1980] for which a comprehensive analysis of salts on the Martian surface is required.

In this work, mainly three studies with a Mars exploration background for three types of LIBS data analysis will be presented accompanied by one smaller study investigating LIBS in low pressure environments. The structure of this work is as follows: In Chapter 3, the basics and principles of LIBS and Raman spectroscopy will be introduced. Also, a brief overview of Mars is given and the capabilities of LIBS and Raman spectroscopy for application in space exploration are discussed in combination with information about the ChemCam instrument and LIBS and Raman instruments on upcoming missions. In Chapter 4, two MVA techniques, namely principal component analysis (PCA) and partial least squares regression (PLS-R), are explained. In Chapter 5, the used experimental setups are presented and their components are described. After these introductory chapters, the actual studies are presented and their outcomes discussed.

The first study in Chapter 6 deals with an approach for LIBS data normalization by using plasma parameters such as the plasma temperature and the electron density. This method was motivated by reported successful normalization of LIBS data with plasma parameters in terrestrial applications, e.g. [Panne et al., 1998]. Measurements were done in simulated Martian atmospheric conditions on samples with known composition which are relevant for Mars exploration. Different scenarios that require normalization were investigated:

- measurement-to-measurement fluctuations at otherwise constant experimental parameters
- univariate calibration curves from samples with different chemical matrices
- signal variations due to changing laser irradiances

Also different methods for plasma parameter derivation were evaluated.

In Chapter 7, a study about characteristics of LIBS data taken in low pressure environments is presented. Here, a special focus is on the degree of ionization in the plasma. The characteristics of LIBS in vacuum are relevant for missions to bodies without an atmosphere, for example, Earth' Moon or asteroids.

The second study which deals with data analysis techniques in a Mars exploration context is presented in Chapter 8 where MVA methods were applied for the identification of apatites ($Ca_5(PO_4)_3$(F, Cl)) and for chlorine quantification by means of molecular emissions (CaCl, CaF). Although LIBS is sensitive to all elements, it is challenged with some elements having high ionization energies and high transition energies. These elements have their strongest emission lines in the UV and only a few usually weak emission lines in the commonly used spectral ranges. Chlorine, fluorine, and phosphorus belong to this group of elements that are

difficult to detect with LIBS, and particular methods are necessary for their quantification. For the first study, PCA was applied whereas PLS-R was used in the second case with the focus on molecular emission bands.

In the last study in Chapter 9, LIBS and Raman data fusion as a potential method for improved identification of salts is investigated. LIBS and Raman spectroscopy deliver complementary data because Raman spectroscopy can give fingerprint spectra of molecules and is particularly sensitive to anionic end-members, for example, the sulfate anion SO_4^{2-}. LIBS on the other hand is particularly sensitive to cations. Mars relevant salts, such as carbonates, chlorides, perchlorates, and sulfates, were measured with miniaturized LIBS and Raman setups. First, pure sulfates and binary mixtures of them were investigated. Second, mixtures of the salt with a Mars relevant basalt were studied, and identification capabilities of LIBS and Raman only data in comparison to their combined data were evaluated. The outcomes of this study can be relevant for future combined LIBS and Raman space exploration instruments such as SuperCam which belongs to the scientific payload of NASA's Mars 2020 mission.

To summarize the outline of this work, three approaches for an improved LIBS data analysis in mostly Mars relevant configurations were investigated. The methods are in particular: (1) using plasma parameters for data normalization, (2) applying MVA techniques in combination with molecular emission bands for chlorine, fluorine, and phosphorus detection, and (3) combining LIBS data with complementary data from Raman spectroscopy. In one additional study, special characteristics such as the high degree of ionization of LIBS plasmas in low pressure environments were approached.

2 LIBS and Raman spectroscopy for Solar System exploration

With the invention and continued development of lasers since the 1960s, LIBS and Raman spectroscopy have found more and more applications, reaching from the steel or nuclear industry over medical applications to cultural heritage, e.g. [Hahn and Omenetto, 2012, Choo-Smith et al., 2002, Mauchien et al., 2014, Colomban, 2012]. Furthermore, both techniques have been frequently proposed for in-situ exploration of extraterrestrial bodies [Colao et al., 2004b, Knight et al., 2000, Sallé et al., 2004, Wang et al., 1995, Haskin et al., 1997, Sharma et al., 2003, Angel et al., 2012]. The ability for remote measurements without sample preparation is one of their major advantages for employing them on extraterrestrial surfaces of bodies in the Solar System.

2.1 Mars - neighbor of special interest

Although LIBS and Raman instruments are promising candidates for exploring several destinations in the Solar System, Mars has a special significance for this work due to the ChemCam LIBS instrument (Section 2.2) and further planned Raman and LIBS instruments for Mars exploration (Section 2.3). Most of the studies in this thesis were motivated by Mars and therefore a brief introduction to Earth's outer neighbor is given. If not indicated otherwise, the information in the following was taken from [Jaumann et al., 2018].

Exploring Mars is highly fascinating and of great interest because it is the most Earth-like planet known so far. But in contrast to Earth, where weathering and alteration of minerals is constantly proceeding, investigating Martian rocks can reveal geological processes up to four billion years ago. Therefore, the exploration of Mars can contribute to the understanding of Earth's history, too.

In Figure 2.1, an image of Mars taken during a Mars flyby by OSIRIS, which was a camera

Table 2.1: Some facts about Mars and its atmospheric composition.

Properties		**Atmospheric composition**	
Mass	6.417×10^{23} kg	Carbon dioxide CO_2	95.32 Vol%
Radius	3386 km	Nitrogen N_2	2.70 Vol%
Density	3934 kg/m^3	Argon Ar	1.60 Vol%
Duration of a Martian day (sol)	24 h, 37 min	Oxygen O_2	0.13 Vol%
Duration of a Martian year	669 sols	Carbon monoxide CO	0.08 Vol%
Average distance to sun	227.9×10^6 km	Water H_2O	0.03 Vol%
Obliquity	25.2 °		
Average ambient pressure at surface	6.35 hPa		

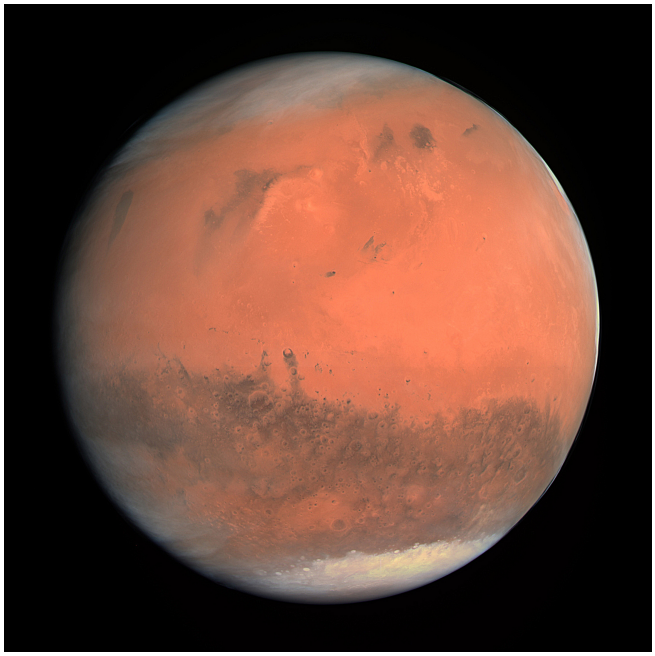

Figure 2.1: Mars in true colors as seen by OSIRIS with its orange (red), green, and blue color filters during a Mars flyby of ESA's Rosetta mission on its way to the comet Churyumov-Gerasimenko. *Image credit: ESA.*

system on ESA's Rosetta mission to the comet Churyumov-Gerasimenko, can be seen. The Martian topography is shown in Figure 2.2 where the difference in altitude between the southern highlands with several impact craters and volcanism and the northern lowlands becomes apparent. The Martian surface exhibits extremes in the Solar System: Mars has the largest mountain on a planet which is located in the volcanic region Tharsis and is called Olympus Mons having a height of 26 km. To the east of this region the largest canyon Valles Marineris in the Solar System that is 4000 km long, 200 km wide, and up to 7 km deep can be found.

Like Earth, Mars has seasons but as one Mars year is twice as long as one Earth year, they also last longer. Furthermore, Mars has extreme temperature fluctuations from $\approx 290\,\mathrm{K}$ at the equator in summer to $\approx 120\,\mathrm{K}$ in winter at the poles. The average temperature on Mars is 210 K. Depending on the season, the Martian south and north pole are covered with layers of water and carbon dioxide ice. Mars has an atmosphere, but in comparison to Earth's atmosphere it is much thinner with 6.5 hPa on average and is dominated by carbon dioxide. The whole atmospheric composition is listed in Table 2.1 (*right*). The atmosphere was probably thicker in the past, see details in next paragraphs. The reason for the atmosphere loss could be the absence of a self-induced magnetic field so that the Martian surface and atmosphere is not protected against high energetic cosmic radiation. Further properties of Mars are summarized in Table 2.1 (*left*).

Several Mars exploration missions have been collecting data either from orbit or in-situ that contribute to our knowledge of Mars. From 56 missions launched towards Mars, 26 missions were successful, indicating how challenging and risky reaching Mars can be. The first lander that succesfully returned data from the Martian surface was NASA's Viking 1 which landed on Mars in 1976 [Soffen and Snyder, 1976]. Since then, eight landers and

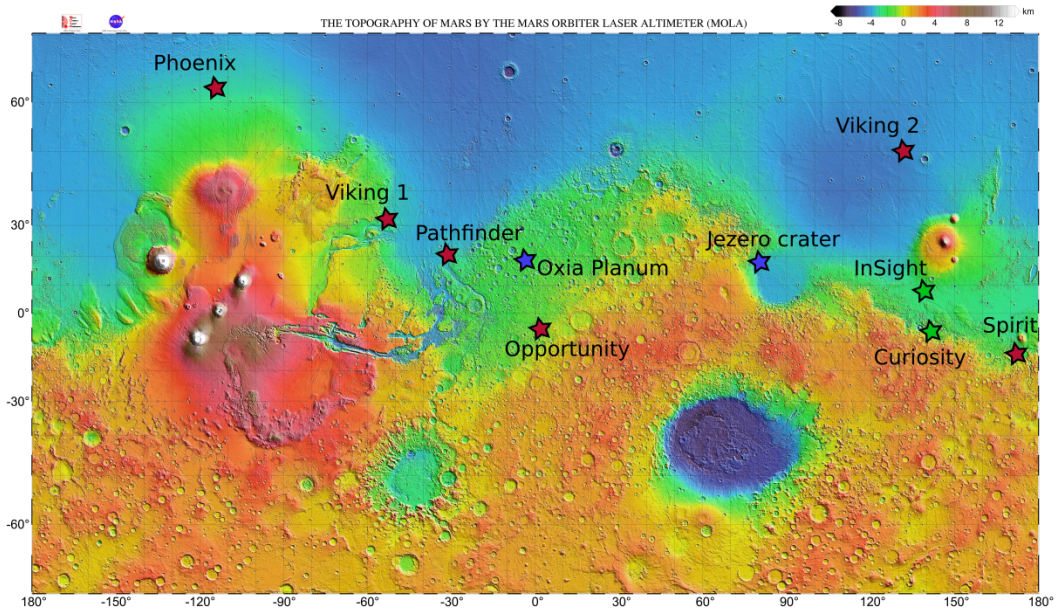

Figure 2.2: The Martian topography showing differences in altitude between the southern highlands with impact craters and volcanoes, and the northern lowlands. Landing sites of successful in-situ exploration missions are marked with a green star when they are still active (Curiosity (MSL) and Insight) and with a red star when they are not active anymore. The blue stars mark the landing sites of the ExoMars (probably Oxia Planum) and Mars 2020 (Jezero crater) mission, both scheduled to launch in 2020. *Image credit*: NASA/MGS/MOLA Science Team.

rovers reached the Martian surface without failure. Two of them are still active which are NASA's Mars Science Laboratory (MSL) rover [Grotzinger et al., 2012] and NASA's lander InSight [Banerdt et al., 2019]. The topography map of Mars in Figure 2.2 shows the landing sites of all successful Mars in-situ rovers and landers so far and also the two landing sites of two planned future missions, Mars 2020 [Wiens et al., 2017] and ExoMars [Rull et al., 2017]. Currently, Mars is further orbited by six active satellites: ExoMars TGO (ESA/Roscosmos), Mangalyaan Mars Orbiter Mission (ISRO), MAVEN (NASA), Mars Reconnaissance Orbiter (NASA), Mars Express (ESA), and Mars Odyssey (NASA).

Martian geology

This paragraph is mainly based on [Ehlmann and Edwards, 2014] where the authors review what is known from orbital and in-situ Mars exploration missions about the mineralogy of Mars' surface. Besides the missions to Mars, SNC (Shergottites, Nakhlites, Chassignites) meteorites contributed to the knowledge about Mars and its geology [McSween Jr., 1994, Treiman et al., 2000].

One mineralogical feature becomes apparent directly from the reddish color of Mars which is responsible for the additional name Red Planet: The surface of Mars is mostly covered in fine-grained dust composed of oxidized iron bearing minerals such as hematite (Fe_2O_3) and goethite ($FeO(OH)$). Based on dating the Martian surface, the geological history of Mars was divided in three eras: The Noachian 4.1 - 3.7 Gyrs before today; Hesperian 3.7 - 3.4 Gyrs before today; Amazonian 3.4 - today. Each of these ages is characterized by the formation of

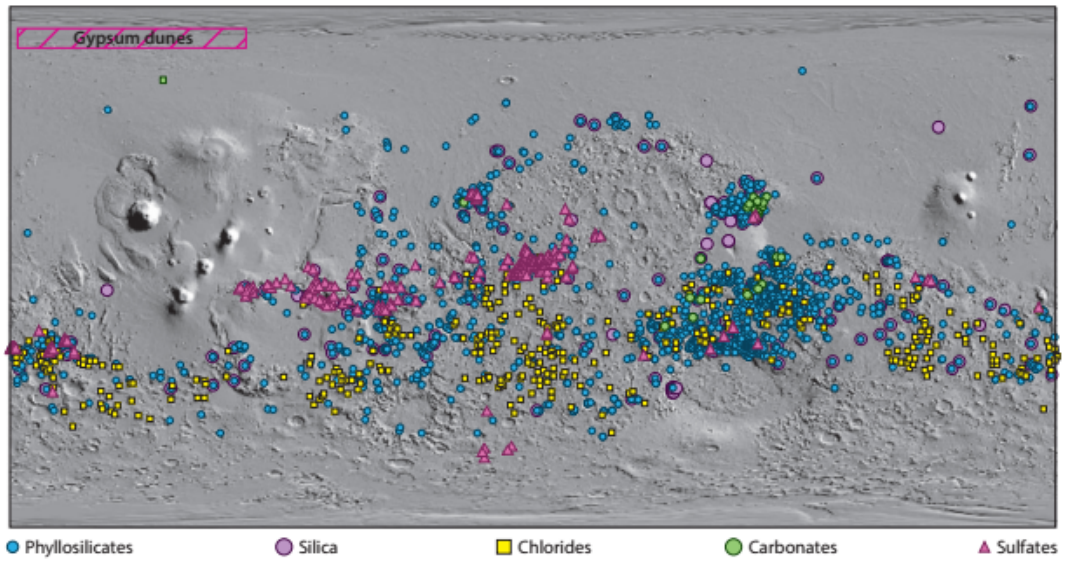

Figure 2.3: Overview of detections of secondary minerals on the Martian surface taken from [Ehlmann and Edwards, 2014]. These minerals formed most likely under wet conditions. Phyllosilicates are more widespread whereas sulfates were detected at regional locations. Carbonates are the less abundant salts detected from orbit.

certain mineral phases. However, in general the upper crust of Mars is mostly basaltic and therefore of an igneous origin. Minerals like plagioclase, pyroxene, and olivine are typically part of basalt and those were found on Mars in locally variable abundances indicating regional differences in the volcanism. Besides igneous basalt, a variety of further rock types can be found on Mars' surface such as sedimentary sandstone, mudstone, rocks formed by impacts, and evaporites. The elemental composition of those rocks is dominated by silicon and oxygen, followed by iron, magnesium, aluminum, calcium, and potassium. In lower abundances, elements such as titanium, chromium, manganese, sulfur, phosphorus, sodium, and chlorine can be found. Minerals that contain these elements and compose the Martian rocks are divided into primary minerals and secondary minerals. The first are the minerals composing basalt (olivine, pyroxene, plagioclase), sulfides, and iron oxides (magnetite and ilmenite). Secondary minerals are altered minerals because of processes such as weathering which can give evidence about the environmental conditions during the time of their formation. On Mars, these are, for example, the mentioned iron bearing minerals (hematite, goethite, akageneite) due to oxidation. Other secondary minerals found on Mars and formed under the influence of liquid water are phyllosilicates (clay minerals). Furthermore, evaporites such as salts (carbonates, sulfates, chlorides, and perchlorates) were found on Mars. Most of the altered minerals due to hydrothermal weathering were found in regions that formed in the late Noachian and early Hesperian age indicating the presence of liquid water in the early stages of Mars' lifetime, see further details in the next paragraph. In Figure 2.3, the global distribution of secondary minerals altered in aqueous conditions is shown. Phyllosilicates are more widespread on the Martian surface while others such as carbonates or sulfates occur more regional.

Water on Mars

There is great interest about past and present water on extraterrestrial bodies because of the important role it plays in making conditions on planets favorable for life. Nowadays, liquid water is unstable on the Martian surface due to a low surface pressure and low temperatures which range between 120 K and 290 K. However, landforms observed from orbit such as valley networks, river deltas, and alluvial fans give strong evidence for the presence of liquid water on Mars in the past [Baker et al., 1991,Carr, 2012]. The past existence of one or even two northern hemispheric oceans was also proposed [Baker et al., 1991, Clifford and Parker, 2001, Carr, 2012,Head et al., 2018]. Regarding the topography of present Mars (see Figure 2.2), features at the transition between the southern highlands and northern lowlands could be interpreted as shorelines [Parker et al., 1989, Citron et al., 2018].

Besides the observed landforms, some minerals detected on the Martian surface from orbit and in-situ give further evidence for water on Mars as they only form under wet conditions, see Figure 2.3. During the transition of the Noachian to the Hesperian age, a global climate change took place on Mars during which the aqueous activities on Mars' surface came to an end [Bibring et al., 2006, Murchie et al., 2009]. Dating of the geology of the Martian surface showed that clay minerals formed under presumed wet conditions early in the Martian history in the Noachian age. Sulfates were formed in more acidic conditions later on in the Hesperian age. In the Amazonian age, anhydrous ferric oxides formed to a large extent due to slow surface weathering without liquid water involved. At present, there is high evidence that Mars once was a wet planet, but it is still under discussion "how wet and warm" Mars really was [Wordsworth et al., 2015, Ramirez and Craddock, 2019, Niles, 2019]. While observations require water to be stable at the Martian surface for long times in the past, climate models are still challenged with adjusting the input parameters (atmospheric pressure, composition, etc.) to match their outcomes [Haberle et al., 2017].

Today, Mars exhibits the majority of its water in the cryosphere as subsurface permafrost in the high-latitude and polar regions as well as in form of water ice at the northern and southern polar caps [Lasue et al., 2013]. Mars' cryosphere has a thickness of up to ≈ 9 km in the equatorial region and 10 - 22 km at the poles [Clifford et al., 2010]. At its landing site close to the north pole, the Phoenix lander exposed subsurface water ice with its robotic arm and water droplets were observed condensing on the lander [Smith et al., 2009]. Seasonal varying amounts of water vapor were detected in the Martian atmosphere [Titov, 2002, Jakosky and Mellon, 2004] for which the origin and charateristics of its cycle are still under discussion [Shaposhnikov et al., 2019]. Another potential form of water on Mars are gullies [Malin and Edgett, 2000] and so called recurring slope lineae (RSL). The latter features are visible as dark channels, forming and growing in spring and summer, and vanishing during the colder seasons [McEwen et al., 2011,McEwen et al., 2014]. However, latest studies suggest that RSL are most likely dry as the available internal and atmospheric amounts of water are not enough for the observed activity of RSL [Dundas et al., 2017,Schmidt et al., 2017,Edwards and Piqueux, 2019]. Recently, evidence for liquid water below the ice layers of Mars' south pole was found from radar data [Orosei et al., 2018].

All of these detected and suggested forms of water on present Mars have in common that salts are most likely involved because the freezing point of water is lower if salts are dissolved in the water [Brass, 1980, Toner et al., 2015]. Therefore, dissolved salts can stabilize liquid water under the current conditions on Mars, at least temporarily. Several salts such as perchlorates,

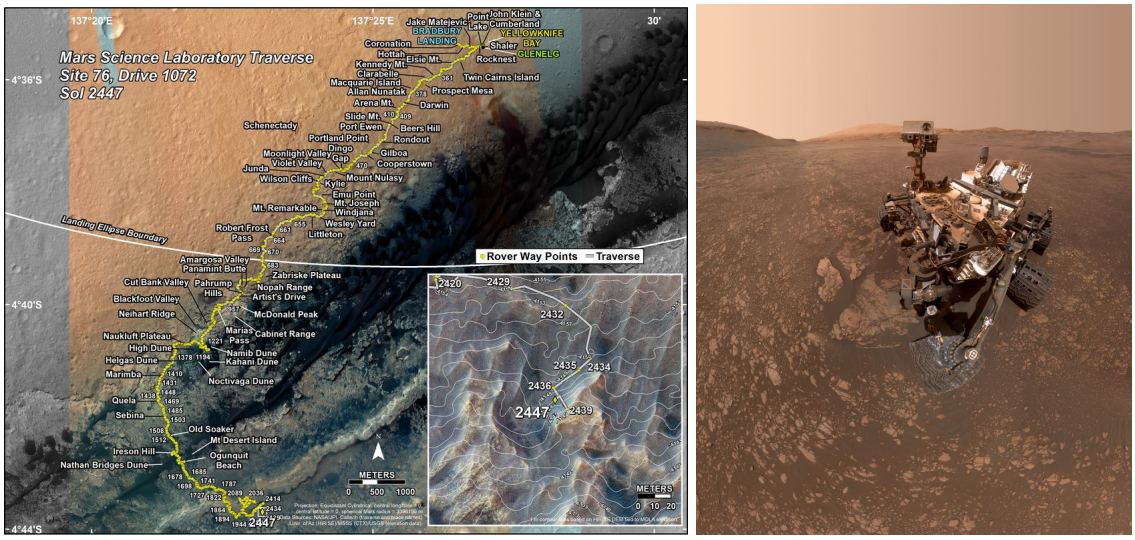

Figure 2.4: *Left*: The traverse of MSL through Gale crater up to sol 2447 (June 25, 2019). Image credit: NASA/JPL-Caltech/Univ. of Arizona. The recent position is located in the clay bearing unit. *Right*: Selfie of Curiosity taken on sol 2405 (May 12, 2019) in the clay bearing unit. The mast unit (MU) of ChemCam is located in the "head" of the rover. Image credit: NASA/JPL-Caltech/MSSS.

sulfates, carbonates, and chlorides have been detected on the Martian surface [Ehlmann and Edwards, 2014], see Figure 2.3. In the context of water detection on Mars, the presence of brines was verified in the exposed water ice at the Phoenix landing site [Hecht et al., 2009] and in spectral orbital data from four RLS sites [Ojha et al., 2015]. Regarding the possible stable liquid water reservoir below Mars' south pole, a high salinity of the water especially from dissolved perchlorates could be one responsible factor [Orosei et al., 2018].

2.2 ChemCam on MSL - the first LIBS instrument in space

In August 2012, the Mars Science Laboratory (MSL), also called *Curiosity* has landed in Gale crater, Mars [Grotzinger et al., 2014, Vasavada et al., 2014, Grotzinger et al., 2015]. Since then, the car-sized rover has travelled more than 20 km climbing *Aeolis Mons*, the mountain in the center of Gale crater, informally known as Mount Sharp. The whole traverse until sol 2447 (June 25, 2019) of the mission and a selfie of Curiosity is shown in Figure 2.4. The scientific payload of the rover includes several instruments to investigate if Mars once supported habitable conditions [Grotzinger et al., 2012]. The study of habitability is the primary science objective of MSL for which the presence of water is a key factor. Recently, the rover reached the clay bearing unit which obtained its name due to strong evidence for clays in orbital spectral data [Milliken et al., 2010, Fox et al., 2019]. This unit was one major reason for selecting Gale crater as landing site for MSL because clays form in the presence of water. One suite belonging to the scientific payload of Curiosity is ChemCam which stands for "chemistry and camera" and combines two instruments for remote sensing: a LIBS instrument and a remote micro imager (RMI) [Maurice et al., 2012, Wiens et al., 2012]. While LIBS provides the elemental composition of targets, high-resolution context images of the targeted

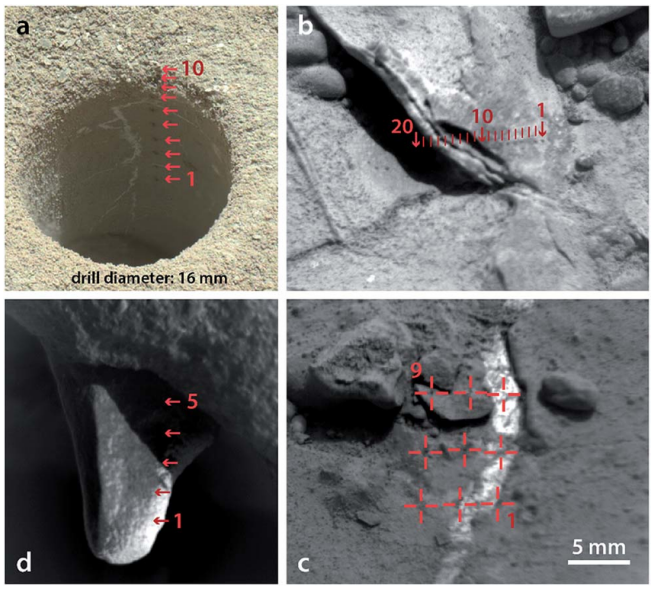

Figure 2.5: Examples of ChemCam rasters: *(a)* 10 × 1 raster in a drill hole, *(b)* 20 × 1 raster, *(c)* 3 × 3 raster, and *(d)* 5 × 1 raster. Each red arrow and reticle marks the position of one LIBS measurement and in some pictures the craters can be seen. With these rasters, it is possible to track changes in elemental composition on a small scale. The image was taken from [Maurice et al., 2016].

area are taken by the RMI. ChemCam has a telescopic system allowing to investigate targets in distances up to 7 m from the rover tracking variations in composition on a submilimeter scale. Usually, ChemCam takes measurements in raster scans of, for example, 3 × 3 or 1 × 10, see Figure 2.5.

The LIBS ChemCam instrument is divided into two parts: the mast unit (MU) and the body unit (BU) for which detailed descriptions can be found in [Maurice et al., 2012] and [Wiens et al., 2012], respectively. The MU contains the infrared laser that has a Nd:KWG crystal and a wavelength of 1067 nm. Its pulses have a duration of 5 ns and a pulse energy of ≈ 14 mJ after having passed the optics. The laser can be operated at repetition rates of 1-10 Hz. Also the telescope containing the focusing optics is part of the MU. Depending on the distance to the target, the laser spot size on the target's surface is between 300 μm and 550 μm. The collected plasma radiation is guided through optical fibers into the BU, separated in a demultiplexer according to wavelength, and then analyzed by the individual spectrometer. The BU has three spectrometers in total covering the following spectral ranges: ultra-violet (UV): 240-340 nm, violet(VIO): 385-469 nm, and visible and near-infrared (VNIR): 492-850 nm. In the three spectral ranges, the average resolutions are 0.049 nm per pixel (UV), 0.042 nm per pixel (VIO), and 0.21 nm per pixel (VNIR), respectively.

In the first six years of exploring Gale crater, ChemCam has measured more than 600 000 spectra [Lasue et al., 2019]. A summary of ChemCam findings during the first two years of the mission is given in [Maurice et al., 2016] and further recent overviews are provided by [Frydenvang et al., 2018, Schröder et al., 2018, Dehouck et al., 2019]. In the following selected examples of ChemCam discoveries relevant for this work will be presented.

ChemCam is the instrument that detected the elements boron and fluorine for the first time

in-situ on Mars [Gasda et al., 2017,Forni et al., 2015]. Boron was mainly detected in calcium sulfate-filled fractures giving new implications about the groundwater in Gale crater [Gasda et al., 2017]. Fluorine was detected by ChemCam indirectly via molecular emission bands of CaF [Forni et al., 2015] at several locations. At some of them, ChemCam also measured phosphorus leading to the identification of fluorapatite ($Ca_5(PO_4)_3F$) [Forni et al., 2015,Meslin et al., 2016]. But also other phases of fluorine were identified such as fluorite which is like apatite a secondary mineral giving indications about the environmental conditions of their formation. Furthermore, salts were analyzed with the ChemCam instrument which play as mentioned above a key role in the detection of present and past liquid water on Mars' surface. In a region called *Yellowknife Bay* along Curiosity's traverse, calcium sulfate veins were first detected by ChemCam [Nachon et al., 2014, Schröder et al., 2015, Rapin et al., 2016]. One example picture of such a vein can be seen in Figure 2.5 (c). Later on, ChemCam identified further calcium sulfate veins and also veins associated with magnesium and iron sulfate in *Pahrump Hills* [Nachon et al., 2017]. These veins are diagenetic features and some are wide spread while others were detected more locally, giving evidence for multiple episodes of fluid circulation. Like fluorine, chlorine can also be detected by molecular emission (CaCl) and was measured at several locations correlated with Na indicating the presence of halite (NaCl) [Forni et al., 2015, Thomas et al., 2018b]. The distribution of presumed halite detections along the traverse also suggests episodic groundwater activities. Furthermore, in laboratory studies, great effort was done to support salt detections on Mars [Schröder et al., 2013, Meslin et al., 2016, Schröder et al., 2017, Anderson et al., 2017].

2.3 Planned LIBS and Raman instruments

At present, ChemCam is the only extraterrestrially employed LIBS instrument and no Raman instrument was yet sent to another body in the Solar System. But there is a great interest in those instruments and there are several instruments currently being prepared for upcoming missions:

- **SuperCam** is the follow-up instrument of ChemCam and is part of the scientific payload of NASA's Mars 2020 mission to Jezero crater. For the first time, LIBS and Raman spectroscopy are combined in one space exploration instrument. Furthermore, SuperCam will have the capability for infrared and luminescence spectroscopy, and for recording sound with a microphone [Wiens et al., 2017]. For LIBS and Raman measurements, the same pulsed laser at its fundamental (1064 nm) for LIBS and in a frequency doubled configuration (532 nm) for Raman spectroscopy will be used to investigate targets up to 12 m away from the rover.
- **SHERLOC** (Scanning Habitable Environments with Raman & Luminescence for Organics & Chemicals) is a Raman instrument which will also be installed on the Mars 2020 rover [Beegle et al., 2015]. In contrast to SuperCam, SHERLOC is located on the rover's arm and uses a continuous wave (cw) laser in the UV at close-up distances of 48 mm with the focus on detecting organics.
- **RLS** (Raman Laser Spectrometer) is an instrument on the ExoMars rover which is a joint mission of ESA and Roskosmos [Rull et al., 2017]. The rover is equipped with a drill for sample collection from depths of up to 5 m below the Martian surface. RLS will analyze the crushed samples inside the rover's body with a green (532 nm) cw laser at a

fixed distance of ≈ 13 mm.

- **MarsCoDe** standing for Mars surface composition detection package is part of the payload of China's first Mars exploration mission (HX-1) and will measure LIBS and high resolution reflectance spectra [Ren et al., 2018]. The mission is scheduled for launch in 2020, too.
- A **LIBS** instrument is on-board of the rover that is part of India's Chandrayaan 2 mission to the Earth Moon [Laxmiprasad et al., 2013,Sundararajan, 2018]. The mission launched in July 2019 and the lander carrying the rover is scheduled to land in September 2019. During its planned lifetime of 1 lunar day (≈ 14 Earth days), the LIBS instrument will be used to map the elemental composition around the landing site. The sampling distance of the LIBS instrument is 200 mm with a fixed focal length.
- **RAX** (Raman for MMX) is a Raman instrument that will be part of JAXA's MMX (Martian Moons Exploration) mission scheduled to launch in 2024 [Hagelschuer et al., 2019]. A rover for the exploration of the surface of Phobos as well as an orbiter for Phobos and Deimos with the capability for sample collection and return to Earth belong to the MMX mission. RAX will be on-board of the rover (CNES and DLR) and is equipped with a focus mechanism for adjusting the working distance of 8 cm. The RAX laser is the same as the one developed for RLS, a continuous wave laser at 532 nm.

2.4 Combining LIBS and Raman spectroscopy

The combination of LIBS and Raman spectroscopy was implemented for several terrestrial studies and led, for example, to improved identification capabilities of inks [Hoehse et al., 2012] or explosives [Moros et al., 2011]. Also for extraterrestrial applications, combined LIBS and Raman spectroscopy instruments were proposed [Wiens et al., 2005,Clegg et al., 2014,Sharma et al., 2007, Misra et al., 2011, Kubitza et al., 2018] and with the SuperCam instrument on NASA's Mars 2020 mission, the first combined LIBS and Raman instrument for space exploration will be send to Mars [Wiens et al., 2017].

Regarding the hardware of a combined instrument, the two techniques can share some components as both need a laser, a spectrometer, and focusing and collection optics. For example, SuperCam has like ChemCam three spectrometers from which the VNIR spectral range will be shared for both LIBS and Raman signal detection. Furthermore, the SuperCam laser which is a Nd:YAG laser can be used for both types of excitation: With its fundamental wavelength (1064 nm) it will create LIBS plasmas and due to frequency doubling its second harmonic mode at 532 nm will be used for time-resolved Raman spectroscopy [Wiens et al., 2017].

Not only the possibility of sharing hardware components is a reason for joint analysis, moreover, the data is highly complementary. LIBS data yields information of elemental compositions of targets having a particular sensitivity to cationic elements, such as alkali and earth alkali metals. Although LIBS is generally capable to detect all elements, it is challenged with anionic elements such as halogens which have low signal intensities in the commonly used spectral ranges (200-900 nm). Raman spectroscopy, on the other hand, measures molecular and lattice vibrations that are mostly influenced by anionic groups such as the silicate or sulfate anion. In contrast to LIBS, cations can often only be detected indirectly with Raman

spectroscopy via small shifts of anionic Raman modes depending on the kind of cation.

Furthermore, LIBS and Raman spectroscopy provide similar capabilities that qualifies them for robotic exploration of extraterrestrial bodies. These are in particular short measurement times (seconds to minutes) and the capability to measure remotely at distances varying from centimeters up to several meters. However, for remote Raman spectroscopy, dust covering the surface can impede the measurements. With combined LIBS and Raman instruments such as SuperCam, this problem can be overcome by removing dust with the shock wave of LIBS plasmas prior to Raman measurements. However, the laser-matter interaction and the shock wave of LIBS measurements can alter the surface including the formation of new molecules [Schröder et al., 2019]. Thus, it can be that subsequent Raman measurements do not sample the original molecules and sample structure which is important to consider for the correct interpretation of Raman data.

3 Theory of LIBS and Raman spectroscopy

In this chapter, the basics of the two spectroscopic methods LIBS and Raman spectroscopy that were applied in the studies in this work are introduced. LIBS has been used for major parts of this thesis and is described in more detail than Raman spectroscopy. Both techniques rely on different physical effects and further information can be found in [Miziolek et al., 2006, Cremers and Radziemski, 2013, Long, 1977, McCreery, 2000].

3.1 LIBS

Laser-induced breakdown spectroscopy (LIBS) is a simultaneous multi-elemental analysis technique. A laser is focused onto the surface of the sample of interest and for high enough irradiances, usually above $\approx 1\,\mathrm{GW/cm^2}$ [Senesi, 2014], mass is ablated that evolves into a plasma. LIBS plasmas consist of electrons, excited atoms, ions, and simple molecules that emit characteristic radiation. Spectral analysis of this radiation provide spectra over a wide spectral range, from UV to NIR, with elemental emission lines and a few molecular emission bands. The information in the following section was mainly taken from [Cremers and Radziemski, 2013] if not indicated otherwise.

3.1.1 Ablation process and dynamics of the LIBS plasma

LIBS is a analytical method which is straightforward and whose experimental implementation is uncomplicated with a high ease of use. However, the simultaneous processes involved during plasma formation and evolution are complex and interact with each other. Furthermore, they are influenced by multiple external factors such as the physical and chemical characteristics of the sample (matrix effects), the laser parameters as well as the atmospheric conditions namely the pressure and composition. In Figure 3.1, relevant stages during the LIBS process are shown which will be further explained in the following steps: ablation processes, plasma expansion and absorption, plasma evolution and emission.

Ablation processes

The duration of the laser pulse is one key factor influencing the ablation process. In most common LIBS applications, lasers with pulse durations of a few nanoseconds are employed. However, there are also applications where shorter (picoseconds and even femtoseconds) pulse durations are used, e.g., [Eland et al., 2001, Sabsabi, 2007]. The ablation process with these short laser pulses strongly differs from those of nanosecond laser pulses. In general, it was found that the ablation process is most effective for short laser pulse duration ($<$ ns) and short laser wavelength (UV). However, lasers emitting in the NIR, especially Nd:YAG lasers at their fundamental wavelength of 1064 nm, are widely used in the LIBS community as these

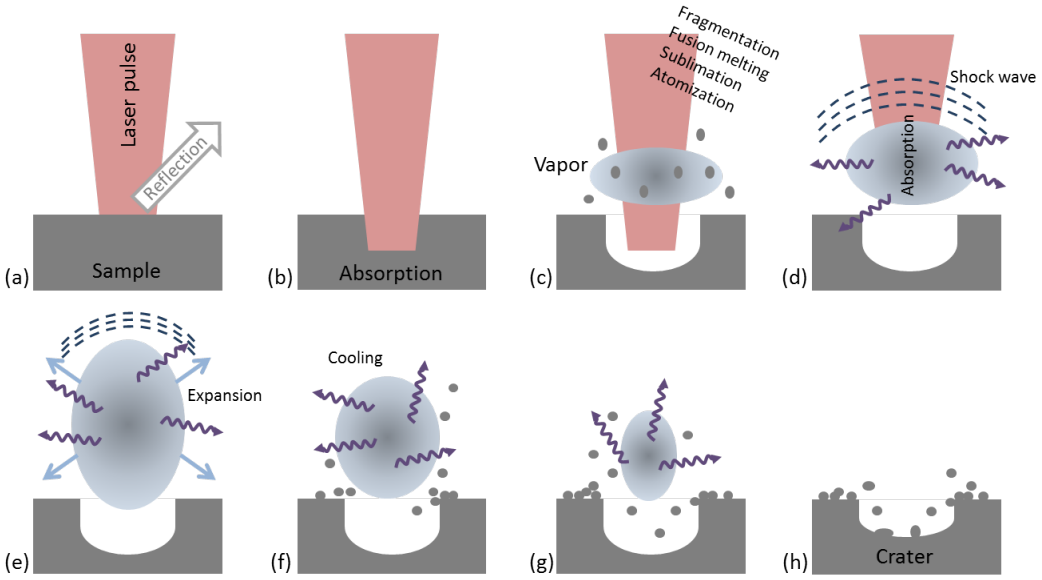

Figure 3.1: Main processes of LIBS plasma formation shown as sketches in chronological order, based on [Vadillo and Laserna, 2004]. The sequence corresponds to LIBS experiments investigating a solid sample with a nanosecond laser pulse and in the presence of a surrounding gas (no vacuum). *(a)* The laser radiation reaches the sample surface where some part is reflected. *(b)* The remaining radiation is absorbed by the sample which gets heated. *(c)* Material is ablated and vaporized. *(d)* The vaporized material absorbs the incoming laser radiation and evolves into an expanding plasma accompanied by a shock wave. Continuous emission is emitted due to bremsstrahlung and recombination. *(e)* The plasma further expands and emits characteristic emission from excited ions and atoms. *(f)* The plasma is not expanding anymore and cooling begins. *(g)* Plasma relaxation continues until the plasma completely vanishes. *(h)* After the LIBS process, a crater remains with the ablated material distributed around and inside.

lasers are reliable and compact [Senesi, 2014]. Since for the studies in this thesis nanosecond lasers with wavelengths in the NIR were used the following descriptions focus on the typical processes attributed to nanosecond pulse durations and laser wavelengths in the NIR. It has to be further noted that the following is not valid for LIBS plasmas in vacuum conditions.

When the high energy laser pulse reaches the sample surface, the first layers of material start to absorb the laser energy while some part of the incoming radiation is reflected (Figure 3.1(a)). The penetration depth and how much energy is absorbed and reflected by the material depend on the optical properties of the sample, in particular on the absorption coefficient. This coefficient depends on the laser wavelength and increases for higher electron densities. In the beginning, only a few electrons are available which can absorb energy of the laser beam by means of inverse bremsstrahlung. The velocity of the electrons increase and in collisions with atoms in the dense melt or already vapor the atoms become ionized resulting in more free electrons which can absorb the laser energy. The energy absorbance leads to further heating accompanied by fragmentation, fusion melting, sublimation, and ionization (Figure 3.1(b)-(c)). Ablated material vaporizes and is further heated by the laser pulse. Finally, the vapor evolves into a plasma which is characterized as a local assembly of atoms, ions, and free electrons overall being electrically neutral. Another process leading to the breakdown is multi-photon absorption which is more probable for short laser wavelengths. Multiple photons are absorbed by an atom whose energies are in sum larger than the ionization potential of the atom. For shorter laser wavelengths the number of photons needed for such a process is smaller enhancing the probability for multi-photon absorption.

Plasma expansion and absorption

In [Root, 1989], the modeling of post-breakdown phenomena is described in detail and the following is, if not indicated otherwise, based on this reference. Between the ablation process including vaporization and the establishment of an emitting plasma, the plasma passes several stages of expansion and absorption mainly influenced by the ambient atmosphere, laser irradiance, wavelength and duration of the laser pulse. The vaporization and ionization of the sample material takes place on a short time scale which is for nanosecond laser pulses only a fraction of the whole laser pulse. Therefore, absorption of the laser energy can take place in the propagating plasma front, shielding the target from further interaction with the laser radiation (Figure 3.1(d)), called *plasma shielding*. Laser absorption by the plasma plays a key role for the propagating plasma and determines the subsequent plasma evolution. Usually, the surrounding gas is transparent to the laser irradiation, but if the gas becomes ionized it can also absorb laser radiation because of free electrons. Primarily, the laser radiation is absorbed by inverse bremsstrahlung (electron-neutral and electron-ion). Which type of absorption is predominant, depends on the temperature: At low temperatures less electrons are available and electron-neutral inverse bremsstrahlung dominates.

Turning to the features of the propagating plasma, one has to consider the main interactions that are happening: A shock wave evolves in the surrounding gas due to the expansion of a high pressure plasma and energy is transferred from the plasma to the ambient gas by means of thermal conduction, radiative transfer, and heating from the shock wave. All these mechanisms contributing to the plasma expansion are influenced by multiple parameters such as the laser parameters (intensity, wavelength, spot size), composition inside the plasma plume, and composition and pressure of the ambient gas. Figure 3.2 shows a sketch of the general concept

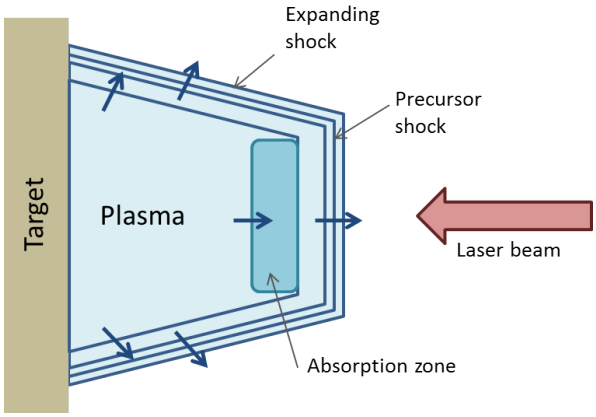

Figure 3.2: The general features of a propagating plasma not representing a specific type of the three absorption wave types, adapted from [Root, 1989]. The important zones are precursor shock, absorption region and the plasma behind the propagating zones which expand away from the target surface. The plasma expands in all directions. This configuration does not aim to reveal plasma shapes, it rather serves as a visualization of important zones evolving during the plasma expansion.

of a propagating absorption wave. The important zones are the shock front, the absorption zone, and the expanding plasma. Depending on the laser irradiance, one distinguishes between three different types of expanding waves and their laser irradiance absorption mechanisms:

- Laser-supported combustion wave (LSC):
  At relatively low laser irradiation ($< 20\,\mathrm{MW/cm^2}$), a precursor shock front is initially separated from the absorption zone and the plasma front. Both propagate into the shock front whose edges are transparent for the laser radiation.
- Laser-supported detonation wave (LSD):
  At intermediate laser irradiance (10-2000 $\mathrm{MW/cm^2}$), the shock wave is strong and the shocked gas is hot enough to absorb laser radiation without requiring additional heating by energy transport from plasma. This leads to an absorption front directly behind the shock front traveling at the same velocity. Such a wave is similar to the chemical detonation wave.
- Laser-supported radiation wave (LSR):
  At relatively high laser irradiance ($> 600\,\mathrm{MW/cm^2}$), the initial plasma is hot enough to heat the surrounding gas which can absorb laser irradiance prior to the emergence of a shock front. This evolves in an energy balance between laser heating of the plasma and plasma heating of the surrounding cold gas. Increasing the laser energy, for example, leads to an increased expansion velocity and a longer plasma lifetime at the same temperature [Yalçin et al., 1999].

The described classes of absorption waves result in laser-induced plasmas with specific distributions of temperature, pressure, and particle densities. It has to be further noted that the transitions between the three types are smooth and that also ambient conditions (pressure and gas composition) have an influence on the absorption processes. The given irradiances were derived for Earth atmospheric conditions and might be different for Martian atmospheric conditions. However, in the studies in this work, laser irradiances were high enough to produce

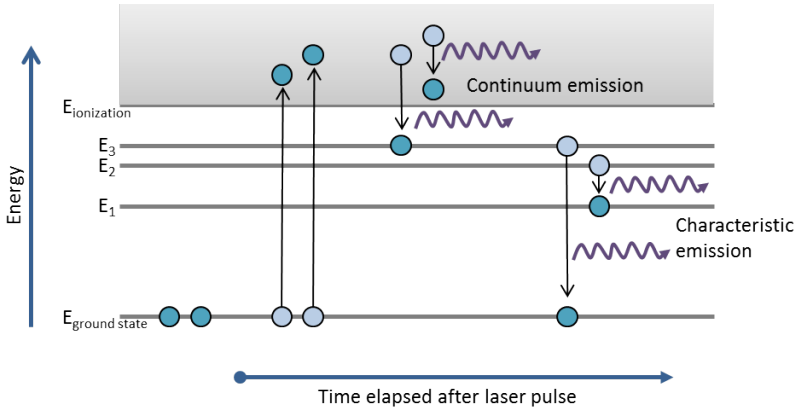

Figure 3.3: Occuring electronic transitions during the plasma lifetime exemplarily shown with a four energy level system adapted from [Schröder, 2012]. Before plasma initiation, electrons are in the ground state of the atom. After the breakdown, ionization takes place giving rise to free electrons. During plasma relaxation, bremsstrahlung and recombination lead to continuous emission. Later on, characteristic atomic and ionic emissions occur due to electronic transitions between distinct energy levels. Note that the time scale, thus, the plasma lifetime, strongly varies for different ambient pressures.

at least LSD waves or even LSR waves.

Plasma evolution and emission

The expansion of a LIBS plasma slows down until its internal pressure is similar to the pressure of the shockwave. The expansion stops and subsequently, the plasma starts to cool and to decay releasing energy through radiation and thermal conduction (Figure 3.1(e)-(g)). Therefore, LIBS plasmas are much smaller in Earth atmospheric conditions (millimeter range) than in Mars atmospheric conditions with a lower pressure (a few centimeters) [Cremers, 2007].

In Figure 3.3, the occurring electronic transitions during the plasma evolution are shown by means of a schematic sketch. In the first stages of the plasma lifetime directly after plasma initiation, its emission is dominated by continuum emission due to bremsstrahlung and recombination. Bremsstrahlung arises from photons emitted by accelerated or decelerated electrons mainly through collisions. These are free-free transitions resulting in a continuous emission. During recombination, a free electron is captured by an ion or atom at a particular energy level releasing its remaining kinetic energy in form of photons. Recombination is a free-bound transition also producing continuous emission. In a next stage, the plasma starts to cool and bound-bound transitions within excited ions and atoms occur, leading to characteristic emission lines. First, emissions from ions dominate the plasma emission due to a high degree of ionization in the early plasma. During the relaxation, recombination and a decreasing plasma temperature lead to a less ionized plasma and neutral emissions become the dominant type of emission. Furthermore, simple molecules can form in the plasma which usually have several modes that overlap and reveal characteristic molecular bands in the spectra.

The LIBS plasma is a transient state and its parameters temperature, electron density, and particle distributions change not only over time but also spatially. Usually, a hot plasma center and colder outer regions are assumed. The plasma shape and its gradients strongly depend

on atmospheric conditions (pressure and composition). Also, the time scale on which plasma parameters auch as temperature and electron density change, is pressure dependent [Iida, 1990, Effenberger and Scott, 2010]. In terrestrial atmospheric conditions, a LIBS plasma has a much longer lifetime than in a reduced pressure environment such as Mars conditions ($\approx 7\,\mathrm{hPa}$) [Brennetot et al., 2003, Colao et al., 2004a]. In general, the plasma lifetime decreases whereas the plasma size increases when going to lower pressures. However, for pressures below $\approx 1\,\mathrm{hPa}$ the plasma size decreases again due to a free expansion in this pressure regime. It was found that Mars atmospheric pressure is close to ideal for LIBS data analysis [Knight et al., 2000] because it is a kind of trade-off between plasma size and lifetime with less self-absorption (more explanation in Section 3.1.2) and continuum emission as in Earth atmospheric conditions.

3.1.2 Broadening mechanisms of emission lines

Investigating the broadening of spectral emission lines in LIBS data can give insight to plasma conditions. The most important contributions to the shape of an emission line are the natural, the Doppler and the pressure broadening [Cremers and Radziemski, 2013].

- Natural broadening is a consequence of the Heisenberg uncertainty principle. Because of Heisenberg's uncertainty principle excited states have finite lifetimes Δt or from the quantum mechanical point of view a finite width in energy ΔE and their product underlies $\Delta E \Delta t \sim \hbar$. The result of this relation is a spread of the emitted frequency. For typical lifetimes of excited states in LIBS plasmas, the contribution of natural broadening is negligible and not observable with common spectrometers [Cremers and Radziemski, 2013].
- Doppler broadening originates from the correspondent effect due to movements of the emitting particle. The spread on the wavelength depends on absolute temperature and atomic mass:
$$\Delta\lambda_D = 7.2 \times 10^{-7} (T/M)^{1/2} \lambda_0, \tag{3.1}$$
with T, M, and λ_0 denoting the temperature, the mass of the emitter, and the center wavelength, respectively. The shape of emission lines that are broadened because of the Doppler effect can be described by a Gaussian function.
- Stark broadening is a sub-category of pressure broadening, which describes in general perturbations of the emitting particle due to interactions with surrounding particles. In case of Stark broadening, the surrounding particles are charged particles and their electric field leads to splitting of energy levels of the emitting particle. This splitting is known as the Stark effect. Besides symmetric line broadening also asymmetric broadening and shifts of the central wavelength can occur due to the Stark effect. Stark broadened emission lines show a Lorentzian shape.

Besides the internal broadening mechanisms, also instrumental broadening occurs which can be usually described by a Gaussian. Thus, emission lines from LIBS plasmas can be fitted by a Voigt function which is the convolution of a Lorentzian and a Gaussian.

In plasma spectroscopy, also self-absorption of an emission line can contribute to the broadening. Self-absorption is a resonance effect meaning that an emitted photon can be reabsorbed by an atom of the same species as it was emitted from. The decay to different energy levels or deexcitation due to collisions can impede its contribution to the intensity of the emis-

sion line belonging to the absorbed photon. The effect of self-absorption increases when many particles of the same species are abundant. Furthermore, transitions to ground states are more prone to self-absorption. In some cases, self-absorption becomes apparent as a central dip in the emission line which is then called self-reversal. This effect is also an indication for strong temperature gradients inside the plasma. The absorption of emitted photons is higher in colder regions because there, more low-lying energy levels are occupied which can absorb the photon.

3.1.3 Local thermodynamic equilibrium (LTE)

The types of energy that contribute to a LIBS plasma are kinetic, excitation, ionization, and radiative energies while their corresponding distributions and densities are described by the Maxwell, Boltzmann, Saha, and Planck function, respectively (e.g. [Thorne et al., 1999, Tognoni et al., 2006]). The equations corresponding to each distribution are:

- **Maxwell-Boltzmann** (velocity)

$$f(v)dv = \left(\frac{m}{2\pi k_B T}\right)^{3/2} \exp\left(-\frac{E(v)}{k_B T}\right) 4\pi v^2 dv, \tag{3.2}$$

  with v: velocity of the particle, m: mass of the particle, k_B: Boltzmann constant, $E(v)$: kinetic energy of the particle.

- **Boltzmann** (excitation)

$$\frac{n_i}{n} = \frac{g_i}{U(T)} \exp\left(-\frac{E_i}{k_B T}\right), \tag{3.3}$$

  with n_i: number of atoms/ions in excitation state i, n: number of all atoms/ions (same species), g_i: degeneracy of the energy level E_i, $U(T)$: partition function.

- **Saha-Eggert** (ionization)

$$\frac{n^Z}{n^{Z-1}} = \frac{(2\pi m_e k_B T)^{3/2}}{n_e h^3} \frac{2U(T)^Z}{U(T)^{Z-1}} \exp\left(-\frac{E_{ion} - \Delta E_{ion}}{k_B T}\right), \tag{3.4}$$

  with n^Z: number of particles in ionization state Z, m_e: electron mass, h: Planck's constant, E_{ion}: ionization potential, ΔE_{ion}: correction of ionization potential for high densities.

- **Planck's law** (thermal equilibrium)

$$\rho(\lambda, T) = \frac{8\pi hc}{\lambda^5} \frac{1}{\exp(hc/\lambda k_B T) - 1} \quad \text{in } \mathrm{Jm^{-3}nm^{-1}}, \tag{3.5}$$

  with ρ: spectral radiance, c: speed of light, λ: wavelength.

Each of these distributions can be in equilibrium independently of the others. They have their own temperature T which is the electron temperature, excitation temperature, and ionization temperature corresponding to the Maxwell-Boltzmann distribution (only velocities of electrons, for other particles it is called gas temperature), the Boltzmann, and the Saha distribution, respectively. In complete thermodynamic equilibrium (TE) these temperatures would have the same value. Physically, in such a TE, the excitation of atoms by collisions

with electrons is equal to the reverse de-activation process, ionization by collisions is equal to three-body collisional recombination, and the emission of radiation is equal to the absorption of radiation. The latter is valid for a radiative equilibrium, which is the black body radiation according to Planck's law. However, this is not the case for typical LIBS plasmas which have tens to hundreds of emission lines. These have often low lying energy levels with high Einstein coefficients of spontaneous emission which are depopulated fast and deviate therefore from radiative equilibrium. Hence, for LIBS plasmas, a state in radiative disequilibrium is a more realistic description. Such a state is called local thermodynamic equilibrium (LTE) in which the remaining distributions (equations (3.2)-(3.4)) are in equilibrium, at least locally. A condition for the existence of LTE is that collisional processes have to exceed the radiative processes or in other words: The probability for de-excitation of an excited state by collision with an electron has to be higher than by spontaneous emission of radiation. The requirement of large electron collisional rates implies that the electron density needs to be high for LIBS plasmas in LTE. Therefore, a condition for LTE can be formulated based on a minimum electron density and can be derived from rate equations for population and depopulation of excited states. The result is known as the McWhirter criterion:

$$n_e \gg 1.6 \times 10^{18} \sqrt{T} (\Delta E)^3 m^{-3}, \tag{3.6}$$

where ΔE is the highest energy difference of all ajacent energy levels of species inside the plasma which is usually the energy difference between a ground state and the first excited energy level. Nevertheless, the criterion is a necessary but not sufficient condition to hold LTE in LIBS plasmas. Additional conditions for LTE next to the McWhirter criterion are necessary and detailed considerations can be found in [Cristoforetti et al., 2010] or summarized in the review [Hahn and Omenetto, 2010]. They discuss mainly two additional requirements addressing the time and the space domain. The temporal variation of the plasma temperature T and the electron density n_e has to be small in comparison to the times that the system needs to reach excitation and ionization equilibrium. On the other hand, the length of variation for the two parameters T and n_e should be larger than the distance that a particle can travel during the relaxation time τ_{relax}. This time is defined as the time that a system needs to achieve a new equilibrium after energy was applied to it. LIBS plasmas have another characteristic time, the expansion time τ_{exp} and if $\tau_{\text{relax}} < \tau_{\text{exp}}$ the plasma is in equilibrium [Hahn and Omenetto, 2010]. However, the calculations of these times and additional conditions are complex if at all possible and in most works only the McWhirter criterion is used to justify LTE conditions. Further evidence for the existence of LTE can be found in the determination of the plasma temperature which will be introduced in the following section.

3.1.4 Plasma parameters

In LIBS plasma diagnostics, the most important and discussed parameters are the plasma temperature T and the electron density n_e. Here, methods for their calculation will be presented. The topic is widely discussed in the literature and detailed theoretical derivations can become arbitrary complex. The most cited and detailed references on general plasma spectroscopy are the books [Griem, 1964, Griem, 1997]. However, there is newer literature dealing with the topic in general and with the focus on LIBS plasmas. The following is based on [Holtgreven, 1968, Thorne et al., 1999, Cremers and Radziemski, 2013, Tognoni et al., 2006, Hahn and Omenetto, 2010, Aragón and Aguilera, 2008b].

Plasma temperature T

The most common methods for the calculation of the plasma temperature from LIBS data are the Boltzmann plot and the Saha-Boltzmann plot methods. For both methods, the plasma has to be in LTE. There are several other approaches, almost all assuming LTE conditions that are listed, for example, in [Hahn and Omenetto, 2010].

The Boltzmann plot method

The occupation of an excited level i among n^S atoms of the same species S, which means same element and ionization stage, is given by the Boltzmann equation

$$\frac{n_i^S}{n^S} = \frac{g_i}{U^S(T)}\exp(-E_i/k_BT) \tag{3.7}$$

with the partition function over all states i of the atom

$$U^S = \sum_i g_i \exp(-E_i/k_BT) \tag{3.8}$$

with n_i^S denoting the number of atoms in state i, E_i and g_i are the energy and the degeneracy of state i, respectively, k_B is the Boltzmann constant and T the temperature. Since this is a local description in the plasma, thus for a certain volume, the n^S and n_i^S are densities [m^{-3}]. The total spectrally integrated radiant emissivity [$\mathrm{W\,m^{-3}\,sr^{-1}}$] of a transition from state i to state j is given by:

$$\epsilon_{ij} = \frac{hc}{4\pi}\frac{A_{ij}g_i}{\lambda_{ij}}\frac{n^S}{U^S(T)}\exp(-E_i/k_BT). \tag{3.9}$$

Another formulation in terms of the integrated line intensity (number of transitions per unit volume per unit time) is:

$$I_{ij} = n_i^S A_{ij} = \frac{A_{ij}g_i}{U^S(T)} n^S \exp(-E_i/k_BT). \tag{3.10}$$

The two formulations consider different kinds of intensities where strictly speaking the latter formulation does not deal with an intensity that is known as energy per time. The detectors that are used in LIBS experiments, mainly CCD devices, detect photons [Tognoni et al., 2006]. These are guided to different pixels on the detector depending on their wavelength and therefore also on their energy. Thus, the pixel position, but not the measured charge in a pixel depends on the energy of an incoming photon. In order to measure emissivity as it is assumed in equation (3.9) it is necessary to multiply the number of photons that arrive in one pixel by the corresponding photon energy hc/λ. To distinguish between emissivity and intensity measured directly with the detectors, the label I_{ij} in equation (3.10) is changed to N_{ij} which stands for the number of photons that were emitted during the electronic transition $i \to j$ [Tognoni et al., 2006].

$$N_{ij} = n_i^S A_{ij} = \frac{A_{ij}g_i}{U^S(T)} n^S \exp(-E_i/k_BT). \tag{3.11}$$

Taking the logarithm of equation (3.11), the following expression is obtained:

$$\ln\left(\frac{N_{ij}}{A_{ij}g_i}\right) = -\frac{1}{k_B T}E_i + \ln\left(\frac{n^S}{U^S(T)}\right). \tag{3.12}$$

An additional constant that compensates for the units in the logarithms was dropped here, since the sum of both terms in the logarithm has no units and the constant would not change anything in the result for the temperature. The equation above describes a straight line in a coordinate system with the upper level energies E_i on the abscissa and the left side of equation (3.12) on the ordinate. The slope is $-1\backslash k_B T$ and the ordinate intercept is the logarithm on the right side of equation (3.12). For the measurement of intensities in terms of N_{ij}, emission lines are fitted with Voigt profiles. Thus, together with the transition probabilities, upper level energies, and degeneracies of the emission lines, the plasma temperature can be obtained by the slope of a linear regression. Using this method for the temperature calculation, no prior knowledge of the total elemental concentration or the partition function is necessary. The best choice for the emission lines are those transitions that have large differences in the upper level energies. Furthermore, ground-state emissions should be avoided due to their tendency for self-absorption. It is also favorable to chose emissions in a narrow spectral range to avoid errors that arise from differences in the detectors sensitivity.

Instead of using multiple transitions and the linear regression, a pair of transitions can also be sufficient for the calculation of the plasma temperature, which is known as the Boltzmann two-line method. In that case, one considers the ratio of the two measured signals, N_{ij} and N_{mn}, according to equation (3.11) and takes again the logarithm. Solving for the temperature gives:

$$T = \frac{E_i - E_m}{k_B \ln\left(\frac{N_{mn}\, g_i A_{ij}}{N_{ij}\, g_m A_{mn}}\right)}. \tag{3.13}$$

Considering the relative error of the temperature, the main disadvantage of this method becomes apparent:

$$\frac{\Delta T}{T} = \frac{k_B T}{E_i - E_m}\frac{\Delta R}{R}, \tag{3.14}$$

where R stands for the ratio of the measured emission lines and their transition probabilities: $R = \frac{N_{mn}\, g_i A_{ij}}{N_{ij}\, g_m A_{mn}}$. The transition probabilities can have high uncertainties up to 50% and control the uncertainty of the temperature since $k_B T$ and $E_i - E_m$ are often of the same order. The method should only be used when not enough emission lines from one species can be observed since the large error is reduced by the linear regression of multiple transitions which are separated well in their excitation energies.

Saha-Boltzmann plots

The Saha-Eggert equation which describes the ionization equilibrium can be derived by applying a Boltzmann distribution to ionization states. It gives the ratio of number densities in two consecutive ionization stages of the same element:

$$\frac{n^z}{n^{z-1}} = \frac{(2\pi m_e k_B T)^{3/2}}{n_e h^3}\frac{2U(T)^Z}{U(T)^{Z-1}}\exp\left(-\frac{E_{ion} - \Delta E_{ion}}{k_B T}\right). \tag{3.15}$$

The number Z denotes the ionization stage (I: neutral, II: single ionized...). The energies are the ionization energy E_{ion} for the Z^{th} ionization stage and ΔE_{ion} is a reduction of the ionization energy due to electric fields from charged particles in the plasma and has only to be considered for high density plasmas.

Combining the Boltzmann equation (3.7) and the Saha-Eggert equation (3.15), leads to a method where emission lines from the same element of consecutive ionization stages can be used to deduce the plasma temperature. Therefore, one solves equation (3.4) for n^Z in terms of n^{Z-1} and substitutes n^S in equation (3.7) by it. This procedure is repeated for decreasing Z and in a next step, terms are summarized by the following definitions:

$$E_i^{z*} = E_i^Z + \sum_{k=0}^{Z-1} \left(E_{ion}^k - \Delta E_{ion}^k \right) \tag{3.16}$$

$$\ln\left(\frac{N_{ij}}{A_{ij}gi}\right)^* = \ln\left(\frac{N_{ij}}{A_{ij}gi}\right) - Z\ln\left(\frac{2(2\pi m_e k_B T)^{3/2}}{n_e h^3}\right). \tag{3.17}$$

Using these, the familiar form of the Boltzmann plot equation is obtained:

$$\ln\left(\frac{N_{ij}}{A_{ij}g_i}\right)^* = -\frac{1}{k_B T}E_i^* + \ln\left(\frac{n^0}{U^0}\right). \tag{3.18}$$

In order to proceed as for the Boltzmann plot method, one has to modify the coordinate axes for ionic transitions. Often only neutrals and singly ionized particles occur in typical LIBS plasmas occur, which limits this method to the cases $Z = 1, 2$. The subtracted term in equation (3.17) depends weakly on the electron density n_e and the temperature T. The electron density has to be obtained with other methods (see following paragraph). To overcome the dependence on T, an iterative approach has to be applied. With an initial guess for T, a linear regression can be performed whose slope gives a new temperature. This iteration has to be performed until the temperature value converges. A two-line approach is also possible with such a combination of Saha-Eggert and Boltzmann equation. As mentioned for the Boltzmann plot method, the error of the temperature can be reduced, when the transitions are well separated in their upper level energy. With the Saha-Boltzmann plot method the effective difference in energy becomes even larger due to the addition of the ionization potential. Thus, this method is favored, in case there are enough suitable emission lines in the spectrum.

Electron density n_e

The determination of the electron density n_e is mainly based on Stark broadening of emission lines and is independent of LTE existence. Assuming that Stark broadening is the main broadening mechanism and dominates over the others, n_e can be derived from the width of a line which is related to n_e in the whole plasma. One has to differ between the linear and the quadratic Stark effect depending on the number of electrons in the atom. The linear effect is a first order perturbation of the electric field and is therefore stronger than the quadratic effect which is a second order perturbation. Their calculations are rather complex and details can be found in [Griem, 1997] where also parameters that determine the effects are listed for several emissions.

Stark broadening of hydrogen lines and hydrogenic ion lines is described by the linear Stark effect and the relation to the electron density n_e is given by:

$$n_e = C(n_e, T)\Delta\lambda_{\mathrm{S}}^{3/2}. \tag{3.19}$$

where $\Delta\lambda_S$ is the full width at half maximum (FWHM) and $C(n_e, T)$ is a function that depends weakly on electron density and temperature. Values for $C(n_e, T)$ are listed in [Griem, 1997] for several temperatures and reference electron densities.

Atoms and ions with more than one electron are subject to the quadratic Stark effect [Tognoni et al., 2006]:

$$\Delta\lambda_S \approx 2w\frac{n_e}{10^{16}}\left[1 + 1.75A(\frac{n_e}{10^{16}})^{1/4}(1 - BN_{\mathrm{D}}^{-1/3})\right]. \tag{3.20}$$

The parameter w is the electron impact width and A is the ion broadening parameter. The first part in brackets describes electron interactions while the second part denotes ion interactions. In the ionic interaction part, two other parameters appear, namely B, a coefficient that is 1.2 or 0.75 for ionic or neutral transitions, and N_{D} that is the number of particles in the Debye sphere. Another common and equivalent formulation of the quadratic Stark effect is [Hahn and Omenetto, 2010]:

$$\Delta\lambda_S \approx 2w\left(\frac{n_e}{10^{16}}\right)\left[1 + 1.75\,\alpha\,10^{-4}n_e^{1/4}(1 - 0.068\,n_e^{1/6}T^{-1/2})\right]. \tag{3.21}$$

Here, α is also known as the ion broadening parameter and by comparison A and α are related as $A = 10^{-4}n_e^{1/4}\alpha$. Furthermore, a third common and equivalent formulation for the Stark width exists [Aragón and Aguilera, 2008b]:

$$\Delta\lambda_{\mathrm{S}} \approx 2w\frac{n_e}{10^{16}}\left[1 + 1.75A(1 - 0.75R)\right]. \tag{3.22}$$

In this formulation the parameter R is the ratio between the mean ion distance and the Debye radius. All three equations describe the same relation at a reference electron density of $10^{16}\,\mathrm{cm}^{-3}$ and with the number of particles in the Debye sphere:

$$N_D = 1.72 \times 10^9\frac{T^{3/2}}{n_e^{1/2}}. \tag{3.23}$$

In LIBS plasmas, the Stark effect is mainly caused by collisions with electrons due to large electron densities. Therefore, contributions from ion collisions can be neglected in most cases, which means in particular $\alpha = 0$ and all formulations (3.20)-(3.22) reduce to:

$$\Delta\lambda_{\mathrm{S}} = 2w(\frac{n_e}{10^{16}}). \tag{3.24}$$

If Stark broadening is not dominating the line broadening, those approaches do not apply. This is, in particular, the case in low density plasmas where less particle interactions take place. Experimentally, those plasmas can evolve in low pressure environments and broadening mechanisms were investigated, for example, in [Gornushkin et al., 1999].

3.1.5 LIBS measurements in practice

In general, the hardware components of LIBS instruments are a high-energy pulsed laser, focusing and collecting optics, and a spectrometer. Depending on the application, different types of focusing mechanisms can be implemented in order to realize a specific distance between the sample and the collecting optics. These distances can range from close-up distances of a few centimeters to remote distances of several meters. The choice of the spectrometer also depends on the particular application. Wide spectral ranges with high spectral resolution can be covered, for example, by using multiple spectrometers in Czerny-Turner configuration or by echelle spectrometers which consist of two dispersive elements. In this work, both types were used and are described in more detail in Chapter 5.

It is favorable to do time-gated LIBS measurements in order to gate out the continuum radiation and to obtain better signal to noise ratios (SNR) of the emission features of interest. As shown in Figure 3.3, the type of emission changes over time and the characteristic emission lines are dominating after a certain delay from plasma initiation. Also in-depth studies of plasma dynamics are only possible with time-gated measurements because of the transient character of the LIBS plasma. Usually, for time-gated measurements, ICCDs are employed. For major parts of this thesis, an ICCD with the possibility to do time-gated measurements was used. With ICCD cameras, on the other hand, the emission from several spectra is necessary to obtain good SNRs. Regarding the use of ICCDs for LIBS instruments for space exploration missions, their size, mass, and power consumption usually exceed the typical constraints on these parameters.

In most LIBS applications, the emission of multiple LIBS plasmas from the same position on the sample is integrated. This is as mentioned necessary when ICCD cameras are employed but is otherwise also a standard procedure in LIBS measurements to increase the SNR and to compensate for variations. Also, for the studies in this work, several (20-30) laser shots were used to investigate one position on the sample surface. In LIBS applications with presumably homogeneous samples, several positions on the sample can be measured in order to further compensate for variations. However, when investigating geological samples which are usually heterogeneous, this proceeding is not feasible. Furthermore, the successive creation of LIBS plasmas at the same position can be used for depth profiling, too, as with each LIBS plasma the crater becomes deeper and layer by layer can be investigated. However, with a certain crater depth, effects of plasma confinement can occur due to the crater walls limiting the space of expansion for the LIBS plasma, e.g. [Hahn and Omenetto, 2012].

The LIBS plasma is complex and influenced by several internal as well as external factors. This leads to a low reproducibility which challenges quantification of elemental abundances, in particular on diverse geological samples [Senesi, 2014]. In univariate calibration models, the intensity of a single emission line is related to its elemental concentration in samples with known composition in order to predict elemental abundances of unknown samples. These models are especially prone to influences from changing experimental conditions and varying sample matrices. By now, statistical methods such as multivariate data analysis (MVA) tools which account for the whole spectrum have established as a standard for LIBS data analysis, e.g., [Sirven et al., 2006] and more about specific MVA techniques used in this work will be introduced in Chapter 4.

3.2 Raman spectroscopy

In this section, the basics of Raman spectroscopy will be introduced mostly relying on [McCreery, 2000, Dubessy et al., 2012]. The Raman effect is an inelastic scattering process in which the energy of the scattered photon is either enhanced (anti-Stokes) or reduced (Stokes). The energy shift is small and can be understood as absorbed or induced molecular or lattice vibrations (phonons). Raman scattered radiation gives characteristic spectra relative to the excitation laser line. In comparison to the elastic scattering without energy transfer (Rayleigh scattering), the Raman effect is weak: Only one of 10^6 scattered photons is shifted in energy due to the Raman effect. That is why Raman spectrometers require a high sensitivity and why narrow optical filters have to be used to suppress the detection of Rayleigh scattered photons. In Figure 3.4, the processes of Raman scattering (Stokes and anti-Stokes) are shown schematically in comparison to other types of interactions between radiation and molecules. In infrared absorption, absorption, and fluorescence, real electronic or vibrational states are involved whereas for Rayleigh, Stokes, and anti-Stokes scattering virtual states are part of the concept. For Rayleigh scattering, the same energy level as before the excitation of the virtual state is occupied. In case of Stokes scattering, the excited virtual state decays into a state with higher energy than before the excitation emitting therefore a photon with less energy. For anti-Stokes scattering, the system is in a state with higher energy before the excitation than after the decay of the virtual state. This transition is accompanied by the emission of a photon with enhanced energy.

Depending on the wavelength of the laser and the energy level distributions in the molecules of the sample, fluorescence can hide Raman signals or even impede their detection. There are several studies about strategies to avoid the interference of fluorescence in Raman spectra, e.g. [Wei et al., 2015]. One relatively straightforward approach is to select an excitation wavelength that has less to little absorption in the investigated materials. For biological samples, excitations in the deep UV are favorable [Beegle et al., 2015]. In case of mineral identification with Raman spectroscopy, lasers with wavelengths in the visible spectral range are frequently chosen. The Raman studies in this work focus on minerals relevant for Mars exploration and a laser with a wavelength of 532 nm was used for excitation which is the frequency doubled mode of Nd:YAG lasers. These lasers are established, reliable, and compact as mentioned before which is a further reason for their frequent use.

As for LIBS, only optical access to the sample is required for Raman measurements. However, at large distances with a large field of view, ambient light can impede the detection of Raman signals due to the low intensities of Raman signals when a continuous wave laser is used. Nevertheless, remote measurements at distances up to several meters are still possible when pulsed lasers in combination with time-gated detection are used [Beyssac et al., 2019]. Another aspect which can impede Raman measurements is the penetration depth of the laser radiation in the target. This depends on the absorption coefficient of the material and the particular laser wavelength. Dust layers of μm thickness can already prevent Raman scattering. Therefore, as mentioned in Section 2.4, the combination of LIBS and Raman spectroscopy in space exploration instruments is useful because the shock wave of LIBS measurements can remove dust.

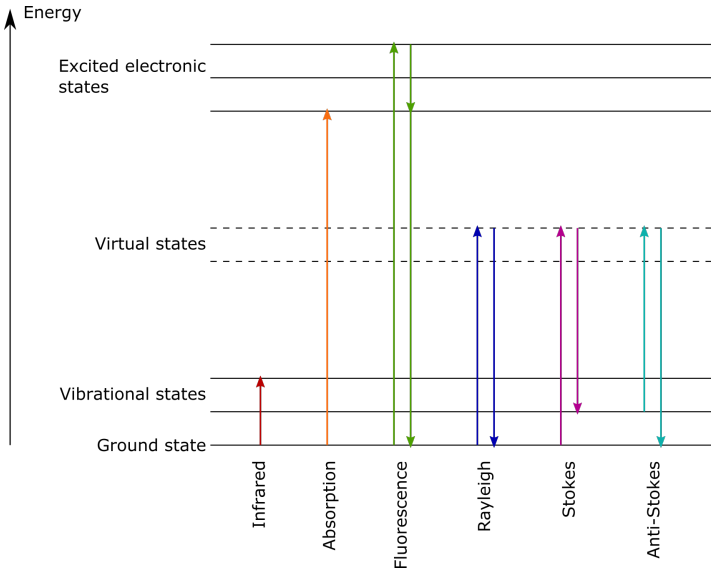

Figure 3.4: Schematic representation of energy states of a molecule with processes that occur during the interaction with light. Transitions between real vibrational and electronic states leading are subject to infrared spectroscopy, absorption (resonance), and fluorescence. The scattering processes (Rayleigh and Raman) involve the excitation to a virtual state.

3.2.1 The Raman effect - classical description

In this section based on [Dubessy et al., 2012], the classical description of the Raman effect will be introduced, which relies on the interaction of an incoming electric field with a scatterer with internal vibrational and/or rotational modes. When the incoming radiation reaches the scatterer, its electric field induces a dipole moment in the scatterer because its electrons oscillate around its nuclei with the same frequency as the incoming electric field. Therefore, the scatterer emits radiation at the same wavelength as the incoming radiation which is known as the elastic Rayleigh scattering process. However, internal modes of the scatterer can modulate the oscillation of the induced dipole moment resulting in the emission of radiation with wavelengths different from those of the incoming radiation. Such a scattering process with changing wavelengths is an inelastic scattering process and can bei either Stokes or anti-Stokes scattering. In terms of equations, this effect can be derived from the dipole moment that is induced by the electric field of the incoming radiation. This field can be described by:

$$\mathbf{E} = \mathbf{E_0} \cos(\omega t), \tag{3.25}$$

The dipole moment $\mathbf{p}$ which is induced in the scatterer is proportional to the incoming electric field:

$$\mathbf{p} = \boldsymbol{\alpha} \cdot \mathbf{E}, \tag{3.26}$$

where $\boldsymbol{\alpha}$ is the tensor of polarizability describing the distortion of the molecule in each direction due to an external electric field. For systems with spherical symmetry such as single atoms, the polarizability is the same in all directions and can be described by a scalar. For molecules with reduced symmetry, the polarizability is different for different directions and has to be described by a tensor whose entries depend on symmetries. For a large difference between ω and resonance frequencies in the molecule, only small displacements have to be considered

and the entries α_{ij} of the polarizability tensor can be expanded in a Taylor series:

$$\alpha_{ij} = \alpha_{ij}(0) + \sum_k \left(\frac{\partial \alpha_{ij}}{\partial q_k}\right)_0 \cdot q_k + \frac{1}{2}\sum_{k,l}\left(\frac{\partial^2 \alpha_{ij}}{\partial q_k \partial q_l}\right)_0 \cdot q_k q_l ..., \tag{3.27}$$

with q_k, q_l being the coordinates of the normal modes of the molecular. Taking only first order contributions into account and assuming the normal modes to be harmonic with $q_k(t) = q_{k0}\cos(\omega_k t)$, the polarizability tensor is inserted in equation (3.26) leading to the following time-dependent induced dipole moment:

$$\mathbf{p} = \left(\boldsymbol{\alpha_0} + \sum_k \left(\frac{\partial \boldsymbol{\alpha}}{\partial q_k}\right)_0 \cdot q_{k0}\cos(\omega_k t)\right) \cdot \mathbf{E_0}\cos(\omega t) \tag{3.28}$$

$$= \boldsymbol{\alpha_0}\mathbf{E_0}\underbrace{\cos(\omega t)}_{\text{Rayleigh}} + \frac{1}{2}\mathbf{E_0}\sum_k \left(\frac{\partial \boldsymbol{\alpha}}{\partial q_k}\right)_0 \cdot q_{k0}(\underbrace{\cos[(\omega+\omega_k)t]}_{\text{anti-Stokes}} + \underbrace{\cos[(\omega-\omega_k)t]}_{\text{Stokes}}) \tag{3.29}$$

The resulting dipole moment consists of three summands characterized by oscillations at three different frequencies. The first has the same frequency ω as the incoming electric field and represents therefore the Rayleigh scattering. The remaining two have frequencies that are shifted relatively to ω. These oscillations correspond to Stokes (ω-ω_k) and anti-Stokes (ω+ω_k) scattering. What can be further seen in the representation of the induced dipole moment is that a change of the polarizability of the molecule during the scattering process is required for Raman scattering. Otherwise, the term $(\frac{\partial \boldsymbol{\alpha}}{\partial q})_0$ would be zero and only Rayleigh scattering occurs. In IR spectroscopy, which also measures molecular vibrations (see Figure 3.4), the selection rule for IR active vibrations is different as here the electric dipole moment has to change. For molecules that have symmetries with an inversion center, Raman active modes are usually IR inactive and vice versa. More about Raman modes will be discussed in the following section. One closing remark about the classical description of the Raman effect is about the intensity ratio of Stokes and anti-Stokes emissions. From the classical approach, this ratio would be one, however, this was not observed in experiments. It was found that the ratio depends on temperature which can be derived from theory only in a quantum mechanical approach. To conclude, there are limitations of the classical approach but it covers all aspects relevant for the studies in this work.

3.2.2 Raman modes

Identifying Raman active modes of a molecule is a complex and extensive task and I will only briefly introduce the concept. Detailed information can be found in [Cotton, 2003, Tuschel, 2014]. As mentioned before, a change of polarizability is necessary for a vibrational mode being Raman active. This property depends on the symmetries of the molecule which can be described by group theory which is a purely mathematical theory. The concept of group theory is to summarize symmetry operations in specific groups with same symmetries. These groups are also called point groups and each of these groups has an associated character table where the symmetries are listed. An example for such a table is given in Table 3.1 for the T_d point group (tetrahedal symmetry) to which, for example, the sulfate anion (SO_4^{2-}) belongs. The first column of character tables contains so called *Mulliken* symbols which correspond to symmetry species. For example, the symbols A and B denote one dimensional symmetries

Table 3.1: Example of a character table: Point group T_d to which the sulfate anion (SO_4^{2-}) belongs. From: `https://www.webqc.org/symmetrypointgroup-td.html`

T_d	E	$8C_3$	$3C_2$	$6S_4$	$6\sigma_d$	linear	quadratic
A_1	1	1	1	1	1		$x^2 + y^2 + z^2$
A_2	1	1	1	-1	-1		
E	2	-1	2	0	0		$(2z^2\text{-}x^2\text{-}y^2, x^2\text{-}y^2)$
T_1	3	0	-1	1	-1	(R_x, R_y, R_z)	
T_2	3	0	-1	-1	1	(T_x, T_y, T_z)	(xy; xz; yz)

which are non-degenerated. The rows in character tables contain individual irreducible representations of symmetry species based on symmetry operations whose designations are given in the top row of character tables. Evaluating how the molecule behaves under the symmetry operations belonging to its point group leads to a irreducible representation of its vibrations. With the help of the character tables, it can be identified which modes of the irreducible representation are Raman (and also IR) active modes. Usually, the last two columns give the axes in linear and quadratic functions (in cartesian coordinates) for which the symmetry operations are valid. Here, the column with the quadratic functions shows binary products of axes along which the polarizability will change during the molecular vibration. Consequently, Raman active modes can be identified by means of this column. IR active modes can be identified by the column with the linear functions which give the axes along the electric dipole moment changes. Identifying the particular point group of a molecule and finding the irreducible representation of the normal modes can be an extensive and complex task, especially for molecules that consist of several atoms. In case of the free sulfate anion, nine modes of internal vibrations were found according to the irreducible representation: $A_1 + E + 2\,T_2$ [Mabrouk et al., 2013]. All models are Raman active, but only the T_2 mode is IR active. The Raman modes are denoted as: ν_1 (A_1, non-degenerated symmetric stretching mode), ν_2 (E, double degenerated bending vibration), ν_3 (T_2, threefold degenerated anti-symmetric stretching mode), and ν_4 (T_2, threefold degenerated bending vibration).

3.2.3 Raman measurements in practice

The hardware components of Raman setups are in general a laser, focusing and collecting optics, a filter to suppress Rayleigh radiation, and a spectrometer. In contrast to LIBS, Raman spectra can be measured either with a pulsed laser or with a cw laser. For remote measurements at large distances, ambient light can superimpose the weak Raman signals. This can be avoided by doing time-gated pulsed Raman measurements which will be done, for example, by the SuperCam instrument [Wiens et al., 2017]. In this configuration, the use of an ICCD is necessary which can increase the size, mass, and power consumption of Raman instruments. The time-gating has further advantage that also fluorescence can be mostly gated out [Beyssac et al., 2019]. Another configuration is the one of the RLS instrument which analyses crushed samples inside the rover shielded from ambient light [Rull et al., 2017]. At a fixed close-up distance of $\approx 13\,\text{mm}$, large parts of the scattered light can be collected and used for analysis. In this case, a cw laser is used for excitation and a CCD for the detection. However, Raman measurements are less flexible in such a configuration as sample preparation and also a quite complex focussing process to optimize the Raman signal are necessary. A

further configuration of a Raman instrument for space exploration is the use of a cw laser at close-up distances of a few centimeters with a focusing mechanism for which the RAX instrument is an example [Hagelschuer et al., 2019].

In laboratory setups, confocal microscopes with close sample distances are often part of Raman instruments which allow to measure Raman signals at a high spatial resolution. There are further techniques in laboratory setups which can increase the efficiency of Raman measurements, which are, however, not relevant for current space exploration instruments. In general, spectrometers with comparatively large entrance slits are favorable in order to ensure a high throughput at the cost of a high spectral resolution. Also, selecting long integration times and averaging of several Raman spectra are possibilities to increase the SNRs of Raman measurements. However, for long integration times, a superimposed background signal, e.g., ambient light or fluorescence can saturate the detector [Kubitza et al., 2019b]. In this case, several Raman spectra can be integrated.

While the LIBS plasma is complex and quantification can be challenging, Raman measurements can suffer from weak signal intensities and superimposing fluorescence. As mentioned before, one strategy to reduce fluorescence is to chose the exciation wavelength depending on the type of samples and the mission objective. One example is the SHERLOC instrument that uses an UV laser for the detection of organics [Beegle et al., 2015]. Besides the fluorescence, correct data interpretation can be challenging when the sample is inhomogeneous on the scale of the laser spot size. In this case, the spectra contain mixed signals which has to be considered in the data analysis. As for LIBS, MVA methods are standard tools for Raman data analysis which can improve the identification capabilities of Raman spectroscopy, e.g. [Lopez-Reyes et al., 2014].

4 Multivariate data analysis

Spectroscopic methods such as LIBS and Raman spectroscopy are often used to identify unknown substances and to quantify their constituents. For the first purpose, the whole spectrum has to be considered in order to account for all present elements (LIBS) or vibrations (Raman). For humans doing the analysis by hand, this can be an extensive task and slight changes of peak areas or positions can be overseen or misinterpreted. In case of quantification, peak intensities can be used to set up univariate linear regression models where known concentrations are related to the peak area of one certain emission line. The main limitation of univariate calibration, however, is that matrix effects or changing experimental conditions affecting the whole spectrum are not considered in these models. Thus, methods that account for the whole spectrum instead of only one spectral feature such as multivariate data analysis (MVA) have become standard techniques for sample identification and quantification. There is a great number of studies where MVA methods have been used for identification and/or quantification in LIBS [Sirven et al., 2006, Sirven et al., 2007, Schröder et al., 2013, Zhang et al., 2018] and Raman experiments, e.g. [Ryder et al., 2000, López-Díez et al., 2003, Lopez-Reyes et al., 2014, Hanke et al., 2016]. Today, MVA methods are standard for the analysis of LIBS and Raman data. Another example for the use of MVA for LIBS data is the analysis of the ChemCam data: Major elements are predicted with a combination of partial least-squares regression (PLS-R) and independent component analysis (ICA) [Forni et al., 2013, Clegg et al., 2017].

In the following, two MVA techniques that were used in this thesis will be introduced. For classification principal component analysis (PCA) while for quantification Partial least squares regression (PLS-R) was applied. The next two sections are based on [Kessler, 2007, Esbensen et al., 2010] and more details can be found in these references.

4.1 Principal component analysis (PCA)

PCA reveals pattern and structures in high-dimensional data by projecting it onto new axes, the so-called principal components (PCs). This transformation reduces the dimensionality and summarizes the important features of the data. PCA computes correlations in the input data and works unsupervised without any prior knowledge about sample groups.

The new axes in PCA are found successively. If a dataset consists of n samples and each has m characteristics, in spectroscopy these are the wavelength channels, the first component points in the direction of the largest variance between the samples in a m-dimensional coordinate system. Figure 4.1 visualizes this in the simple case of m=2 dimensions. The following components are found in the same way but with the additional requirement that all components have to be uncorrelated to each other which means geometrically orthogonal.

Mathematically, an Eigenwert problem has to be solved to find the new axes. In Figure 4.2,

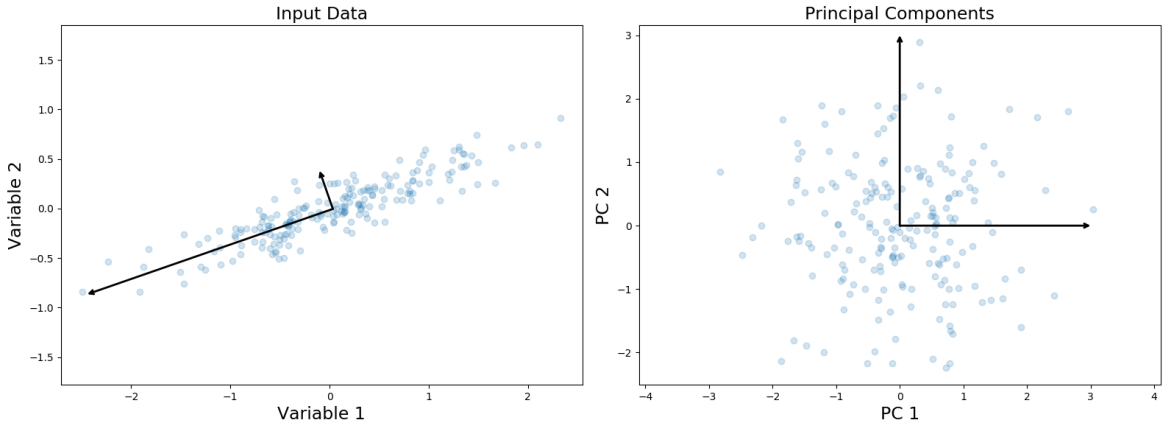

Figure 4.1: *Left*: Original two dimensional data with arrows that correspond to the directions of the first two components along the largest variance in the original data and their length to the standard deviation, respectively. *Right*: Representation of the data on the new axes. Here, the data points have the largest possible distanceto each other.

this problem is visualized. The original data matrix $\mathbf{X}$ is factorized in the dot product of the scores matrix $\mathbf{T}$ and the loading matrix $\mathbf{P}$ plus the residuals matrix $\mathbf{E}$.

$$\mathbf{X} = \mathbf{T}\mathbf{P}^{\mathbf{T}} + \mathbf{E} \tag{4.1}$$

Mean centering of the data before building the PCA model is recommended, otherwise the first component would represent only the mean of all input samples. The dimensions of $\mathbf{T}$ and $\mathbf{P}$ are determined by the number of components k. Every component is a linear combination of the original data and the belonging coefficients are stored in $\mathbf{P}$. Thus $\mathbf{P}$ can be interpreted as a rotation matrix from the original axes to the new system in which the new data points for every sample, the scores, are given in $\mathbf{T}$. Remaining variance in the data that is not explained by the previously found PCs is stored in the residual matrix $\mathbf{E}$. After a certain number of PCs were found, this matrix contains only noise. Once a PCA model is built, the data of unknown samples can be projected into the model by applying $\mathbf{P}$ and their obtained scores can assign them to samples or clusters of samples used to build the PCA model. In spectroscopic data, the number of PCs k is often much smaller than the usually large number of wavelength channels m. Thus, dimensions of datasets can be efficiently reduced by PCA. Plots of the loadings of single components of PCAs from spectroscopic data appear as spectra showing the correlations of each wavelength channel with the particular component. This allows to identify also correlations between spectral features in the data, for example, in LIBS data emission lines of the same element usually correlate with each other.

Unless otherwise stated, the commercial software *The Unscrambler* was used to perform the MVAs in this thesis. For PCA, it emloys the non-linear iterative partial least squares (NIPALS) algorithm to solve the Eigenvalue problem in equation (4.1). NIPALS is an iterative method initialized with some values which are expected to converge after several repetitions of the in the following described stepwise algorithm (based on [Kessler, 2007]).

1. The staring point is the mean centered data matrix $\mathbf{X}$ and the first principal component i = 1.
2. As a first estimate of the scores vector $\mathbf{t}_i$ the column with the largest variance of $\mathbf{X}$ is

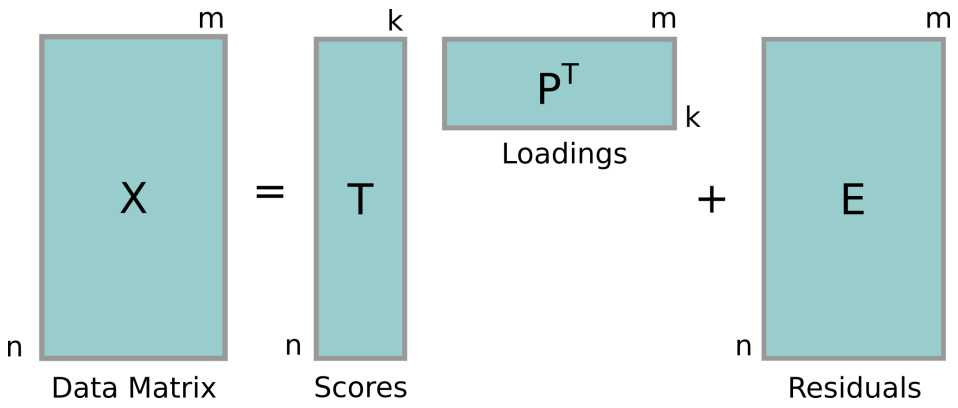

Figure 4.2: Eigenvalue problem of the PCA. The dimensionality in the representation in terms of scores and loadings is reduced as the original data $\mathbf{X}$ is now represented in linear combinations. The sketch was adapted from [Kessler, 2007]

taken.

3. For $\mathbf{t}_i$, the unnormalized loadings vector $\mathbf{p'}_i$ is calculated by projecting $\mathbf{X}_i$ on $\mathbf{t}_i$:

$$\mathbf{p'}_i = \frac{\mathbf{X_i^T t_i}}{|\mathbf{t_i^T t_i}|} \tag{4.2}$$

4. In order to build up a coordinate system $\mathbf{p'}_i$ has to be normalized to unity:

$$\mathbf{p}_i = \frac{\mathbf{p'}_i}{\sqrt{\mathbf{p_i'^T p_i'}}} \tag{4.3}$$

5. With this new loadings vector the estimate of $\mathbf{t}_i$ is expected to improve by projecting in turn $\mathbf{X}_i$ on $\mathbf{p}_i$:

$$\mathbf{t}_i = \frac{\mathbf{X}_i \mathbf{p}_i}{\mathbf{p^T}_i \mathbf{p}_i} \tag{4.4}$$

6. This new score vector is compared with the previous score vector by means of their eigenvalues:

$$\tau_i = \mathbf{t^T}_i \mathbf{t}_i \tag{4.5}$$

7. Convergence is achieved when the difference between the eigenvalues drops below a defined threshold. If the difference remains larger, the procedure starts again at 3.

8. In case of convergence, the principal component i has the loadings vector $\mathbf{p}_i$ and the scores vector $\mathbf{t}_i$ whose information has to be subtracted from the data matrix:

$$\mathbf{X}_{i+1} = \mathbf{X}_i - \mathbf{t}_i \mathbf{p^T}_i \tag{4.6}$$

   For the next component $i = i + 1$ the algorithm starts with $\mathbf{X}_{i+1}$.

The number of principal components k has to be fixed in advance and determines how often the process is repeated, in particular when $i = k$. The choice of number of PCs is essential for the robustness of a PCA model. There should be enough PCs to explain the majority of

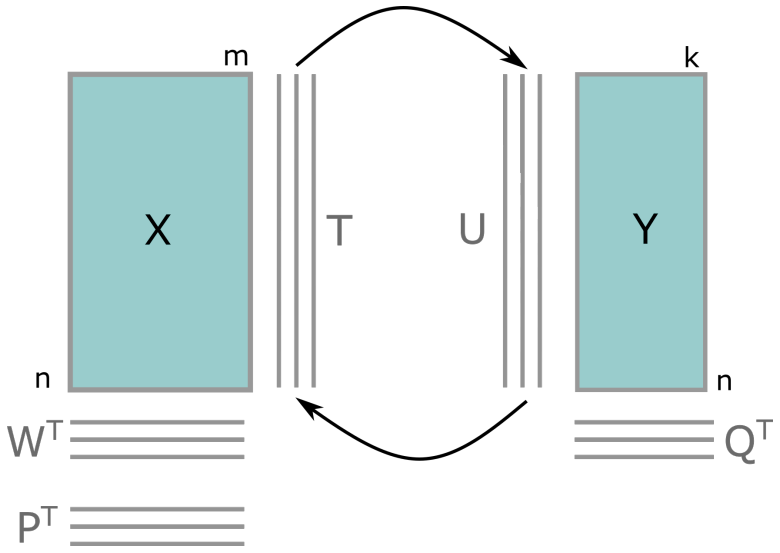

Figure 4.3: Schematic overview of mechanisms in PLS regression and the involved matrices. In PLS,both the response variables and the data matrix influence the PCAs of each other. The sketch was adapted from [Kessler, 2007].

variance in the data but on the other hand overfitting by a model with too many components should be avoided. Depending on the purpose and the data, a defined amount of explained variance of the original data by the PC model can serve as a cut-off value. Anyway, no more PCs than number of samples n can be determined. If not mentioned otherwise, the cut-off value for the accumulated explained variance in the studies of this thesis is 95 %.

4.2 Partial least squares (PLS) regression

Partial least squares regression (PLS-R) is one of the most frequently used multivariate regression methods. While PCA is an unsupervised technique, PLS-R is supervised meaning that it incorporates prior knowledge about the samples. In spectroscopy, this information are often known concentrations of elements or groups in characterized calibration samples. Thus, PLS-R is a multivariate regression between the data matrix $\mathbf{X}$ and a response matrix $\mathbf{Y}$ in which the information is stored. In practice, a PCA of $\mathbf{X}$ and $\mathbf{Y}$, each, is done and the outer relations of both PCAs are:

$$\mathbf{X} = \mathbf{T}\mathbf{P}^{\mathbf{T}} + \mathbf{E} \tag{4.7}$$

$$\mathbf{Y} = \mathbf{U}\mathbf{Q}^{\mathbf{T}} + \mathbf{F} \tag{4.8}$$

where $\mathbf{T}$ and $\mathbf{U}$ are score, $\mathbf{P}$ and $\mathbf{Q}$ are loadings, and $\mathbf{E}$ and $\mathbf{F}$ residual matrices, respectively. A schematic overview of the conncections in PLS is shown in Figure 4.3. PLS-R can be done for one or several dependent variables that are stored in $\mathbf{Y}$ called PLS-1 or PLS-2, respectively. In PLS, the components are usually called latent variables (LVs). The alogrithm used by the software *The Unscrambler* for PLS is again the NIPALS algorithm and will be described in the following for PLS-2 (based on [Kessler, 2007]).

1. The matrices $\mathbf{X}$ and $\mathbf{Y}$ are mean center and one starts as for PCA with the first PLS-component i = 1.
2. As a first estimate of the scores some random values could be used but usually the vector of $\mathbf{Y}$ with the largest absolute value is taken: $\mathbf{u_i} = \max|\mathbf{Y_k}|$
3. With the help of least squares, a solution of

$$\mathbf{X_i} = \mathbf{u_i}\mathbf{w_i^T} + \mathbf{E} \tag{4.9}$$

is found and the weighted loadings vector $\mathbf{w_i}$ is normalized to unity:

$$\mathbf{w_i} = \frac{\mathbf{X_i^T u_i}}{\sqrt{(\mathbf{X_i^T u_i})(\mathbf{X_i^T u_i})^\mathbf{T}}}. \tag{4.10}$$

Relying on these weighted loadings the scores are derived with least-squares.

4. For $\mathbf{X_i}$ the equation with its solution look like:

$$\mathbf{X_i} = \mathbf{t_i}\mathbf{w_i^T} + \mathbf{E} \rightarrow \mathbf{t_i} = \mathbf{X_i}\mathbf{w_i} \tag{4.11}$$

5. From these $\mathbf{t_a}$ scores the corresponding loadings can be calculated via least-squares:

$$\mathbf{X_i} = \mathbf{t_i}\mathbf{p_i^T} + \mathbf{E} \rightarrow \mathbf{p_i} = \mathbf{X_i^T}\mathbf{t_i}/(\mathbf{t_i^T}\mathbf{t_i}) \tag{4.12}$$

6. Turning now to the response variables in $\mathbf{Y}$, their loadings are found via regression to the $\mathbf{t_i}$ scores:

$$\mathbf{Y_i} = \mathbf{t_i}\mathbf{q_i} + \mathbf{F} \rightarrow \mathbf{q_i} = \mathbf{t_i^T}\mathbf{Y_i}/(\mathbf{t_i^T}\mathbf{t_i}) \tag{4.13}$$

7. In order to test for convergence the determined scores $\mathbf{t_i}$ in 4. are compared to the scores from the previous step which are $\mathbf{u_i}$ in the first iteration. Is there a difference, usually larger than 10^{-6}, between them the $\mathbf{u_i}$ scores have to be derived from the in 6. determined $\mathbf{q_i}$ loadings:

$$\mathbf{Y_i} = \mathbf{u_i}\mathbf{q_i^T} + \mathbf{F} \rightarrow \mathbf{u}_i = \mathbf{Y_i}\mathbf{q_i}/(\mathbf{q_i^T}\mathbf{q_i}). \tag{4.14}$$

With these $\mathbf{u_i}$ scores the procedure restarts at 3. until convergence is reached.

8. In case of convergence, the first PLS component is determined and has to be subtracted from the data:

$$\mathbf{X}_{i+1} = \mathbf{X}_i - \mathbf{t}_i\mathbf{p}_i^T \quad \text{and} \quad \mathbf{Y}_{i+1} = \mathbf{Y}_i - \mathbf{t}_i\mathbf{q}_i^T \tag{4.15}$$

9. All following components will be determined in the same way after setting i = i+1 until the maximum number of PLS components $I_{\max}$ is reached.
10. The remaining variance in the data sets that is not explained by the derived PLS components also called factors is given by:

$$\mathbf{E} = \mathbf{X}_{I_{\max}+1} \quad \text{and} \quad \mathbf{F} = \mathbf{Y}_{I_{\max}+1} \tag{4.16}$$

11. In the final step the regression coefficients have to be calculated in order to use the model for predictions:

$$\mathbf{B} = \mathbf{W}(\mathbf{P^T}\mathbf{W})^{-1}\mathbf{Q^T} \tag{4.17}$$

with $\mathbf{b}_0 = \overline{\mathbf{y}}^T - \overline{\mathbf{x}}^T\mathbf{B}$. The matrix $\mathbf{B}$ contains a regression vector $\mathbf{b_j}$ for each column of $\mathbf{Y}$. For a new object k with measured data $\mathbf{x}_k$ the target value $\mathbf{y}_i$ is calculated by:

$$y_{ik} = b_0 + \mathbf{x_i^T b_k}. \tag{4.18}$$

Like for PCA it is crucial to choose the optimal number of PLS factors. For PLS, the root mean square error (RMSE) can give evidence about the best suitable model size. For increasing model dimensionality, the RMSE should decrease until a transition to convergence appears. The particular number of LVs at which the convergence starts is usually the best suited number of LVs. The RMSE is also called prediction error and is defined as:

$$\text{RMSE} = \sqrt{\frac{1}{n}\sum_{i=1}^{n}(y_i - \hat{y}_i)^2} \tag{4.19}$$

where n is the number of samples, y_i the predicted value by the model for sample i and $\hat{y}_i$ is the true or reference value. The RMSE can also be used as a figure of merit of PLS models as it describes how much a predicted value by the model deviates from the true value. It is therefore a measure of prediction capability.

PLS regression can also be used for classification purposes. In this case, the response values in $\mathbf{Y}$ are discrete numbers, such as 1 and 0, standing for "member" and "not member" of a particular class, respectively. The sample class is treated as a dependent variable of $\mathbf{Y}$. Thus, the predicted values of such a PLS-R should be close to 1 for class members and close to 0 if the sample is not a member of the class. It is worth noting that one model can be used to predict several classes as in PLS-2. The term for this kind of PLS is discriminant analysis (PLS-DA).

4.3 Validation

The validation is an important issue for scientific models that are used to predict sample characteristics such as the described MVA models. A proper validation can give estimates about errors of the predicted quantities and evidence about the stability of the model for varying samples. In general, there are several possibilities for validation depending mainly on the size of the set of samples [Westad and Marini, 2015]. If there is a large enough number of samples with known characteristics, one can divide them into a group of samples to build the model and a group that is used for validation which is known as test-set validation. This is not possible when the number of samples is limited meaning in particular less than 40 samples [Westad and Marini, 2015]. In such a case, a cross-validation should be preferred over the test-set validation. Since the purpose of the studies presented here was to examine particular sets of samples with particular objectives, all of their data was used to build the MVA models and the sample sets fall into the category "limited number" of samples. Consequently, cross-validations were employed whose concept will be explained in the following.

Cross-validation

For a cross-validation, samples that were used to build the model are also used to validate the model. The general procedure of a cross-validation is:

1. Calculation of the MVA model with all samples.
2. Calculation of a model without selected samples and predict/project the left-out samples with/into the model.
3. Calculate the difference between the true/in 1. obtained value and the predicted/projected one.
4. Repeat this until every sample (either alone or in a group) has been left out once
5. Calculate the predicted residual sum of squares (PRESS)

$$\text{PRESS} = \sum_{i=1}^{n} (y_i - \hat{y}_i)^2, \tag{4.20}$$

with y_i is predicted/projected value and $\hat{y}_i$ the true/in 1. obtained value. Note that the RMSE in equation (4.19) is $\sqrt{\text{PRESS}/n}$.

Different types of cross-validation exists depending on the kind of selection of the left-out samples. In a full cross-validation every single sample is taken for validation while in a systematic cross-validation defined sample groups are used. For models which contain repetitive measurements of the same sample, it is advisable to do a systematic cross-validation with groups that contain all repetitive measurements. There is also the possibility to do a random cross-validation in which samples are arbitrarily grouped together and are left-out in these groups.

5 Experimental setups and sample preparation

This work contains various studies for which different experimental setups were used. All experimental work was done in the LIBS/Raman laboratories at the German Aerospace Center (Deutsches Zentrum für Luft- und Raumfahrt e.V., DLR). In this chapter, I will introduce these setups and describe the sample preparation procedure. Two kind of setups were used for the experiments: rather big, cutting-edge high performance instruments and setups built from miniaturized components with reduced performance. With the first kind, the general feasibility and performance of the applied data analysis methods were investigated. Moreover, physical phenomena that play an important role for proper data interpretation were studied with these setups. The second kind of setups was employed in order to simulate the performance of space mission instruments that are limited in size, weight, and power consumption leading to a decreased performance compared to large laboratory setups.

5.1 Aryelle Butterfly LIBS setup

The Aryelle Butterfly LIBS setup belongs to the category of high performance laboratory instruments and a sketch of the components can be seen in Figure 5.1. Furthermore, details of them are listed in Table 5.1. The main hardware components are a pulsed high power infrared laser, an echelle spectrometer with an ICCD, and a simulation chamber for the imitation of atmospheric conditions of different extraterrestrial bodies.

Laser

The laser installed at the Aryelle Butterfly LIBS setup is a Q-switched Nd:YAG laser (manufacturer: *Continuum*, model: *Inlinte II-20*) at its fundamental wavelength of 1064 nm with a pulse length of 6 ns and with a flat-top intensity profile. In all experiments, it was operated with 10 Hz repetition rate. The maximum output energy per pulse is 220 mJ which can be reduced to various lower laser energies due to combinations of neutral density filters. The applied laser energies for the studies in this work will be mentioned in the particular sections.

First, the laser beam passes the neutral density filters and is then reflected by two mirrors. With a combination of two lenses a concave and a convex lens which have together an effective focal length of 40 cm, the laser beam is focused. It is then reflected once more by a mirror and enters the simulation chamber slightly tilted (5°) to the normal of the sample stage. The focused beam diameter on the sample surface is $\approx 300\,\mu$m.

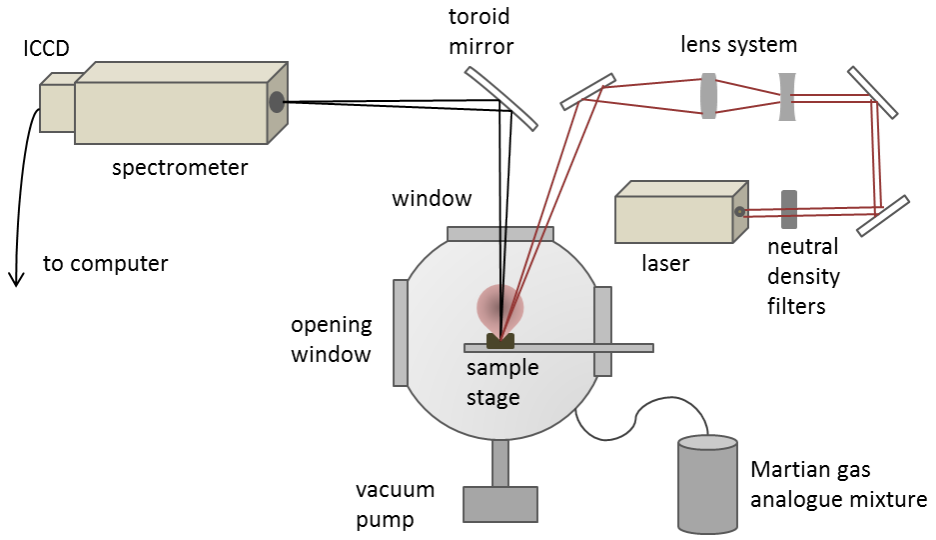

Figure 5.1: Schematic drawing of the components and their arrangement in the Aryelle Butterfly LIBS setup.

Table 5.1: Overview of the hardware components in the Aryelle LIBS setup with specifications.

Component	**Properties**	
Laser	type	Nd:YAG
	Wavelength	1064 nm
	Pulse energy	max: 220 mJ
	Pulse length	6 ns
Spectrometer	type	echelle
	Wavelength range	UV: 190-370 nm
		UV/VIS/NIR: 270-850 nm
	Spectral resolution	0.03 nm (UV) to 0.09 nm (UV/VIS/NIR)
	Detector	ICCD camera 1024×1024 pixel
Simulation chamber	Pressure range	down to 0.002 hPa
	Composition Mars analogue gas	95.3 Vol % CO_2
		2.7 Vol % N_2
		1.6 Vol % Ar
		0.1 Vol O_2

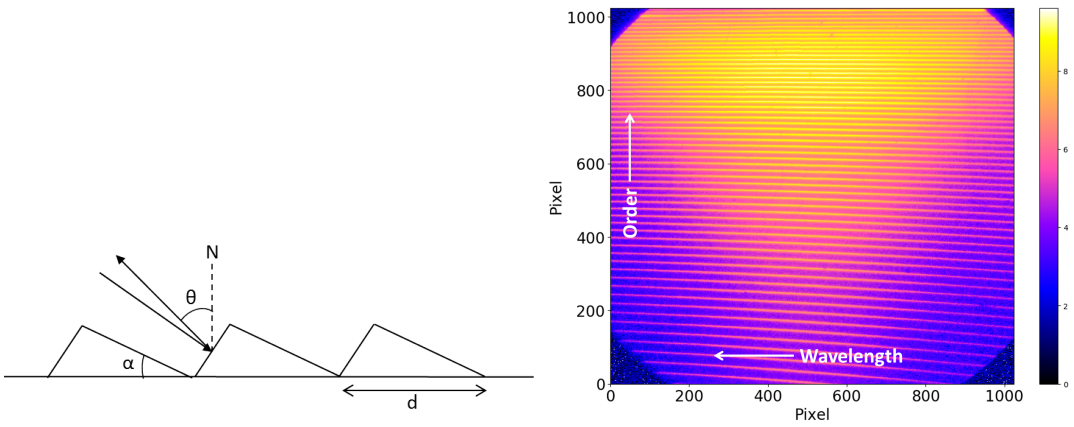

Figure 5.2: *Left:* Schematics of an echelle grating where the diffraction takes place at the small facet of a blazed grating. Usually, these gratings are employed in Littrow configuration. *Right:* Two dimensional spectrum of a laser driven light source (LDLS) that continuously covers both spectral ranges, here the UV/VIS/NIR is shown. The intensity is shown in logarithmic scale and the separated orders are observable.

Spectrometer

The spectrometer is an echelle spectrometer (manufacturer: *Laser Technik Berlin (LTB)*, model: *Aryelle Butterfly*) with the possibility to switch between two spectral ranges: the UV (190-370 nm) and the UV/VIS/NIR (270-850 nm) range. One can not measure simultaneously in both spectral ranges. A toroid mirror reflects and focuses parts of the plasma radiation onto the entrance slit of the spectrometer. Inside the spectrometer, a movable mirror directs the incoming light in the particular spectral range. In both branches UV and UV/VIS/NIR further mirrors are used to guide the light through a prism and onto an echelle grating, respectively.

Echelle gratings work with high diffraction orders to achieve a large dispersion which is given by the diffraction equation:

$$n\lambda = d(\sin\alpha + \sin\beta), \tag{5.1}$$

where n is the order of diffraction, λ the diffracted wavelength, d the grating constant, and α the angle of incidence while β is the angle of diffraction both measured from the grating's normal. Figure 5.2 (*left*) shows the schematics of an echelle grating where the light is reflected at the small facet of the saw tooth shaped blaze grating. Due to the large diffraction angle several orders are overlapping which requires a second dispersive element to separate them. In the echelle spectrometer used for this thesis, an additional prism separates the orders and produces thereby a two dimensional spectrum on the chip of the ICCD (manufacturer: *Andor*, model: *iStar*). With a laser driven light source (LDLS, manufacturer: *Energetiq*, model: *EQ-99X*) that covers continuously a broad spectral range (170 - 2100 nm), the structure of the orders on the chip were visualized for both spectral ranges. The LDLS uses a diode pumped continuous wave (cw) laser to generate a xenon plasma in a proprietary bulb. Figure 5.2 (*right*) shows the picture measured in the UV/VIS/NIR range when the LDLS was put at the position where the plasma evolves in LIBS measurements. The structure of the separated orders can be clearly seen and with an algorithm provided by the software *Sophi* (LTB) the orders are

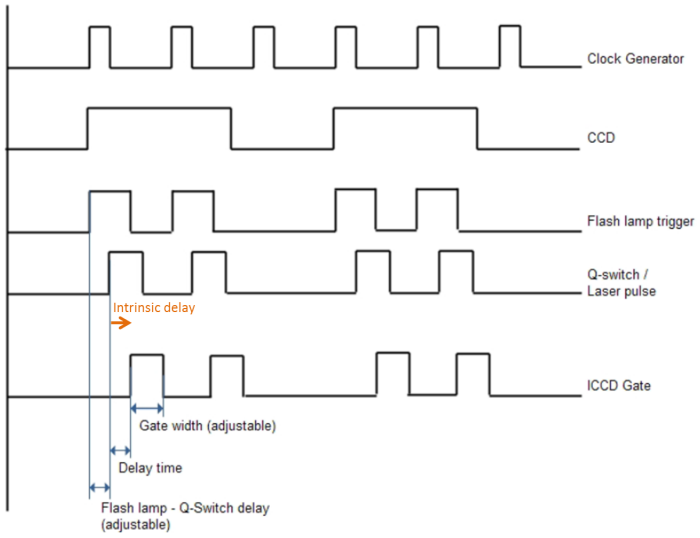

Figure 5.3: Schematic synchronization of LIBS Aryelle Butterfly system, taken from the manual by LTB. It was observed in experiments that the system has an intrinsic delay which is most likely due to an additional delay of the laser pulse which is marked in the sketch by the orange arrow.

read out and merged into one spectrum. This results in a broad spectral range with high resolution. In the UV/VIS/NIR range, the spectral resolution is 0.09 nm while it is 0.03 nm in the UV range.

Simulation chamber

The chamber that is used to experimentally simulate different planetary atmospheric conditions has a volume of $\approx 5000\,\mathrm{cm}^3$. It contains a stage for the sample holder that is controlled by a motor and can be moved in x, y, and z direction. For measurements in Martian atmospheric conditions, the chamber is first evacuated with a membrane pump down to $\approx 1\,\mathrm{hPa}$ and is then flooded by the Martian gas analogue until $\approx 15\,\mathrm{hPa}$ before the Martian pressure of 7 hPa is adjusted. During the measurements a constant flow is generated with ideally the inflow of the Mars analogue gas and the outflow in equilibrium. For measurements in vacuum conditions, a turbomolecular pump is employed in addition to the membrane pump which is used first for the evacuation down to 1 hPa. With the turbomolecular pump pressures down to 0.002 hPa can be currently reached at this setup.

Timing between laser pulse and gate

Laser and camera triggering is controlled by an electronic box with an internal clock. The synchronization of the whole system is shown in Figure 5.3. Concerning the delay time which is the time between the laser pulse (Q-Switch) and the intensification of the CCD, an intrinsic delay between these two events was observed which shifts the intensification before the laser pulse when the delay time in the measurement settings is set to zero. Most likely, the laser pulse has this additional delay which is marked in Figure 5.3 with an orange arrow. Several measurements have shown that the intrinsic delay is not constant but is in the range of 70-

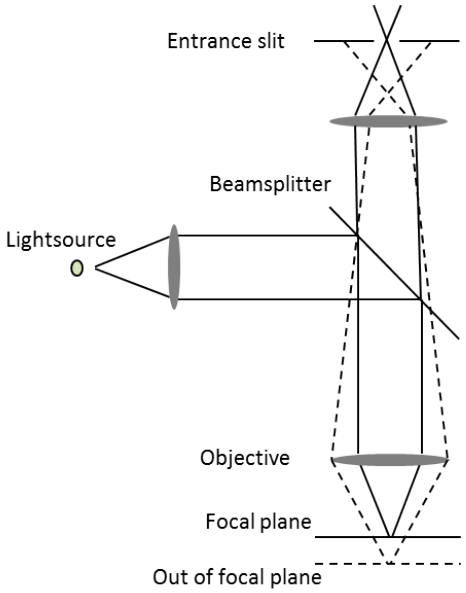

Figure 5.4: Principle of confocal Raman microscopes. Only radiation coming from the focal plane reaches the spectrometer and allows therefore for a high spatial resolution. With opaque samples it is possible to measure depth profiles.

150 ns and stays the same as long as the hardware is not switched off. It can be determined before the particular measurements by doing a time resolved measurement on a dedicated sample in which the sum of delay and integration time is kept constant. Summing up the total emission intensity of each measurement and plotting it for increasing delay times, the intrinsic delay time is the time at which the total emission intensity starts to decrease. The effective delay is then the delay time of the measurement settings minus the intrinsic delay. For the studies in this thesis, I will use the term delay time for the actual effective delay time.

5.2 Witec Raman setup

The second high performance instrument used for this thesis is a Raman instrument consisting of a confocal microscope with an ultra high throughput spectrometer (manufacturer: *WITec*, model: *alpha 300*) and a CCD camera. The beam path of a confocal microscope is shown in Figure 5.4. A high spatial resolution is achieved with such a type of microscope because out of focus radiation is blocked. In the setup, a frequency doubled cw Nd:YAG laser with a wavelength of 532 nm and maximum output power of 50 mW is used for excitation. The power can be adjusted and usual working powers used for this work were around 3 mW. A rotatable revolver provides the possibility to measure with different objectives, thus with different magnifications and working distances. Also, different gratings resulting in different spectral ranges and resolutions can be chosen. For the studies in this thesis, the 600 mm^{-1} grating resulting in a spectral range up to 3800 cm^{-1} with a pixel resolution of more than 3 cm^{-1}/px was used.

Table 5.2: Overview of the components of the miniaturized LIBS and Raman setups.

Mini-LIBS	
Laser	Nd:YLF, 1053 nm, 2 ns pulse length, 2 mJ/pulse, manufacturer: *neoLASE*
Spectrometers	Information valid for each single spectrometer, manufacturer: *Avantes*
Concept	Symmetric Czerny-Turner
Detector	CMOS linear array, 4096 pixels (7×200μm), uncooled
Entrance slit and gratings	10 μm and 1800 lines/mm (UV, VIS1); 1200 lines/mm (VIS2, NIR)
Spectral resolution	$\approx$ 0.2 nm
Spectral ranges	UV: 240-350 nm; VIS1: 350-510 nm; VIS2: 540-750 nm; NIR: 750-870 nm
Mass	175 g
Dimension	95 × 68 × 20 mm
Focal length	150 mm
Mini-Raman	
Laser	Nd:YAG, frequency doubled; 532 nm; cw, 22 mW output
Spectrometer	Manufacturer: *Ocean Optics*, model: *Flame-T*
Concept	Asymmetric crossed Czerny-Turner
Detector	CCD, 3648 pixels (8×200μ,), uncooled
Entrance slit and grating	25 μm and 1800 lines/mm
Spectral resolution	25 cm^{-1} (0.74 nm)
Spectral range	529-698 nm
Mass	265 g
Dimension	88.9 × 63.5 × 32 mm
Focal length	Variable, here: 30 mm and 200 mm

5.3 Miniaturized LIBS and Raman setups

As mentioned above, miniaturized LIBS and Raman setups were used in order to simulate the performance of space mission instruments which are limited in their dimensions, mass, and power consumption. Sketches of the LIBS and Raman setups are shown in Figure 5.5 and 5.6, respectively and were adapted from the representation in [Kubitza et al., 2018]. Furthermore, an overview of the hardware components with specifications is given in Table 5.2.

In the Mini-LIBS setup, the focusing optics is the same as the collection optics, namely a parabolic mirror with a focal length of $f = 150$ mm. The collected plasma radiation is directed through four dichroic beamsplitters in order to guide it to four spectrometers with different spectral ranges and also to avoid backscattering into the laser. Together, the four spectrometers cover a broad spectral range from 240 to 870 nm with an average spectral resolution of 0.2 nm. As the LIBS plasma is strongly affected by atmospheric conditions the samples can be embedded in a small custom-made vacuum chamber. This chamber can be connected to the big simulation chamber of the Aryelle LIBS setup (Section 5.1)in order to create Martian atmospheric conditions due to pressure equalization. During the measurements and sample exchange, the small chamber is disconnected from the larger simulation chamber.

The laser of the Mini-Raman setup has a fiber output which is connected to a fiber coupler and a collimation lens to expand the laser beam. Like in the Mini-LIBS setup, the optical path for excitation and signal collection uses the same focusing optics which is why a dichroic beamsplitter is employed for the separation of the two paths. For laser focusing and signal collection, a plano-convex lens is installed which can be exchanged for different sampling distances. The dichroic beamsplitter reflects the collected radiation which passes through

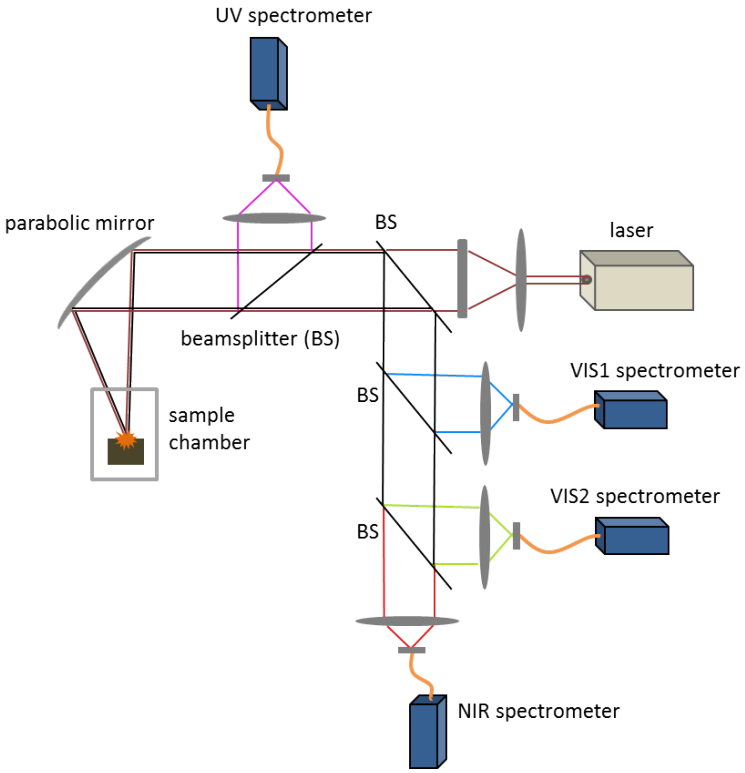

Figure 5.5: LIBS setup with miniaturized components. The plasma radiation is separated with dichoric beamsplitters and guided to four spectrometers with different spectral ranges. The sketch is adapted from [Kubitza et al., 2018].

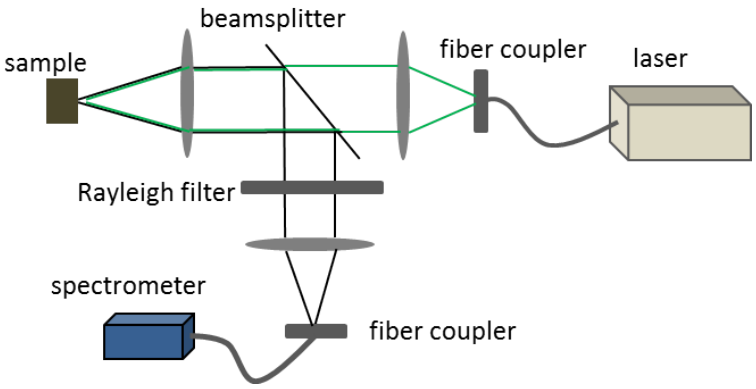

Figure 5.6: Mini Raman setup with an exchangeable focusing lens, thus variable sample distances. A dichroic beamsplitter reflects the scattered radiation which is focused in the spectrometer. The sketch is adapted from [Kubitza et al., 2018].

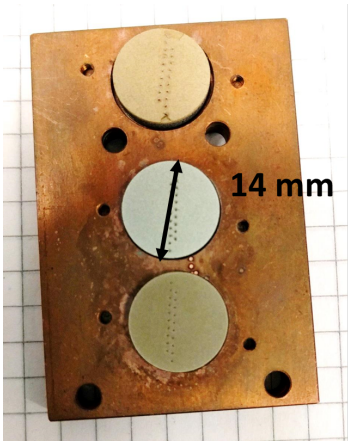

Figure 5.7: Example of pellets which were used for the study in Chapter 6. They are certified geological samples (see Table 6.1) with known elemental composition. The sample holder is made of copper and is used for LIBS measurements with the Aryelle setup (Section 5.1).

a Rayleigh filter in order to suppress the excitation wavelength. Another lens focuses the remaining light into the spectrometer.

5.4 Sample preparation

The samples investigated for this thesis were prepared from powders and pressed into pellets. This was done with a manual hydraulic press (manufacturer: *Specac*) and press dies which can be evacuated. The possible applicable pressures are in the range of 1-15 t and I usually pressed the samples with 5 t in 10 minutes. The diameter of the prepared pellets is 14 mm and a picture of three samples in the sample holder is given in Figure 5.7.

Pellets of mixtures from different components were produced by crushing and mixing them with a mortar and pistil. Prior to that, a scale was used for mixtures that were supposed to have a particular mixing ratio. Usually, 1 g of powder is taken for one pellet.

6 Plasma parameters for Martian LIBS data normalization

LIBS has become a widely used technique for elemental analysis due to several advantages such as its relative simplicity in experimental implementation, fast aquisition times, and its requirement of no to little sample preparation. However, one drawback of LIBS is a poor repeatability and reproducibility of emission signals [Hahn and Omenetto, 2012, Tognoni and Cristoforetti, 2016]. This is due to complex laser-sample and laser-plasma interactions which are influenced by many experimental parameters including laser and sample characteristics [Niemax, 2001]. In addition, LIBS plasmas are transient and sensitive to atmospheric conditions. All those factors are not independent of each other leading to different phenomena which can introduce uncertainties in the analytical performance of LIBS [Niemax, 2001]. Influences of sample characteristics are summarized as matrix effects which can be divided into physical (grain size, thermal conductivity, etc.) and chemical (elemental composition) matrix effects [Takahashi and Thornton, 2017]. These effects become apparent when an analyte signal from a particular element is compared among samples with different sample matrices, for example, in univariate calibration curves. Matrix effects but also minimal changes in the experimental conditions are also responsible for the poor repeatability of LIBS measurements showing up as shot-to-shot fluctuations in successive measurements of the same measurand under same measurement conditions. Physical and chemical heterogeneity within the laser spot size or instabilities of the laser energy per pulse could be reasons for these fluctuations [Cremers and Radziemski, 2013, Tognoni and Cristoforetti, 2016]. The reproducibility of emission signals is mostly affected by changes in the experimental conditions as it describes the agreement between successive measurements on the same measurand but under changing conditions.

One way to improve the analytic capabilities of LIBS is to avoid the sources of changing signals, thus to keep experimental settings as constant as possible [Sirven et al., 2008]. Furthermore, calibration samples for quantitative analysis should be matrix matched, meaning that among the samples for one calibration model, variations of their physical appearances and their overall chemical compositions should be in a narrow range [Hahn and Omenetto, 2012]. Fluctuations of signals can be avoided by using averages of several repetitive measurements [Sirven et al., 2008]. Nevertheless, those arrangements are not possible in LIBS applications with less controllable experimental conditions and with little prior knowledge about the samples under investigation. Furthermore, when analyzing geological samples with LIBS, repetitive measurements are not possible as even different positions of a relatively homogeneous sample present a different mineral grain and therefore have different compositions [Senesi, 2014]. In Figure 6.1, a scenario for LIBS measurements by the ChemCam instrument on the MSL rover in Gale crater on Mars is shown. This is one example of LIBS where experimental conditions as well as the sample matrix are not controllable. In this particular case, critical parameters are, for example, the sample distance which affects the irradiance on the sample, the structure of the sample surface, or the incidence angle of the laser [Schröder et al., 2019a]. In such

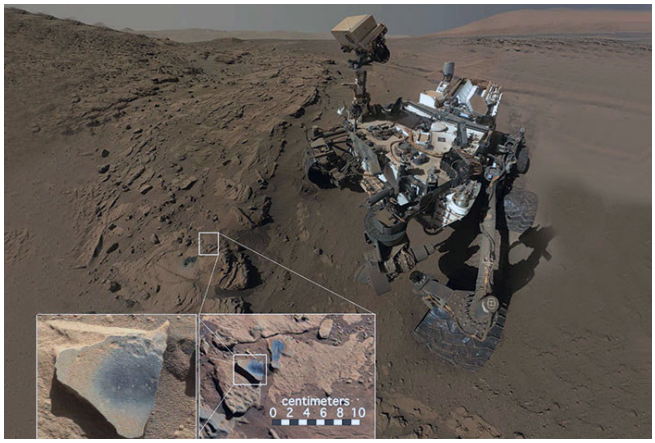

Figure 6.1: The MSL rover Curiosity in Gale crater. The zooms show a target measured by ChemCam during the rover was in the shown position. This picture illustrates that experimental conditions are less controllable for space mission LIBS instruments like ChemCam as parameters such as the roughness of the sample surface, the distance to the target, or the angle of incident of the laser beam, change for each new target. *Image credit: MSSS/JPL/NASA (PIA 18390)*

applications with limited control, data normalization is even more necessary to reduce the influence of matrix effects and varying experimental conditions. A large variety of normalization approaches exists in literature which use different parameters either to normalize the analyte signal intensity or the whole spectrum [Zorov et al., 2010, Takahashi and Thornton, 2017]. The usual data treatment, for example, of ChemCam data for the quantification of major elements with mutlivariate data analysis includes the normalization of each spectral range by its total emission intensity after continuum subtraction [Wiens et al., 2013, Maurice et al., 2016]. However, further approaches are used in univariate analysis of ChemCam data, such as normalization of single line emission intensities to emission line intensities of elements from the Martian atmosphere [Rapin et al., 2017, Thomas et al., 2018a]. Recently, a study of our group [Schröder et al., 2019a] has shown that such a normalization to elements contributing from the atmosphere does not provide a reliable approach and in particular normalizing to the carbon emission is critical. Also other tested normalization approaches, for instance, normalization to the continuum emission [Schröder et al., 2015] or to the total emission intensity with removed continuum [Body and Chadwick, 2001] can work under specific limited conditions but do not provide an universal normalization method. In another Mars relevant study [Sallé et al., 2006], the authors compared three different approaches for the correction of matrix effects: using an external reference sample to derive a correction factor for the sum of all elemental concentrations, normalizing by the oxygen signal as an internal standard, and applying calibration free LIBS (CF-LIBS). They found that taking into account variations of the number of vaporized atoms by means of an external standard is best suited for matrix effect correction among their particular set of geological samples.

The objective of the following study is to test another approach for normalization of LIBS data taken under Martian atmospheric conditions for which plasma parameters, namely the temperature and the electron density, are used. The derived plasma parameters are tested for the normalization of single emission lines. I will briefly discuss the idea of using plasma parameters for normalization together with some general considerations on emission signal normalization in Section 6.1.

To evaluate if normalization with plasma parameters is feasible for Martian LIBS data, different experiments with nominally constant experimental parameters or controlled changes were done. Under nominally constant experimental parameters, fluctuations from measurement to measurement on the same sample were investigated. In another experiment, the influence of mainly chemical matrix effects were studied by using a set of 18 certified powdered geological samples with varying chemical compositions. The laser energy was changed in a third study in order to simulate changing experimental conditions such as for ChemCam on Mars. For the analysis, correlations between plasma parameters, total emission intensity, emission lines, and ratios of them were analyzed. In addition, univariate calibration models as well as relative standard deviations (RSD) before and after normalization were computed. Different approaches to derive the plasma parameters from the spectral data were tested and compared regarding their reliability, applicability to Martian data, and general practicability.

6.1 Plasma parameters for normalization - some considerations

Normalization is not only important for LIBS data, it is also necessary in other analytical emission spectroscopy methods. In general, a common method for normalization of spectroscopic data is to take the intensity ratio of the analytical line to another line of another constituent in the sample, also known as the internal standard [Barnett, 1968,Hahn and Omenetto, 2012,Takahashi and Thornton, 2017]. For the choice of the internal standard element and a particular line from that element, certain criteria with regard to the analyte were formulated in [Barnett, 1968]. While some of the criteria are unfeasible for LIBS applications as they involve adding the internal standard in a defined quantity to the sample, others can be relevant to LIBS. For example, the internal standard and the analyte element should have similar volatization rates and comparable ionization energies. However, depending on the experimental conditions, also these criteria are challenging to meet for the choice of an internal standard. The concept of an internal standard was therefore transferred to LIBS as a reference signal which does not necessarily have to be the signal of an emission line. In the LIBS community, various types of reference signals for normalization were investigated, see for example the reviews [Zorov et al., 2010,Takahashi and Thornton, 2017].

One choice of a reference signal of normalizing LIBS data are plasma parameters, namely the temperature T and the electron density n_e. Those parameters control on the one hand the plasma characteristics and dynamics and are on the other hand influenced by matrix effects and changes due to experimental conditions. Thus, their fluctuations or behaviour can reflect how much the LIBS plasma state changes. In terrestrial LIBS applications, normalization with plasma parameters was used leading to reduced signal fluctuations and an improved linearity of calibration curves [Panne et al., 1998,Feng et al., 2010,Lazic et al., 2004,Chaleard et al., 1997]. In those approaches, the authors made use of relations between emission line intensities and plasma parameters derived from Boltzmann and Saha equilibria. The emission lines or ratios of emission lines used for quantification were not just divided by the parameters, they were in a way modified according to the particular relations. Another more sophisticated way to overcome the influence of matrix effects by employing plasma parameters is to use nonlinear calibration curves where T and n_e enter already in the model parameters [Aragón and Aguilera, 2015,Frydenvang et al., 2013].

All of these approaches have in common that either complex models are involved or that the

normalization applies only to a particular sample set and experimental setup. For this study, the objective is to test plasma parameters together with their derivation for normalization applications of LIBS data in scenarios most likely feasible for space exploration missions.

6.2 Certified samples

In this section, the LIBS data of 18 certified standards (see Table 6.1) of known compositions which were measured under simulated Martian atmospheric conditions (see Section 2.1) is investigated. The standards cover a variety of compositions that were expected to be encountered on Mars. The objective is to test if plasma parameters can compensate for fluctuations in repetitive measurements and if they further suit for normalization of elemental signals that were measured in different matrices. Therefore, correlations of signals and plasma characteristics for each sample and among the samples were investigated. Furthermore, univariate calibration curves were computed and compared before and after normalization.

Experiments

Measurements were performed with the Aryelle LIBS setup (see Section 5.1) and the samples were placed in a Martian gas analogue mixture at a pressure of about 6.5 hPa. As a trade-off between a stationary plasma probably in LTE which would require rather short integration times, on the one hand, and good SNRs that require longer integration times on the other hand, an integration time of 500 ns was chosen. The delay time was set to 350 ns and the laser energy adjusted to 15.4 mJ with the laser operating at a repetition rate of 10 Hz. Measurements were done in both spectral ranges but for the analysis the data from the UV (190-375 nm) was chosen since several promising Fe and Si emission lines for temperature determination are available in that range. Two scenarios were investigated for which the described timing, laser, and atmospheric parameters were the same.

- On each of the 18 certified standards pressed to pellets, measurements were done at 10 different positions. One measurement consists of 30 consecutive laser pulses and spectra of all 30 induced plasmas were summed up.
- Using the measurements from above, I compared emission lines from the different sample matrices by taking the different elemental concentrations into account.

An overview of the samples can be found in Table 6.1 where their reference numbers, their origins, and their Si and Fe concentrations are given. The same set of samples was used in a previous study in which the detection and quantification capabilities of a potential miniaturized low-energy LIBS instrument for in-situ Martian exploration were tested [Rauschenbach et al., 2010]. The powdered samples which were pressed into pellets in the usual procedure described in Section 5.4. Figure 5.7 shows three of the pressed samples in the sample holder.

Plasma parameter determination

The plasma temperature was determined with the Boltzmann plot method introduced in Section 3.1.4 for which emission lines were fitted with Voigt profiles. As the focus of this study is on a possible application to Martian data, the choice of emission lines for the Boltzmann

Table 6.1: Overview of certified rocks and soils samples.

Reference number	Type (and origin)	Fe [at %]	Si [at %]
NIST SRM 688	basalt rock	7.23	22.65
NIST SRM 679	brick clay	9.05	24.37
NIST SRM 698	bauxite	13.70	0.32
NIST SRM 2702	marine sediment	7.91	unknown
NIST RM 8704	river sediment	3.97	unknown
CRM 4233-88 (IGI-SDU-1)	dunite	6.23	18.52
IGEM RM 1017-94 (MO-15)	andesite-basalt	7.04	23.19
NCS DC 71302 (GBW 07110)	andesite	3.30	29.51
NCS DC 71305 (GBW 07113)	rhyolite	2.24	34.06
NCS DC 72302 (GBW 07102)	ultrabasic rock	4.92	17.67
NCS DC 73302 (GBW 07104)	andesite	3.43	28.37
NCS DC 73303 (GBW 07105)	basalt	9.37	20.89
NCS DC 73308 (GBW 07310)	river sediment	2.70	41.60
NCS DC 73309 (GBW 07311)	river sediment	3.07	35.69
NCS DC 73317 (GBW 07307)	river sediment	4.55	30.28
NCS DC 73318 (GBW 07308)	river sediment	1.54	38.79
NCS DC 73322 (GBW 07404)	soil	7.20	23.84
NCS DC 73371 (GBW 07301a)	river sediment	4.54	27.64

Table 6.2: Overview of Fe(II) emission lines used for Boltzmann plots.

λ [nm]	Ag [$\times 10^8\,s^{-1}$]	E_{up} [eV]	λ [nm]	Ag [$\times 10^8\,s^{-1}$]	E_{up} [eV]
Fe (II)					
241.79	11.0	8.37	258.79	16.9	8.94
242.84	26.8	9.01	259.15	3.4	5.82
243.23	12.6	7.94	259.28	43.8	8.86
243.29	40.0	9.17	262.17	1.2	4.85
245.46	13.9	9.13	266.47	19.1	8.04
246.13	18.7	8.27	266.66	15.0	8.07
246.19	24.3	8.26	269.26	16.8	8.37
246.95	15.5	8.92	270.40	11.0	7.97
256.35	6.0	5.88	271.44	3.4	5.55
257.44	9.6	7.40	273.07	1.1	5.62
257.79	2.4	5.90	275.33	22.7	7.77
258.26	3.5	5.88			
Si (I)					
212.41	20.80	6.62	251.61	8.40	4.95
221.09	1.73	5.62	251.92	1.65	4.92
221.67	3.18	5.62	252.85	2.71	4.92
250.69	2.74	4.95	288.16	6.51	5.08
251.43	2.22	4.92			

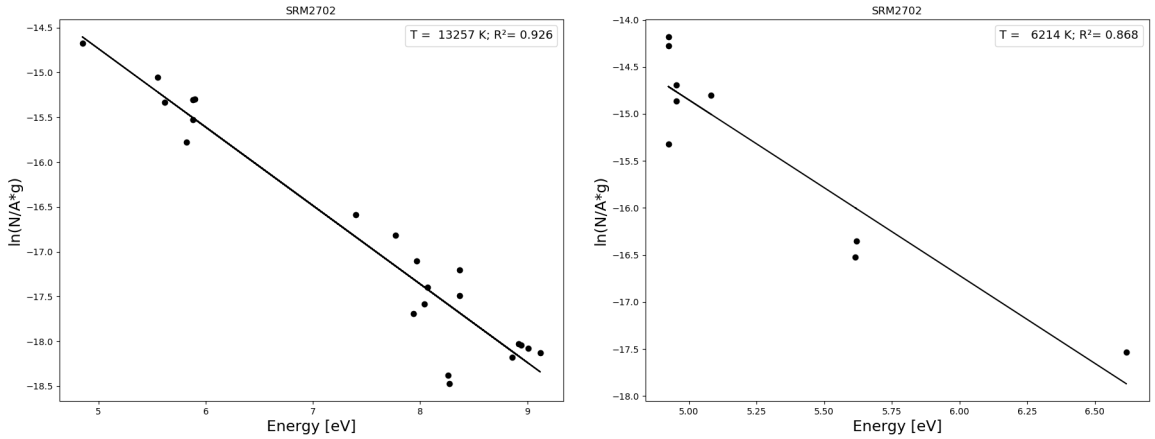

Figure 6.2: Examples of Boltzmann plots derived from one measurement on the sample SRM 2702. *Left*: Linear fit of Fe (II) line intensities divided by gA whose slope gives the plasma temperature. *Right*: Boltzmann plot of Si (I) emissions which are less separated in their upper level energies than the Fe (II) lines.

plots should also be applicable for real Martian LIBS data. Therefore, two major rock forming minerals, namely Fe and Si were selected. Both elements are present with several emission lines in almost all ChemCam spectra due to average concentrations of $\approx 45\,\mathrm{wt\,\%}$ SiO_2 ($\approx 21\,\mathrm{at\,\%}$) and $\approx 18\,\mathrm{wt\%}$ FeO_T ($\approx 13\,\mathrm{at\,\%}$) [Maurice et al., 2016] in Martian targets. The certified samples (Table 6.1) have mostly lower Fe and higher Si concentrations, however, they still suit as a representative set for Martian surface geology and to test this approach. The UV spectral range provides many Fe (II) and Si (I) emission lines. Regarding the separation of the the upper level energies, the Fe (II) lines are promising since they cover a wide range from 5 to 9 eV which is recommended for proper temperature calculation (see Section 3.1.4). By contrast, the upper level energies of the observable Si (I) transitions are not well separated in their upper level energies which are in the range of 4.9 to 6.6 eV. An overview of the selected Fe (II) and Si (I) emission lines is given in Table 6.2. The ChemCam UV range, however, starts at 240 nm and would exclude some of the Si (I) emission lines in case of temperature determination from ChemCam data.

In Figure 6.2, two examples of Boltzmann plots are shown. Both were derived from the same measurement on a marine sediment standard (SRM 2702), with the Fe (II) and the Si (I) lines, respectively. This standard has a medium Fe concentration ($7.9\,\mathrm{at\,\%}$) within the sample set whereas its Si concentration is unknown but high enough to detect the Si (I) emission lines for Boltzmann plots. Although not all points in both examples are on a straight line, the R^2 values of 0.93 and 0.87 indicate a sufficiently good fit quality. At this point, the linearity of Boltzmann plots can give evidence about the plasma being in LTE. The better the fit is, the more probable LTE conditions are met [Aragón and Aguilera, 2008a]. However, what can be seen here, is the difference between the temperatures derived from Fe (II) emissions ($T_{Fe} = 13300\,\mathrm{K}$) and from Si (I) emissions ($T_{Si} = 6200\,\mathrm{K}$). Since the same data was used, the reason for this deviation has to be related to the plasma and the experimental conditions. The LIBS plasma is known to have complex distributions which can include a non uniform temperature distribution or in other words, spatial temperature gradients can exist [Aguilera et al., 2003, Aragón and

Aguilera, 2008a, Tognoni et al., 2010, Mercadier et al., 2013]. These change over time, in particular during the expansion and the cooling process. Due to the Boltzmann distribution, atoms and ions of a certain element do not emit in every temperature range. Thus, even during the already short integration time of 500 ns the plasma temperature changes and the emission of Si and Fe was most likely captured in different temperature ranges. Furthermore, the derived temperatures might correspond to different spatial positions inside the plasma volume seen by the spectrometer (line of sight) corresponding to the spatial distribution of Fe and Si ions and atoms. In spatially integrated measurements, this is an usual observation and led to the concept of apparent or population-averaged excitation temperatures [Aguilera and Aragón, 2007]. This means in particular that temperature derivations without spatial resolution give averages of the local temperatures in the plasma.

The electron density was derived from the broadening of the Mg (I) 285.21 nm and the Si (I) 288.16 nm emission lines, respectively. Those lines are affected by the quadratic Stark effects and I used equation (3.24) for which the electron impact widths w were taken from [Griem, 1997].

Signal fluctuations among 10 measurements

In order to investigate signal fluctuations between measurements on the same sample and whether they can be reduced by normalization with plasma parameters, Pearson correlations between emission signals and plasma characteristics were computed. Single shot measurements with the ICCD were too noisy and a minimum number of shots is required. Therefore, instead of shot-to-shot fluctuations, measurement-to-measurement fluctuations were studied. Although the experimental conditions were kept constant and only the position on the sample was changed, signal fluctuations appear in the 10 measurements as typical for LIBS. For this sample set, the fluctuations appear most likely due to inhomogeneities of the samples on a scale of the laser spot size. By eye, the samples seem to be homogeneous, however, this is not the case which can be seen in Figure 6.3, where an image taken with a microscope of a soil standard sample (DC 73322) with LIBS crater is shown exemplarily. It can be seen that the sample is not homogeneous on the scale of the crater size because the variation of grains appears on a larger scale than the crater size. Therefore, the sample has to be treated as inhomogeneous which is at least one reason for the measurement-to-measurement fluctuations.

The investigated fluctuating emission signals are, in particular, several Fe and Si emission lines. The derived plasma characteristics are the plasma temperatures T_{Fe} and T_{Si} calculated from Fe (II) and Si (I) emissions, respectively, electron density, emission line ratios, and the total emission intensity. In the following, the Fe (II) emission line at 275.33 nm and the Si (I) emission line at 288.16 nm will serve as examples for the emission signals. These lines were selected because of sufficiently high intensities in almost all measurements and because they are not superimposed by other emission lines. In Table 6.3, selected correlations are listed for all samples. Other correlations that are not shown did not reveal other findings than those presented here.

It can be seen that for some samples positive correlations between emission line intensities and plasma temperature as well as total emission intensity were obtained, see for example, the bauxite (SRM 698) and the basalt standard (SRM 688). Nevertheless, no correlations and even negative correlations were observed, too. For example, one river sediment standard

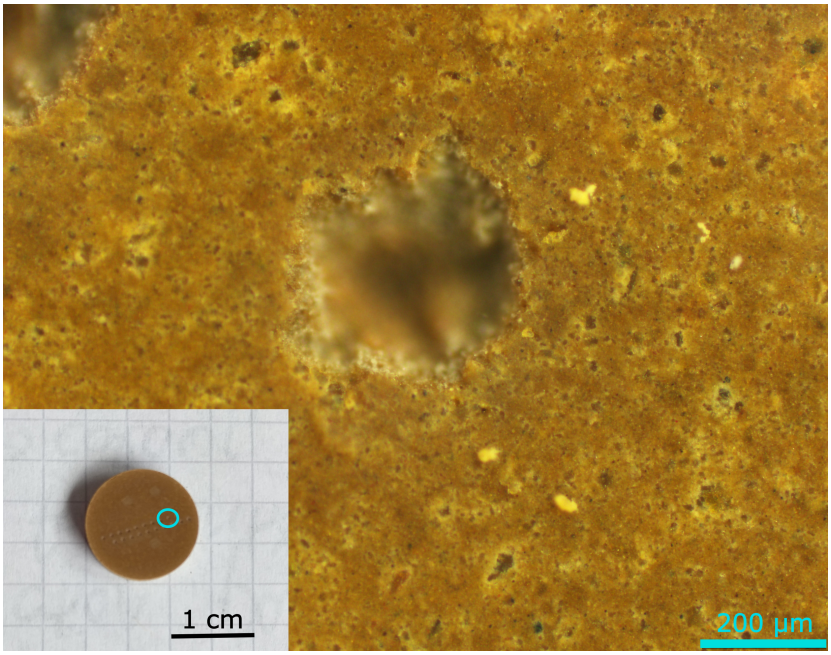

Figure 6.3: Microscope image of the soil standard DC 73322 with a LIBS crater. The inset shows the pellet with all craters where the particular crater is marked by a light blue circle. The whole sample appears homogeneous, but on the smaller scale, variations in grains can be seen. The crater size is large in comparison to the individual grains, however, the variation of the grains is on a larger scale than the crater size.

(DC 73371) has no significant correlations at all and another river sediment (DC 73309) has a positive correlation with the total intensity but a negative one with T_{Fe}. In Figure 6.4, three examples for the investigated correlations with the Fe (II) emission line at 275.33 nm are shown as plots over the 10 measurements. The first is a basalt standard (DC 73303) which has the highest correlation with the total emission intensity but almost no correlation with T_{Fe} (Figure 6.4, *top row*). The second example is from bauxite (SRM 698) whose Fe emission has a positive correlation with both features (Figure 6.4, *middle row*). The last one shows the mentioned river sediment (sample DC 73371) without any significant correlation (Figure 6.4, *bottom row*). To summarize, there is no overall trend of correlations between the plasma characteristics and Fe (II) emission line intensities. However, what can be seen in Table 6.3 is the positive correlation (> 0.5) of the total emission intenstiy and the Fe (II) intensity for almost all samples except for four samples. One of these samples, a river sediment (DC 73318), has the lowest Fe concentration (1.5 at %) in the sample set. However, the other three samples have average Fe concentrations and no distinct explanation for the missing correlation with the total emission intensity could be found. The highest correlations (> 0.9) are observed for samples with comparatively high Fe concentrations. Except for rhyolite (DC 71305) that contains 2.24 at % Fe, all samples with a correlation higher than 0.9 between the total intensity and the Fe (II) emission line have Fe concentrations above 7 at %. This is in agreement with our observation reported in [Schröder et al., 2019a] that the total emission intensity can have strong variations depending on the substrate material. Some elements, especially Fe, have a large number of emission lines and lead therefore to an enhanced total emission intensity. Thus, for the certified samples with higher Fe content, the total emission intensity is mainly

Table 6.3: Pearson correlations among 10 measurements of each sample between emission lines of Fe and Si with temperature and total emission intensity. For some samples not enough Si lines were present for calculating T_{Si}.

	Fe (II) 275.33 nm		**Si (I) 288.16 nm**	
Sample	$\mathbf{T_{Fe}}$	**Total int.**	$\mathbf{T_{Si}}$	**Total int.**
CRM 4233	0.15	0.78	-0.06	-0.63
DC 71302	-0.13	0.72	0.38	-0.17
DC 71305	0.45	0.92	0.04	0.47
DC 72302	0.04	0.46	-	0.46
DC 73302	-0.35	0.58	-	-0.57
DC 73303	-0.15	0.96	-	-0.07
DC 73308	-0.01	0.61	0.41	0.55
DC 73309	-0.47	0.73	-0.21	0.78
DC 73317	0.14	0.74	0.55	0.70
DC 73318	-0.08	0.20	0.39	-0.28
DC 73322	-0.30	0.263	-0.09	0.54
DC 73371	-0.07	-0.02	0.37	0.50
RM 1017	0.16	0.96	0.65	-0.35
RM 8704	0.41	0.76	0.22	-0.51
SRM 679	0.48	0.95	0.45	-0.36
SRM 688	0.51	0.79	0.28	0.18
SRM 698	0.69	0.92	-	-
SRM 2702	-0.09	0.59	0.16	0.37

influenced by Fe emission lines leading to the observed positive correlations. By contrast, Si has much less emission lines than Fe and has therefore less influence on the total emission intensity. This can also be seen in the data by means of correlations between the Si (I) intensity and the total intensity. For Si (I), there is no overall trend as seen for the Fe (II) emission line as the correlations with the total emission intensity range from -0.63 (CRM 4233) to 0.78 (DC 73309).

Regarding the correlations with T_{Fe}, only for bauxite (SRM 698, 13 at % Fe) and one basalt standard (SRM 688, 7 at % Fe) correlations > 0.5 with the Fe (II) intensity were found. For temperature T_{Si}, one significant positive correlation (0.65) with the Si (I) intensity is given by the andesite-basalt standard (RM 1017) which has a medium concentration of Si (23 at %) in comparison to the other samples.

This study of signal fluctuations in 10 repetitive measurements at otherwise constant experimental parameters has shown that the plasma temperature is not suitable for compensation of measurement-to-measurement fluctuations due to insufficient correlations with the investigated emission lines within the given experimental conditions. Also other plasma characteristics as the electron density whose correlations are not shown here seem not useful for the purpose of normalization. The total emission intensity shows best results in the particular case of Fe emission lines for samples with Fe concentrations above 7 at %.

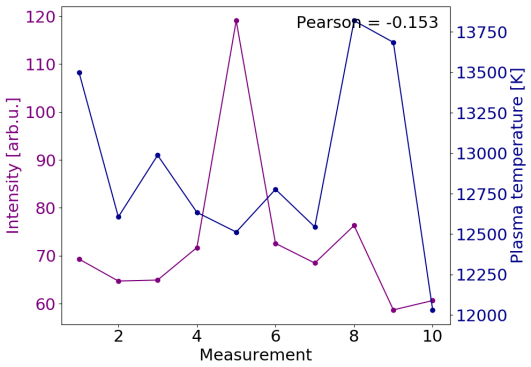

(a) **DC 73303**: Fe (II) 275.33 nm and T_{Fe}

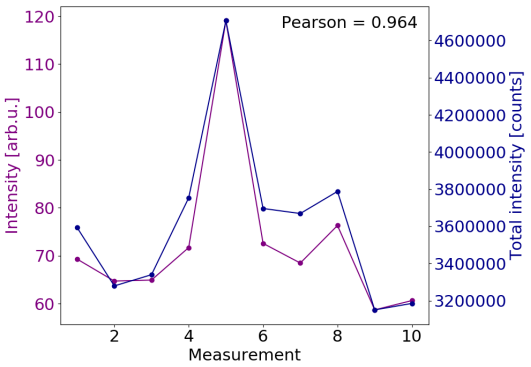

(b) **DC 73303**: Fe (II) 275.33 nm and total emission intensity

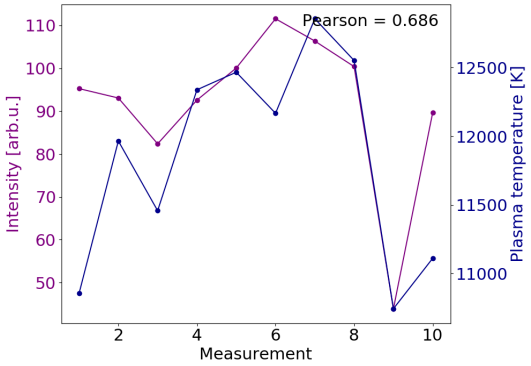

(c) **SRM 698**: Fe (II) 275.33 nm and T_{Fe}

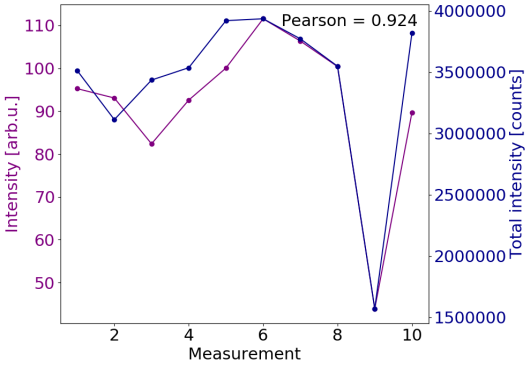

(d) **SRM 698**: Fe (II) 275.33 nm and total emission intensity

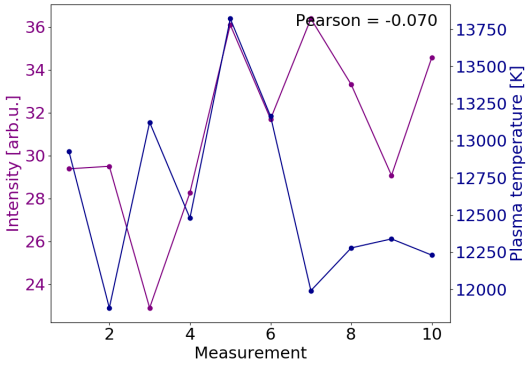

(e) **DC 73371**: Fe (II) 275.33 nm and T_{Fe}

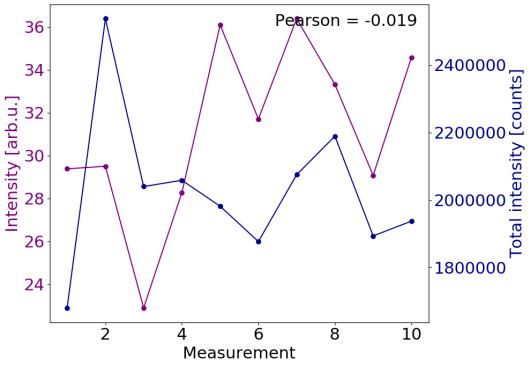

(f) **DC 73371**: Fe (II) 275.33 nm and total emission intensity

Figure 6.4: Examples of the Fe (II) 275.33 nm signal fluctuations in comparison with T_{Fe} and the total emission intensity within 10 repetitive measurements. The corresponding Pearson correlation coefficients are given in the particular plot. *(a)/(b)*: Sample DC 73303 has the largest correlation with the total emission intensity but no correlation with T_{Fe}. *(c)/(d)*: High and positive correlations for both characteristics are given for sample SRM 698 which has the highest Fe concentration of 13 at %. *(e)/(f)*: No significant correlation was found for sample DC 73371.

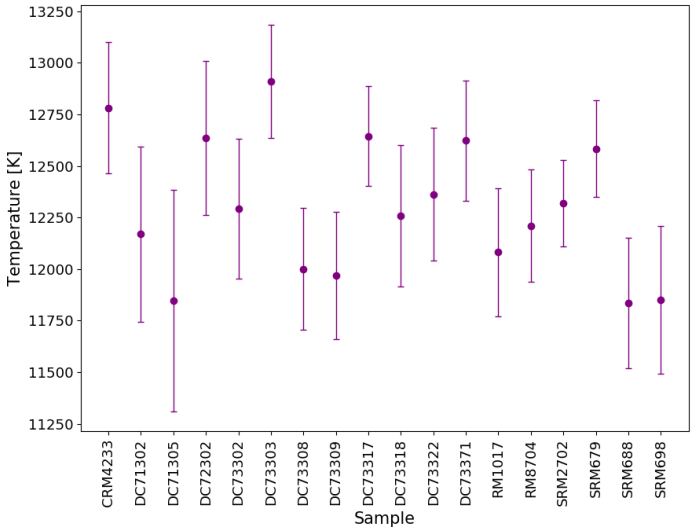

Figure 6.5: Mean temperatures of 10 repetitive measurements derived by Boltzmann plots of Fe (II) emission lines for all reference samples. The error bars indicate the standard deviation. Among the samples only a small temperature variation can be observed.

Normalization of signals from different sample matrices

It was further investigated if the plasma parameters can be used to reduce variations of emission lines due to varying sample matrices. For this purpose, I compare univariate calibration curves, in particular for Fe concentrations, before and after normalization with plasma parameters.

The same data of the previous study was used but this time mean values of the 10 repetitive measurements were taken. Since it was shown before that different temperatures are obtained depending on which element was chosen for the derivation, I focus here on T_{Fe} and Fe emissions. However, other elements were also tested and the analysis did not reveal other results than those presented in the following for Fe. The temperatures for each measuerement were already derived in the previous study from Boltzmann plots of Fe (II) emission lines and their means for each sample are plotted with standard deviations in Figure 6.5. What can be seen in the plot is that the plasma temperature varies in a narrow range between 11800 K and 12900 K for the different samples. Furthermore, standard deviations are large compared to the variability among the samples. This observation proposes that the LIBS plasmas of the different sample matrices behave on average similiar during the integration time of 500 ns after a delay of 350 ns. This is in accordance with the outcomes reported in [Sallé et al., 2006].

Univariate calibration models were built for several elements and emission lines. As before, the Fe (II) 275.33 nm emission line was used representative for Fe (II) emissions. Figure 6.6 (a) shows the curve of growth without any normalization. Besides matrix effect, self-absorption can affect the linearity of calibration curves: For higher Fe concentrations (*grey points*), the growth is not linear anymore and shows a trend towards saturation. This is the typical effect of self-absorption on the shape of curves of growth [Hahn and Omenetto, 2012]. Although the concentration in the plasma of the particular element increases, its emission intensity does not increase with the same proportion. This is because more particles are available in

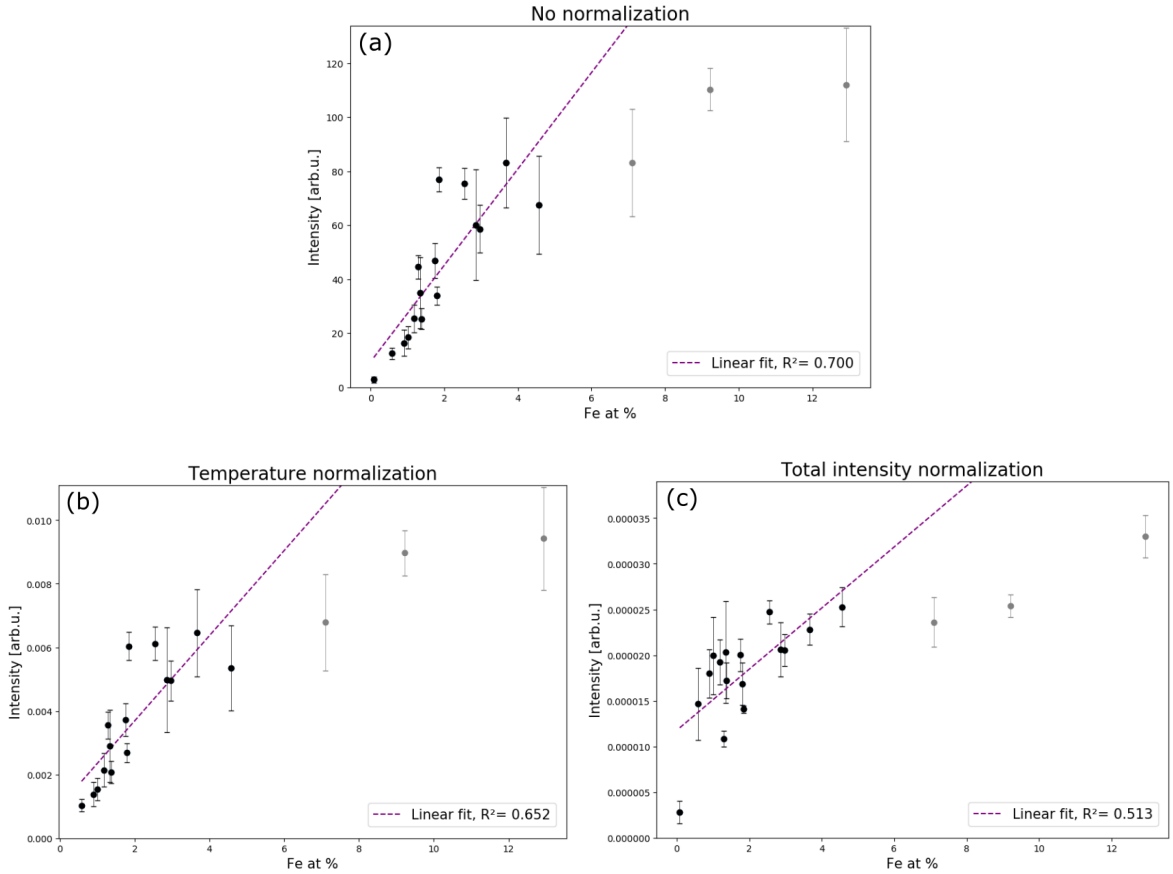

Figure 6.6: Curves of growth for the Fe (II) emission line at 275.33 nm. Only samples with Fe concentrations below 5 at % (*black points*) were considered for the linear fits (*purple dashed*) in order to avoid contributions of self-absorption. Error bars are the standard deviation of 10 repetitive measurements. *(a)*: No normalization was applied to this data resulting in a linear fit with $R^2 = 0.7$. *(b)*: Normalization by T_{Fe} does not improve the linearity of the curve: $R^2 = 0.65$ *(c)*: Normalization by the total emission intensity even leads to a decrease of the linear fit quality to $R^2 = 0.51$.

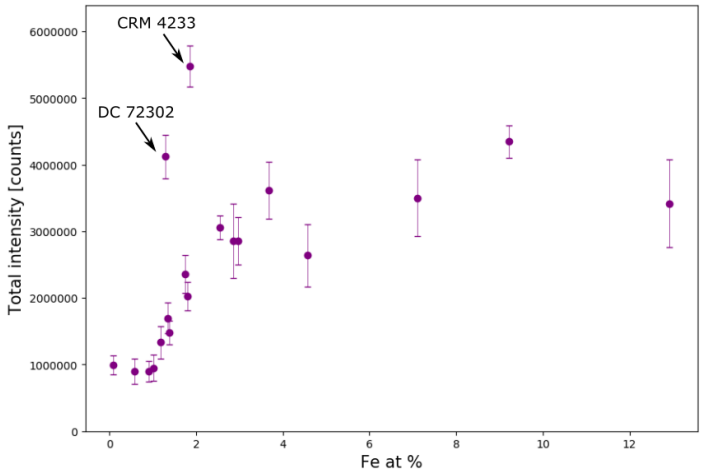

Figure 6.7: Total emission intensity for increasing Fe concentrations of the certified samples. The two outliers marked by arrows have higher Mg concentrations than the average Mg concentration of the sample set. This results in the deviation from the nearly linear trend for the samples with Fe concentrations below 4 at %. Also in this plot, the effect of self-absorption becomes apparent for higher Fe concentrations.

the plasma at higher concentrations which can reabsorb the particular emission in the colder outer regions of the plasma. In order to avoid intensities of self-absorbed emission lines in the linear calibration curve, only the data of samples with Fe concentrations below 5 at % (Figure 6.6,*black points*) was fitted by a linear function (*dashed, purple*, $R^2 = 0.7$).

Next, I normalized the Fe (II) emission line intensities by T_{Fe} as well as by the total emission intensity. The resulting calibration curves are also shown in Figure 6.6 (b)/(c). To compare the quality of the calibration models without and with normalization, also linear fits for Fe concentrations below 5 at % (*black points*) were done. The outcomes show that the normalizations applied here do not improve the linearity of the models. Moreover, they reduce the linear fit quality to $R^2 = 0.65$ and $R^2 = 0.51$ for the temperature and the total intensity normalization, respectively. Regarding the temperature normalization, the decrease is small indicating that the effect of normalization is small. This is in accordance with the observation that T_{Fe} varies only in a narrow range among the samples, see Figure 6.5. The total emission intensity, on the other hand, varies among the samples which can be seen in Figure 6.7 where the total emission intensity is plotted for increasing Fe concentrations in the sample set. Overall, an increase of the total emission intensity towards higher Fe concentrations is observable as expected because of the high number of Fe emission lines in the particular spectral range. There are two exceptions which are the ultrabasic rock (DC 72302) and the dunite (CRM 4233) samples. These samples have much higher Mg concentrations (DC 72302: 24.0 at % and CRM 4233: 29.7 at %) than the other samples (average: 5.2 at %). These higher Mg concentrations are responsible for the higher total emission intensities. In Figure 6.7, it can be seen that there are variations among the samples of the total emission intensity, however, these correlate not always with the increasing Fe concentrations. Furthermore, the variations do not correlate with the effects arising from varying sample matrices, otherwise, the linearity of the total intensity normalized calibration curve (Figure 6.6 (c)) would have improved. Even though the objective of this study was to reduce the influence of matrix

effects by normalization, it can also be seen that the effects of self-absorption remain almost unchanged after normalization. In both shown cases (Figure 6.6 (b)/(c)), a trend towards saturation is observable for higher Fe concentrations.

To summarize, in the data of the certified samples, the ionic Fe (II) emission at 275.33 nm was investigated and normalized by plasma parameters and the total emission intensity. Further Fe emission lines and lines from other elements were also studied but did not reveal other results than those presented here. The emission of Fe (II) in different chemical matrices could not be normalized by either the plasma temperature nor by the total emission intensity. The plasma temperature was derived from Boltzmann plots of Fe (II) emission lines and shows no significant trend among the samples. The total emission intensity, however, shows a trend with increasing Fe concentration but not for all samples which is strongly related to elemental concentrations.

6.3 Iron and JSC mixtures - varying laser energies

The irradiance is one major factor conctrolling emission line intensities [Singh and Thakur, 2007]. For the ChemCam instrument, varying distances to the target lead to changes of the spot size from 300 μm at 1.56 m distance to 550 μm at 7 m [Maurice et al., 2012] and, because the laser energy remains constant, the irradiance on the sample surface changes. Varying irradiation is not only relevant to ChemCam but to all LIBS instruments with the capability to focus the laser at different sample distances. Here, I test normalization with plasma parameters applied to data obtained with different laser irradiances. In the Aryelle LIBS setup (see Section 5.1), the spot size remains constant and the variation of irradiance could therefore be realized by changing laser pulse energies. Therefore, the changes of irradiance will be denoted as laser energy changes in the following.

Experiments

Experiments were performed with the Aryelle LIBS setup with the samples in simulated Martian atmospheric conditions (see Section 2.1). All measurements were performed on the same sample, for which the Martian soil analogue JSC-1A was mixed with $Fe_2(SO_4)_3$ in a 80:20 wt % ratio and pressed into a pellet. The $Fe_2(SO_4)_3$ was added in order to increase the Fe concentration in the sample and to therefore ensure a large number of Fe emission lines with high SNRs for temperature determination. The energy of the laser pulses was varied in a range from 6 mJ to 35 mJ per pulse using different combinations of neutral density filters. As the spot size in the Aryelle setup is $\approx$300 μm these energies correspond to irradiances of $\approx$ 16 - 83 MW/mm^2. With each laser energy, three measurements at different positions were done and for each measurement the emission of 30 LIBS plasmas was accumulated. An integration time of 500 ns and a delay of 350 ns after the laser pulse was chosen. For this study, measurements were done in the UV/VIS/NIR spectral range in order to cover a wide range of emissions including this time the H_α line for electron densitiy calculations. A picture of the sample after the measurement is shown in Figure 6.8 where an increase of the diameter of the LIBS craters with increasing laser energy can be seen. From this first observation, it can be concluded that more mass is ablated for higher laser energies which is in accordance with the literature, e.g. [Russo et al., 2007].

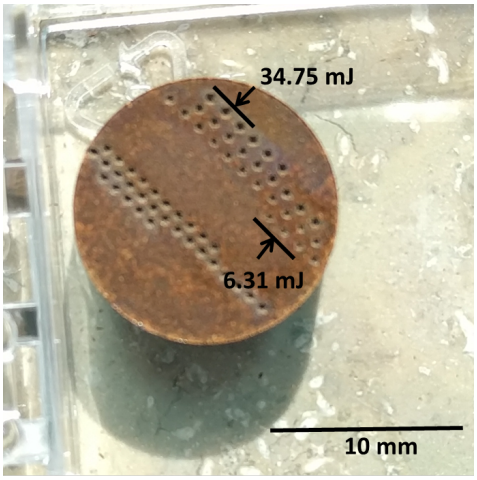

Figure 6.8: Pellet of the mixture of JSC-1A with $Fe_2(SO_4)_3$ after the measurements with varying laser energy, see upper right craters. The amount of ablated mass increases for higher laser energies, which becomes apparent by the larger crater diameters.

Emission line intensities with laser energy

In Figure 6.9 a representative atomic *(a)* and ionic *(b)* emission line of Fe is shown, respectively. Regarding the ionic line, the measurements with different laser energies can be distinguished due to a trend of the amplitudes for increasing laser energy which is not the case for the atomic line. For better comparison, the shown emission lines and further neutral and single ionized Fe lines were fitted with Voigt profiles and their amplitudes plotted against the applied laser energy, see Figure 6.10. The error bars indicate the standard variation of three measurements with the same laser energy. What can be clearly seen is the continual growth of the ionic emission lines *(b)* in contrast to the atomic emission lines *(a)* that show no distinct trend. This behaviour was not only observed for Fe emission lines. Further emission lines of other elements were fitted with Voigt profiles and trends of their intensities with increasing laser energy were evaluated (plots are not shown here). In order to compare how much emission line intensities change within the laser energy range, their RSDs were determined. The outcomes are listed in Table 6.4. Almost all neutral emission lines have a RSD around 20 % except of the Fe (I) at 381.58 nm (25.6 %) and Mg (I) at 285.21 nm (31.5 %). By contrast, the ionic emissions reveal much larger values. The smallest RSD from ionic emissions was determined from Ti (II) at 338.38 nm (36.3 %) while the largest was obtained from Mg (II) at 292.86 nm (81.8 %). This is a further confirmation for what has been observed in Figures 6.9 and 6.10: Ionic emission lines are more affected by changes in the laser energy than the neutrals. This is in accordance with observations reported in our study [Schröder et al., 2019a].

The increased intensities of ionized emission lines and the low effect of varying laser pulse energies on neutral emission lines indicate a higher degree of ionization in the plasma for higher laser pulse energies. For ionization, the plasma temperature is a key factor as given by the Saha-Eggert equation (3.4). Thus, for higher laser energies the plasma is most likely more heated during the time of the incoming laser pulse which increases the initial plasma temperature before the plasma starts to cool. The higher ionic emission is mostly captured in the early times of the integration window of 500 ns. Differences between the behaviour of

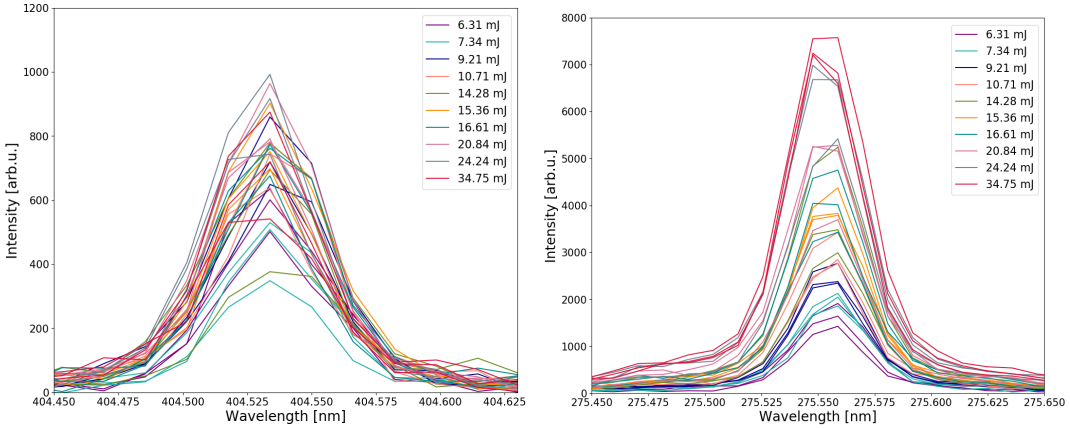

(a) Fe (I) emission line at 404.58 nm (b) Fe (II) emission line at 275.57 nm

Figure 6.9: Fe emission lines with varying laser energy. All three measurements at each laser energy are shown. While the atomic emission line *(a)* does not show an obvious trend with the laser energy, the ionic emission line *(b)* increases continuously with increasing laser energy.

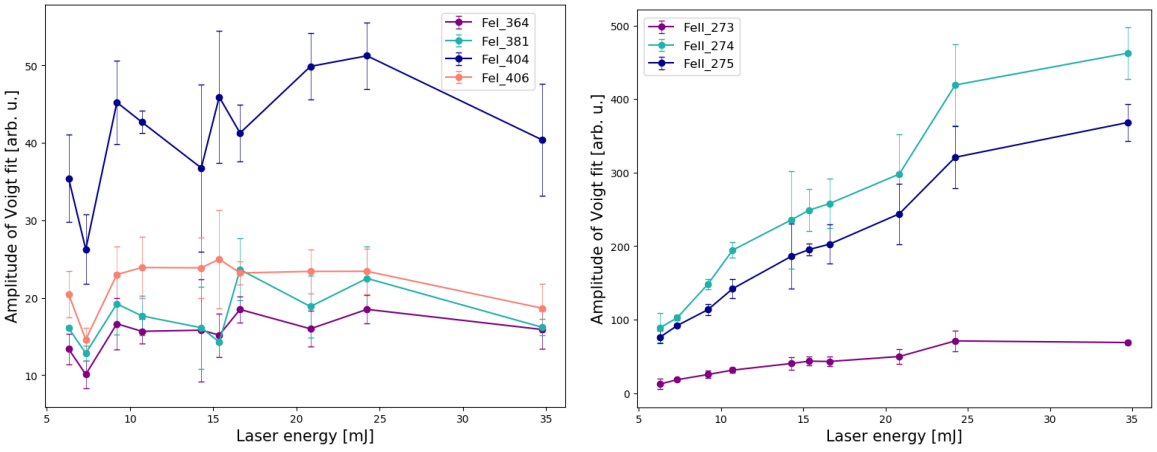

(a) Fe(I) emission lines (b) Fe(II) emission lines

Figure 6.10: Fe(I) and Fe(II) emission lines, the values are averages of three measurements and the error bars indicate their standard deviations. The intensity of neutral emission lines *(a)* do not reveal a trend with increasing laser energy. On the other hand, the intensity of ionic emission lines *(b)* increases with increasing laser energy.

Table 6.4: Relative standard deviations of emission lines with varying laser energy.

Element	Wavelength [nm]	RSD [%]	Element	Wavelength [nm]	RSD [%]
Fe (I)	381.58	25.6	Ti (I)	499.11	18.5
Fe (I)	404.58	22.4	Ti (II)	336.12	38.9
Fe (I)	406.36	21.2	Ti (II)	337.28	39.4
Fe (II)	273.70	49.4	Ti (II)	338.38	36.3
Fe (II)	274.93	50.1	Na (I)	589.00	20.2
Fe (II)	275.57	48.8	Na (I)	589.59	18.9
Mg (I)	285.21	31.5	Al (I)	394.40	18.1
Mg (II)	292.86	81.8	Al (I)	396.15	18.8
Mg (II)	293.65	72.4	Al (II)	281.62	80.2
Ti (I)	498.17	23.1	Si (I)	288.16	19.04

Table 6.5: Overview of the emission lines that were used for the two-line temperature determination.

Element	λ [nm]	Ag [$\times 10^8$ s^{-1}]	E_{upper} [eV]
Mg (II)	279.07	16.00	8.864
Mg (II)	280.27	5.14	4.422
Fe (II)	273.95	17.70	5.511
Fe (II)	275.33	22.70	7.769
Ca (II)	315.89	12.00	7.047
Ca (II)	393.37	5.88	3.151
Al (I)	308.22	2.35	4.022
Al (I)	394.40	1.00	3.143

ionized emission lines from different elements can be explained by their ionization energies and transition probabilities.

Correlations and normalization with plasma parameters

For this experiment, two further methods of plasma parameter calculation were used. Plasma temperatures were determined by Saha-Boltzmann plots based on Fe emission lines and by the two line method relying on Boltzmann excitation relations with different elemental emission lines. Both methods were introduced in Section 3.1.4 and are useful here as the UV/VIS/NIR spectral range provides neutral and ionic Fe emission lines, as well as line pairs of several elements. Starting with the latter method, the selected emission line pairs from Al, Ca, Fe, and Mg are listed in Table 6.5. Although it is recommended to use transitions that are well separated in the energy of their upper levels and to avoid ground state excitations it is not always possible to find line pairs that meet these criteria and that have high enough intensities for error free line fitting. Nevertheless, the chosen line pairs can at least give an approximation of the plasma temperature. In Figure 6.11 the inferred temperatures are plotted for the applied laser energies. The major finding here is again that the temperatures strongly deviate from each other depending on the element whose emission was used for the determination as observed before in Section 6.2. The differences might again be due to emission from different locations depending on the local temperatures in the plasma plume. But also non-equilibrium

Table 6.6: Pearson correlations between two-line method temperatures. The left part of the table corresponds to each single measurement while the right part shows the correlations between the mean temperatures at one laser energy.

	T_{Al}	T_{Ca}	T_{Fe}	T_{Mg}		$\overline{T}_{Al}$	$\overline{T}_{Ca}$	$\overline{T}_{Fe}$	$\overline{T}_{Mg}$
T_{Al}	1.00	-0.07	0.12	-0.33	$\overline{T}_{Al}$	1.00	0.00	0.21	-0.51
T_{Ca}		1.00	0.49	0.29	$\overline{T}_{Ca}$		1.00	0.72	0.53
T_{Fe}			1.00	0.27	$\overline{T}_{Fe}$			1.00	0.62
T_{Mg}				1.00	$\overline{T}_{Mg}$				1.00

Table 6.7: Overview of Fe emission lines used for Saha-Boltzmann plots.

	λ [nm]	Ag [$\times 10^8\,s^{-1}$]	E_{up} [eV]		λ [nm]	Ag [$\times 10^8\,s^{-1}$]	E_{up} [eV]
Fe (II)	273.07	1.12	5.62	Fe (I)	381.58	7.84	4.73
Fe (II)	273.70	2.44	5.60	Fe (I)	382.59	4.18	4.15
Fe (II)	273.95	17.70	5.51	Fe (I)	382.78	5.25	4.80
Fe (II)	274.32	7.88	5.62	Fe (I)	383.42	2.26	4.19
Fe (II)	274.65	12.30	5.59	Fe (I)	404.58	7.76	4.55
Fe (II)	274.70	10.10	5.55	Fe (I)	406.36	4.66	4.61
Fe (II)	275.33	22.70	7.77	Fe (I)	407.17	3.82	4.65
Fe (II)	275.57	21.5	5.48				
Fe (II)	276.75	11.80	9.70				
Fe (II)	278.37	10.60	7.70				

effects can not be excluded which restrict the validity of the Boltzmann equilibrium equation.

A further observation is that no distinct trend of the temperatures with increasing laser energy is observable. However, for each element, at least a rise of the temperature between plasmas induced by the lowest and the highest applied laser energy is recognizable. Previous works have shown that an increase of the plasma temperature for higher laser energies does not necessarily occur at least in Earth atmospheric conditions [Yalçin et al., 1999, Aragón and Aguilera, 2008b]. The authors of both works argue with the concept of a laser-supported radiation (LSR) wave, see Section 3.1.1 which describes mainly the laser absorption mechanism of the plasma. A LSR wave is supposed to form for high irradiances and has an expanding and absorbing gas region that shields the gas left behind from the laser energy. As a result, the created plasma has a nearly uniform pressure and temperature. In this study, the almost constant plasma temperatures could indicate the existence of such an expanding wave. On the other hand, an increasing degree of ionization was observed which gives evidence for higher plasma temperatures in the early stages. It is also possible that a laser-supported detonation (LSD) wave, see Section 3.1.1, evolves for which the plasma temperature would indeed increase for higher laser energies. In this case, the two line Boltzmann plot method was not able to reveal the actual trend of plasma temperature with increasing laser pulse energy.

Next, Pearson correlation coefficients between the temperatures were calculated which can be found in Table 6.6. The objective is to investigate if the different temperatures show at least similar trends with changing laser pulse energies. The left part of the table displays the correlations between all derived temperatures of each measurement while the right part gives the correlation between the averaged temperatures $\overline{T}$ for each laser energy. Clearer

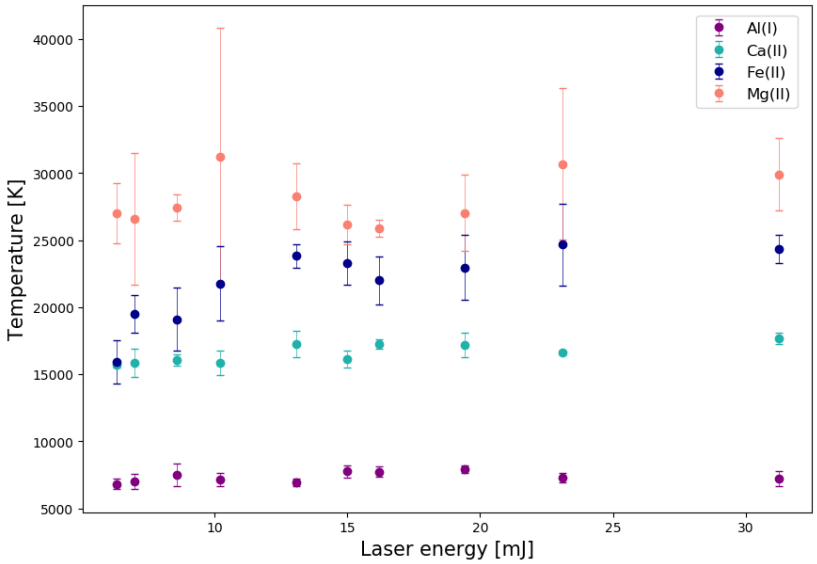

Figure 6.11: Plasma temperatures derived by line pairs of Al, Ca, Fe, and Mg. No explicit trend with the laser energy is observable. Although the values were determined from the same measurements, the temperatures differ depending on the element used.

correlations or anti-correlations appear between the mean temperatures, where the largest reaches 0.72 between $\overline{\mathrm{T}}_{\mathrm{Ca}}$ and $\overline{\mathrm{T}}_{\mathrm{Fe}}$. However, no overall correlation between the temperatures for varying laser energies can be observed as they are either positive, negative, or show no correlation at all. This means in particular that no general trend of the plasma temperature with varying laser energy was found since the temperatures derived from different elements behave differently. From these observations including the different behavior of atomic and ionic species, it becomes clear that no universal applicable normalization that compensates for varying laser irradiance can be achieved with the plasma temperature, at least under the given experimental conditions.

With another method for plasma temperature calculation, namely with the Saha-Boltzmann plot method, I derived further plasma temperatures from the spectra measured with varying laser pulse energies. For this method, atomic and ionic emission lines are used and Fe was chosen due to a large number of available emission lines. All lines that were employed are listed in Table 6.7. Furthermore, electron densities were inferred from linear Stark broadening of the H_α line. The electron density was also used as input for the temperature determination since one term of the Saha-Boltzmann plot method weakly depends on n_e. In Figure 6.12(*left*), the determined temperatures are plotted for different laser energies. In this case, they reveal a continuous growth over a temperature range of $\approx$ 1700 K. However, this growth is small compared to the increase of ionic emission intensities, see Figure 6.10. As mentioned before, an increase of the plasma temperature with increasing irradiance is not always given and its absence can be explained by the expansion of a LSR wave. But in contrast to the temperatures derived by the two-line method, the temperatures derived by the Saha-Boltzmann plot method show an increase for higher laser energies. This indicates that the expanding wave might not be of the LSR type and could rather be a LSD wave. In this case, the higher laser energies can reach the plasma without being absorbed by the gas front and can therefore heat

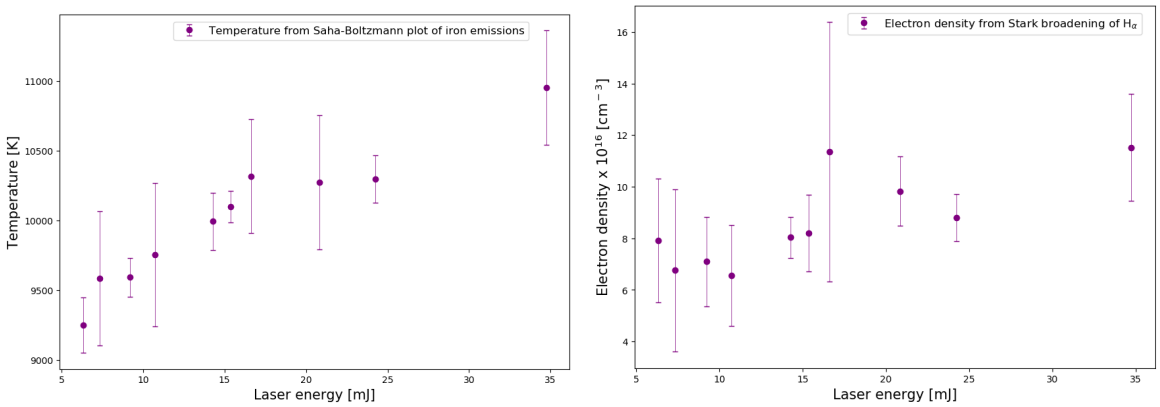

Figure 6.12: *Left*: Plasma temperatures derived from Saha Boltzmann plots of Fe (I) and Fe (II) emission lines. *Right*: electron densities from H_α Stark broadening for different laser energies. Error bars correspond to the sample standard deviation obtained from three measurements each. The temperature grows when going to higher laser energies while the electron density show a slight tendency to increase.

the plasma further.

Despite the discrepancy between the temperatures derived from different elements (Figure 6.11), an additional discrepancy becomes apparent when comparing the two methods of plasma temperature determination used here. The temperatures derived by the ionic Fe line pair (*blue* in Figure 6.11) reaches from 16 000 K to 24 000 K while the temperatures obtained by Saha-Boltzmann plots of neutral and ionic Fe emission lines have values between 9 300 K and 11 000 K (Figure 6.12(*left*)). Those differences can not be explained by different spatial distributions as Fe emission lines were used for both methods. Such a non unique temperature indicates that the plasma might not be in LTE in which the excitation and ionization temperature would be the same, see Section 3.1.3.

Furthermore, in Figure 6.12(*right*) the electron density is plotted and a slight increase for samples with Fe concentrations below 4 at % is observable with increasing laser pulse energy. It was found in several studies that hydrogen shows a complex behaviour in LIBS plasmas probably because of its low weight and complex bondings [Sobron et al., 2012, Kurniawan et al., 2014, Schröder et al., 2015]. This can introduce uncertainties in the electron density when derived from the H_α emission line which is probably the reason for the large error bars in Figure 6.12(*right*). However, H_α is present in each Martian LIBS spectrum and is in general a popular candidate for electron density derviation in the LIBS community because of its linear Stark effect relation and relatively high intensity [Hahn and Omenetto, 2010]. Nevertheless, higher temperatures as seen based on the Saha-Boltzmann plot lead to higher ionizations with larger electron densities. To conclude, although the electron density derivation relying on H_α is prone to uncertainties, it can be used to give an indication and to reveal general trends.

The potential of using T and n_e for normalization of particular emission lines is discussed in the following. Correlations between emission lines (Fe and Mg) and plasma characteristics namely the plasma temperature derived by Saha-Boltzmann plots of Fe, the electron density inferred from the H_α linear Stark broadening, the total emission intensity, the ratio of two Fe lines of different ionization stages, and the ratio of ionization calculated from the plasma

Table 6.8a: Pearson correlation coefficients between all measurements.

		Fe(II)			Fe(I)				Mg(I)	Mg(II)						
		273	274	275	364	381	404	406	285	292	293	Fe(II)/Fe(I)	total int.	temperature	density n_e	ratio ion.
Fe(II)	273	1.00	0.97	0.97	0.38	0.41	0.52	0.23	0.52	0.60	0.65	0.78	0.93	0.73	0.24	0.80
	274		1.00	0.99	0.41	0.37	0.45	0.19	0.52	0.60	0.65	0.86	0.96	0.74	0.25	0.83
	275			1.00	0.36	0.35	0.40	0.18	0.53	0.68	0.73	0.88	0.97	0.75	0.25	0.85
Fe(I)	364				1.00	0.62	0.64	0.50	0.00	0.16	0.10	0.10	0.25	0.24	0.19	0.06
	381					1.00	0.51	0.48	0.10	-0.01	-0.03	0.13	0.22	0.09	0.03	0.09
	404						1.00	0.37	0.12	0.16	0.07	-0.02	0.34	0.24	0.19	0.10
	406							1.00	-0.12	-0.16	-0.14	0.04	0.09	0.09	0.02	-0.01
Mg(I)	285								1.00	0.84	0.83	0.47	0.62	0.33	0.04	0.44
Mg(II)	292									1.00	0.96	0.66	0.75	0.47	0.09	0.63
	293										1.00	0.73	0.80	0.54	0.14	0.68
Fe(II)/Fe(I)												1.00	0.89	0.68	0.17	0.86
total int.													1.00	0.76	0.27	0.86
temperature														1.00	0.74	0.64
density n_e															1.00	0.74
ratio ion.																1.00

Table 6.8b: Pearson correlation coefficients between mean values of three measurements.

		Fe(II)			Fe(I)				Mg(I)	Mg(II)						
		273	274	275	364	381	404	406	285	292	293	Fe(II)/Fe(I)	total int.	temperature	density n_e	ratio ion.
Fe(II)	273	1.00	0.99	0.99	0.64	0.42	0.62	0.27	0.89	0.87	0.92	0.89	0.95	0.92	0.53	0.87
	274		1.00	1.00	0.61	0.38	0.57	0.20	0.88	0.92	0.92	0.93	0.98	0.93	0.57	0.89
	275			1.00	0.57	0.35	0.54	0.16	0.88	0.92	0.92	0.95	0.98	0.94	0.59	0.90
Fe(I)	364				1.00	0.86	0.79	0.74	0.48	0.43	0.37	0.35	0.52	0.53	0.57	0.30
	381					1.00	0.61	0.49	0.10	0.29	0.25	0.15	0.14	0.26	0.30	0.12
	404						1.00	0.76	0.47	0.50	0.34	0.24	0.47	0.42	0.36	0.22
	406							1.00	0.13	0.06	-0.04	-0.11	0.12	0.12	0.17	-0.11
Mg(I)	285								1.00	0.98	0.94	0.83	0.90	0.79	0.31	0.85
Mg(II)	292									1.00	0.97	0.89	0.94	0.84	0.40	0.88
	293										1.00	0.94	0.94	0.84	0.38	0.92
Fe(II)/Fe(I)												1.00	0.96	0.93	0.55	0.94
total int.													1.00	0.95	0.59	0.91
temperature														1.00	0.73	0.91
density n_e															1.00	0.42
ratio ion.																1.00

parameters based on the Saha-Eggert equation (3.15) were computed and can be found in Table 6.8. The table is divided into two parts where in Table 6.8a the correlations between all measurements are shown while Table 6.8b gives the correlations between mean values of the measurements with the same laser energy. Correlations become larger, thus clearer, through averaging as already observed in Table 6.6. Hence, more measurements might lead to even better correlations. Nevertheless, on extraterrestrial bodies the targets are not homogeneous like in this laboratory setting and obtaining more than one measurement of the same composition is usually not possible.

Turning to the results in Table 6.8, it can be seen that the largest positive correlation between emission lines and plasma features is obtained for the total emission intensity. Although the plasma temperature has high correlations especially for the averaged values with the ionized Fe lines and all Mg lines, the correlations with the total intensity exceed these. The neutral Fe lines correlate only among themselves and those correlations are weak compared, for example, to the correlations among the ionized Fe lines. The calculated ratio of ionization and the electron density show no significant correlations, except for the ionization ratio with Fe (II) emissions.

To further analyse the normalization capability of plasma characteristics, RSDs before and after normalization were determined exemplarily for selected emission lines. After a successful normalization, the RSD of a signal is expected to be smaller than before. Normalizations with the plasma temperature, the total intensity, and the calculated ratio of ionization were examined and the results are given in Table 6.9. What can be seen in this table is the unchanged RSD of the Fe (II) emission line after normalization by the plasma temperature although a positive correlation (0.748 for all measurements, 0.943 for averaged values) was obtained. This suggests that not only a positive correlation is necessary to compensate for changes in the signal. In the particular case, the signal which has to be normalized and the reference signal vary on a different scale. While the Fe (II) emission line has a RSD of 44.8 %, the one of the temperature is only 0.06 %. In contrast, the total emission intensity has a RSD of 41.5 % that is similar to the RSD of the Fe (II) emission and therefore better suited for normalization. Indeed, normalization with the total intensity decreases the RSD of the Fe (II) emission to 13.3 %. In general, the total emission intensity achieves the best normalization in this study for the signals of ionized species. The neutral emissions show no significant change of RSDs after normalization with the plasma temperature. Instead, an increase takes place after normalization with the total intensity and also with the ratio of ionization. The different findings for neutrals and ions can be explained by the different temperatures in the plasma. Assuming the expansion of a LSD wave which is supported by the observations in Figure 6.12(*left*), plasma temperatures are higher in the early stages of the plasma for higher laser energies leading to emissions of ionized particles. During the plasma cooling, the ionic emissions become less probable and neutrals dominate the plasma emission [Cremers and Radziemski, 2013, Schröder et al., 2019a]. For lower laser energies, the initial plasma temperature before cooling is lower and the time window of ionic emissions therefore smaller. Thus, ionic emissions are more affected by laser energy changes than neutral emissions by varying laser energies. However, the temperatures derived by Saha-Boltzmann plots do not change on a scale that corresponds to that of the ionic emissions. Again, the reason for this can be found in the spatially and temporally integrated measurements where gradients can not be resolved [Aguilera and Aragón, 2004, Aguilera and Aragón, 2007].

Table 6.9: RSD values before and after normalization with various plasma characteristics.

Feature	RSD [%]	RSD [%] after normalization with		
		Temperature	Total intensity	Ionization ratio
Fe (II) 275.6 nm	44.8	44.8	13.3	25.7
Fe (I) 404.6 nm	22.4	21.8	38.0	43.2
Mg (II) 293.7 nm	72.4	69.9	49.8	55.6
Mg (I) 285.2 nm	31.5	30.6	32.8	36.5
Ti (II) 336.1 nm	38.9	35.7	21.7	29.1
Ti (I) 499.1 nm	18.5	19.2	39.8	37.5

6.4 Conclusions for normalization with plasma parameters

For this study, normalization with plasma parameters of LIBS data taken under Martian atmospheric conditions was investigated and compared to other normalizations. Three different cases which require normalization were investigated: fluctuations among repetitive measurements with constant experimental parameters, univariate calibration curves relying on geological samples with different chemical matrices, and varying irradiances on the sample surface realized by varying laser energies. For the three cases, also different approaches for plasma temperature derivation were tested which are the Boltzmann and Saha-Boltzmann plot methods, and the two-line approach.

For the measurement-to-measurement fluctuations, no significant correlations between emission lines and plasma parameters were observed. The only correlation was found for the total emission intensity and Fe emission lines for samples with highest Fe abundances in the set of certified geological samples.

Univariate calibration curves for Fe were investigated using the averaged data of the repetitive measurements on the certified samples. Effects from the different chemical matrices can interfere the linearity which was observed for the emission signals from samples with Fe concentrations below 5 at %. Normalization neither with the plasma temperature, nor with the total emission intensity could improve the linearity.

In the third case, a controlled change of the laser irradiance was investigated and the data revealed correlations between ionized emission lines and the plasma temperature as well as the total emission intensity. An increase of the plasma temperature derived by Saha-Boltzmann plots for increasing laser energy was observed. However, this increase was small in comparison to the increase of ionic emission line signals and the total emission intensity. Due to the small scale variation of the plasma temperature, the RSD of ionic emission lines could not be reduced. Here, the normalization by the total emission intensity led to best results. It has to be mentioned, however, that here only one sample matrix was used and the usual problem with normalization to total emission intensity for changing elemental composition does not become apparent.

Regarding the derivation of plasma temperatures, the different methods gave different values. This is an indication for the LIBS plasma most likely not being in LTE in the particular time window (350 ns delay and 500 ns integration time) and under the particular experimental conditions. Different temperatures are derived from different elements which can be a result of spatially and time-integrated measurements. Also non-equilibrium effects can be responsible

for this observation. The LIBS plasma has a shorter lifetime in Mars atmospheric conditions than in ambient Earth pressure [Brennetot et al., 2003] which can be one reason for reduced performance of normalizing with plasma parameters compared to terrestrial applications, e.g. [Panne et al., 1998]. The LIBS plasma is a transient state and undergoes large temperature changes on shorter time scales in Martian atmospheric conditions. Consequently, derived temperatures are population-averaged and do not reflect the trends of local temperatures which mainly influences the emission characteristics of a LIBS plasma [Aguilera and Aragón, 2007]. Furthermore, the assumption of LTE is most likely not fulfilled in these measurements even though time-gated LIBS data was used. While these results suggest that even shorter integration times would be necessary for improved plasma parameter derivation, plasma parameters derived from LIBS data integrated over the full plasma lifetime such as done with ChemCam will be even less useful. Also, the data in this study measured with an echelle spectrometer is highly resolved and data collected by a LIBS space instrument has typically a much more limited performance.

Another aspect is that although from a theoretical point of view plasma parameters should be best suited for normalization as they best reflect the LIBS plasma conditions their derivation is not straightforward. Different approaches for their calculation lead to different values. The true characteristics might not be well reflected in these calculated values. Also, their calculation is comparatively complex and not as simple as mere division by the total emission intensity. It seems from these experiments that the additional effort of normalization with the tested plasma parameters does not pay off for a considerably improved way to treat the data. Time- and spatially resolved investigations of LIBS plasmas in Martian atmospheric conditions as well as modelling of the LIBS plasma under these special conditions can give further input for an improved determination of plasma parameters [Vogt et al., 2018a,Hansen et al., 2018,Schröder et al., 2019b], but it remains questionable if these can provide useful and practical ways for Martian LIBS data.

7 LIBS in low pressure

The Solar System comprises bodies with various atmospheres, ranging from the thin CO_2 atmosphere of Mars to a high pressure environment such as on Venus and Titan. But most of the known bodies have no atmosphere, meaning vacuum and even ultra high vacuum conditions ($< 10^{-7}$ Pa). Examples for these are the Earth Moon, asteroids, or the Martian moons Phobos and Deimos. Because of the dependency of the LIBS plasma on atmospheric conditions, LIBS instruments for exploration of atmosphereless bodies will deliver a different type of data than, for example, LIBS instruments on Mars such as ChemCam. In July 2019, the Indian Chandrayaan 2 mission launched to Earth's Moon and the touch-down of a lander containing a rover on the Lunar surface is scheduled for September 2019[1]. The scientific payload of the rover involves the first LIBS instrument for robotic in-situ exploration of an extraterrestrial body in vacuum conditions [Sundararajan, 2018]. Several studies have shown that the LIBS plasma in vacuum is less confined and has a shorter lifetime than in terrestrial conditions, e.g. [Lasue et al., 2012, Effenberger and Scott, 2010]. As a trade-off between plasma size and lifetime it was found that Martian atmospheric conditions with a pressure of about 7 hPa are close to ideal for LIBS analysis [Knight et al., 2000, Cremers, 2007]. However, the interest in LIBS instruments for in-situ surface analysis of other bodies than Mars is high [Lasue et al., 2012, Pavlov et al., 2012, Laxmiprasad et al., 2013].

Regarding the intrinsic characteristics of the LIBS plasma, it was observed that LIBS plasmas in low pressure environments have a higher degree of ionization than in terrestrial atmospheric conditions [Knight et al., 2000, Cremers and Radziemski, 2013, Cremers, 2014]. This was deduced from the appearance of emission lines from higher ionized spezies when reducing the surrounding pressure and keeping the laser irradiance constant. In particular, in LIBS spectra of soil measured in an argon atmosphere for pressures below ≈ 13 hPa, O(II) emission lines were observed which did not occur in the spectra measured at ≈ 770 hPa [Knight et al., 2000]. It was also reported that Fe (III) emission lines were observed in vacuum measurements which did not appear in measurements in terrestrial atmospheric conditions [Cremers and Radziemski, 2013]. Similar observations were made for O (II) and Si (II) emission lines reported in [Cremers, 2014]. The appearance of further emission lines of higher ionization stages in LIBS spectra measured in vacuum conditions can have an impact on the choice of spectral ranges of LIBS instruments for in-situ exploration of extraterrestrial bodies without an atmosphere. Furthermore, it is expected that Stark broadening in LIBS plasmas under vacuum conditions is reduced due to less particle interactions [Gornushkin et al., 1999]. This, for example, is important for data analysis methods when deriving electron densities or when fitting particular profiles to the emission lines. Also ionic emission lines are more affected by changes in irradiation [Schröder et al., 2019a], an experimental parameter that might not be constant for a space instrument, see Chapter 6. This could have an influence, for example, on the outcomes of MVA analysis.

[1] Information from `https://www.isro.gov.in/chandrayaan2-latest-updates` visited on 12th of August 2019.

The objective of this study is to investigate LIBS plasmas in low pressure environments with a focus on the previously reported higher degree of ionization [Knight et al., 2000, Cremers and Radziemski, 2013]. Relatively simple sample matrices were selected by means of different salts and a Fe sample which do not have a distinct relevance for a particular space mission. The samples were measured with LIBS in varying pressure conditions (all ≤ 20 hPa) and with different temporal parameters.

Besides the LIBS experiments, a theoretical approach which is based on solving the Saha-Eggert equation is part of this study in order to compare the experimental observations with theoretical predictions. Similar to the samples in the experiments, conceptually simple models were chosen to reveal general differences when going to low pressures.

7.1 Low pressure LIBS measurements

Experiments

All experiments in this study were done with the Aryelle LIBS setup described in Section 5.1. Pellets of NaCl, Na_2CO_3, and Fe were investigated. The samples were chosen as they have simple matrices which allow to study effects due to the pressure conditions with presumably little interference from matrix effects. In Table 7.1, the samples and the investigated measurement parameters of the experiments in this chapter are listed. For all these measurements, the UV spectral range was used due to several Fe and Na emission lines in this range. For the surrounding gas, no special composition was used and all measurements were done in terrestrial atmosphere at varying pressures. The laser energy was adjusted to 30 mJ per pulse for each measurement. This rather high laser energy was chosen to ensure a LIBS plasma resulting in good SNRs for proper data interpretation. As the lifetime of the LIBS plasma strongly depends on atmospheric pressures, the integration time was 1 ms for each pressure setting in order to capture the whole emission of each plasma. In all measurements, the emission of 30 consecutive LIBS plasmas was accumulated.

Observations

During the experiments, different plasma shapes for the different pressures were apparent based on observations by eye. While the plasma seemed rather spherical and confined for pressures above 1 hPa it has a conical and expanding shape for pressures below 1 hPa which is in accordance with literature, e.g., [Lasue et al., 2012, Cremers, 2014]. Due to these differences in confinement, distinct differences in the lifetimes were measured. As expected, the duration of plasma emission is significantly shorter for the lower pressures than for pressures above 1 hPa.

Table 7.1: Samples and Experiments in this study. All samples were pressed into pellets.

Sample	Pressures [hPa]	Delay times [ns]	No. of repetitive meas.
NaCl	0.02, 0.2, 2, 7, 15	100	3
NaCl	0.01, 0.1, 1.5, 20	0, 100, 200	5
Na_2CO_3	0.01, 0.1, 1.5, 20	0, 100, 200	5
Fe	0.01, 0.1, 1.5, 20	0, 100, 200	5

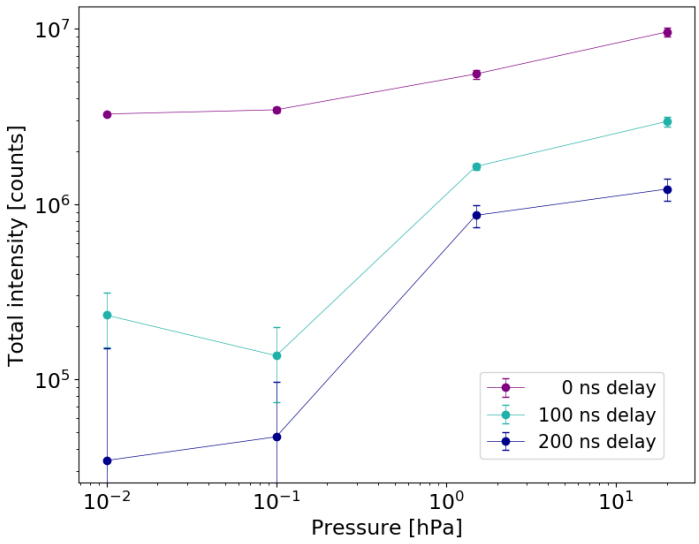

Figure 7.1: Integrated emission intensity of the UV range from measurements of NaCl for different ambient pressures. Shown are the results from measurements at different delay times (marked with different colors) and the values are the mean of five measurements while the error bars indicate the standard deviation. For pressures below 1 hPa almost the whole emission takes place in the first 100 ns after plasma ignition.

In Figure 7.1, the accumulated emission intensity (sum of all counts) of NaCl measurements is shown for increasing pressure at different delay times. What can be clearly seen in this plot is the rapid decrease of the plasma lifetimes for pressures below 1 hPa at delay times ≥ 100 ns. Almost the whole emission of LIBS plasmas in lower pressure environments takes place in the first 100 ns after plasma ignition. Moreover, the total emission intensity increases for higher pressures in the investigated pressure range which is in accordance with reported low pressure LIBS studies, e.g., [Scott et al., 2014]. The trend of total emission intensity indicates that for the early stages of the plasma evolution, all plasmas in different ambient conditions, in particular their temperatures and electron densities, are similar but that their decay rates decrease for increasing pressures which was also reported in [Hermann et al., 1998]. In a low pressure environment, less collisions between plasma species and ambient gas species occur. However, collisions, especially inelastic collisions, are responsible for longer lifetimes of plasmas as the transferred energy is partially transformed into excitation energy. Thus, decay rates of excitations and, therefore, of the plasma parameters T and n_e are smaller in high pressure environments resulting in longer plasma lifetimes [Hermann et al., 1998].

Another observation is that emission lines from higher ionized species are present in the spectra for lower pressures at shorter delay times but vanish for increasing pressure and when the plasma evolves. This was observed, for example, in the spectra of NaCl at different delay times and pressures which show Na (III) emission lines for short delay times only in the lower pressure range. In Figure 7.2, a part (245-250 nm) of the UV spectral range is shown at two delay times. With no delay time, the Na (III) emission lines in that spectral range have higher intensities for lower pressures (0.01; 0.1; and 1.5 hPa) than for the pressure of 20 hPa, in which these lines are almost not detectable. This is not the case, for example, for the Na (II) emission line at 249.3 nm which is also shown in Figure 7.2. In the measurements with an delay time

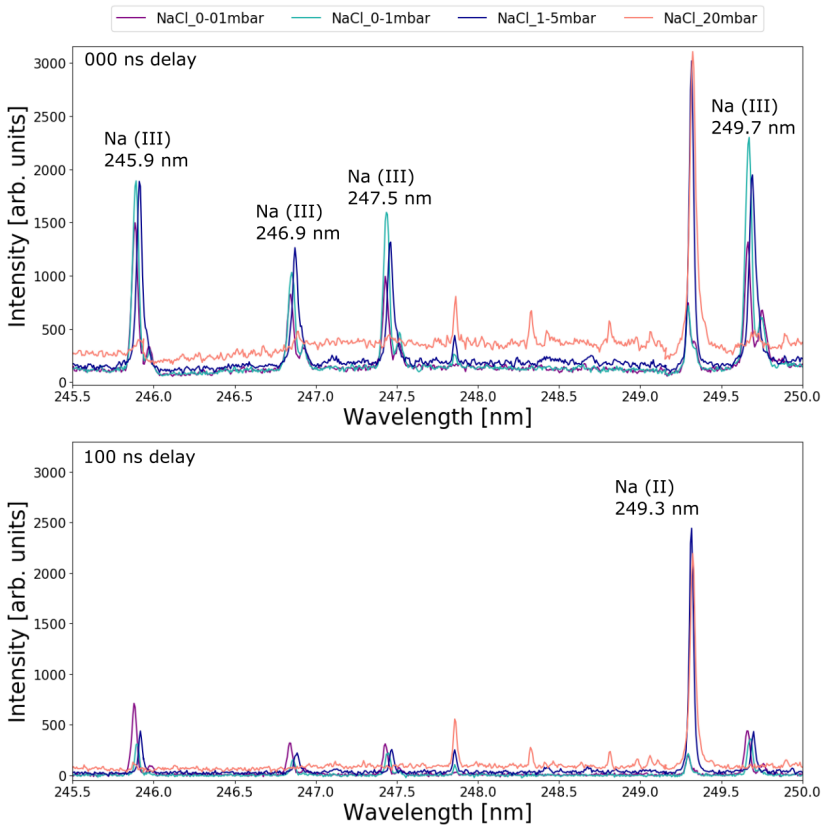

Figure 7.2: Na (III) and Na (II) emission lines at different pressures for two delay times: without delay (*top*) and with 100 ns delay (*bottom*). The Na (III) emission lines appear only for the lower pressures and decrease strongly in the first 100 ns of the plasma lifetime. Furthermore, they show an asymmetric self-reversal.

of 100 ns, the higher ionized lines strongly decrease. In all experiments of NaCl and Na_2CO_3, Na (III) emission lines were observable for low pressures at early plasma stages and all of these observed Na (III) lines are listed in Table 7.2.

In Figure 7.3, the fitted emission line intensities of several Na (II) and Na (III) emissions are plotted for increasing pressure. The data were derived from NaCl measurements at an delay time of 100 ns. The intensity of the Na (II) emission lines steadily rises until a maximum around 7 hPa followed by a slight drop around 15 hPa. By contrast, the emission intensities of the Na (III) lines decrease around 2 hPa and vanish around 15 hPa. In the measurements on the Fe sample, emission lines from higher ionized species were observed for all pressures, however, the intensity of Fe (III) emission lines was relatively higher for lower pressures (not shown here). To conclude, this study showed that plasmas in low pressure environments are higher ionized compared to plasmas in the higher pressure environments of the experiments that were done for this study. This is in accordance with the observations reported in [Knight et al., 2000, Cremers and Radziemski, 2013, Cremers, 2014] at least for Na emission lines. An explanation for the higher degree of ionization is the larger mean free path in plasmas under low pressure conditions. Due to the lack of confinement, these plasmas expand almost freely and their particles therefore have a larger mean free path which impedes recombination. Usually, Na (III) ions are supposed to recombine quickly due to a high second ionization potential of 47.3 eV.

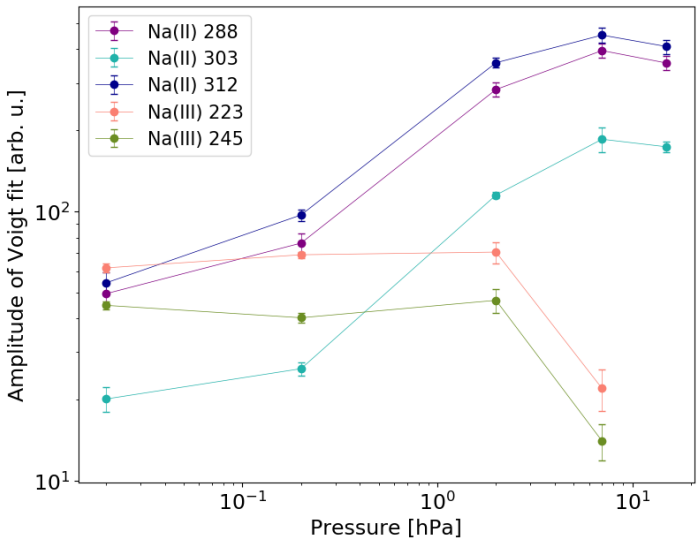

Figure 7.3: Integrated intensities from fits of Na (II) and Na (III) emission lines for increasing pressure from NaCl measurements with 100 ns delay time. Shown are mean values with standard deviations as error bars. The behavior of the emission lines of the two ionization stages shows strong differences as the Na (II) lines have high intensities for higher pressures whereas the Na (III) lines have an opposite trend and are not detectable for pressures above 10 hPa at the delay of 100 ns.

Therefore, emissions of Na (III) can only be observed when recombination is suppressed as it is the case in vacuum conditions. In comparison to Na, the second ionization potential of Fe (16.2 eV) is lower. Thus, Fe (III) species tend to recombine not as fast as Na (III) species, nevertheless, their recombination rate is also slowed down in a freely expanding plasma. To conclude, the ionized species have longer lifetimes in a free expanding plasma in vacuum conditions. Similar explanations for the appearance of ionized oxygen emission lines O (II) for reduced pressures were found in [Knight et al., 2000].

What was also observed in this study when going to lower pressures, is that emission lines are less red shifted. As an example, the Na (II) emission line at 288.1 nm and its line center from Voigt fits are shown in Figure 7.4 for increasing pressure. The reason for the shifts of emission line positions in different pressure conditions is that the Stark effect is reduced when the mean free path in the plasma increases like it does in vacuum conditions. Thus, the red shift that emission lines have in denser plasmas due to the Stark effect vanishes [Gornushkin et al., 1999, Thakur, 2007].

A further observation when going to lower pressures are dips in the red wing of emission lines, which result in an enhanced blue part of the emission lines. This asymmetric self-reversal is even more pronounced for emission lines of higher ionized species. The self-reversal can be seen, for example, in Figure 7.2 and by means of the Na (III) emission at 223.0 nm for different delay times and pressures in Figure 7.5. The plots show that not only the ambient pressure and ionization but also the temporal stage of the plasma influences the appearance of the asymmetric dip in the emission line. Two vertical and dashed lines in the plots mark the spectral position of the center of the enhanced blue part and the center of the self-reversal dip, respectively, in the measurements with a pressure of 0.01 hPa. Again, shifts of line positions

Table 7.2: Na (III) emission lines that were identified in LIBS spectra acquired in low pressure environments (<10 hPa). The data is taken from NIST and wavelengths may deviate due to shifts.

Wavelength [nm]	Term	E_{low} - E_{up} [eV]
220.28	^4P - $^4D^0$	45.40 - 51.02
222.59	^4P - $^4D^0$	45.51 - 51.08
223.03	^4P - $^4D^0$	45.40 - 50.95
223.22	^2P - $^2P^0$	46.32 - 51.88
223.95	^4P - $^4D^0$	45.57 - 51.10
224.67	^4P - $^4D^0$	45.51 - 51.02
225.15	^4P - $^4D^0$	45.57 - 51.08
227.84	^2P - $^2P^0$	46.45 - 51.89
227.95	^2S - $^2P^0$	53.94 - 59.37
228.57	^2P - $^2P^0$	46.45 - 51.88
231.00	^2P - $^2S^0$	46.32 - 51.69
238.70	^2D - $^2F^0$	49.49 - 54.68
239.40	^2D - $^2F^0$	49.49 - 54.67
245.93	^2P - $^2D^0$	46.32 - 51.36
246.89	^2P - $^2D^0$	46.45 - 51.47
247.47	^4P - $^4P^0$	45.40 - 50.41
249.70	^4P - $^4P^0$	45.40 - 50.36
251.03	^4P - $^4P^0$	45.51 - 50.44
255.35	^4P - $^4P^0$	45.51 - 50.36
256.33	^4P - $^4P^0$	45.57 - 50.41

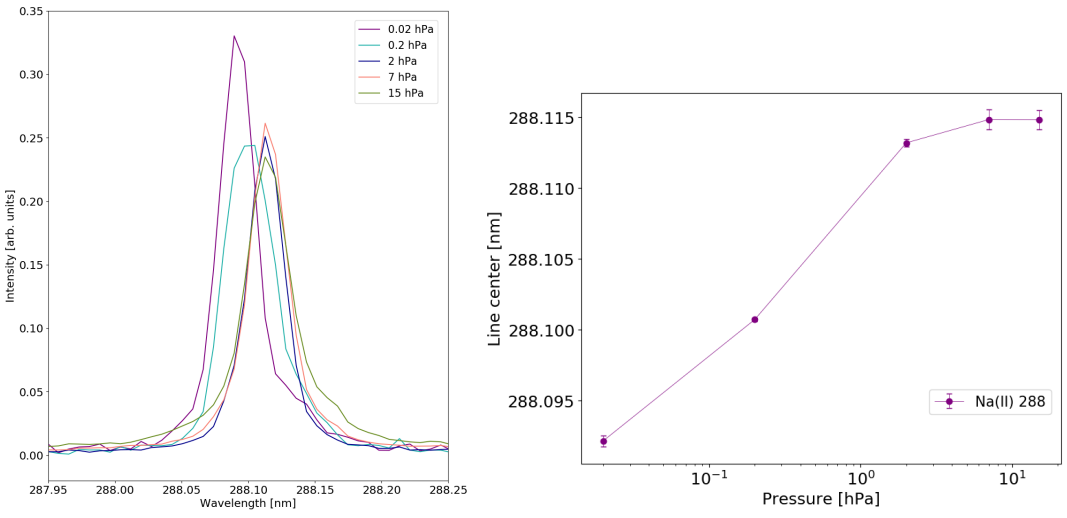

Figure 7.4: The Na (II) emission line in different pressures at a delay time of 100 ns has a blue shift for lower pressures (*left*). Voigt fits of the line were done and the fitted spectral position plotted for increasing pressure (*right*). Shown are mean values from three measurements with the standard deviation as error bars.

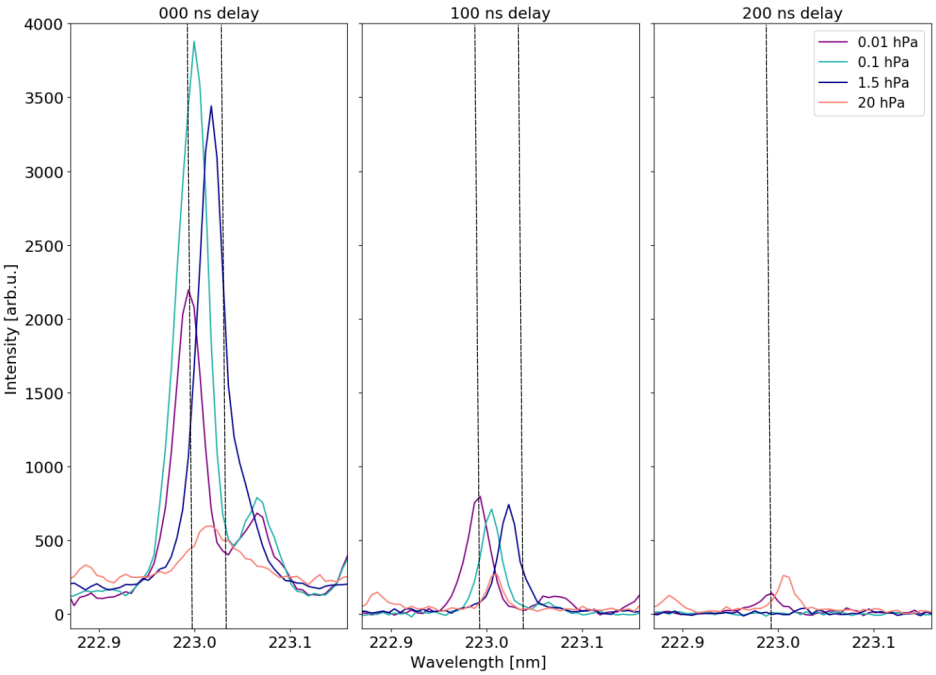

Figure 7.5: Na (III) emission line at different temporal stages of plasmas in different pressure conditions. The asymmetric self-reversal is most distinct for pressures below 1 hPa and within the first 100 ns of plasma emission. The two vertical dashed lines in each plot mark the position of the center of the enhanced blue part and the position of the dip of the emission line measured at 0.01 hPa, respectively. They indicate how the emission line is red shifted for increasing pressure.

occur when varying the pressure. Regarding the temporal behavior of the dip, it can be seen that the degree of asymmetry is reduced for later times in the plasma emission.

The occurence of self-reversal in emission lines of LIBS plasmas usually indicates the presence of strong temperature gradients in the plasma [Hermann et al., 1998]. As already discussed, the LIBS plasma in low pressure environments is less confined resulting in a free expansion with colder outer regions of the plasma. Due to lower electron temperatures in the colder outer regions, ground and low lying energy states are more populated which enhances the probability of absorption which can result in self-reversed emission lines [Hermann et al., 1998]. Regarding now the shifts of the emission lines for lower pressures towards shorter wavelengths, which is shown in Figure 7.3 for the Na (II) emission line at 288.1 nm, an explanation for the asymmetry of the self-reversal can be found: Photons that were emitted from species in the inner core of the plasma where the electron density and the temperature are larger, are absorbed by species of the outer plasma region with lower electron density and temperature. The difference in electron density causes different Stark shifts and the photon emitted with a red shift is absorbed by a species with no shift of energy levels due to a reduced Stark effect. Thus, the shifts lead to an enhanced blue part with the self-reversal dip appearing in the red wing of the emission line. Similar observations were reported in [Hermann et al., 1998] but further experiments using, for example, spatially resolved LIBS data in vacuum conditions are needed to proof this explanation. In such measurements, the asymmetry should change for different positions in the plasma from which the emission was collected due to different path

lengths of the photons within the plasma.

7.2 Solving the Saha-Eggert equation

This section contains numerical solutions of the Saha-Eggert equation to support the experimental observations. As for the experiments, these calculations have the objective to reveal general differences for plasmas in different pressures. Complex interactions and temporal influences are not considered here.

All following calculations are based on the Saha-Eggert equation for the ionization equilibrium, see equation (3.4). By using this, it is assumed that the plasma is in LTE or at least that ionization is in equilibrium. At this point, dynamics are not included, thus a static point in the plasma lifetime is considered. The goal of these calculations is to better understand how the ionization depends on the temperature T in plasmas under different pressure conditions. The different pressures enter the equations by means of the total particle density n_{tot} which is smaller in lower ambient pressures.

Based on the Saha-Eggert equation, a temperature-, species-, and ionization-dependent constant is defined as:

$$C_S^Z(T) = \frac{(2\pi m_e k_B T)^{3/2}}{h^3} \frac{2U(T)_S^Z}{U(T)_S^{Z-1}} \exp\left(-\frac{E_{ion} - \Delta E_{ion}}{k_B T}\right), \tag{7.1}$$

where the variable meanings are the same as for the Saha-Eggert equation (3.4). In order to solve the Saha-Eggert equation, constraints are necessary resulting in a system of non-linear equations. The constraints are, in particular, charge and particle conservation. Furthermore, it is assumed that the highest ionization stage in the plasma is three, thus the maximum exponent is $Z = III$. The equations are then:

$$1 = \sum_S n_S \tag{7.2}$$

$$n_e = n_{tot}\left(\sum_S n_S^{II} + 2\sum_S n_S^{III}\right) \tag{7.3}$$

$$n_S = n_S^I + n_S^{II} + n_S^{III} \tag{7.4}$$

$$\frac{n_S^{II}}{n_S^I} = \frac{1}{n_e} C_S^{II} \tag{7.5}$$

$$\frac{n_S^{III}}{n_S^{II}} = \frac{1}{n_e} C_S^{III} \tag{7.6}$$

The total number density of particles in the plasma n_{tot} is like n_e in m^{-3} while each n_S is dimensionless and given in fractions of n_{tot}. The total number of equations depends on the number of species that are assumed to be in the plasma because all equations, except for equation (7.2) and (7.3), describe one single species S.

The system of equations was solved numerically with the *fsolve* root finding algorithm provided by the *python* scipy.optimize package. In particular, the equations were solved for the densities in the three ionization stages of one species n_S^Z and the electron density n_e. For

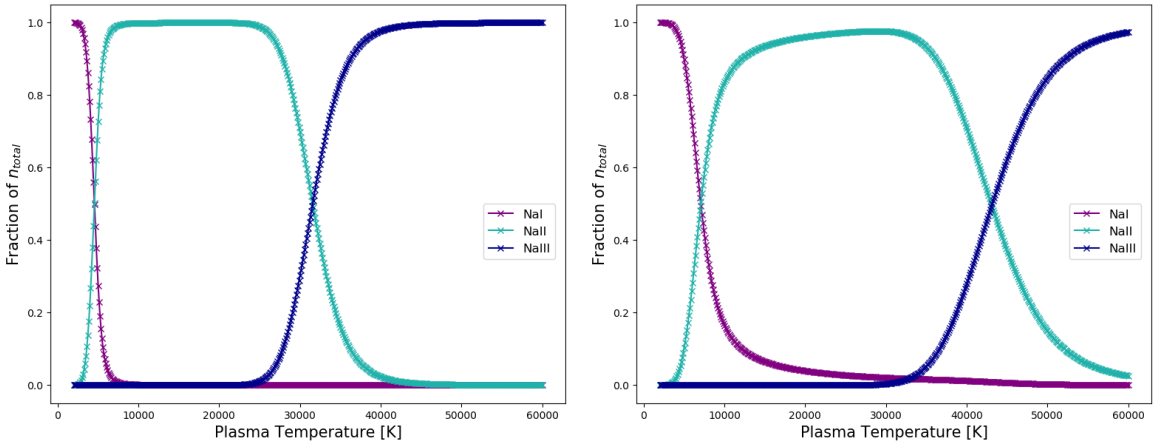

Figure 7.6: Numerical solutions of the Saha-Eggert equation for increasing temperatures at two different total particle densities. Each point is the solution at one temperature. Shown are fractions of these total particle densities for three ionization stages. *Left*: Simulation of vacuum conditions with $n_{tot} = 3 \times 10^{21}\mathrm{m}^{-3}$. *Right*: Higher pressures were implemented with $n_{tot} = 5 \times 10^{23}\mathrm{m}^{-3}$. The temperatures at which transitions between the ionization stages take place are lower for plasmas in vacuum conditions.

this, the total particle density n_{tot} was fixed as well as a defined temperature range from which a certain number of temperatures with equidistant spacings were taken for solving the equations. Thus, the trend of particle densities with increasing temperature could be investigated and is shown in Figure 7.6 for a plasma of Na (I), Na (II), and Na (III) particles at two different total particle densities. As an estimate of the two total particle densities n_{tot} in the plasma, the particle densities in the simulation chamber at pressures at 0.1 hPa and 20 hPa were used, respectively. Assuming that the gas in the simulation chamber behaves like an ideal gas and that the temperature is the conventional room temperature of 293 K, particle densities of $\approx 3 \times 10^{21}\mathrm{m}^{-3}$ and $\approx 5 \times 10^{23}\mathrm{m}^{-3}$ were derived for pressures of 0.1 hPa and 20 hPa in the chamber, respectively. In both cases, transitions between the dominant ionization stages can be observed, see Figure 7.6. For lower temperatures, almost no ionization occurs and the plasma consists of neutral particles. With increasing temperatures, the density of neutrals decreases and the density of single ionized particles increases until they constitute the major part of particles in the plasma. With further increasing temperatures, a similar transition between the single and double ionized particles takes place. This corresponds to the expected behavior of ionization in a plasma with increasing temperature. The important observation here is that the transition temperatures, at which the density of lower ionized particles decreases and that of the next higher ionization stage increases, are different for the plasmas with different total particle densities. For the simulation of a plasma in lower pressure conditions, the transitions occur around 4 500 K and 31 600 K (Figure 7.6, *left*). The same transitions in the plasma with a higher total particle density happen around 7 200 K and 43 100 K (Figure 7.6, *right*). To conclude, in low pressure environments lower temperatures are sufficient to reach a high degree of ionization including double ionized species. This derivation does not aim to be a complete proof but is in accordance with the experimental observations. As mentioned above, LIBS plasmas are highly complex with temporal dependencies, spatial gradients, and particle interactions which were not included in the presented simulation. But

already with those conceptually simplified assumptions, differences of the physics in plasmas in low pressure environments could be observed.

7.3 Summary

The experiments have shown that indeed emission lines of higher ionized species appear in LIBS plasmas in low pressure environments as previously observed for O (II) emission lines in [Knight et al., 2000]. In the present study, Na (III) emission lines could be detected for pressures around and below $\approx 1\,\mathrm{hPa}$ which was not possible when the pressure was higher. Recombination of ionized species with electrons is impeded in free expanding plasmas with a larger mean free path than in confined plasmas. Especially, emission lines from species with high ionization energies, which would recombine fast in a dense plasma can be observed when reducing the surrounding pressure. The numerical simulation based on solving the Saha-Eggert equation gave also evidence for a higher degree of ionization for lower particle densities in the plasma. Besides these higher ionized emission lines appearing in the experiments, asymmetric self-reversal of emission lines was observed when the surrounding pressure was decreased. Strong temperature and electron density gradients in the free expanding plasma can be responsible for the asymmetric self-reversal. Red shifted photons from the inner hotter and denser plasma core are absorbed by particles in the outer colder and less denser plasma region. The Stark effect is reduced in the less denser region and the particles are not red shifted resulting in the self-reversal dip in the red wing of emission lines.

To conclude, the appearance of higher ionized emission lines can have an influence on the selection of useful spectral ranges for LIBS for in-situ space exploration instruments on atmosphereless bodies. Furthermore, the line shapes can appear differently for LIBS in low pressure environments and self-reversal can affect, for example, line fitting procedures and proper quantification. With regard to future LIBS instruments for the exploration of bodies without an atmosphere, the particular mission objectives are most determining which spectral ranges can be used. More studies for particular missions, also on geological samples, have then to be done in order to design a LIBS instrument best suited to meet the scientific objectives. In vacuum atmospheric conditions, further ionized emission lines can indeed be observable, however, they are also more sensitive to changes in experimental conditions (see Section 6.3) and to effects that influence their line shapes. So despite providing additional spectral features for qualitative analysis, quantification is probably more complicated.

8 Fluorine, chlorine, and phosphorus detection in Martian atmospheric conditions

The emission lines of the halogens fluorine and chlorine usually have high detection limits in the common spectral ranges (200-900 nm) for LIBS analysis. It was shown, however, that their indirect detection via the emission of the diatomic molecules CaF and CaCl can increase the sensitivity for these elements [Gaft et al., 2014]. The first detection of fluorine on Mars was possible due to the CaF emission at 532 nm (the "Green System") and at 603 nm (the "Orange System") in ChemCam LIBS data [Forni et al., 2015]. It was further investigated if also chlorine could be better detected via molecular emission [Cousin et al., 2015]. Moreover, a first study for the calibration of apatites was done with a replica instrument of ChemCam showing CaF and CaCl emissions in the LIBS data [Meslin et al., 2016]. In further studies on this topic in our group, it was shown that the molecular emission in particular of CaCl but also of CaF has interdependencies and that an univariate calibration accounting only for the halogene concentration can be misleading [Vogt et al., 2018b, Vogt et al., 2020].

This chapter contains two studies which both use MVA methods to approach the use of molecular emissions for the identification and quantification of fluorine, chlorine, and phosphorus. The latter is also challenging to detect with LIBS and is additionally often superimposed by the molecular emission of CaF.

The objective of the first study is to use PCA to differentiate between two types of apatite, namely fluor- and chlorapatite. In preparation for the PCA, important elemental and molecular emissions were identified. Apatite is a magmatic mineral and appears as chlor-, fluor-, or hydroxylapatite with the chemical formula: $Ca_5(PO_4)_3$(F, Cl, OH). In the context of Mars mineralogy, mostly fluorine and chlorine bearing apatites were detected in almost all SNC (Shergotty, Nakhla, and Chassigny) meteorites [Johnson et al., 1991, Beck et al., 2006]. From these metorites the abundances of halogens on Mars were estimated [Douce et al., 2011]. Halogens such as fluorine and chlorine are volatiles which play an important role in magmatic processes and in alteration processes [McCubbin et al., 2013]. In Gale crater, fluorapatite has been identified by X-ray diffraction with the CheMin instrument in the Windjana drill target [Treiman et al., 2016] and was further identified by ChemCam at various locations [Forni et al., 2015]. These identifications in ChemCam LIBS data were based, if possible, on correlations between CaF molecular emission and rare phosphorus emission lines. The information about the apatites being enriched in either fluorine or chlorine can help to clarify if Mars is depleted in fluorine. The current in-situ observations of fluorapatites [Forni et al., 2015, Treiman et al., 2016] are in contrast to the SNC meteorite analyses which show rather low fluorine and high chlorine levels [McCubbin et al., 2013].

For the second study, the data acquired for [Vogt et al., 2018b] was taken for a PLS-R to evaluate how such a MVA technique deals with the interdependencies of the CaCl mole-

cular emission [Rammelkamp et al., 2018]. Chlorine can be found in apatites but is part of other minerals, too, and can in particular be found in salts that are of high interest for the geochemical analysis of the Martian surface. Salts act like tracers of an aqueous history and their detection can give further insight to present and past processes on the Martian surface in which liquid water is or was involved, see Section 2.1.

8.1 Identification and differentiation of apatites

The objective of this study is to evaluate if different apatites can be distinguished according to their LIBS spectra. The samples vary in particular in F, Cl, and P concentrations, i.e., elements that are difficult to be analyzed with LIBS. For that purpose, molecular and elemental emissions of halogens were identified and studied in spectra of binary mixtures with varying concentrations of salts whose elemental compositions are equivalent to the one of apatites.

Experiments

The data for this study was taken with the Aryelle LIBS setup described in Section 5.1 with the samples in simulated Martian atmospheric conditions (see Section 2.1). The laser energy was set to 15.4 mJ and for each measurement the emission of 30 consecutive LIBS plasmas was integrated. Each sample was measured at least at five different positions. From prior measurements [Vogt et al., 2018b], the temporal parameters for an optimized observation of molecular bands were known and used for this investigation. These are a delay time of 350 ns and an integration time of 10 μs. The molecular emission bands that are of major interest in this study are located in the spectral range of 500-650 nm so that the UV/VIS/NIR spectral range (270-850 nm) was chosen. Additionally, the halogen emission lines are present and P emission lines are partly superimposed with the molecular emission bands in that spectral range.

Some of the samples were provided by the Institut de Recherche en Astrophysique et Planétologie (IRAP) in Toulouse and used for comparison to measurements with the replica instrument of ChemCam at IRAP [Meslin et al., 2016]. The major part of the samples was prepared as mixtures or pure salts with the usual sample preparation procedure (Section 5.4). Additionally, a fluorapatite crystal and powdered fluorapatite pressed in a pellet were measured. Thus, the whole set of samples is:

- 0.4 CaF_2; 1.5 CaF_2 and 2 $CaCl_2$ from IRAP,
- $CaCl_2\times\ 2\,H_2O$, $CaSO_4\times\ 2\,H_2O$, CaF_2, and $Ca_3(PO_4)_2$ as pure samples,
- three mixtures of $CaCl_2\times\ 2\,H_2O$ and $Ca_3(PO_4)_2$ at different mixing ratios simulating chlorapatite,
- nine mixtures of CaF_2 and $Ca_3(PO_4)_2$ at different mixing ratios simulating fluorapatite,
- fluorapatite crystal and as powder pressed into a pellet.

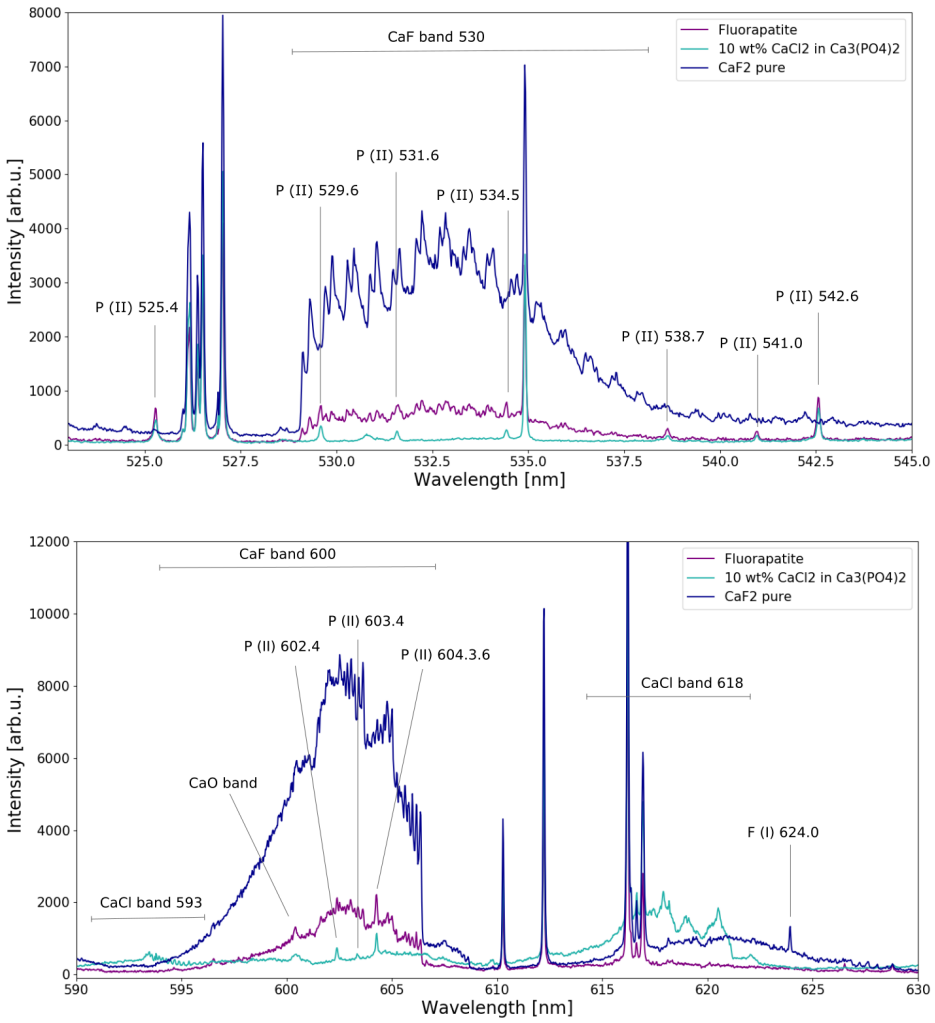

Figure 8.1: Spectral ranges with molecular emission bands that are superimposed with elemental emission lines. Spectra of three samples are shown here to clarify the identifications of the indicated features. Emission lines of Ca are not labeled. *Top*: CaF emission around 532 nm known as the "Green system" ($B^2\Pi$-$X^2\Sigma$). *Bottom*: CaF emission around 603 nm known as the "Orange system" ($A^2\Pi$-$X^2\Sigma$) and CaCl emission around 620 nm known as the "Red system" ($A^2\Pi$-$X^2\Sigma$).

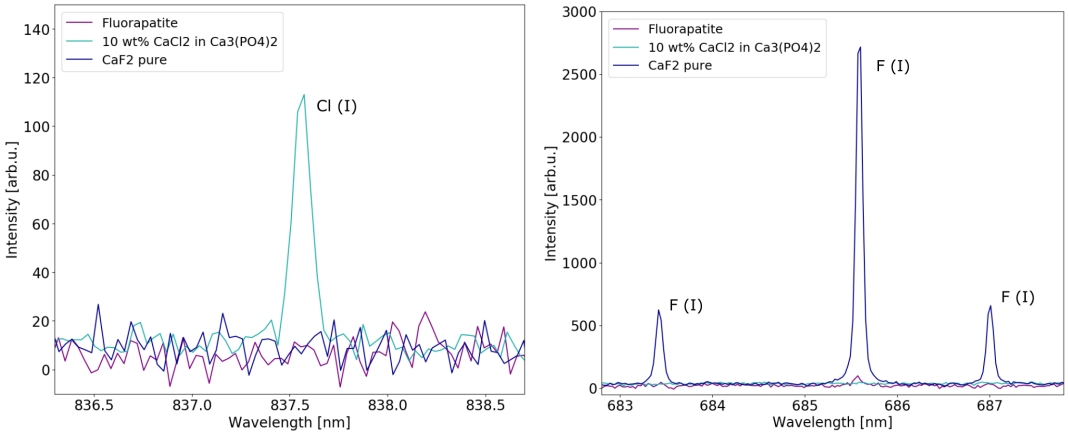

Figure 8.2: Neutral emission lines in the spectra of three selected samples of F and Cl that are the strongest lines in the used spectral range. *Left*: Cl (I) emission line at 837.6 nm. *Right*: The F (I) emissions at 683.4, 685.6, and 687.0 nm are strong for the pure CaF_2 sample while only a weak signal of the 685.6 nm line is observable for the fluorapatite crystal.

Identification of important emission lines

In Figure 8.1 parts of the spectra are shown where the molecular emission bands of CaF and CaCl appear. The CaF band around 530 nm as well as the one around 600 nm superimpose ionized P emission lines. There is a further CaF band around 584 nm which is not shown in the two plots. In LIBS data of fluorapatite, these ionized P (II) emission lines will always be superimposed by quite intense molecular emission. However, to obtain other indications for the sample being fluorapatite, another P (II) emission line at 542.6 nm can be used for fluorapatite identification when also the CaF molecular bands appear. Further P (I) emission lines were identified in the spectra: P (II) at 417.8 nm and P (II) at 460.2 nm. The UV spectral range of the ChemCam instrument covers also strong neutral P emission lines around 255 nm which are not accessible with the spectral range in the present study. However, also these lines have a low detection sensitivity [Blank et al., 2015, Maurice et al., 2016].

Elemental emission lines of Cl and F are also observable in the spectra and the corresponding spectral ranges are shown in Figure 8.2. The neutral emissions of Cl (I) at 837.6 nm and of F (I) at 685.6 nm have lower intensities in comparison to the molecular emission bands. Besides the F (I) emission line at 685.6 nm, two further neutral F (I) emission lines appear for the pure CaF_2 sample in which the F concentration is of course comparatively high (66 at %). By contrast, the fluorapatite crystal (assuming a pure crystal: 0.05 at % of F) does not show the two additional lines and reveals only a weak signal of the F (I) line at 685.6 nm. In those cases, where the elemental emissions are weak or even absent, the molecular emissions can be the key factor for the identification of F or Cl containing minerals such as apatites.

PCA of apatites and mixtures

After the identification of important emission features for the detection of apatites, a PCA was performed in order to evaluate if the two types of apatite can be distinguished by such a MVA method. For that purpose, the whole study is focused on the elements F, Cl, and P

Table 8.1: Overview of selected spectral ranges for PCA. The features in bold were found to be the most important ones for differentiation.

Component	Emission lines and bands [nm]
Fluorine	≈ **603** (596-606, CaF)
	≈ **530** (525-540, CaF)
	≈ 584 (580-588.5, CaF)
	683.4; 685.6; 687.0; 690.3; 691.0; 733.2; 739.9
Phosphorus	**460.2**
	417.9
	542.6
Chlorine	≈ **620** (614.5-621, CaCl)
	≈ **593** (592.5-594, CaCl)
	479.5; 481.1; 837.6

which have usually weak emission lines in the common spectral ranges of LIBS analysis as also observed in this study. In order to prevent the MVA being dominated by the strong major element emission lines, the spectral ranges for the PCA were preselected. Such a dominating influence of, for example, Ca emission lines was observed in previously performed PCAs with the whole spectral range. With these PCA models (not shown here), it was not possible to distinguish between the different apatite-like compositions. The preselected spectral ranges are given in Table 8.1 and were chosen according to the identified emission lines and molecular bands of F, P, and Cl. In some cases, not the whole spectral range of the molecular emissions was taken for PCA as in these cases the molecular bands are superimposed by Ca emission lines which were not considered in the models.

For the PCA, a model with four PCs was chosen and a random cross-validation (see Section 4.3) was done. In Figure 8.3 a score plot of the first two components is shown. The first component explains already 95 % of the variance in the data and mostly separates between low and high concentrations of F. The remaining 5 % are explained by PC 2 that accounts for the concentration of Cl. To keep the plot readable, labels with the mixing ratios of the $CaCl_2/CaF_2$ with $Ca_3(PO_4)_2$ mixtures were dropped. It was observed that the mixtures are indeed aligned by increasing content of $CaCl_2$ or CaF_2 along PC 2 and PC 1, respectively. The correlations of F and Cl concentrations with PC 1 and PC 2 were further confirmed by the loadings of the first two PCs, see Figure 8.4. A positive correlation of features accounting for the presence of F with PC 1 can be seen. Especially, the CaF bands show strong correlations over their whole spectral range. Similar observations can be made for features indicating Cl, which positively correlate with PC 2. Again, the molecular emission, here the CaCl bands, have the highest correlations with PC 2.

To summarize the outcomes of the PCA, the molecular emissions were identified as the most important features to distinguish between Cl and F bearing apatites (*bold*, Table 8.1). Apatites can be distinguished based on their spectral features of CaCl, CaF, F, P, and Cl with PCA when these were preselected as input data. Among these features, it was observed that the PCA corresponds well to the molecular emissions and can use these as major features for

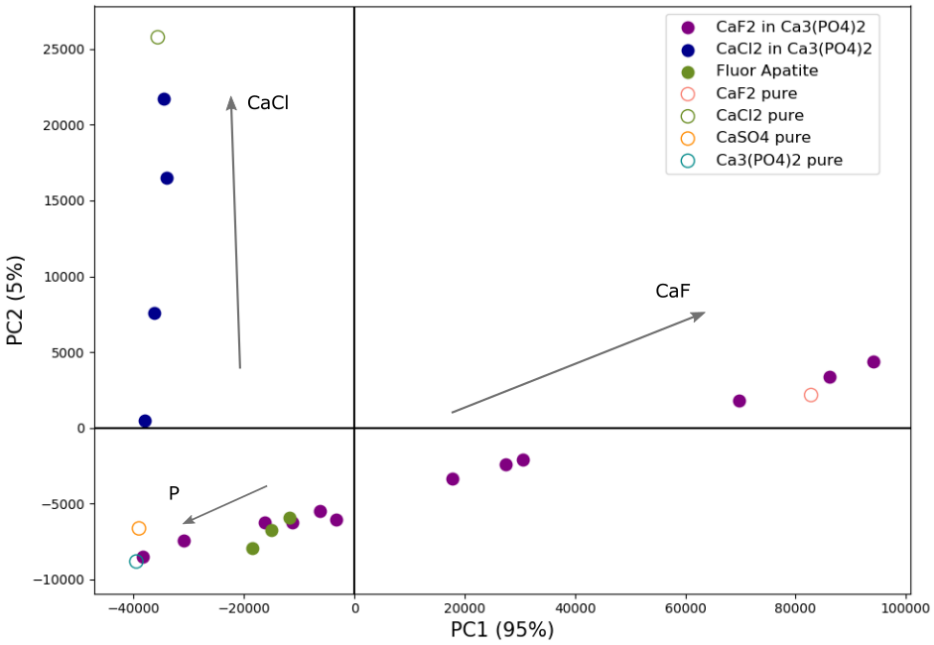

Figure 8.3: PC 1/PC 2 scores plot of all samples with preselected spectral ranges to avoid a predominance of Ca emission lines. The values in brackets give the explained variance. The mixed samples of CaF_2 and $CaCl_2$ with $Ca_3(PO_4)_2$ have different mixing ratios that are not displayed here in order to keep readability.

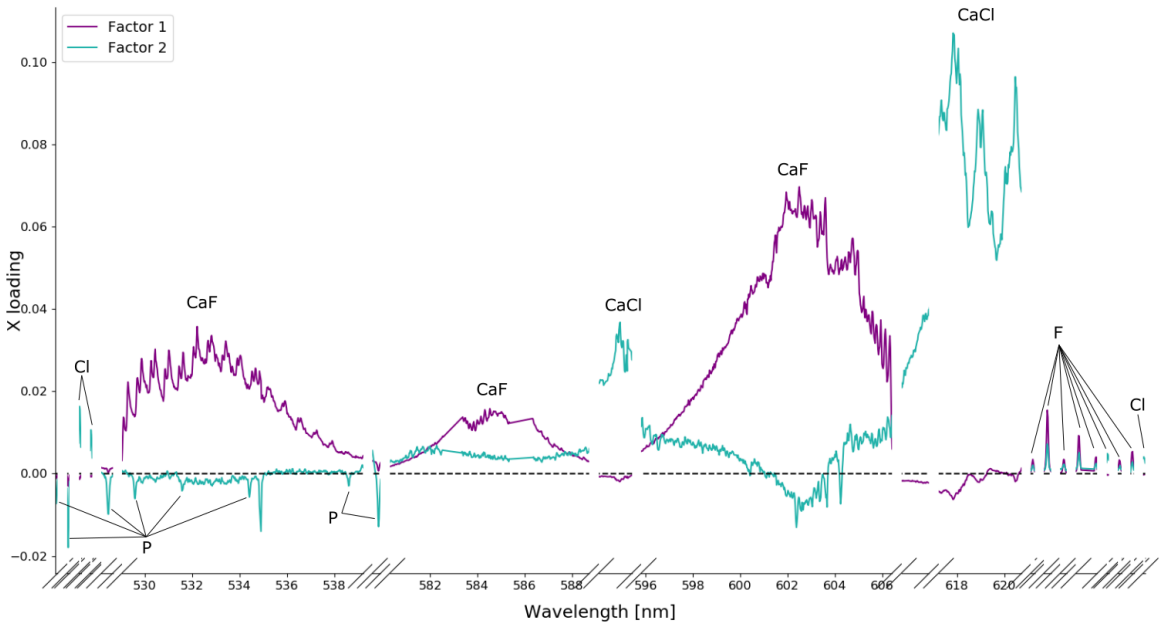

Figure 8.4: Loadings of PC 1 and PC 2 where the gaps appear because not the whole spectral range was taken for analysis. In agreement with the scores plot in Figure8.3, a correlation between PC 1 and the CaF emission and between PC 2 and the CaCl band is observable. Furthermore, their influence is larger and on a wider scale than the influence of the atomic emission lines.

Table 8.2: Overview of the samples with correlated and anti-correlated Ca and Cl concentrations. JSC is a Martian regolith simulant and contains 5-6 wt % CaO.

Sample/mixture	Cl concentrations [at %]	Ca concentrations [at %]	# of samples
$CaCl_2$ + $MgSO_4$	0 - 15.4	0 - 7.7	17
KCl + $CaSO_4$	0 - 29.3	8.3 - 3.4	14
NaCl + $CaSO_4$	0 - 32.9	8.3 - 2.9	11
$CaCl_2$ + JSC	0.3 - 6.7	2.6 - 5.1	7
KCl + JSC	0.3 - 5.4	2.4 - 2.2	9
NaCl + JSC	0 - 26.8	2.4 - 1.1	8

differentiating between different compositions.

8.2 Chlorine quantification using CaCl molecular emission

In this section, the molecular emission of CaCl in simulated Martian atmospheric conditions was tested for multivariate calibration with PLS-R. In another study [Vogt et al., 2018b] relevant for Mars and using univariate approaches it was shown that interdependencies can complicate the quantification of Cl based on CaCl bands. In particular the amount of Ca was found to be crucial for the CaCl emission. The objective of my study is to evaluate the suitability of the CaCl band for Cl quantification with PLS-R. For ChemCam, a detection limit for Cl of 3-6 wt % was derived based on individual emission lines [Anderson et al., 2017]. The CaCl emission is so far not used for quantification of Cl content in Martian LIBS data.

Experiments

The same data as in [Vogt et al., 2018b] was used for this investigation. This was taken with the Aryelle LIBS setup, see Section 5.1, with the samples in Martian atmospheric conditions (see Section 2.1). In order to generate experimental conditions close to the ones of ChemCam, the laser energy was adjusted to 22 mJ per pulse. Also the timing parameters were selected in order to simulate ChemCam measurement conditions which means no delay and an integration time of 3 ms. As in the previous study, measurements were done in the UV/VIS/NIR spectral range (270-850 nm) where the molecular emissions appear.

The data was acquired on six sets of samples by [Vogt et al., 2018b] resulting in data from more than 60 samples, an overview is given in Table 8.2. All samples were measured at ten different positions each, except of the $CaCl_2$ + $MgSO_4$ samples which were measured at three different positions. Each measurement is an integration of the emission of 30 consecutive induced LIBS plasmas. In two of the sample sets, the concentrations of Ca and Cl are correlated which are the mixtures containing $CaCl_2$. In the remaining four series their concentrations are anti-correlated. With these samples it was shown in [Vogt et al., 2018b] that no linear relationship between the Cl concentration of a target and the intensity of the CaCl emission band exists. Moreover, the Ca concentration is an equal factor like the Cl concentration for the dynamics of molecular formation and emission that influence the band's intensity.

As an example of the $B^2\Pi$-$X^2\Sigma$ CaCl molecular band, the particular part of the spectra

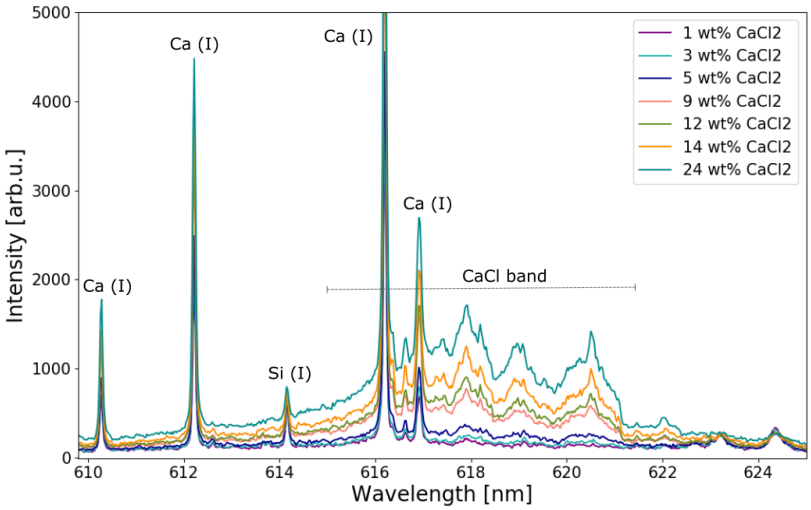

Figure 8.5: The "orange system" $B^2\Pi$-$X^2\Sigma$ of CaCl in the spectra of $CaCl_2$ mixtures with the Martian regolith simulant JSC where the Ca and Cl concentrations are correlated.

of the $CaCl_2$ in the martian regolith simulant JSC series is shown in Figure 8.5. As for these samples the Ca and Cl concentrations are correlated, an increase of the band is observable for higher concentrations of $CaCl_2$.

PLS-R for chlorine quantification

Like in the previous section, it was necessary to use preselected spectral ranges for the analysis. Otherwise, strong emission lines of major elements would dominate the outcomes of the PLS-R model. Therefore, two spectral ranges that were either used alone or in combination were selected:

- CaCl molecular emission: 614.6 - 621.3 nm
- Cl (I) atomic emission: 837.3 - 837.8 nm

Although Cl has rather strong ionic emission lines around 480 nm, these were not used as input. They show large fluctuations and are additionally not relevant for ChemCam LIBS data analysis because they are located in the gap between the VIS and the NIR spectral ranges.

PLS-R models were computed from all samples but also from subgroups. The best results were obtained when using for factors (equivalent to PCs in PCA or LVs), taking the average spectra of one sample instead of all single measurements, and when doing a full cross-validation. Except for normalization of the whole spectra to the total emission intensity (sum of all counts) and the usual mean centering, no prior data treatment was done. As this analysis is concerned with a phenomenon that has co-dependencies on two constituents, the concentrations of these two, namely Ca and Cl, were given as response variables to the PLS-R. Thus, the resulting models could also be used to predict Ca concentrations which, however, will not be further discussed because this study focuses on Cl quantification. Since Ca has multiple strong emission lines the quantification is not as challenging as for Cl [Clegg et al., 2017].

In Figure 8.6(*left*), the loadings of the first two factors and a predicted vs. reference plot of the PLS-R model from all samples are shown. The first factor shows that the Ca emission is correlated with the molecular CaCl emission and that the Cl emission has no influence. Regarding the second factor, the molecular emission correlates now with the Cl emission and not with the Ca emission lines anymore. In other words, the correlated and anti-correlated sample series are covered by these two different correlations for the two factors. Turning to the predicted vs. reference plot in Figure 8.6(*right*), a linear behavior is observable that is dominated by samples with Cl concentrations above 70000 ppm. Such high Cl concentrations are usually not expected on Mars. Therefore, a further model based only on the spectra of samples with Cl concentrations below 70000 ppm was built for which the loadings and the predicted vs. reference plot can be found in Figure 8.7. In the spectra of the samples with the lower Cl concentrations, the elemental emission line Cl (I) was not observable and it shows therefore no correlation with any factor of the PLS model, see Figure 8.7(*right*). The Ca emission has a positive correlation with factor 1 and a negative one with factor 2. By contrast, the molecular emission shows almost no correlation with the first factor but correlates with the second factor. This indicates that even the molecular emission has low intensities compared to the Ca emission lines for the lower Cl concentration samples. In the predicted vs. reference plot in Figure 8.7(*right*), not all sample series follow a linear trend. In particular, the $CaCl_2$ + JSC, KCl + JSC, and NaCl + $CaSO_4$ are close to the dashed line with slope 1. The other three series have almost constant predicted Cl concentrations although the reference values increase.

As figure of merit, the RMSE-C and RMSE-CV of the Cl concentration were computed for PLS-R models of all samples and of selected subgroups. The outcomes and can be found in Table 8.3. Additionally, the coefficient of determination R^2-C of the calibration model is given, which corresponds to a linear fit of the predicted and reference Cl concentrations. For the PLS-R of all samples, a RMSE-C of 21 500 ppm was achieved with only the Cl (I) spectral range which reduces to 16 300 ppm when also taking the molecular emission into account. These are promising results since the sample with the highest Cl concentration contains more than 300 000 ppm of Cl. What is striking here is the discrepancy between the RMSE-C and RMSE-CV for the CaCl + Cl (I) spectral range. Such a difference indicates that not all samples are well described by the model. This can be either caused by matrix effects that introduce differences between the single sample series or might be an indication that the PLS-R is not capable to describe series of samples with correlated as well as anti-correlated concentrations of Ca and Cl. For the samples with < 70000 ppm of Cl, much smaller RMSE values are achieved which is not surprising due to the lower concentrations. In Table 8.3, also the outcomes from two models based on single sample series, namely the $CaCl_2$ + JSC (correlated Ca and Cl concentrations) and the KCl + JSC (anti-correlated Ca and Cl concentrations) are shown. The PLS-R models of these selected single sample series show significant differences between the RMSE-C and RMSE-CV when only the Cl (I) emission was given as input. Most likely, this line has not enough variance among the spectra to describe the varying Cl concentrations which results in unstable models. With both spectral ranges the Cl (I) and the CaCl emission the differences decrease and small RMSE values indicate a low detection limit of Cl. In contrast to the model of all samples, these single models have a reduced complexity as no co-dependencies occur since the Ca and Cl concentrations are either correlated or the opposite.

To conclude this section, PLS-R is capable to identify the co-dependencies of the CaCl molecular emission in our data as seen in the loadings plots in Figures 8.6 and 8.7. However,

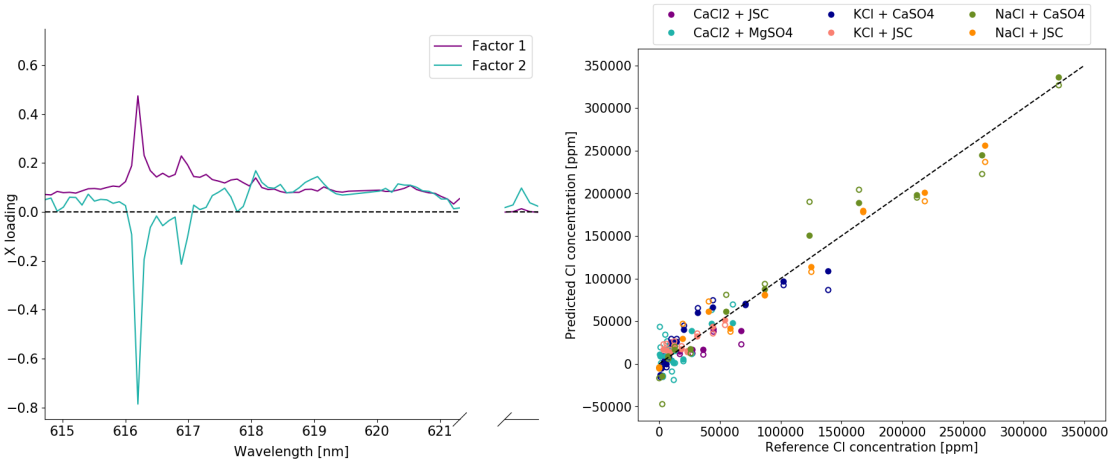

Figure 8.6: Characteristic plots of PLS-R model of all samples. *Left*: The loadings of the first two factors show a positive correlation between the molecular emission and the Ca lines (factor 1) but also with the Cl emission line (factor 2). *Right*: The predicted and the reference concentrations of Cl are close to the dashed line with slope 1 but are dominated by a few samples with high Cl concentrations. Filled circles denote the predictions of the calibration model and the empty circles belong to the validation model.

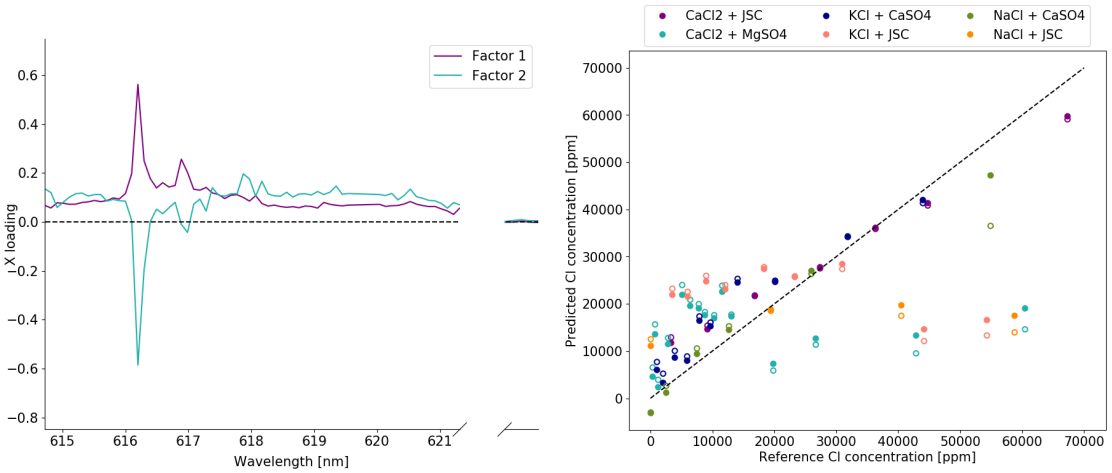

Figure 8.7: Plots of the PLS-R model based on samples with Cl concentrations below 70000 ppm. *Left*: The elemental chlorine emission line is not detectable for these lower concentrations and shows therefore no correlations with the factors of the PLS-R. *Right*: While the predicted Cl concentrations of some samples follow a linear trend no increase is observable for the other samples. The filled and empty circles have the same meaning as in Figure 8.6.

Table 8.3: Overview of PLS-R outcomes, RMSE values in ppm.

Samples	Range	RMSE-C	RMSE-CV	R^2-C
All	Cl (I)	21500	22600	0.913
All	CaCl + Cl (I)	16300	25500	0.950
$<$ 70000 ppm Cl[a]	CaCl + Cl (I)	4600	5400	0.913
$CaCl_2$ + JSC	Cl (I)	7200	14900	0.877
$CaCl_2$ + JSC	CaCl + Cl (I)	2000	3700	0.991
KCl + JSC	Cl (I)	5700	10200	0.882
KCl + JSC	CaCl + Cl (I)	5000	8800	0.912

[a] Outliers were removed here.

instabilities of the PLS-R models were observed, most likely because the concept of PLS-R relies on linear relationships between the variables and responses, see Section 4.2. It was shown in [Vogt et al., 2018b] that the relationship between the intensity of CaCl (variables) and the Cl concentration (responses) is not linear. Furthermore, matrix effects influence the outcomes which has been observed for the PLS-R model based on the spectra of samples with Cl concentrations lower than 70000 ppm. To overcome those problems in LIBS space exploration applications such as ChemCam on Mars, dedicated models for the classification of subgroups could be used for quantification. In the case of this laboratory study, the subgroups would be the single sample series. Unknown samples would be assigned, for example with PCA, to a subgroup for which individual PLS-R models could be used for Cl quantification.

8.3 Summary

In this chapter, two applications of MVA methods with the objective to improve the identification and quantification of elements which often have low intensities in the common LIBS spectral ranges such as Cl, F, and P were evaluated. In both cases, the molecular emission bands of CaF and CaCl were used as input which usually have higher intensities than the elemental emission lines of F and Cl [Gaft et al., 2014, Forni et al., 2015, Vogt et al., 2018b, Vogt et al., 2020].

In the first study, it was shown that PCA can distinguish between fluor- and chlorapatite and that quantification of the Cl as well as the F concentration could be possible with an approach relying on MVA methods. As shown in [Vogt et al., 2018b], the dependence of the CaCl emission on the concentrations of both reactants can interfere an univariate calibration of Cl based on the CaCl emission only. Regarding a calibration of apatites, the concentrations of Cl and F would always be correlated with the Ca concentration as Ca is naturally part of apatite. Therefore, for apatites, a calibration based on molecular emissions can be successful especially when using MVA techniques. Furthermore, it was observed that it is necessary to use preselected spectral ranges of important features for the differentiation between the apatites in the PCA. Otherwise, the strong emission lines of major elements, such as Ca dominate the outcomes of the PCA.

The second study has confirmed what was observed in [Vogt et al., 2018b] with an analytical approach: There are co-dependencies of the molecular emission on the concentrations of both

reactants. In PLS-R models of sample series having correlated and anti-correlated Ca and Cl concentrations, the molecular emission has a positive correlation with Ca emission for one PLS-R factor while it has a negative correlation for the other factor. The PLS-R model of all samples has relatively small prediction errors, however, it is dominated by samples with high Cl concentrations which are usually not expected on Mars. In a further PLS-R model with lower Cl concentrations ($< 70000\,\mathrm{ppm}$), the influence of matrix effects due to the different sample series was observable. Therefore, an approach with classification of sample groups prior to the quantification might be better suited for Cl quantification. The assignment to particular sample groups could be done with MVA methods such as PCA and for each sample group, dedicated PLS-R models could be implemented.

9 LIBS and Raman data fusion

In this chapter[1], the potential of LIBS and Raman data fusion for in-situ Mars exploration is investigated. At the current stage, SuperCam will be the first instrument in space that combines LIBS and Raman spectroscopy for the in-situ investigation of Martian geochemistry and mineralogy [Wiens et al., 2017]. Besides the advantage that LIBS and Raman spectroscopy can share hardware components, their data is highly complementary as LIBS reveals the elemental composition of a target and Raman spectroscopy the molecular or lattice structures. The combination of data from different analytical sensors measuring the same sample is known as data fusion and is especially valuable when the data is complementary as in the case of LIBS and Raman spectroscopy. Different levels of data fusion exist and will be introduced in Section 9.1. This study evaluates the qualification of low-level data fusion for LIBS and Raman spectra. Additionally, concepts for high-level data fusion were implemented and tested.

As targets for the evaluation of LIBS and Raman data fusion, salts were chosen. Salts play a key role in the detection and interpretation of past and present liquid water on Mars, see Section 2.1. As potential evaporite minerals, salts can give evidence of past aqueous activity. Furthermore, the global climate change on Mars during the transition from the Noachian to the Hesperian age was accompanied by a change in mineralogy from clays to sulfates indicating an environmental change from more alkaline to more acidic conditions. In Gale crater, for example, $CaSO_4$ veins were characterized by the ChemCam instrument which appear to be hydrated, thus being most likely gypsum or bassanite [Nachon et al., 2014, Schröder et al., 2015, Rapin et al., 2016]. Understanding their formation including knowing the hydration state is essential for the interpretation of past geological and geochemical processes especially with regard to the global climate change.

On the surface of present Mars, liquid water is not stable. Solutions, however, in which salts are dissoveld have lower freezing points and could therefore be stable at least temporarily. Recently, the existence of a liquid water reservoir below the ice layers of Mars' south pole was proposed relying on orbital radar data [Orosei et al., 2018]. Such a potentially stable reservoir could be explained by a high salinity especially from dissolved perchlorates. Besides this example, there are more findings of salts related to water or water ice on Mars, see Section 2.1.

All salts in this study have been detected on Mars [Ehlmann and Edwards, 2014] and will be further on of great interest for future Mars exploration. For instance, orbital data of Jezero crater (landing site of Mars 2020) shows signatures of carbonates and the crater contains a preserved river delta [Goudge et al., 2015]. Because one of the mission goals of Mars 2020 is to probe the early Martian climate, salt identification and detection is of high relevance.

This chapter contains two studies with different samples and objectives. The results from single LIBS and Raman measurements were compared with the outcomes of their combined data. With the high performance laboratory LIBS and Raman instruments, the LIBS Aryelle setup (Section 5.1) and the Witec Raman microscope (Section 5.2), the identification of the

[1] Major parts of this chapter were published in [Rammelkamp et al., 2019]

samples with each technique alone would be a comparatively straightforward task. However, in the present studies miniaturized setups for LIBS and Raman spectroscopy described in Section 5.3 were employed in order to simulate the typical constraints on size and mass for space exploration instruments. LIBS experiments were conducted in simulated Martian atmospheric conditions. By using the miniaturized setups, I evaluate if data fusion can improve the identification capabilities of LIBS and Raman instruments that are limited in spectral and pixel resolution, in laser power, and in measurement precision.

For the first study, five different sulfates, namely $BaSO_4$, $CaSO_4 \times 2H_2O$, K_2SO_4, $MgSO_4 \times 7H_2O$, and Na_2SO_4 as pure samples and binary mixtures of them were chosen. Here, PCA models of the pure sulfates were built from LIBS and Raman data alone and from their combined data. The spectra of the mixtures were projected into the models (see Section 4.1) and the results were evaluated with the help of distance and spread calculations of the clusters in the models.

In the second study, I investigated different salts (carbonates, chlorides, perchlorates, and sulfates) in a basaltic matrix. Again, PCA models were computed and their clustering assessed with distance and spread calculations. Additionally, PLS-DA models were used for the identification of the salt in the basalt. For that purpose, different groupings as response variables according to the cation and the anion of the salt as well as to every single salt were tested. Besides these low-level data fusion analyses, I tested two approaches of high-level data fusion. In both cases, the identification of the salt was divided into anion and cation assignment by the Raman and the LIBS data, respectively. PCA models in combination with distance calculations as well as identifications based on similarities derived by Pearson correlation coefficients were implemented.

9.1 Data Fusion

One of the first definitions of data fusion was formulated by the Joint Directors of Laboratories (JDL) [White, 1991]: "multi-level, multifaceted process handling the automatic detection, association, correlation, estimation, and combination of data and information from several sources." Since then, many definitions of data fusion have been widely used in the literature from which several are reviewed and discussed in [Boström et al., 2007]. The authors point out that the most likely correct definition depends on the application and the type of data. In general, the term "information fusion" has established as the overall term valid for any kind of data. A widely applied and discussed subset of information fusion, which is also the apropriate term for LIBS and Raman data fusion, is "sensor fusion" or "multisensor data fusion" [Hall and Llinas, 1997,Pohl and Van Genderen, 1998,Elmenreich, 2002,Mandic et al., 2005,Khaleghi et al., 2013]. One definition of sensor fusion provided in [Elmenreich, 2002] is: "Sensor Fusion is the combining of sensory data or data derived from sensory data such that the resulting information is in some sense better than would be possible when these sources were used individually." Sensor data fusion is a multidisciplinary research area covering concepts and methods from signal processing, information theory, statistical estimation and inference, and artificial intelligence [Khaleghi et al., 2013]. Consequentely, many mathematical theories and concepts as well as algorithms of data fusion exist. In practice, applications in a wide field of analytic measurements where samples are measured with multiple sensors can be found, reaching from food and beverage quality control [Borràs et al., 2015] over pigment classification

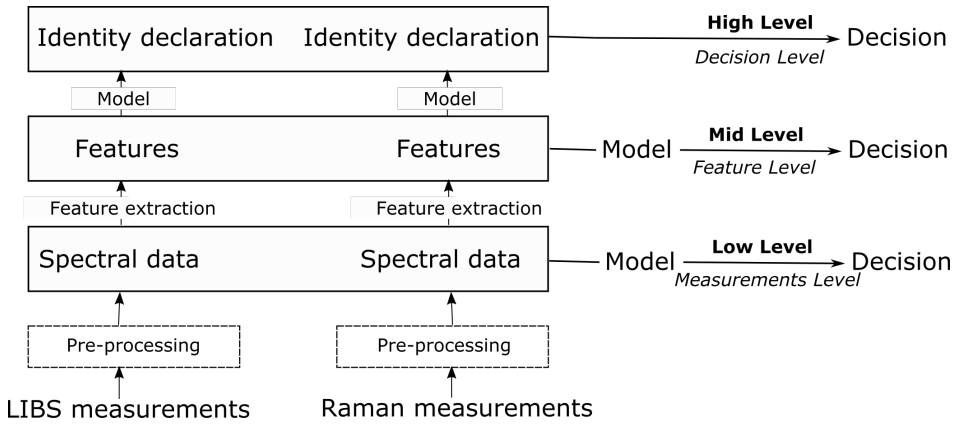

Figure 9.1: The different schemes of the data fusion levels are shown using LIBS and Raman data. At the low-level, no analysis is done before the fusion of the data, except of some individual pre-processings. For the mid-level data fusion, features are extracted which are fused in the next step. At the high-level the two datasets are analyzed by individual models and their results are combined for the final decision. This sketch was adapted from [Borràs et al., 2015].

in cultural heritage [Ramos et al., 2008] to spaceborne imaging spectroscopy [Yokoya et al., 2017]. Generally, three levels of data fusion are distinguished [Borràs et al., 2015]:

- **Low-level data fusion** corresponds to the classical understanding of data fusion using a sample-wise concatenation of the datasets for further analysis. This level of data fusion was mainly used in my study where one Raman spectrum is attached to one LIBS spectrum resulting in one single spectrum.
- The second level of data fusion is called **mid-level data fusion** or feature level fusion as it extracts already important features from each individual dataset. The actual fusion is then applied to the features which are used for subsequent analysis. Those features could be, for example, scores of PCA analysis.
- In the third case no direct merging of datasets takes place. Instead, the datasets are analyzed and evaluated separately and their outcomes are used for final analysis, including, for example, identifications based on decision trees. This level is called **high-level data fusion** or decision level fusion and was also computed and evaluated for the measured Raman and LIBS spectra in this study.

A schematic representation of the general proceedings in the three different cases and the corresponding nomenclature are shown in Figure 9.1. It has to be mentioned here that also other terms for the levels of data fusion are used in the literature. Nevertheless, in this study the above introduced terminology will be used. Low-level data fusion is conceptually straightforward and often the first attempt as it was for this study.

LIBS and Raman data fusion in terrestrial studies was investigated, for example, for the identification of inks [Hoehse et al., 2012], explosives [Moros et al., 2011, Moros and Javier Laserna, 2015], and paleofluids [Fabre et al., 2002]. First approaches of LIBS and Raman data fusion with a space exploration background have been reported [Sobron et al., 2014, Manrique et al., 2018, Cousin et al., 2018, Parente and Gemp, 2018]. One recently published Mars-relevant study used simultaneously measured LIBS and Raman data with high performance

instruments for the identification of minerals [Moros et al., 2018]. Their approach is based on a step-wise decision chain corresponding to high-level data fusion. They first identify the cation member with LIBS and then compare the measured Raman spectrum with selected Raman spectra of minerals that contain the particular cation and that are stored in an appropriate database. By contrast to that study, MVA tools and miniaturized setups are used in the present work. In general, this study aims to expand upon the limited existing studies of LIBS and Raman data fusion relevant for space exploration focusing in particular on Mars relevant salts and measurement conditions.

9.2 Data analysis procedure

The data of both experiments was processed as described in the following. As discussed in Chapter 6, spectra have to be normalized and for this study, normalization of whole spectra by the total emission intensity (sum of all counts) was chosen. The miniaturized LIBS setup consists of four spectrometers (Section 5.3) and the LIBS spectra were therefore normalized in each spectral range separately. After this normalization, the four LIBS spectra were merged into one LIBS spectrum where overlaps between spectral ranges were removed.

Some data pretreatment was also applied to the Raman spectra measured with the miniaturized Raman setup (Section 5.3). Subtraction of the background was necessary due to different shapes of the fluorescence background. The fluorescence contains no relevant information for the present study and keeping it in the spectra would unnecessarily influence the outcomes of the MVA. The fluorescence was fitted with a modified polynomial fitting based on [Lieber and Mahadevan-Jansen, 2003]. In order to obtain good background fits the Raman spectra were smoothed with a moving average (interval size: 11 bins, bin size: $\approx 1.2\,\mathrm{cm}^{-1}$). For the Raman spectra of the sulfates (Section 9.3), the fluorescence fit was subtracted from the raw and unsmoothed data while for the salt/basalt mixtures (Section 9.4) the smoothed data was also used in the further analysis. The Raman data was also normalized to the total emission intensity.

Regarding the differences in spectral range and pixel number between the Raman spectrometer and the four LIBS spectrometers, it was found that a weighting is necessary within the low-level fused spectra in order to avoid overestimating the LIBS spectra in the MVA models. One Raman spectrum has ≈ 3650 channels while one LIBS spectrum has $\approx 14\,000$ channels after the merging of the four spectral ranges. Thus, one could assume that a weighting factor of ≈ 3.8 for the Raman spectra in the combined spectra is necessary. However, not every channel has relevant and non redundant information which rules out the comparison of the channel numbers as an estimate for the weighting factor. In order to find the best weighting, loadings of PCA models from combined data with different weightings were investigated. Thereby, the influences of the two spectra to the models became apparent and was balanced by weighting the Raman spectra with a factor of 2.

The described data processing prior to the analysis with MVA tools was applied to all spectra. Additional individual data treatments will be described for the samples in the particular section.

Table 9.1: Overview of the sulfate mixtures. Note that two salts were hydrated: $CaSO_4 \times 2H_2O$ and $MgSO_4 \times 7H_2O$.

Mixture	Ratios [wt %]	Mixture	Ratios [wt %]
$BaSO_4$: $CaSO_4$	50:50; 30:70	$CaSO_4$: $MgSO_4$	50:50; 30:70
$BaSO_4$: K_2SO_4	50:50; 70:30	$CaSO_4$: Na_2SO_4	50:50; 30:70
$BaSO_4$: $MgSO_4$	50:50; 70:30	K_2SO_4 : $MgSO_4$	50:50; 70:30
$BaSO_4$: Na_2SO_4	50:50; 30:70	K_2SO_4 : Na_2SO_4	50:50; 30:70
$CaSO_4$: K_2SO_4	50:50; 70:30	$MgSO_4$: Na_2SO_4	50:50; 70:30

9.3 Sulfates and their mixtures

The first study on LIBS and Raman data fusion was done with pure sulfates and binary mixtures of them. In this section, the samples and the measurements, general spectral observations, the PCA models, and their cluster analysis are described.

9.3.1 Experiments

The present study is concerned with the pure sulfates $BaSO_4$, $CaSO_4 \times 2H_2O$, K_2SO_4, $MgSO_4 \times 7H_2O$, and Na_2SO_4 and binary mixtures of them. The mixtures were prepared for all possible combinations in 50:50 wt % ratios and for each pairing in one additional 70:30 wt % ratio. An overview of all samples is given in Table 9.1. All in all, 25 samples were prepared by pressing them into pellets as described in Section 5.4. With each technique five different positions on every sample were investigated. A focusing lens with $f = 200\,\mathrm{mm}$ was used in the Raman setup and the integration time was set to 1 s without any averaging. For the LIBS experiments, the samples were measured in a small chamber with simulated Martian atmospheric conditions. Because the laser pulse repetition rate was 10 Hz the integration time was set to 3 s in order to ensure that the emission of 20 laser-induced plasmas in 2 s was collected.

9.3.2 Spectral feature identification

Figure 9.2 shows the mean Raman and LIBS spectra of the pure sulfates which were normalized and fluorescence (Raman) corrected. All sulfates have their strongest Raman feature at around $1000\,\mathrm{cm}^{-1}$ that comes from the non-degenerate symmetric stretching mode $\nu_1(\mathrm{A}_1)$ of the oxygen atoms in the sulfate ion SO_4^{2-}. The sulfate ion belongs to the T_d point symmetry group and has nine internal vibration modes [Mabrouk et al., 2013]. Additional to the ν_1 mode these are the doubly degenerated $\nu_2(\mathrm{E})$ bending vibration and two triply degenerated modes, namely the $\nu_4(\mathrm{T}_2)$ bending vibration and the $\nu_3(\mathrm{T}_2)$ anti-symmetric stretching mode. These modes appear in all Raman spectra but with different shapes and positions due to differences in the splitting of the degenerated modes. These differences occur because of varying cations and hydration states of the sulfates. The cations, for instance, differ in their polarizing powers that scale with the atomic radius r with Z/r^2 where Z is the ion charge. Besides the sulfate modes, OH stretching modes are observable for the hydrated sulfates $MgSO_4 \times 7H_2O$ (epsomite) and $CaSO_4 \times 2H_2O$ (gypsum). Similarly to the sulfate modes, a difference in the shape of the OH-Stretching modes appear due to the different cations and number of water molecules bound to the sulfate.

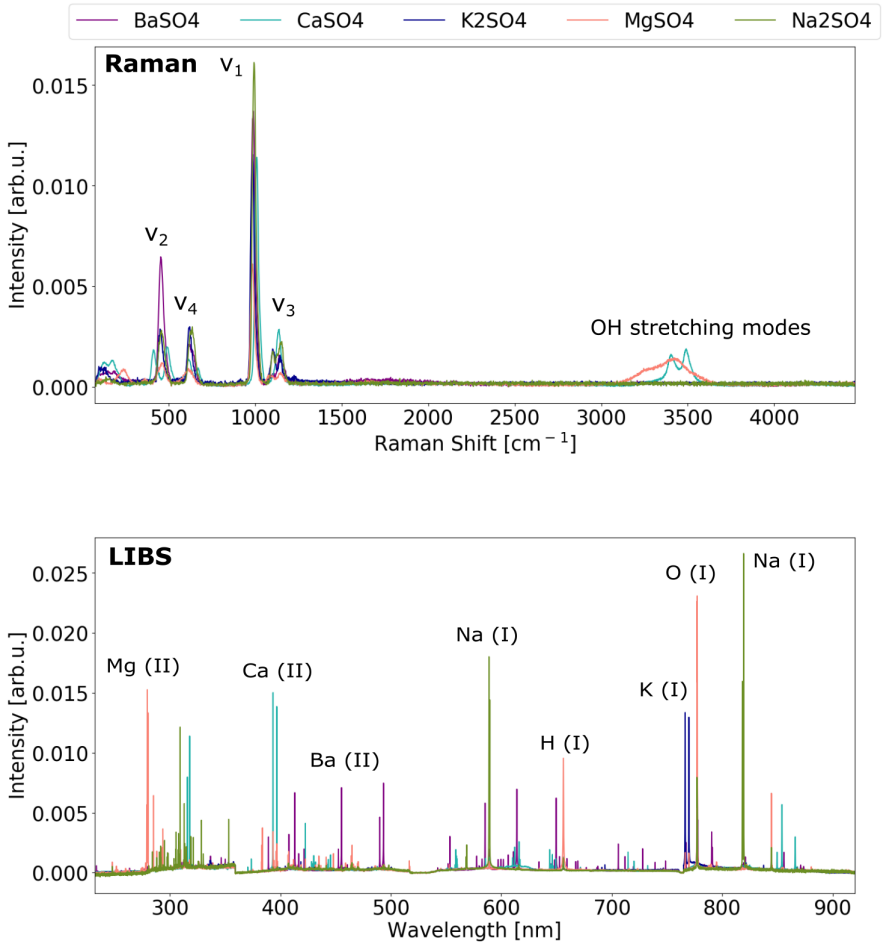

Figure 9.2: *Top*: Mean normalized Raman spectra of the pure sulfates where fluorescence was subtracted. Around 3500 cm^{-1}, the hydrated salts $MgSO_4 \times 7\,H_2O$ and $CaSO_4 \times 2\,H_2O$ show the typical stretching modes of OH. *Bottom*: Mean LIBS spectra of the pure sulfates where each spectral range was normalized by its total intensity, respectively. Every sulfate shows strong emission lines of its particular cation, oxygen, and hydrogen.

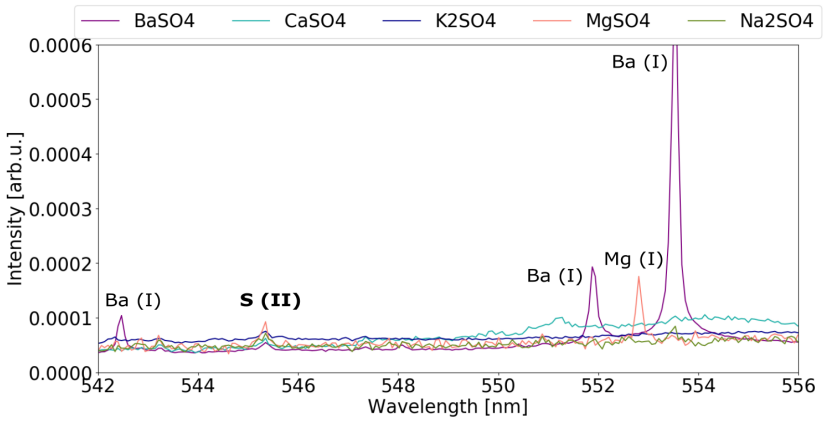

Figure 9.3: Zoom to the spectral range in the LIBS spectra where the strongest sulfur emissions are expected in this experiment. The S (II) emission line at 545.4 nm is apparent but weak and is the only indication that the samples contain sulfur.

Turning to the LIBS spectra shown in Figure 9.2, the sulfates can be distinguished by their cationic emission lines. Each of the cations shows at least two strong and distinct emission lines in the present spectral range. Besides these lines that are characteristic for the particular cation, emission lines from oxygen and hydrogen are present in every spectrum. They originate mostly from the samples as oxygen belongs to the sulfate ion and also comes from bound water molecules, or water that is adsorbed on the samples. Some contribution can further come from the atmosphere. Hydrogen has the strongest emission in spectra of the hydrated sulfates, but appears also for the anhydrous sulfates due to exposure to air during the preparation of the pellets and therefore possibly adsorbed water or a hydrated surface layer. Sulfur lines are weak in the used spectral range, in which the S (II) emission line at 545.4 nm was found to be the strongest one in accordance with [Schröder et al., 2013]. However, only indications of this emission line can be observed, see Figure 9.3, although sulfur is a major part of each sample.

9.3.3 Principal component analysis

PCA models of the pure sulfates were built from three datasets, Raman and LIBS data alone as well as their combined spectra. The explained variance by the sum of the components is shown in Figure 9.4 up to PC 4. The variance in all datasets is explained at least with 98 % by four components. This is sufficient ($>$ 95 %, see Section 4.1) and also with an increasing number of PCs no significant increase of the explained variances was observed. Thus, with four PCs the explained variance converges for all three models. The five pure samples show differences between their spectra of both techniques so that a full cross-validation was chosen, see explanation in Section 4.3. A systematic cross-validation with leaving out all five measurements of one sample at the same time is here not meaningful since for every set of left-out samples, completely different PCA models would be calculated because of the differences between the spectra of different samples. Thus, the left-out samples would be not well or even not at all described by the PCA models relying on the remaining samples. Thereby, the error of the cross-validation would increase, which can be avoided by doing a full cross-validation.

The explained variance by the validation model is shown in Figure 9.4, too, represented

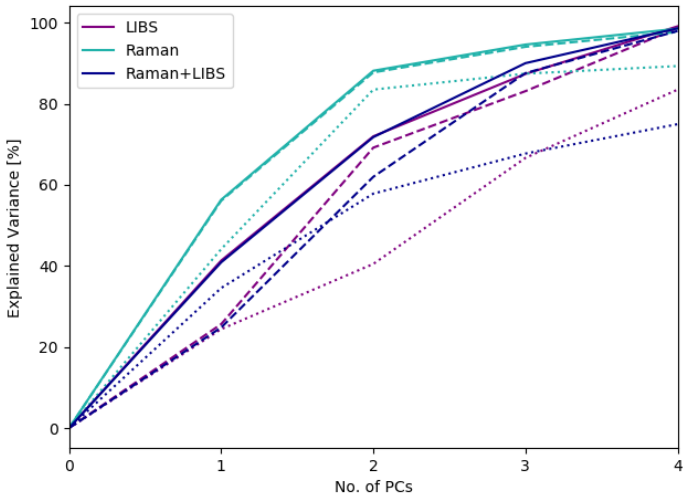

Figure 9.4: Accumulated explained variance of each model dependent on the number of principal components. *Solid*: Calibration model; *Dashed*: Validation model; *Dotted*: Explained variance of the projected mixtures by the calibration model.

as dashed lines. As one can see, it reaches also 98 % with four PCs although it differs for some intermediate components from the calibration models. Next, the data of the binary mixtures was projected into the corresponding pure sulfates models. The explained variance of the mixtures' spectra by the pure models is shown in Figure 9.4 as dotted lines. For these, the values achieved with four components differ as the Raman model explains 89 %, the LIBS model 83 %, and the combined model 75 % of the variance in the mixtures' data. The values are smaller than for the calibration and validation models but nevertheless, they are promising since the binary mixtures are described by models of pure samples with $\geq 75\%$.

Score plots of PC 1/PC 2 and PC 3/PC 4 for each dataset are given in Figure 9.5. The LIBS PC 1/PC 2 plot reveals a clear separation of Mg and Na sulfate samples from the others which are close together. However, the situation is reversed in the PC 3/PC 4 plot where the Ba, Ca, and K sulfate clusters are well separated from each other. Turning to the Raman model, distinct clusters for each sample can be observed in both representations while the $CaSO_4$ cluster is more separated from the others in the PC 1/PC 2 score plot. As in the LIBS model PC 4 splits between Ba and K sulfate, while they are close together in the PC 1/PC 2 representation. The clustering of the combined data is likewise clear in both representations and shows a similar distribution as in the Raman model. In all cases, the two dimensional plots do not reveal the overall clustering of the models as it would appear in a representation with all four dimensions. Nevertheless, all models show distinct cluster formation regarding the two representations shown here.

Loading plots of all PCA models are shown in Figure 9.6 where correlations and anti-correlations between spectral features become apparent. Additionally, the loading plots indicate the influence of spectral features on the particular PC. For example, K_2SO_4 and $BaSO_4$ anti-correlate in the LIBS and Raman+LIBS data which influences the model only in PC 4. This is observed in the score plots where a separation of the K_2SO_4 and $BaSO_4$ clusters shows up in the PC 3/PC 4 plot, see Figure 9.5.

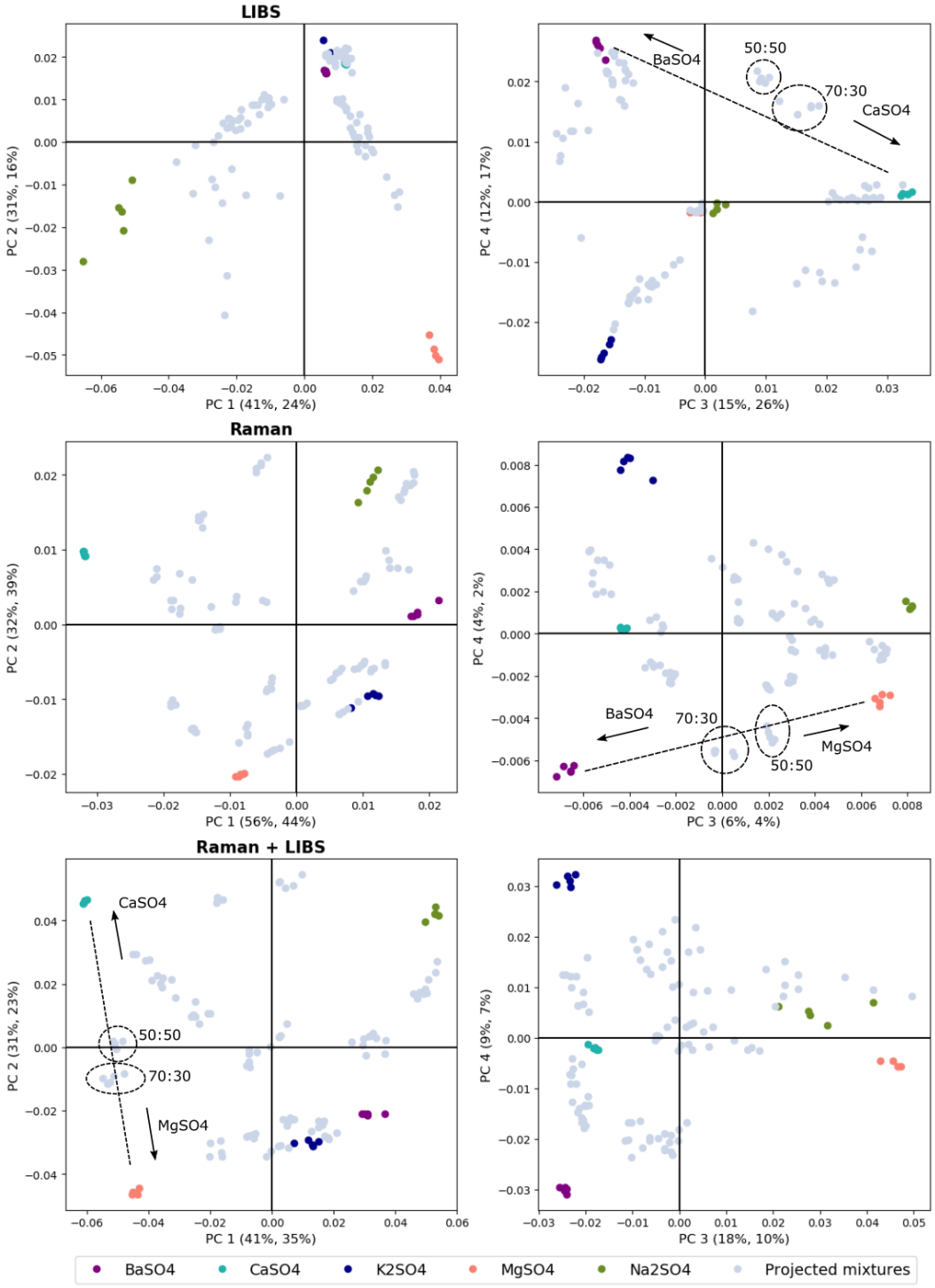

Figure 9.5: Score plots of the pure sulfate models including the projected mixtures in grey color. Shown are two combinations in the four dimensional space of principal components. The values in brackets give the explained variance by the component of the pure sulfate model and the projected mixtures, respectively.

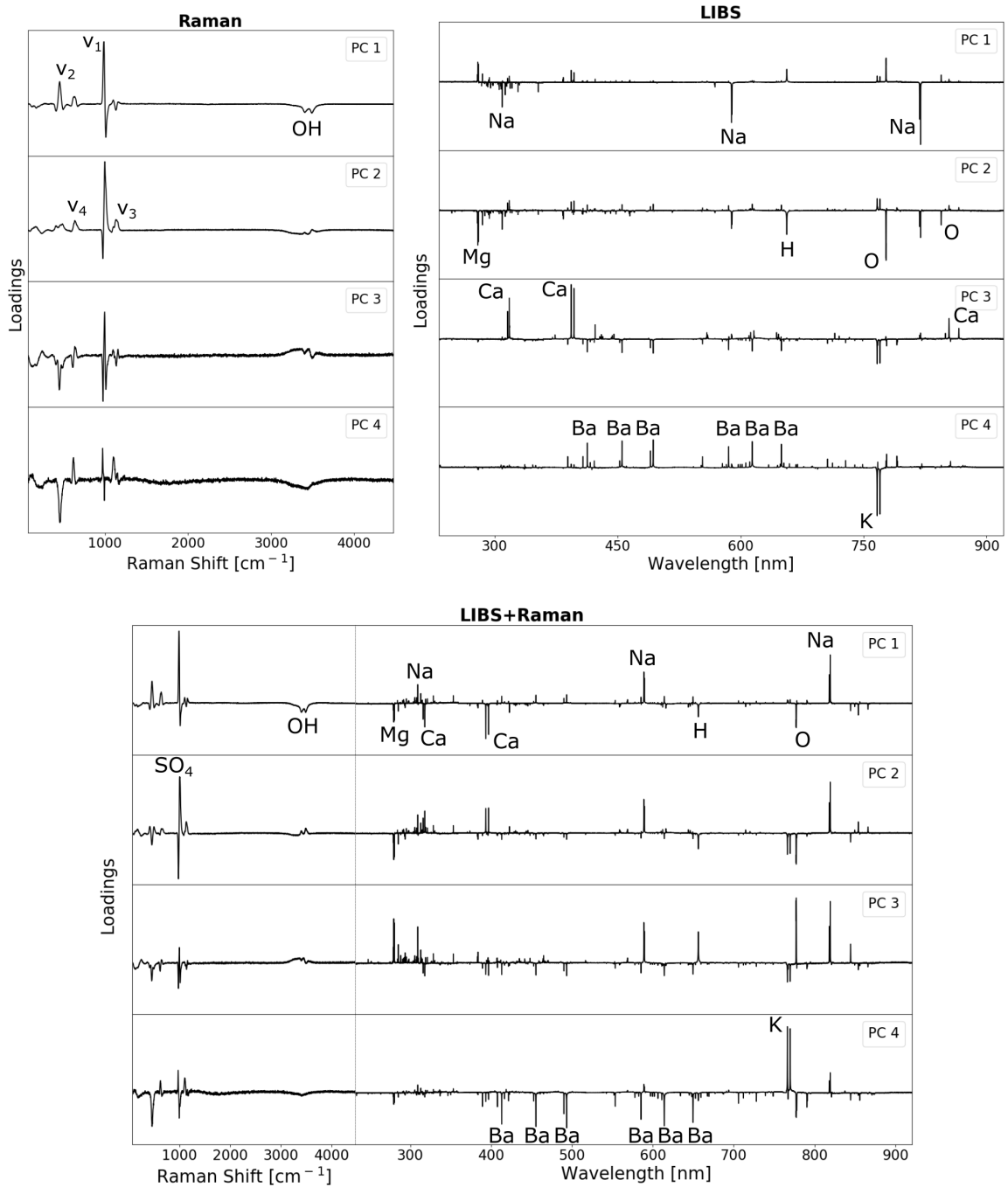

Figure 9.6: Loading plots of the Raman only (*upper left*), the LIBS only (*upper right*), and the combined model (*bottom*) with four PCs. The plots indicate which spectral features have the strongest correlation or anti-correlation with the particular component.

The loadings also visualize the major difference between the Raman and the LIBS data of the sulfates in this analysis: Features in the Raman loadings have shapes that resemble derivatives with zero crossings of peak-shaped functions while the emission lines of LIBS spectra appear in the loading plots as emission lines but with both positive and negative amplitudes. The derivative-like shape observed in the Raman loadings indicates that the spectral position of the emission line correlates with the particular PC. Physically, the influence of the different cations on the Raman modes is responsible for the changing spectral positions among the different sulfates which was already observed in Figure 9.2. For LIBS, on the other hand, the PCs correlate with the presence and the intensity of emission lines at a fixed spectral position. As seen in Chapter 7, line positions in LIBS spectra can also change but this is usually related to changing pressures which is not the case in the present study. Thus, no influence of line shifts on the loadings of the LIBS model is observed.

Besides the pure sulfate clusters, the score plots in Figure 9.5 show the scores of the projected mixtures. In some plots, connecting lines spanned by the scores of the projections between pure sulfate clusters become apparent. For each model, such a trajectory was exemplarily marked in the particular plot. This observation motivates the question if the constituents of the mixtures can be identified according to their relative positions to the pure sulfate clusters in PCA space. In order to evaluate this approach, euclidean distances between the scores of each projected mixture measurement to each center of the pure sulfate clusters were calculated according to the following equation:

$$D_{a,b} = \sqrt{\sum_{i=1}^{N} (\overline{y}_{i,a} - y_{i,b})^2}, \tag{9.1}$$

where a is the pure sulfate cluster with its center coordinates $\overline{y}$, given by the mean coordinate on each axis:

$$\overline{y}_i = \frac{1}{n} \sum_{j=1}^{n} y_{i,n}, \tag{9.2}$$

where n is the number of elements belonging to the cluster. Furthermore, b denotes an arbitrary point not belonging to cluster a. The number of dimensions (principal component axes) is given here by N. The outcomes of these distance calculations are visualized in Figure 9.7 for the LIBS, Raman, and their combined model.

The color coding indicates to which of the five pure sulfate clusters the distance was determined. For each of the five spectra from one mixture five distances were calculated, one to each pure cluster, respectively. In the ideal case, all spectra of a mixture have their two smallest distances in PCA space to the two pure sulfate clusters which are the actual constituents of the particular mixture. Moreover, based on the distance calculations, estimates about the mixing ratio are possible. As an example, all LIBS spectra of the 30:70 $BaSO_4/CaSO_4$ mixture have their smallest distance in the four dimensional PCA space to the pure $CaSO_4$ cluster. Furthermore, their second smallest distances were obtained to the $BaSO_4$ cluster. Thus, the spectra were sorted according to their actual mixing ratio. In this example, the identification of the two constituents was correct including the right order reflecting that the sample contains more $CaSO_4$ than $BaSO_4$, however, this is not the case for all mixtures. The same 30:70 $BaSO_4/CaSO_4$ sample, for instance, is wrongly identified in the Raman only model. In order to compare the capability of mixture identification among the three models, I defined the following criteria for different levels of correct identification:

- *Semi quantitative identification*($\star$, +): Samples that have their two smallest distances to the pure sulfates clusters which are the actual constituents. Additionally, the spectra are sorted accordingly to their mixing ratios.
- *Correct identification*($\star$): Cases in which the actual constituents can be derived by the distances to the pure clusters no matter if their order reflect the mixing.
- *Half correct identification*($\circ$): Samples whose distances allow for the correct identification of one of the two constituents.

With these definitions 4, 3, and 6 semi quantitative identifications and 8, 8, and 11 correct identifications were achieved with the Raman, the LIBS and the combined model, respectively. Taking also the half correct identifications into account, the Raman and the combined model are each left with two completely unidentified samples and the LIBS model with one sample. These results show that the combined model has the best identification capability of the samples in this study.

On the other hand, the low-level Raman+LIBS fusion model does not represent all benefits of the single models. There are, for example, the semi quantitative identifications of the 30:70 $BaSO_4/CaSO_4$ mixture in the LIBS model and of the 50:50 $BaSO_4/Na_2SO_4$ mixture in the Raman model that was only half correctly identified in the combined model. Another example are the comparably small fluctuations between the measurements of one sample in the Raman only model that is not given anymore to that degree in the combined model. In particular, this is observable for the mixtures of Na_2SO_4 and $MgSO_4$, which are more spread in the data fusion model than in the Raman alone model.

It has to be noted here that samples with $MgSO_4$ were challenging to measure with LIBS, especially the pure sample. This was probably because $MgSO_4$ is hydrated with seven water molecules which changes the physical appearance of the sample. The pure $MgSO_4$ pellet has a much lower density than the other samples and its surface appears more transparent. These differences in the physical matrix can cause, for instance, a different laser coupling in LIBS experiments which was observed by means of weaker plasma emissions during the measurements. This physical matrix effect can be seen in the LIBS PCA scores (see Figure 9.5) and consequently also in the distances analysis in form of a clear separation from the other samples (see Figure 9.7). Also, the Na_2SO_4 cluster is clearly separated from the others in PCA space (see Figure 9.5). In this case, the physical appearance of the sample does not reveal any particularities. Here, the reason could be the high intensity of the Na (I) doublet around 589 nm and the large number of Na emission lines in the UV spectral range, see also the loadings of PC 1 in Figure 9.6 (*upper right*).

Another figure of merit for the pure sulfate models besides the identification capability of mixtures is the confinement and separation of the pure sulfate clusters. For that purpose the distance of each pure sulfate cluster to its nearest neighbor was calculated and compared to its spread. The spreads of clusters with n members are determined by the following expression:

$$S = \frac{1}{n}\sum_{i=1}^{n}\left(\sqrt{\sum_{j=1}^{N}(\overline{y}_j - y_{j,i})^2}\right), \tag{9.3}$$

where $\overline{\mathbf{y}}$ is the center of the cluster and N is the number of axes, thus the number of principal components. Usually, unambiguous sample identification improves when distances between clusters become larger and when the spread of each cluster gets smaller. Thus, a ratio defined

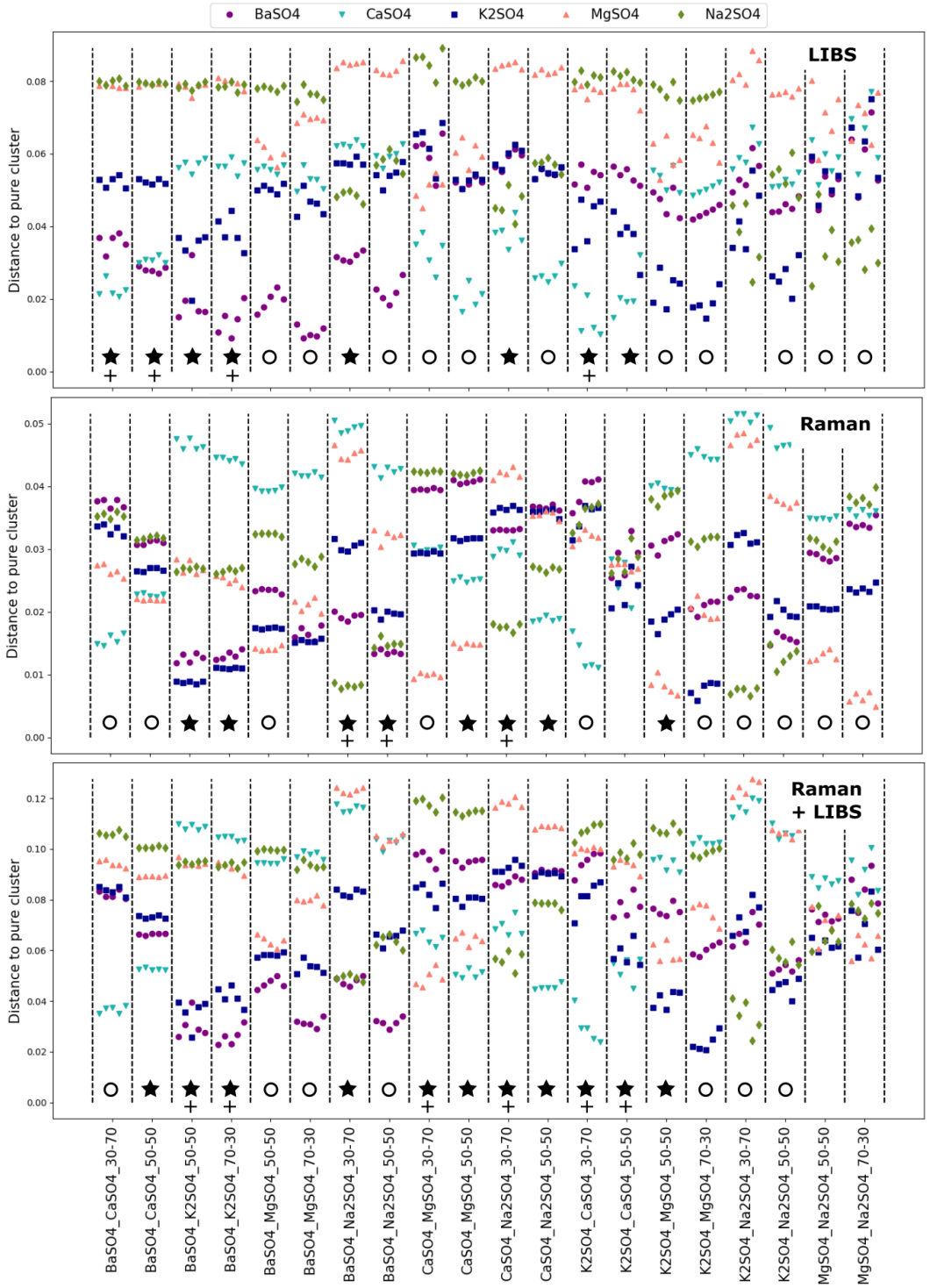

Figure 9.7: Distances between the spectra of the binary sulfate mixtures and each cluster center of the five pure sulfates in the four dimensional PCA space. The colors indicate to which pure sulfate the distance between the particular mixture was calculated, see legend above the plots. In several cases a correct assignment of the constituents in the mixtures is possible based on the smallest derived distances.

Table 9.2: PCA cluster distances and spreads.

Sample	NN	$D \times 10^3$	$S \times 10^3$	q
LIBS				
$BaSO_4$	K_2SO_4	50.8	1.14	**44.6**
$CaSO_4$	K_2SO_4	56.3	1.03	55.3
K_2SO_4	$BaSO_4$	50.8	2.00	**25.3**
$MgSO_4$	$BaSO_4$	79.4	2.29	34.6
Na_2SO_4	$BaSO_4$	78.1	6.64	11.8
Raman				
$BaSO_4$	K_2SO_4	20.1	1.37	14.7
$CaSO_4$	$MgSO_4$	39.6	0.31	**129.2**
K_2SO_4	$BaSO_4$	20.1	1.46	13.8
$MgSO_4$	K_2SO_4	26.9	0.54	**49.6**
Na_2SO_4	$BaSO_4$	25.1	1.51	**16.6**
Raman+LIBS				
$BaSO_4$	K_2SO_4	64.8	2.23	29.0
$CaSO_4$	K_2SO_4	110.7	0.89	124.0
K_2SO_4	$BaSO_4$	64.8	2.86	22.6
$MgSO_4$	K_2SO_4	97.6	1.99	49.2
Na_2SO_4	$BaSO_4$	92.8	5.86	15.8

as $q = D/S$ indicates how good those requirements are met [Neumaier et al., 2015]. In Table 9.2 the D, S, and q values of the pure sulfate clusters are listed with respect to their nearest neighbors (NN). The outcomes show that a good clustering is given in every model because $q \gg 1$ was achieved for all pure sample clusters in all models. The q values of the Raman+LIBS model lie inbetween the values of the LIBS and Raman only models. For $BaSO_4$ and K_2SO_4, the LIBS model provides the largest q ratios while the Raman model has the largest q ratios for the remaining $CaSO_4$, $MgSO_4$, and Na_2SO_4 clusters. Comparing the distances and spreads of the models separately, the largest distances are given by the combined Raman+LIBS model. The next largest distances were obtained from the LIBS model, thus the distances increased due to the data fusion with the Raman spectra. Regarding the spreads, the clusters are better confined in the Raman only model, except for $BaSO_4$, where the LIBS model has the smallest spread. However, the spreads of the models do not have a clear trend since the second smallest spreads are provided by either the LIBS or the combined model.

The larger distances in the LIBS model compared to the Raman model can be explained by the clear differences between the LIBS spectra: The strong emission lines of the cations are either present or absent. But since the Raman spectra are also able to differentiate between the sulfates although less explicitly, the distances increased in the low-level data fusion model. The ablation process and the plasma of LIBS are highly complex and consequently LIBS data can have typically rather large fluctuations between repetitive measurements of one sample (see also Chapter 6). This explains the larger spreads in the LIBS model in comparison to the cluster spreads in the Raman model. Combining the data can therefore not decrease the already small spreads of the Raman model as the LIBS data contributes with larger fluctuations. This increase of the spreads in the combined model in comparison to the Raman only model compensates the larger distances resulting finally in q ratios of the combined model

which are not larger than those of the individual models. Nevertheless, the q ratio of each cluster in the combined model is always close to the q ratio of the particular cluster in the individual models which provides the largest q ratio. Accordingly, the characteristics of the combined model are a "mixture" of those from the LIBS and Raman models alone and do not result in an improved clustering.

9.3.4 Summary

To summarize the outcomes of the Raman and LIBS low-level data fusion with PCA models, an improved identification of binary sulfate mixtures was observed with the combined model. Here, the spectra of the mixtures were projected into PCA models which rely on only five pure sulfate samples. The identification was done according to distances in PCA space between the spectra of projected mixtures and the center of the pure sulfates. Evaluation of the cluster quality of the pure sulfates showed that the largest distance to spread ratio was given either by the LIBS or the Raman model but never by the combined LIBS+Raman model. Thus, in this example of low-level data fusion, not all benefits from the single models were transferred into the fused model. Moreover, drawbacks of them such as the fluctuations in the LIBS data, contribute to the combined model, too.

9.4 Salt identification in basaltic matrix

In this section the results of mainly low-level but also high-level data fusion of Raman and LIBS measurements of samples containing the same alkali basalt but different salts are presented. The objective of this study is to identify the salt in the basalt. Therefore, PCA models were built and their clustering was evaluated. In addition, PLS-DA was performed where class membership was analyzed not only for single sample classes but also for cation and anion class membership. In all approaches, the outcomes of single LIBS and Raman analysis were compared to the results given by their low-level fused data. Additionally, approaches of high-level data fusion based on PCA models and distance calculations, and on correlations between the spectra were tested.

9.4.1 Experiments

The salts were mixed with a powdered and certified basalt with high alkali content (GBW 01705: 3.38 ± 0.05 wt% Na_2O and 2.32 ± 0.06 wt% K_2O) in a mixing ratio of $\approx$30:70 wt %. The basaltic matrix is Mars relevant because Mars' surface is known to be mainly basaltic, see Section 2.1. At least three carbonates, chlorides, perchlorates, and sulfates that provide the cations Ca^{2+}, Mg^{2+}, and Na^{+} were used. $MgSO_4$ was available in two different hydration states and an overview of all samples is given in Table 9.3. In total, 13 samples were pressed into pellets and investigated. Like the sulfates in Section 9.3, the salt/basalt mixtures were measured with the miniaturized LIBS and Raman setups described in Section 5.3, each sample at five different positions with each technique. This time, a lens with $f = 30$ mm focused the laser beam onto the sample in the Raman setup. Additionally, some of the mixtures and a pure basalt pellet were measured with the Witec confocal Raman microscope (Section 5.2) to characterize the basalt on a smaller scale.

Table 9.3: Overview of the salt/basalt 30:70 wt % mixture samples.

	Carbonates	Chlorides	Perchlorates	Sulfates
Basalt GBW 07105	$CaCO_3$	$CaCl_2 \times 2H_2O$	$Ca(ClO_4)_2 \times H_2O$	$CaSO_4 \times 2H_2O$
	$MgCO_3$	$MgCl_2 \times 2H_2O$	$Mg(ClO_4)_2 \times H_2O$	$MgSO_4 \times 1H_2O$; $MgSO_4 \times 7H_2O$
	Na_2CO_3	NaCl	$NaClO_4$	Na_2O_4

9.4.2 Spectral feature identification

In Figure 9.8, Raman and LIBS mean spectra of the salt/basalt mixtures are shown. Smoothing with a moving average was applied to the Raman data as described in Section 9.2. The color coding for the Raman spectra corresponds to the different anions and to the type of cation for the LIBS spectra. All salts, except for the chlorides which do not have Raman active modes, have their strongest Raman mode in the region around 1000 cm^{-1}. As already seen for the pure sulfates (see Section 9.3.2), these modes are symmetric stretching modes of their anions $\nu_1(A_1)$. This characteristic mode appears for the perchlorate ion around 950 cm^{-1}, for the sulfate ion around 1000 cm^{-1}, and for the carbonate ion around 1100 cm^{-1}. But also the salts with the same anion do not have exactly the same Raman shift of the $\nu_1(A_1)$ mode. These small inner-group shifts have already been observed for the sulfates in Section 9.3.2 and can be explained by the influence of cations and bound water molecules. In general, the signals of the salts in the basaltic matrix are weaker compared to pure salt samples. For example, the other stretching and bending modes (ν_2, ν_3, ν_4) of the sulfates that have been observed in their Raman spectra are not clearly recognizable anymore.

The Raman spectra in Figure 9.8, show further modes which are observable in every measurement and which come most likely from the basaltic matrix. Typical basalt contains Raman active minerals such as plagioclase ($Na_xCa_{x-1}Al_{2-x}Si_{2+x}O_8$), augite (pyroxene, (Ca, Mg, Fe)$_2Si_2O_6$), and olivine ((Mg, Mn, Fe)$_2SiO_4$, only in alkali basalts) [Markl, 2014]. Spectra with high spectral resolution and from a small spot (1 μm) were measured with the confocal Witec Raman microscope (Section 5.2) for comparison and identification. Measurements were done in line-scan mode which means that Raman spectra were acquired at ten equidistant positions (distance $\approx 65\,\mu$m) on a defined line across the sample's surface. One example of such a line-scan measurement is shown in Figure 9.9. Like for the spectra measured with the miniaturized setup, fluorescence was subtracted with the multipolynomial fit procedure (Section 9.2). Some of the spectra reveal the typical double peak of plagioclase at $\approx 500\,cm^{-1}$ or modes of the pyroxene augite around 400 cm^{-1}; 650 cm^{-1}; and 1000 cm^{-1}. In another measurement at another position on the sample (not shown here), the characteristic double peak of olivine at $\approx 830\,cm^{-1}$ was observed. Since the miniaturized Raman setup has a large spotsize of 50 μm in comparison to the spot of the Witec Raman microscope (1 μm) the mineral variation of the basalt could not be resolved with the miniaturized Raman setup. However, the spectra measured with the Witec Raman microscope confirmed the spectral features that were observed in the Raman spectra of the salt/basalt mixtures measured with the miniaturized setup. Those are modes which appear in all spectra in the following ranges: 400-550 cm^{-1} (augite and plagioclases), around 650 cm^{-1} (augite) and 830 cm^{-1} (olivine), but they slightly differ in shape. The reason for the different shapes are the additional stretching and bending modes of the salts' anions besides the $\nu_1(A_1)$ mode. These modes vary for the different salts and overlap in some cases with the modes from the minerals in the basalt. The observed features in these data were interpreted as a superposition of the modes from the basalt and the mixed

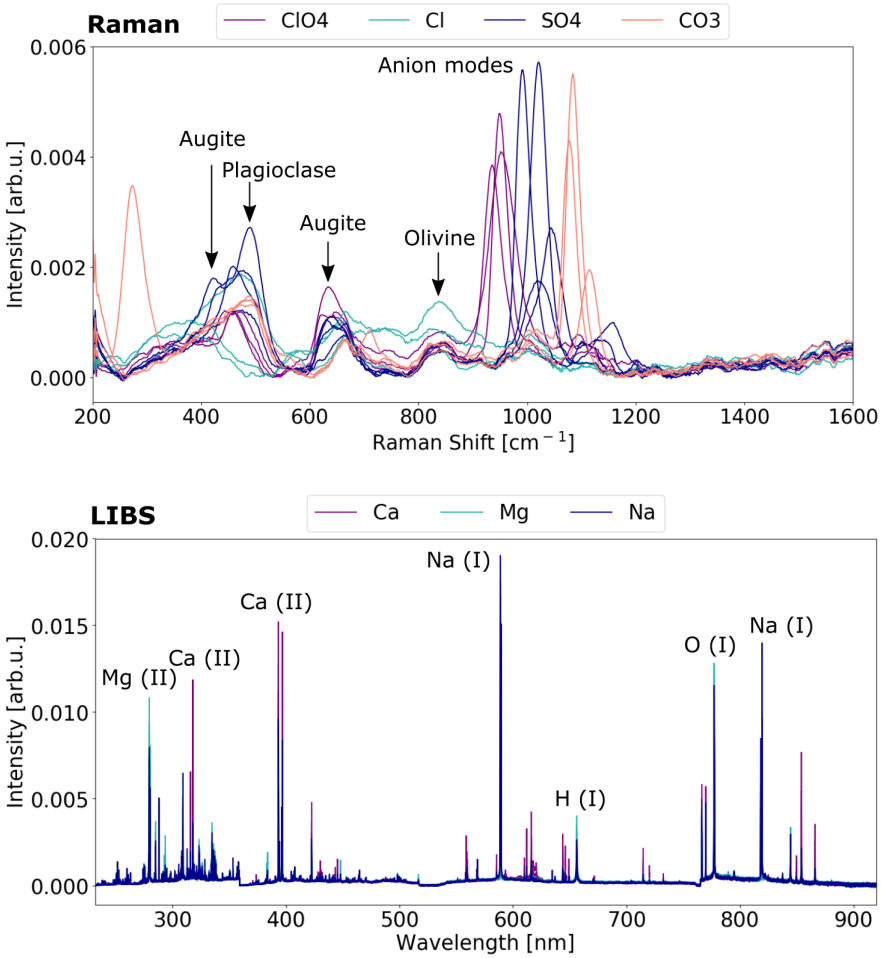

Figure 9.8: *Top*: Raman mean spectra of all salt/basalt mixtures, the color coding corresponds to salts with the same anion. The modes of the anions are well visible. Modes of minerals which are part of typical basalt were identified. However, their shapes vary due to superpositions with further modes of the anions. *Bottom*: LIBS mean spectra of all salt/basalt mixtures, here the colors represent salts with the same cation. The emission lines of Ca, Mg, and Na are present in all spectra but vary in their intensities due to the cation of the particular salt.

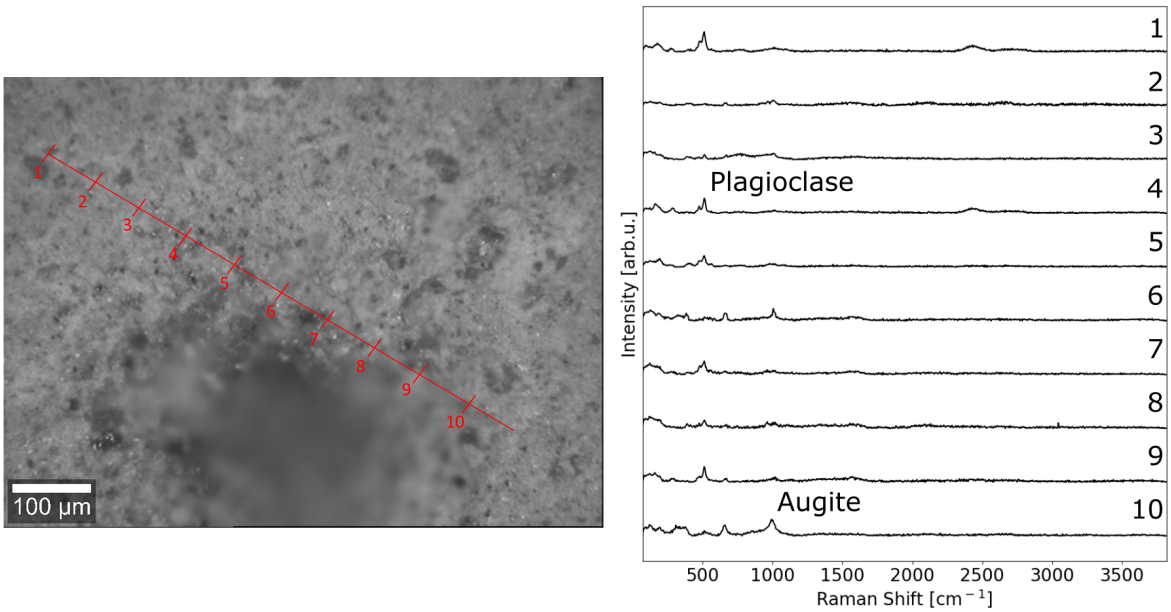

Figure 9.9: Raman line-scan of a pure basalt pellet with the *Witec* confocal Raman microscope. The measurements were performed at ten different positions that are separated by $\approx 65\,\mu$m. The modes of plagioclases and augite are clearly observable. The sample was also measured with the echelle LIBS setup and the Raman line-scan passes close to a LIBS crater.

salts which results in different shapes for each salt.

Regarding the LIBS spectra (Figure 9.8, *bottom*), many emission lines appear, mainly from the major elements in the basalt including emission lines from the cations of the mixed salts. Since the salt cations Ca, Mg, and Na are also naturally part of the basalt, their emission lines can be observed in all LIBS spectra and not only in mixtures that contain the salt with a particular cation. However, depending on the added salt, the emission lines of the particular cation have enhanced intensities. On the other hand, differentiation between the anions of the salts is challenging. In the spectra of the perchlorates and chlorides, a weak Cl (I) emission line is observable at 837.6 nm. Another indication for chlorine is given by the CaCl molecular emission around 618 nm which appears in the spectra of the salt/basalt mixtures that contain $CaCl_2$ or $Ca(ClO_4)_2$. In these samples the Ca concentration is therefore high enough for the formation of CaCl molecules [Vogt et al., 2018b]. Sulfur emission lines that could differentiate the sulfates from the other salts are not observable in these LIBS spectra. As carbon is part of the Martian atmosphere (see Section 2.1), every LIBS spectrum also shows the weak C (I) 247.9 nm emission line but with no significant variation between the measurements of samples with added carbonate or without. Therefore, it is no easy indicator to identify the carbonate mixtures among the samples.

While in Raman spectra the peak positions indicate differences in composition, the LIBS spectra feature differences in line intensities. By comparing all LIBS spectra, it is possible to identify the cations of the salts due to larger intensities. Almost no indications of the anions can be derived from the LIBS spectra. The Raman spectra allow for a discrimination between the anions, but also the slight shifts within one anion group of the $\nu_1(A_1)$ mode could be used

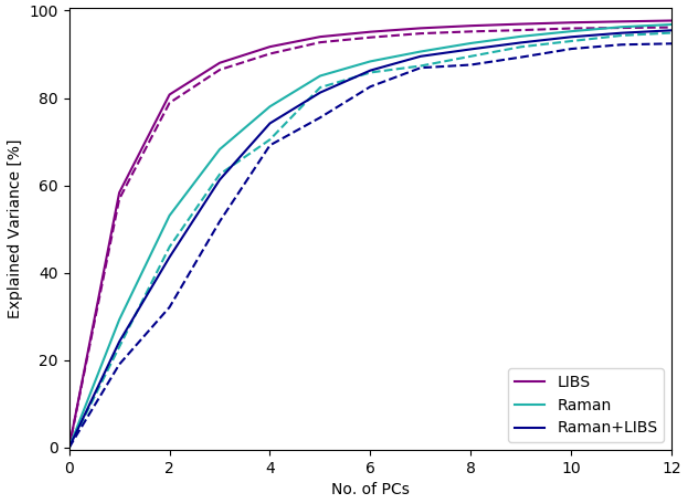

Figure 9.10: Explained accumulated variance that is explained by the PCs. The LIBS model reaches already a convergence with four PCs while the Raman and the Raman+LIBS models need eight PCs.

to identify the cations. But as these shifts are small, the determination of the cation from the Raman data is rather challenging.

9.4.3 Principal component analysis

A PCA was performed with the data of all 13 salt/basalt mixtures. Especially the Raman spectra are different for every sample which makes a full cross-validation necessary as already seen for the sulfates in Section 9.3. For the LIBS only model, systematic cross-validation would have been possible as the cationic emission lines appear in all LIBS spectra but with varying intensities. However, to be consistent, the LIBS spectra were validated with a full cross-validation, too. In Figure 9.10, the explained accumulated variances of every model for an increasing number of PCs up to twelve PCs are shown. As one can see, the LIBS model needs only four PCs until a convergence and an explained variance of more than 95 % are reached. The Raman and the Raman+LIBS combined model both start to converge only with eight PCs reaching also 95 % of explained variance. As discussed for the spectral feature identification, more differentiating information is given in the Raman spectra. That is why more components are needed to explain the major part of the variance in the Raman as well as in the combined dataset. The LIBS spectra mainly show differences between the three cations, thus most of the variance in the LIBS dataset is already explained by three components (87 %) from which each correlates with the emission lines of one of the three cations, respectively. In the Raman model, on the other hand, some PCs correlate with the spectral features of single salt/basalt mixtures and consequently more components are needed to explain the variance in the Raman data.

Regarding the scores of the PCA models, see Figure 9.11, where two dimensional combinations of PC 1/PC 2 and PC 3/PC 4 are shown for each model, the differences between the datasets become even more apparent. The LIBS scores in the PC 1/PC 2 representation show a clear clustering of the salt/basalt mixtures due to their cation (Figure 9.11, *top, left*). PC 1

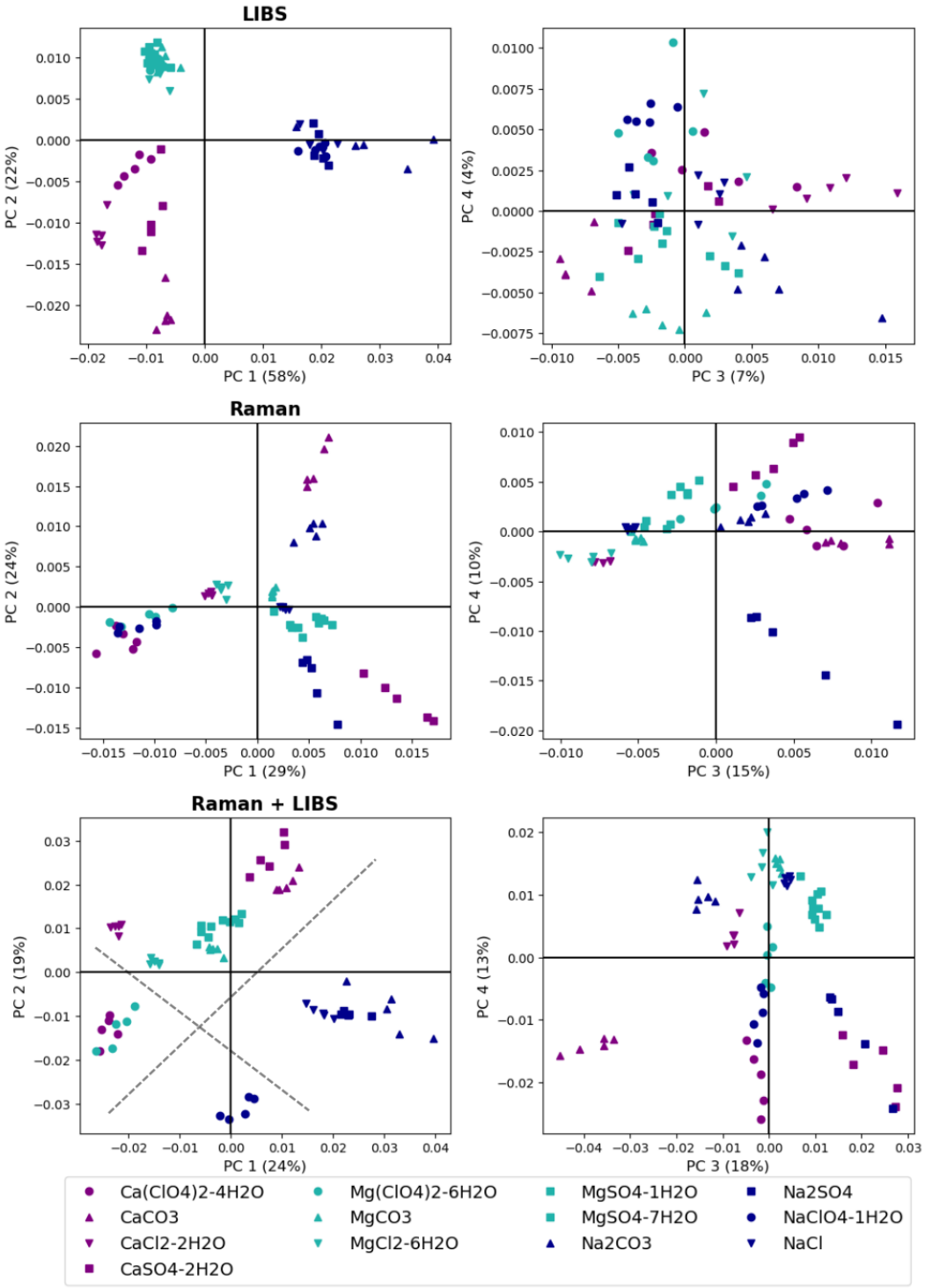

Figure 9.11: Score plots of the three PCA models from the salt/basalt mixtures, *top*: LIBS, *middle*: Raman, and *bottom*: Raman + LIBS. Shown are two dimensional plots of the first four components and the values in brackets are the explained variances by the PC. The color indicates the cation of the salt while the marker shape corresponds to the anion.

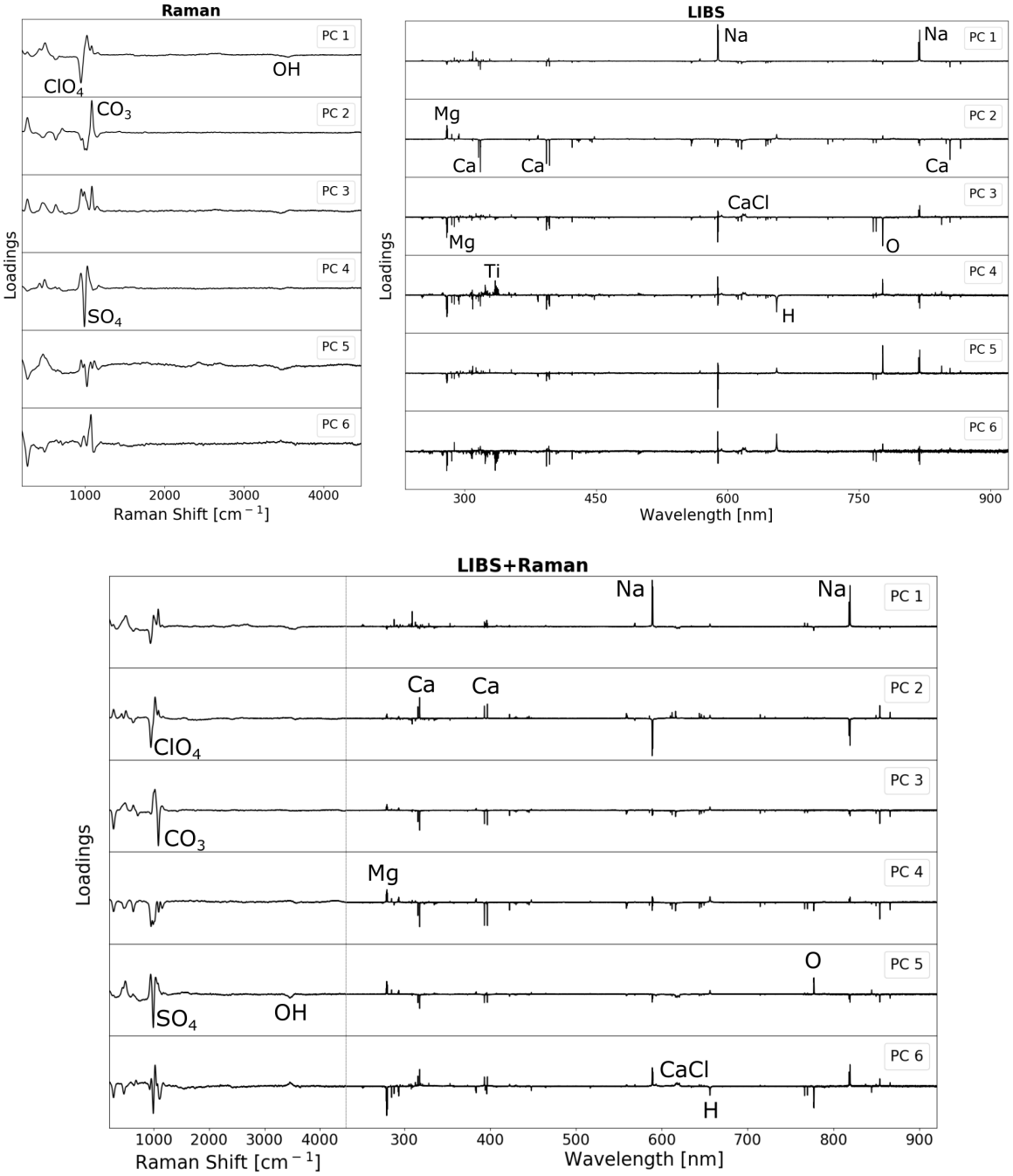

Figure 9.12: Loading plots of the Raman only (*top, left*), the LIBS only (*top, right*), and the LIBS+Raman (*bottom*) models. Shown are the first six PCs. From this representation one can derive which features correlate or anti-correlate with the appropriate PC. For example, PC 1 of the LIBS and also of the LIBS+Raman model correlates with the emission of Na. This was also observed in the score plots shown in Figure 9.11.

separates between Na and the other two cations Mg and Ca which, in turn, are distinguished on PC 2. In Figure 9.12, the loadings of each model up to PC 6 are shown. The LIBS loadings (Figure 9.6, *top, right*) confirm the observed separations in the score plots: PC 1 has a strong positive correlation with Na emission lines whereas PC 2 reveals opposite correlations with Mg (positive correlation) and Ca (negative correlation) emission lines. Turning back to the scores, inside the Ca cluster in the PC 1/PC 2 plot (Figure 9.11, *top, left*), sub-clustering due to the anion of the salt can be observed. As mostly Ca emission lines correlate with PC 2 (negative correlation, see loadings in Figure 9.12), these sub-cluster appear most likely due to different Ca concentrations in the salt/basalt mixtures. Comparing the particle concentrations of Ca in the four Ca-salts, the largest Ca concentration with 20 at % has $CaCO_3$ whose spectra have the largest negative scores on PC 2. On the other hand, the salt with the smallest Ca concentration (3 at %) is $Ca(ClO_4)_2 \times 4\,H_2O$ which has the on average the smallest negative scores on PC 2 within the Ca cluster. However, a inner-clustering does not form for the Mg and Na clusters. There is no apparent clustering with cation species visible in the PC 3/PC 4 plot (Figure 9.11, *top, right*) and the scores are spread over the four quadrants. Nevertheless, slight trends can be identified, such as a positive correlation of chloride and perchlorate spectra versus a negative correlation of sulfate and carbonate spectra with PC 4. One reason for this could be the CaCl emission which has positive loading values on PC 4 and appears only in the chloride and perchlorate spectra. Furthermore, emission lines from elements that are part of the basalt such as Ti appear in the loading plots starting on PC 4. Their variation among the salt/basalt mixtures can not be related directly to the salts, moreover their concentrations in the mixtures vary as they were produced according to weight ratios (30:70 wt % of salt:basalt). This means that depending on atomic weights of the elements in the salts and the basalt, the actual concentrations of elements can vary among the mixtures. Nevertheless, 80 % of variance in the LIBS spectra is explained by PC 1 and PC 2 confirming that the main information in the LIBS data is about the cation of the added salt in the basalt.

Turning to the Raman score plots, the situation is different (Figure 9.11, *middle row*) because the information in the data is more distributed over the components. In the PC 1/PC 2 plot, a separation according to the anion of the salt can be observed. PC 1 separates the carbonates and sulfates from the perchlorates and chlorides. In a less distinct way, PC 2 differentiates between chlorides and perchlorates. Also carbonates and sulfates are separated by PC 2, where some of them are more apart than the others. Similar trends can be seen in the loadings of the Raman model (Figure 9.12, *top, left*). Like for the sulfates (see Figure 9.6), the shape of the Raman loadings indicate that line positions are responsible for the variance in the data. In accordance with the scores, the loadings of PC 1 have negative values for the spectral position of the ClO_4 mode and positive ones for the modes with larger Raman shifts as those of CO_3 and SO_4. Regarding the loadings of PC 2, they have positive correlations with the CO_3 mode which was already observed in the scores plot. The PC 3/PC 4 score plot shows the isolation of only one sample group (Na_2SO_4) from the other salt/basalt mixtures. Responsible for this is a sharp negative correlation of the SO_4 mode with PC 4. Up to PC 10, one can find a two dimensional score plot combination of PCs for almost every salt/basalt mixture in which it is isolated from the others. This observation indicates that after a large part of the variance in the data has been explained by PC 1 and PC 2 (46 %), each subsequent PC correlates or anti-correlates with single salt/basalt mixtures meaning that in the multidimensional model isolation and therefore identification of salt/basalt mixtures should also be possible.

For the scores of the combined Raman+LIBS model (Figure 9.11, *bottom row*), no clear

separation due to anions or cations can be seen in the PC 1/PC 2 plot. Instead, a separation of the Na-salts and also of the perchlorates from the other salt/basalt mixtures is found. This does not correlate directly with PC 1 or PC 2 but with a combination of them, indicated with grey dashed lines in the plot. In the loadings (Figure 9.12, *bottom*), this can be seen as Na lines in the LIBS part have positive and strong correlations with PC 1, and negative correlations with PC 2. The perchlorates are separated from the others due to negative correlations of their Raman modes with PC 1 as well as with PC 2 where the latter correlation is stronger. Additionally, sub-clusters appear that rely on single sample groups but also structures due to the cations or anions are visible. As in the case of the Raman PCA model, almost half of the variance in the data is explained by PC 1 and PC 2 (45 %) and subsequent PCs correlate or anti-correlate with single salt/basalt mixtures. One example is given by the PC 3/PC 4 plot where $CaCO_3$ is isolated from the others due to a negative correlation with PC 3 which is also observable in the loadings of PC 3, mainly in the Raman part. But also the LIBS data contributes here, as also Ca emission lines have negative correlations with PC 3.

To evaluate and compare the PCA models of the single techniques with their combined data model, I employed distance and spread calculations as in Section 9.3 for the pure sulfates. Here, the distance to spread ratio q was calculated for each salt/basalt mixture. As one can see from equations (9.1) and (9.3) for the distance and the spread, respectively, the dimensionality of the models affects the values of both. Including more axes leads to larger distances and spreads, but although the ratio of them is taken, the increases do not compensate each other as they have different dependencies on the number of axes. Consequently, models which have different dimensions are not comparable based on their q values which means that models with the same dimensionality need to be found for the following evaluation.

In this study, the optimal number of PCs is different for the three datasets which becomes clear regarding the explained variances of the three models in Figure 9.10. The LIBS model reaches 95 % already with six, the Raman model with ten, and the combined model with twelve components. Therefore, the requirement of same dimensionality is not fulfilled when the q ratios would be considered at their optimal number of PCs. I fixed the number of components to six and ten in order to discuss two different scenarios as compromises. Those numbers were chosen since major parts of the variance in the LIBS data is explained by six PCs and in the Raman as well as in the combined model by ten PCs.

The distances, spreads, and their ratios are listed in Table 9.4 for all three models with six and ten PCs. Overall, the outcomes show general differences, although the fixed number of components is not the best choice for each model but mostly a compromise. First, the cluster's quality is better in the Raman and the Raman+LIBS model than in the LIBS model because all salt/basalt mixtures have the smallest q ratios in the LIBS model. Second, increasing the number of PCs from six to ten has different effects on the q ratios of the three models. The clusters in the LIBS almost show no significant changes in their q ratios. By contrast, the Raman only model with ten PCs shows an improved cluster quality for 9 samples of the 13 included salt/basalt mixtures in comparison to the 6 PCs model. However, in three cases, the q ratio is smaller for more PCs. Comparing the 6 PCs and the 10 PCs Raman+LIBS models, the ratio is larger for 6 samples and smaller for 4 samples in the 10 PCs model.

In order to evaluate which model provides the best clustering, the outcomes of the Raman and Raman+LIBS model for the two numbers of PCs are summarized in the following (LIBS only already dropped out):

Table 9.4: Nearest neighbors (NN), distances to NN and spreads in the PCA models of the salt/basalt mixtures, comparison of the results from models built from six and ten PCs.

		6 PCs				**10 PCs**		
Sample	NN	$D \times 10^{-3}$	$S \times 10^{-3}$	q	NN	$D \times 10^{-3}$	$S \times 10^{-3}$	q
LIBS								
$Ca(ClO_4)_2$	$CaSO_4$	8.6	5.30	1.6	$CaSO_4$	9.1	5.73	1.6
$CaCl_2$	$Ca(ClO_4)_2$	13.3	3.60	3.7	$Ca(ClO_4)_2$	14.2	4.65	3.1
$CaCO_3$	$CaSO_4$	14.8	2.61	5.7	$CaSO_4$	15.1	2.80	5.4
$CaSO_4$	$Ca(ClO_4)_2$	8.6	5.33	1.6	$Ca(ClO_4)_2$	9.1	6.00	1.5
$Mg(ClO_4)_2$	$MgCl_2$	6.8	3.68	1.8	$MgCl_2$	6.9	4.12	1.7
$MgCl_2$	$Mg(ClO_4)_2$	6.8	5.46	1.2	$Mg(ClO_4)_2$	6.9	5.88	1.2
$MgCO_3$	$MgSO_4 \times 1\ H_2O$	7.7	2.69	2.9	$MgSO_4 \times 1\ H_2O$	8.0	2.77	2.9
$MgSO_4 \times 1\ H_2O$	$MgSO_4 \times 7\ H_2O$	4.6	3.22	1.4	$MgSO_4 \times 7\ H_2O$	5.9	3.46	1.7
$MgSO_4 \times 7\ H_2O$	$MgSO_4 \times 1\ H_2O$	4.6	3.76	1.2	$MgSO_4 \times 1\ H_2O$	5.9	4.02	1.5
Na_2CO_3	NaCl	13.4	8.95	1.5	NaCl	13.8	9.53	1.5
Na_2SO_4	NaCl	4.5	2.87	1.6	NaCl	5.8	3.47	1.7
$NaClO_4$	Na_2SO_4	5.3	2.75	1.9	Na_2SO_4	6.9	2.98	2.3
NaCl	Na_2SO_4	4.5	4.00	1.1	Na_2SO_4	5.8	4.46	1.3
Raman								
$Ca(ClO_4)_2$	$NaClO_4$	8.0	3.07	2.6	$NaClO_4$	9.6	3.34	2.9
$CaCl_2$	$MgCl_2$	4.4	0.95	4.6	$MgCl_2$	4.5	1.32	3.4
$CaCO_3$	Na_2CO_3	16.6	3.13	5.3	Na_2CO_3	17.1	3.18	5.4
$CaSO_4$	$MgSO_4 \times 1\ H_2O$	15.8	4.00	4.0	$MgSO_4 \times 1\ H_2O$	17.8	4.05	**4.4**
$Mg(ClO_4)_2$	$NaClO_4$	5.2	3.20	1.6	$NaClO_4$	11.7	3.73	3.1
$MgCl_2$	$CaCl_2$	4.4	2.44	1.8	$CaCl_2$	4.5	3.34	1.4
$MgCO_3$	NaCl	2.9	0.58	5.0	NaCl	9.2	1.01	**9.1**
$MgSO_4 \times 1\ H_2O$	$MgSO_4 \times 7\ H_2O$	5.8	1.19	**4.9**	$MgSO_4 \times 7\ H_2O$	8.8	1.84	**4.8**
$MgSO_4 \times 7\ H_2O$	$MgSO_4 \times 1\ H_2O$	5.8	1.83	3.2	$MgSO_4 \times 1\ H_2O$	8.8	2.21	**4.0**
Na_2CO_3	$MgSO_4 \times 1\ H_2O$	13.2	1.75	**7.5**	$MgCO_3$	15.7	1.92	**8.2**
Na_2SO_4	$MgSO_4 \times 7\ H_2O$	17.6	5.75	3.1	$MgSO_4 \times 7\ H_2O$	17.9	5.83	3.1
$NaClO_4$	$Mg(ClO_4)_2$	5.2	2.30	2.3	$Ca(ClO_4)_2$	9.6	2.40	4.0
NaCl	$MgCO_3$	2.9	0.54	5.3	$MgSO_4 \times 7\ H_2O$	9.2	1.11	8.3
Raman+LIBS								
$Ca(ClO_4)_2$	$Mg(ClO_4)_2$	22.1	6.83	**3.2**	$Mg(ClO_4)_2$	27.3	7.33	**3.7**
$CaCl_2$	$MgCl_2$	23.1	2.21	**10.4**	$MgCl_2$	28.0	3.18	**9.0**
$CaCO_3$	Na_2CO_3	51.9	5.18	**10.0**	Na_2CO_3	55.0	5.79	**9.5**
$CaSO_4$	$MgSO_4 \times 1\ H_2O$	36.1	8.60	**4.2**	$MgSO_4 \times 1\ H_2O$	39.9	9.43	4.2
$Mg(ClO_4)_2$	$Ca(ClO_4)_2$	22.1	6.27	**3.5**	$Ca(ClO_4)_2$	27.3	7.46	**3.7**
$MgCl_2$	$MgCO_3$	19.3	4.28	**4.5**	$MgSO_4 \times 7\ H_2O$	24.5	5.50	**4.4**
$MgCO_3$	$MgSO_4 \times 7\ H_2O$	12.6	1.95	**6.5**	$MgSO_4 \times 7\ H_2O$	19.2	2.65	7.2
$MgSO_4 \times 1\ H_2O$	$MgSO_4 \times 7\ H_2O$	11.8	2.86	4.1	$MgSO_4 \times 7\ H_2O$	14.9	3.66	4.1
$MgSO_4 \times 7\ H_2O$	$MgSO_4 \times 1\ H_2O$	11.8	3.66	3.2	$MgSO_4 \times 1\ H_2O$	14.9	4.37	3.4
Na_2CO_3	NaCl	23.8	7.29	3.3	NaCl	35.1	8.03	4.4
Na_2SO_4	NaCl	37.3	10.52	**3.5**	NaCl	39.8	11.72	**3.4**
$NaClO_4$	$Mg(ClO_4)_2$	32.9	4.72	**7.0**	$Ca(ClO_4)_2$	36.7	5.02	**7.3**
NaCl	Na_2CO_3	23.8	3.04	**7.8**	$MgCO_3$	34.5	3.57	**9.7**

6 PCs

- The largest q ratio is given by the Raman only model for 3 samples and by the Raman+LIBS model for 10 samples
- The average q ratio of Raman+LIBS model (5.5) is larger than that of the Raman only model (3.9)
- The medians of the q ratios are 4.2 and 4.0 for the combined and the Raman only model, respectively.

10 PCs

- Largest q ratio given by the Raman only model for 5 samples and by the Raman+LIBS model for 8 samples
- The average q ratio of Raman+LIBS model (5.7) is larger than that of the Raman only model (4.8)
- The medians of the q ratios are 4.4 and 4.0 for the combined and the Raman only model, respectively.

From the direct comparison of cases with larger q ratios and from the average values, the combined model reveals a better clustering. However, the median values indicate a large variety of the q values among the samples and show no significant difference between the two models. Thereby, no general conclusion can be obtained since the clustering strongly depends on the sample and changes with the dimensionality of the models in both directions, meaning both improvement and degradation. In particular for the Raman only model, no significant improvement of the clustering capability due to the data fusion with LIBS spectra was observed, although the combined model provides the larger q ratios for more samples.

9.4.4 Partial least squares discriminant analysis

In the next step prior knowledge about the samples was incorporated in PLS-DAs of all samples and with different groupings as input. Analyses were performed including information about class memberships corresponding to the anions, the cations, and the single samples. An overview of the three groupings is given in Table 9.5. Like the PCA, the PLS-DA models were validated with a full cross-validation.

For PLS-DA, the prediction error or RMSE is not only a figure of merit but also an indicator for the best suited number of LVs, as introduced in Section 4.2. I determined the RMSE for all scenarios, but present here only selected plots, see Figure 9.13, in order to keep clarity. The RMSE is shown with increasing number of LVs. The plots include the prediction errors of LIBS and Raman models once with the cation groups as input and once with the anion groups. The prediction errors for the single sample groups are shown only for the combined Raman+LIBS model. The RMSEs are plotted including 16 LVs, although more LVs than the number of samples are meaningless. However, the higher dimensions are shown to better visualize trends of the RMSEs. In case of the LIBS model, the RMSE of anion groups shows neither a step nor are they converging. On the contrary, the prediction errors of the cations have clear steps, i.e. no change with increasing number of LVs, already after four LVs. For the Raman model, the situation is different as the RMSEs reach minima for the anion grouping while a continuous decrease for the cation grouping can be observed. This indicates what has

Table 9.5: Groups and their members for PLS-DA. For readability, hydration states are not shown except for $MgSO_4$ because of the two different hydration states.

PLS-DA grouping	Groups	Members
Cation grouping	Ca	$Ca(ClO_4)_2$, $CaCl_2$, $CaCO_3$, $CaSO_4$
	Mg	$Mg(ClO_4)_2$, $MgCl_2$, $MgCO_3$, $MgSO_4\times 1\,H_2O$, $MgSO_4\times 7\,H_2O$
	Na	Na_2ClO_4, NaCl, Na_2CO_3, Na_2SO_4
Anion grouping	Cl	$CaCl_2$, $MgCl_2$, NaCl
	ClO_4	$Ca(ClO_4)_2$, $Mg(ClO_4)_2$, Na_2ClO_4
	CO_3	$CaCO_3$, $MgCO_3$, Na_2CO_3
	SO_4	$CaSO_4$, $MgSO_4\times 1\,H_2O$, $MgSO_4\times 7\,H_2O$, Na_2SO_4
Sample grouping	each sample	the particular sample

already been observed: The Raman data contains mainly information about the anion and the LIBS data about the cation. Regarding the combined model, almost all samples have prediction errors that show a step-like trend appearing at different numbers of LVs. From this, it can be concluded that almost every LV correlates with one single sample, similar to what was observed in the PCA before.

As already done for the previous PCAs, I will discuss the explained variance for the different PLS-DA models in the following to obtain further evidence for optimal numbers of LVs and to analyze which information is given by each dataset. Figure 9.14 shows the plots of the explained variances with increasing number of LVs for all three input groups and for all three datasets. Regarding the single sample groups (Figure 9.14, *left*), the Raman and the Raman+LIBS explained variance curves are almost the same except after twelve LVs where the Raman+LIBS curve shows a clear step followed by convergence, while the step is softer for the Raman model. The accumulated explained variance obtained from the LIBS model increases beyond the number of samples and still reaches a lower total than the other two models. Regarding the cation groups for PLS-DA (Figure 9.14, *middle*), the explained variances of the LIBS and the combined model behave similar. Both reveal a strong increase within the first two LVs up to almost 90 %, followed by a small increase which evolves into convergence. The curve of the Raman model is below the other two curves but also with a transition between increase and convergence for higher LVs, however, this transition is less explicit as for the other two models. With the anion grouping as input, the explained variance of the Raman and the combined model are similar (Figure 9.14, *right*). Both start with a steep increase that evolves into a less steep one followed by convergence. The transition takes place with five LVs, which coincides almost with the number of different anions that is four. For both summarized input groups by which the cation or anion groups are meant, it turns out that the combined model follows a similar trend as the model of the appropriate technique (LIBS model for cations and Raman model for anions). This can be described as an adaptive behavior and shows the capability of the combined model to select important features from both datasets to best describe the given response variables of the samples.

Next, the prediction errors of each model were analyzed to evaluate their classification capability. The RMSEs are listed in Table 9.6 where only the minimum, the maximum, and the average are shown in order to keep clarity. Regarding the prediction errors (Figure 9.13) and the explained variances (Figure 9.10), the RMSEs were determined of models with twelve LVs for all sample groups as input and with six LVs for the summarized input groups. Similar

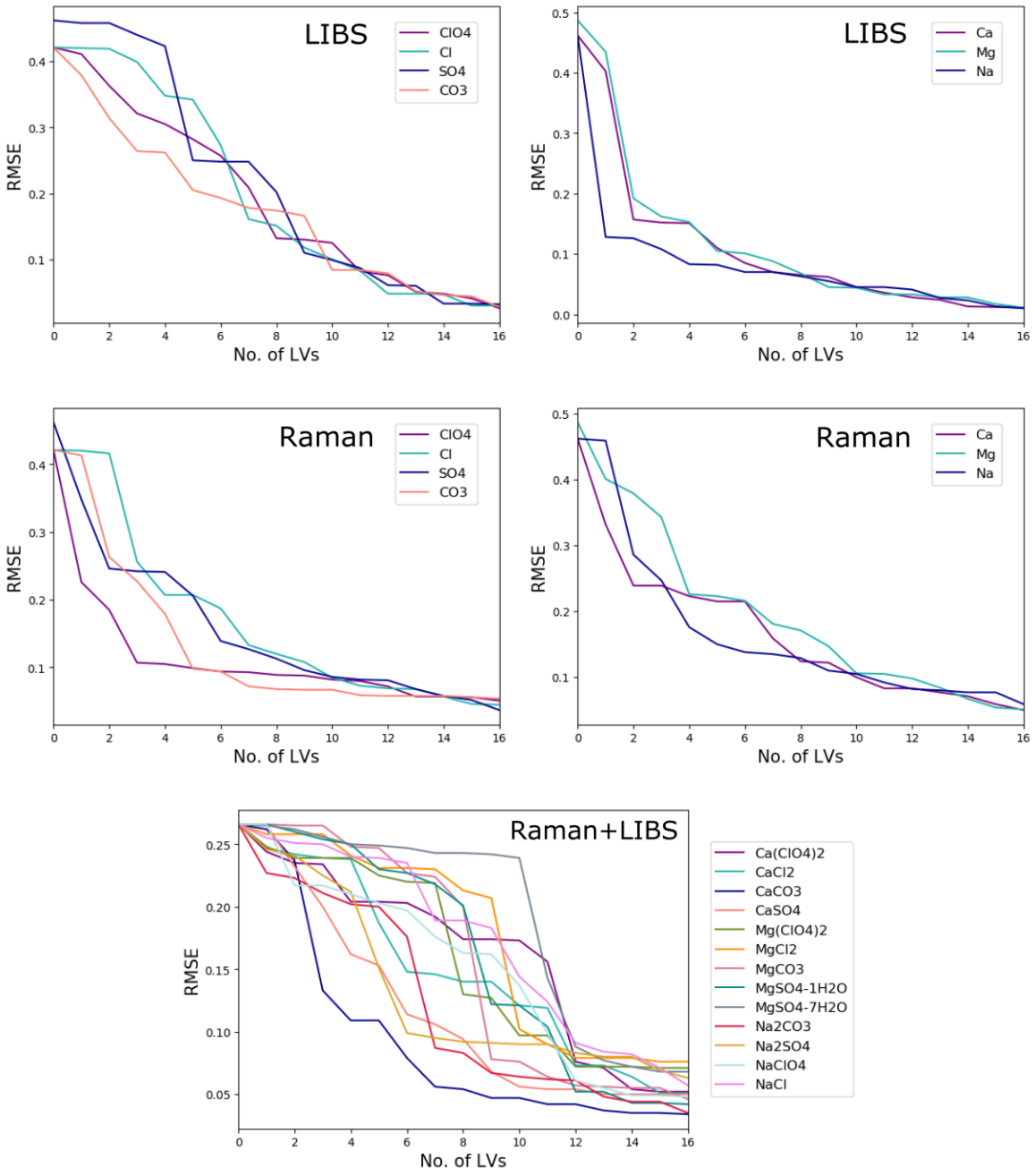

Figure 9.13: Trend of RMSE with increasing number of LVs for various PLS-DA models with different response variables. *Top row*: LIBS model with anion (*left*) and cation (*right*) grouping. In contrast to the cation groups, the RMSE does not converge for the anion groups as input. *Middle row*: Raman model with anion (*left*) and cation (*right*) grouping, where a convergence for the anion response variables is observable. *Bottom*: RMSE of the combined model with the single sample groups as input. Step-like drops occur for almost each sample at a different number of LVs.

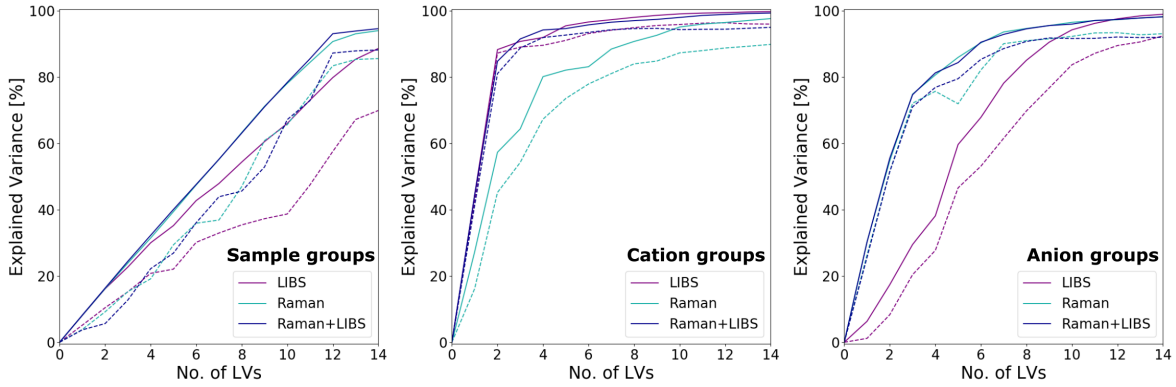

Figure 9.14: Explained accumulated variances of the PLS-DA models with different groupings as input. Solid lines correspond to the model and the dashed lines to the validation. *Left*: Single samples as groups were given to the PLS-DA, the number of LVs that is needed to reach the plateau is similar to the number of sample groups. *Middle*: Three groups corresponding to the cations were given as input, the Raman+LIBS model follows the LIBS model. *Right*: For the four anions, four groups were given to the model. The Raman+LIBS curve has a similar trend as the Raman curve.

Table 9.6: RMSE-C and RMSE-CV for the different groupings and datasets in PLS-DA. Not all results are shown but the minimum, maximum, and average values. Note that models with different numbers of LVs were used for the single sample grouping and the anion/cation grouping.

	Calibration			**Validation**		
Dataset	min [%]	max [%]	average [%]	min [%]	max [%]	average [%]
Sample grouping (12 LVs)						
LIBS	$MgCl_2$	$MgSO_4 \times 1H_2O$		Na_2CO_3	$MgSO_4 \times 1H_2O$	
	7.1	17.4	11.6	12.4	23.0	17.3
Raman	Na_2CO_3	$MgSO_4 \times 7H_2O$		Na_2CO_3	$MgSO_4 \times 7H_2O$	
	3.4	13.6	7.5	4.4	18.3	10.2
Raman+LIBS	$CaCO_3$	NaCl		$CaCO_3$	$MgSO_4 \times 7H_2O$	
	4.2	9.1	6.8	5.4	12.7	9.4
Anion grouping (6 LVs)						
LIBS	CO_3^{2-}	Cl^-		CO_3^{2-}	Cl^-	
	19.3	27.3	24.3	23.7	33.9	29.8
Raman	CO_3^{2-}, ClO_4^-	SO_4^{2-}		ClO_4^-	SO_4^{2-}	
	9.4	18.7	12.8	10.5	24.8	17.8
Raman+LIBS	CO_3^{2-}	SO_4^{2-}		ClO_4^-	SO_4^{2-}	
	7.5	17.7	12.7	11.4	22.6	16.1
Cation grouping (6 LVs)						
LIBS	Na^+	Mg^{2+}		Na^+	Mg^{2+}	
	7.0	10.1	8.5	9.3	14.9	12.3
Raman	Na^+	Mg^{2+}		Na^+	Mg^{2+}	
	13.8	21.6	18.9	17.3	25.3	22.2
Raman+LIBS	Na^+	Mg^{2+}		Na^+	Mg^{2+}	
	8.3	10.5	9.6	9.7	13.7	12.0

to the distance and spread analysis of the PCA models, the RMSEs of PLS models should only be compared when the models were computed with the same number of LVs. Besides the RMSE of the calibration model (RMSE-C) the RMSE of the validation is given (RMSE-CV).

With the sample groups as input all datasets reach on average a RMSE-C below 12 % whereof the Raman and the Raman+LIBS model have even smaller values. The combined model has the better prediction capability of single sample groups with 6.8 % in comparison to the Raman model with 7.5 %. Additionally, the range between the minimum and maximum RMSE-C is smaller for the combined model. However, the difference of the RMSE-C between the Raman and the combined model is not significant enough to generally conclude that the combined model has the better classification capability. The average RMSE-CV of the LIBS model strongly differs from the RMSE-C which indicates that the LIBS data has no information that can be linked to the sample groups or in other words, it cannot differentiate between the single samples. This is not surprising as already in the LIBS spectra (Figure 9.8) no clear evidence for the elements of the polyatomic anions was observed. However, the discrepancy between the RMSE-C and RMSE-CV of the LIBS model emphasizes this observation and serves as an example how important it is to carefully chose which information fits to the appropriate data as input for PLS-DA. Also, for the other two models the RMSE-CVs are larger than the RMSE-Cs but to a smaller extent. Under those circumstances, the Raman and the combined model spectral data has information that can be related to single samples. For some of them the corresponding spectral features are more explicit than for the others. That is why the RMSEs generally differ between the samples.

In case of the anion class membership, the LIBS model again is not able to identify spectral characteristics that correlate with the given information which can be seen by the large prediction errors for the anions. On the other hand, the Raman and the combined model have prediction errors between 7.5 % and 18.7 % which reveals a good prediction capability. Nevertheless, discrepancies between the RMSE-C and the RMSE-CV become apparent which suggests that either six LVs might not be sufficient or that spectral differences inside the anion groups hamper their classification. Since the Raman model reaches good prediction errors for the single samples it might rather have the capability to distinguish the sample at this level than the anion.

Going further to cation groups as classification information, the LIBS model shows its distinct capability to distinguish and predict the type of cation. The RMSE-C is on average 8.5 % and the RMSE-CV 12.3 % which is a good result in the framework of this study. This time, the prediction errors of the Raman model exceed the ones of the other two models. This shows again that no proper predictions can be made, when no evidence is given in the spectra. In both cases of summarized groupings, the adaptive behavior already discussed for the explained variance of the combined model can be observed. In the cation case, the RMSEs of the combined model are close to the values of the LIBS model while they are even smaller but in the same range as for the Raman model in the anion case.

Besides the prediction errors, the actual predictions are a figure of merit. Again, only a selection of prediction plots is shown in order to keep clarity but to give an impression of the predictions. Thus, for each model their "best case" is shown in Figure 9.15 where a prediction of 1 indicates class membership and 0 the contrary. The LIBS model with given cation groups predicts every salt correctly, as almost all samples are predicted with values between 0.8 and 1.2 for their actual class and values below 0.2 for classes the sample does not belong to. The

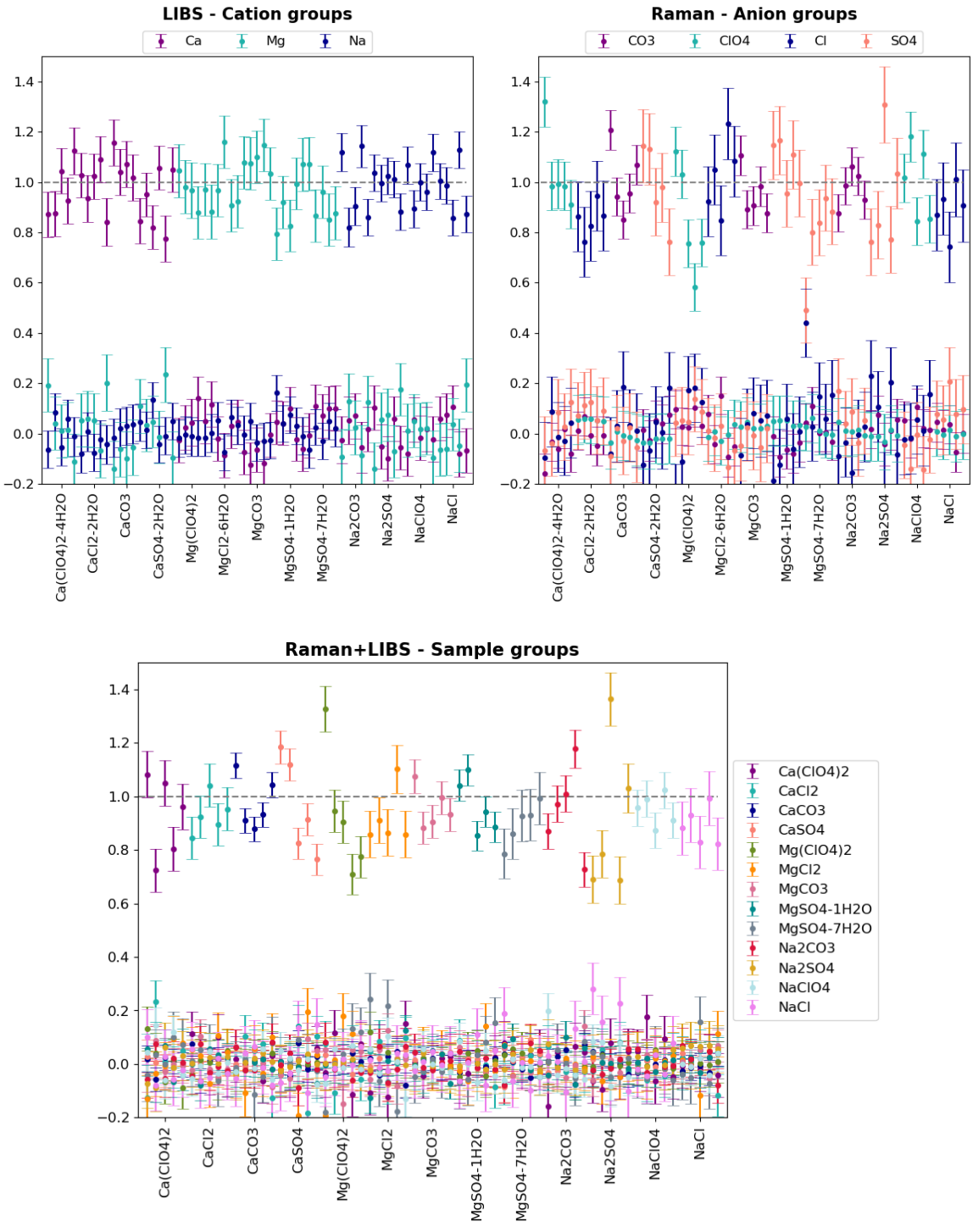

Figure 9.15: Predictions from PLS-DA with different classification information. Ideally, salts should obtain a 1 for their actual class and a 0 for the other classes. Shown are the prediction values of one input class for each model. The LIBS and the Raman models have six LVs while the combined model was built with twelfe LVs.

predictions of the Raman model fluctuate more but also here, almost all salts have predictions between 0.7 and 1.2 for their particular anion. Additionally, the salts that do not provide the actual anion have predictions below 0.3 and only one case is not unambiguous, see the first measurement of $MgSO_4 \times 1\,H_2O$. The predictions of single sample groups provided by the Raman+LIBS model are successful, too. Although the predictions for some salts drop below 0.7, the distinction to the prediction values from salts outside of the class is unambiguous.

9.4.5 Concepts of high-level data fusion

In this section, I tested two different approaches of high-level data fusion with the Raman and LIBS data of the salt/basalt mixtures. The first is based on PCA models and distance calculations while the second uses the similarity rates based on Pearson correlation coefficients between the spectra. For the distance calculations, I considered also the Mahalanobis distance next to the previously used euclidian distance. Both approaches for classification follow the proposed strategy to identify the salt's cation with the LIBS spectra and the anion with the Raman spectra, separately.

PCA models and distances

Here, two PCA models with 10 of the 13 samples were computed from the LIBS and the Raman data, respectively. For the first set (set 1), the samples that do not contribute to the model (model 1) are $CaCl_2 \times 2H_2O$, $MgCO_3$, and Na_2SO_4 while for the second set (set 2) $CaCO_3$, $MgSO_4 \times 1H_2O$, and $NaClO_4$ were left out in the model (model 2). These selections of sample sets were made in order to leave out each cation in each model once and to further leave each anion out at least once in both models. As only 13 samples were available for this study, two sets were studied in order to derive more general observations. Since the LIBS PCA model is used for cation identification and the Raman PCA model for anion identification, the selected sets ensure that nothing "unknown" has to be predicted as both models comprise all anions and cations. This is important as PCA models can not predict sample characteristics which are not incorporated by the models.

Score plots of PC 1/PC 2 and PC 3/PC 4 for model 1 and model 2 of the LIBS data and of the Raman data are shown in Figure 9.16 and in Figure 9.17, respectively. The center of the scores coordinates from samples with the same anion (Raman model) or the same cation (LIBS model) were determined. In the next step, the data of the samples that were not accounted for in the PCA models was projected into the models, see also Figure 9.16 and 9.17. For identification, the euclidian distance d_{eucl} (9.1) of every projected spectrum to each cluster center of the cations in the LIBS model and the anions in the Raman model was calculated. In all calculations, I considered only the first four components. According to these euclidian distances, an automated routine finds the minimal distance and suggests by that the particular ion. This procedure was also done with a distance known as *Mahalanobis* distance d_{mahal} instead of d_{eucl} [De Maesschalck et al., 2000, Forni et al., 2013]. This distance accounts for covariances among the points that belong to one cluster. In other words, it accounts for the shape of a cluster that is often not sphere-like which is a drawback for the use of euclidian distances. The covariance matrix is defined by

$$Cov(\mathbf{X}) = E\left((\mathbf{X} - \mu)(\mathbf{X} - \mu)^T\right) = \mathbf{\Sigma} \tag{9.4}$$

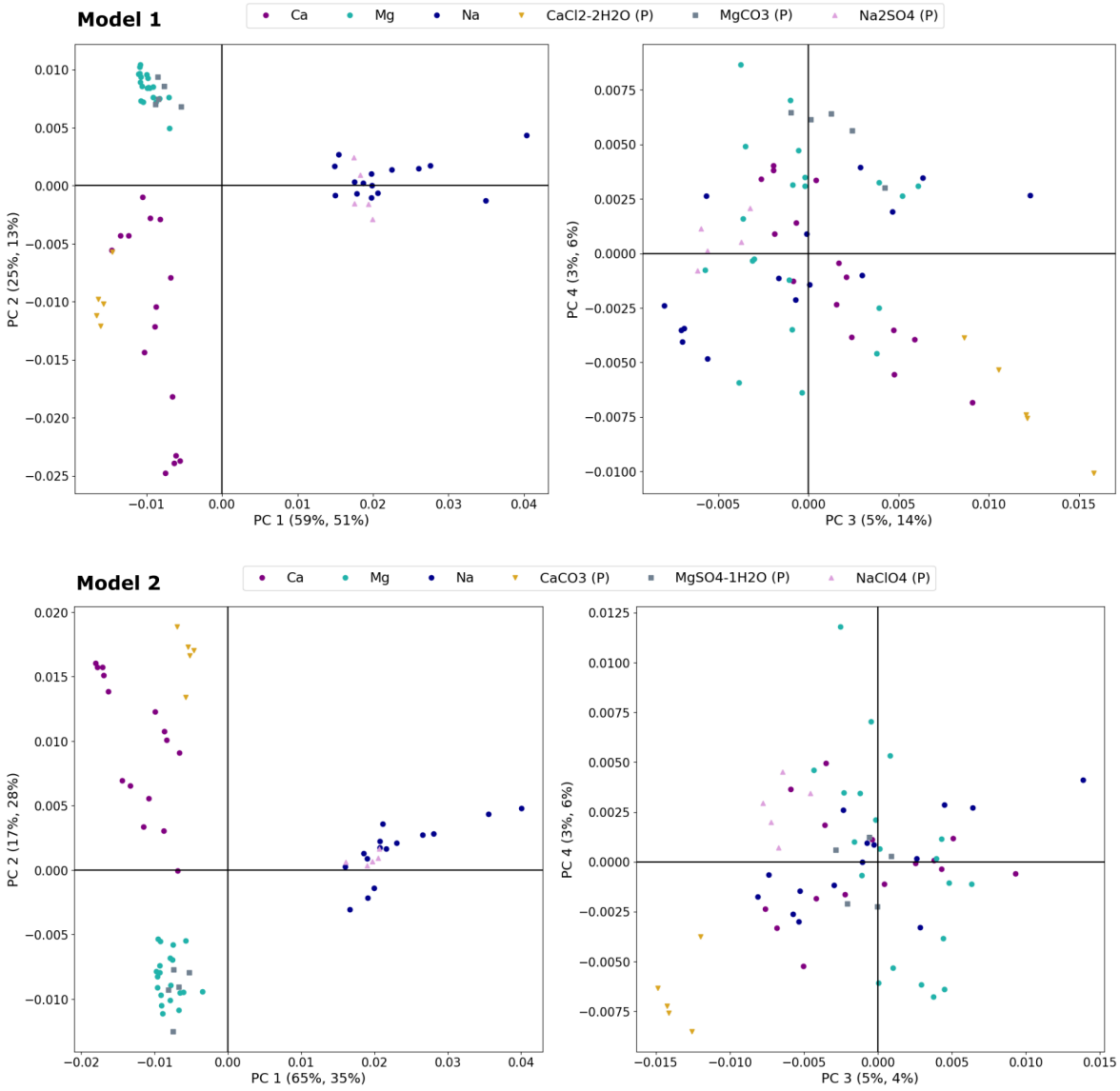

Figure 9.16: Score plots of LIBS PCA model 1 (*top*) and model 2 (*bottom*). The (P) label indicates the samples whose spectra were projected into the existing model. The explained variance by each component is given in brackets for the calibration model and for the projected spectra.

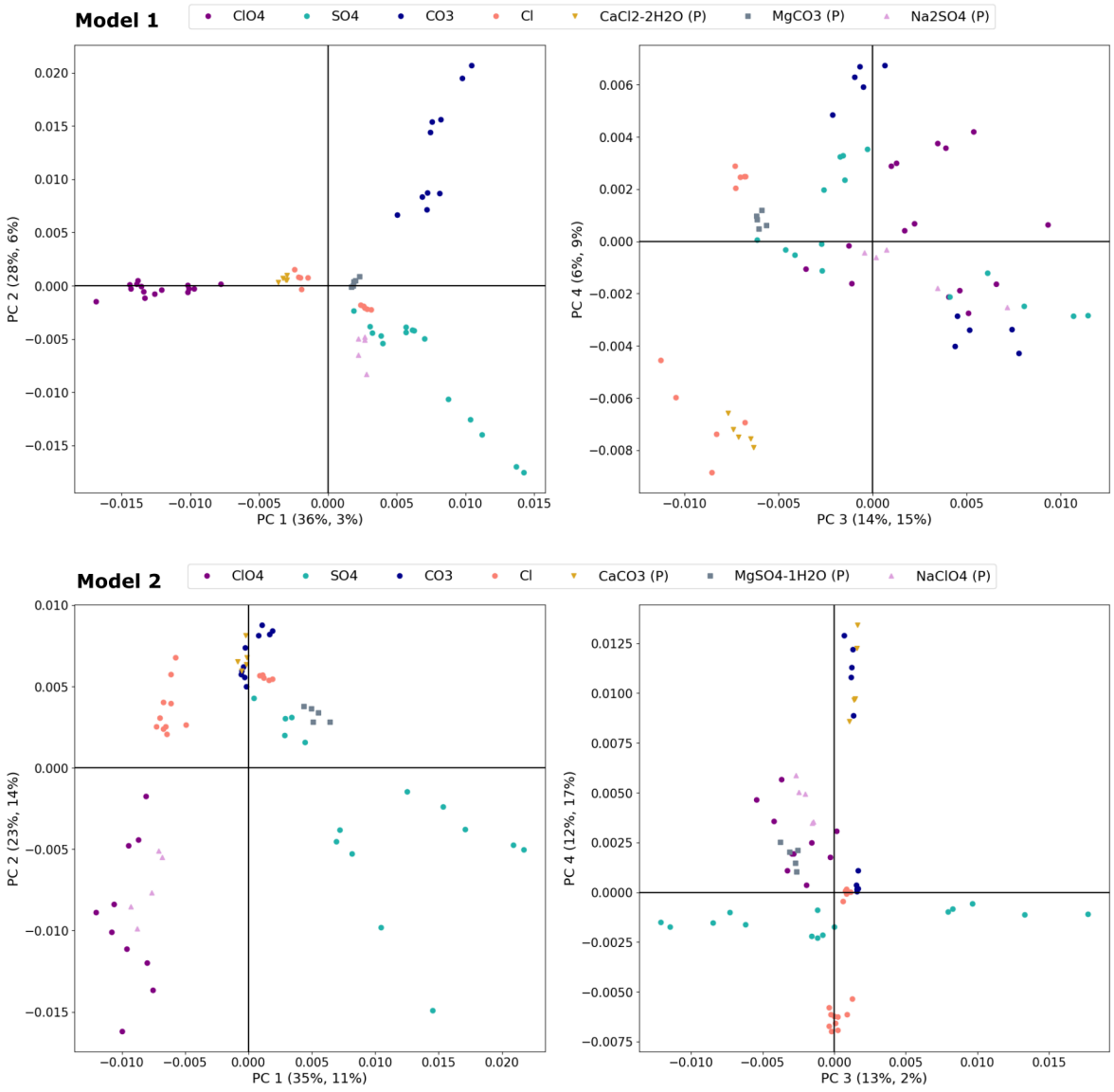

Figure 9.17: Score plots of model 1 and model 2 relying on the Raman spectra. The left-out samples which were projected into the models are labelled by (P). The values in brackets give the explained variance by the calibration model (first value) and the projected spectra (second value).

Table 9.7: Predictions of the ions that were automatically derived from the distance calculations of the projected samples in the PCA model 1 and model 2. Cation and anion predictions were derived from the LIBS and Raman models, respectively. Wrong identifications are marked in italic and were observed for the anion of $MgCO_3$, $CaCl_2 \times 2H_2O$, Na_2SO_4, and $MgSO_4 \times 1H_2O$.

Set 1						**Set 2**					
Sample	#	Cation		Anion		Sample	#	Cation		Anion	
		eucl	*mahal*	*eucl*	*mahal*			*eucl*	*mahal*	*eucl*	*mahal*
$CaCl_2 \times 2H_2O$	1	Ca	Ca	Cl	*ClO_4*	$CaCO_3$	1	Ca	Ca	CO_3	CO_3
	2	Ca	Ca	Cl	*ClO_4*		2	Ca	Ca	CO_3	CO_3
	3	Ca	Ca	Cl	*ClO_4*		3	Ca	Ca	CO_3	CO_3
	4	Ca	Ca	Cl	Cl		4	Ca	Ca	CO_3	CO_3
	5	Ca	Ca	Cl	Cl		5	Ca	Ca	CO_3	CO_3
$MgCO_3$	1	Mg	Mg	*Cl*	*SO_4*	$MgSO_4 \times 1H_2O$	1	Mg	Mg	*CO_3*	SO_4
	2	Mg	Mg	*Cl*	*SO_4*		2	Mg	Mg	SO_4	SO_4
	3	Mg	Mg	*Cl*	*SO_4*		3	Mg	Mg	SO_4	SO_4
	4	Mg	Mg	*Cl*	*SO_4*		4	Mg	Mg	*CO_3*	SO_4
	5	Mg	Mg	*Cl*	*SO_4*		5	Mg	Mg	*CO_3*	SO_4
Na_2SO_4	1	Na	Na	SO_4	SO_4	$NaClO_4$	1	Na	Na	ClO_4	ClO_4
	2	Na	Na	SO_4	*Cl*		2	Na	Na	ClO_4	ClO_4
	3	Na	Na	SO_4	*Cl*		3	Na	Na	ClO_4	ClO_4
	4	Na	Na	SO_4	*Cl*		4	Na	Na	ClO_4	ClO_4
	5	Na	Na	SO_4	*Cl*		5	Na	Na	ClO_4	ClO_4

where $\mathbf{X}$ is a random vector whose rows contain variables X_i that have an expectation value μ_i and a variance $Var(X_i) = \sigma_i^2$. The expectation values of the individual variables are stored in μ and E denotes the expectation value of the expression in brackets. Thus, the entries on the diagonal of the covariance matrix are the variances of $Var(X_i)$ and the off-diagonal entries are covariances of the different variables $Cov(X_i, X_j)$. The Mahalanobis distance between a cluster b and one variable a is given by

$$d_{mahal} = \sqrt{(a - \bar{b})^T \mathbf{\Sigma}^{-1} (a - \bar{b})} \tag{9.5}$$

where $\bar{b}$ represents the centroid of cluster b and $\mathbf{\Sigma}^{-1}$ is the inverse of the covariance matrix of b. In the present example, the clusters b are given by the known samples in the two described PCA models and d_{mahal} was calculated for every measurement of the unknown samples in the PCA space a to each cluster.

In Table 9.7, the outcomes of both sets for both kinds of distance are summarized. For all models, the number of PCs was set to four to enable comparison. Both LIBS models were able to correctly identify the cation of each salt independent on which distance type was used. With the Raman model, correct assignments of the anion were not reached for every spectrum. With the euclidian distance, all $MgCO_3$ and some of the $MgSO_4 \times 1H_2O$ were matched with a wrong anion. Regarding the score plots of the Raman models in Figure 9.17, a separation with respect to the anion is observable in the PC 1/PC 2 representation, but a clear cluster confinement and separation from the other spectra are not observable. Thus, it is not surprising that these particular models had trouble to correctly assign all anions with the euclidian distance which requires spherical cluster shapes. However, regarding the Mahalanobis distances, the anion identification in model 1 is only correct for three measurements ($2 \times$ Cl, $1 \times SO_4$). By contrast, in Raman model 2, all anions were correctly identified by d_{mahal}. To conclude, the

different distances give indeed different results for the Raman models, but none of them is better suited in the framework of this study. Additionally, the explained variance (given in Figure 9.17 in brackets) of the left-out samples strongly deviates from the one of the calibration models. This indicates that the built models are not able to explain the data of the left-out samples. Moreover, a Raman model might be more capable to identify single samples which means on the other hand that more samples are needed to calibrate or train multivariate models for identification purposes. One has to mention here that also the explained variances of the LIBS models and the projected LIBS spectra differ (Figure 9.16 in brackets) but not as much as for the Raman models.

Correlations between spectra as measure of similarity

As another approach of high-level data fusion for the identification of the salt in basalt, the Pearson correlation coefficient r was used as an indicator of the similarity rate between spectra. This approach was inspired by [Moros et al., 2018] where similarity rates between Raman spectra were employed in a decision tree concept for high-level data fusion of LIBS and Raman data from Mars relevant minerals. The objective of the present high-level data fusion approach is to identify the cation of an unknown salt by LIBS spectra and the anion by Raman spectra of known samples. Therefore, r is calculated pairwise between all "known" spectra and the one "unknown" spectrum. For this study, r values between the spectra of the samples that were treated as unknowns in set 1 and set 2 from the PCA distance analysis above and the spectra of the remaining samples were calculated, respectively. Exemplarily, the outcomes for one measurement of the unknown sample Na_2SO_4 of set 1 are shown in Figure 9.18. Here, the similarity rates of the particular Na_2SO_4 LIBS and Raman spectrum between the known spectra of set 1 are shown, respectively. They are ordered from the most to the least similar spectrum and the first five spectra with the highest r values were used to derive the cation and the anion of the salt. The five Raman spectra with the highest correlation are provided by sulfates, see Figure 9.18 (*box in upper plot*), leading to the correct anion identification of sulfate. The same proceeding, but this time for cation identification, was done with the LIBS spectra resulting in the correct identification of Na, see Figure 9.18 (*box in bottom plot*). In this way, all unknown spectra were compared to the known spectra with the purpose to identify the cation and the anion separately. For the unknown samples of set 1, the five highest Pearson correlation coefficients of the five most similar LIBS and Raman spectra, respectively, are given together with the derived ion identification in Table 9.8.

As a general observation, the similarity rates between the LIBS spectra were higher than between the Raman spectra. A step in the correlation coefficient plot of the LIBS spectra (Figure 9.18, *bottom*) according to the salts with Na is observable. Such a step (for some samples even two steps according to the cations) appears also in all other LIBS spectra comparisons (not shown here). This clear distinction between the cations allowed for correct cation identifications of all "unknown" samples of both sets, see for set 1 Table 9.8. To conclude, a differentiation between the cations is possible in this study due to the similarity of LIBS spectra. On the other hand, the correlation coefficients of the Raman spectra do not show such a clear discrimination between the anions. The anion of the left-out samples of set 2 were all correctly identified according to the correlation coefficients between the Raman spectra. However, the identification of the carbonate anion of $MgCO_3$ in set 1 failed, see Table 9.8

Similar to the outcomes of the PCA distance study of set 1 and set 2, it was observed that

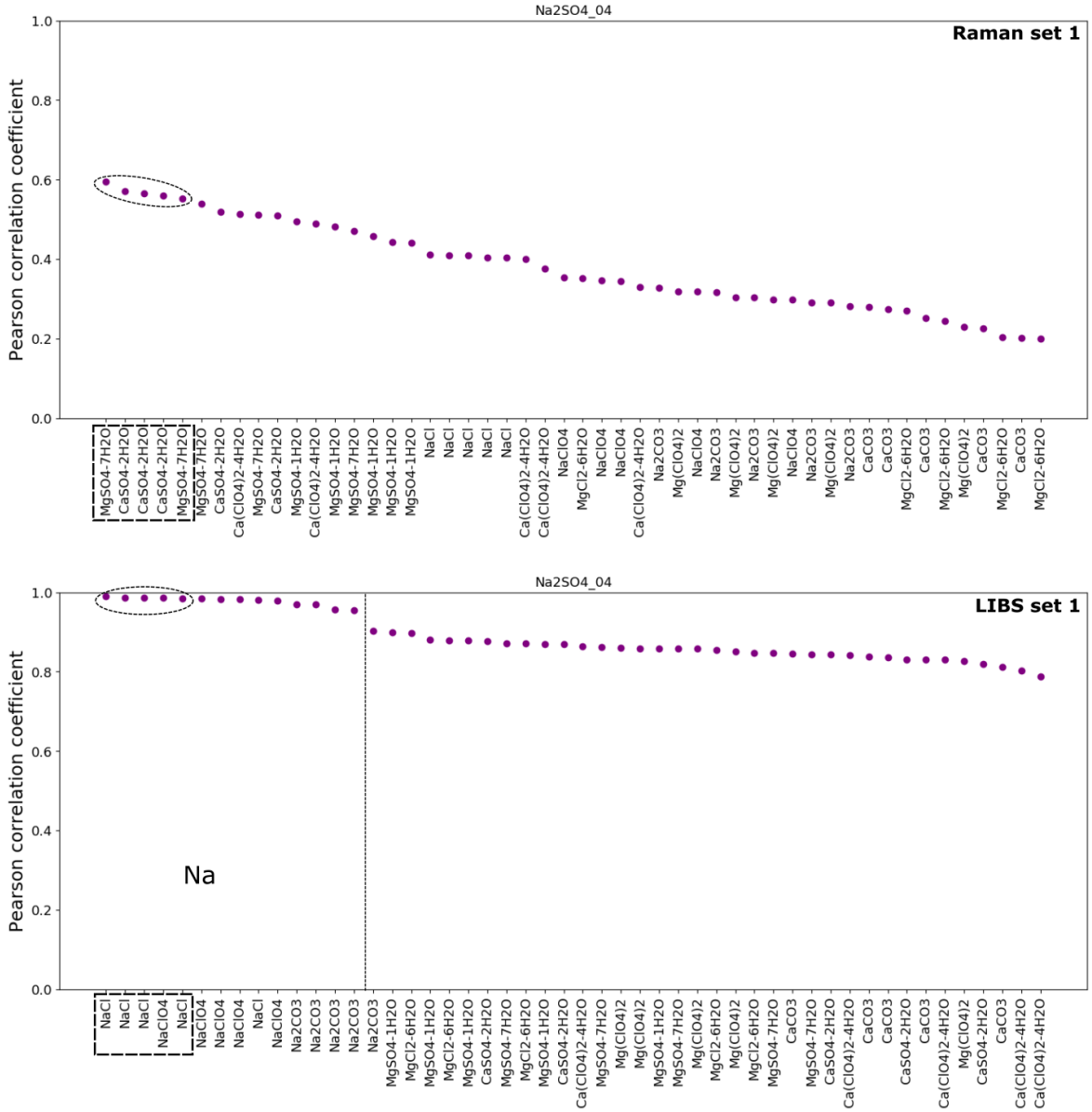

Figure 9.18: Pearson correlation coefficients between one particular spectrum of an "unknown" sample of set 1 and all spectra of the "known" samples. The five most similar spectra that were considered for the identification are marked with an ellipse. *Top*: Raman spectra comparison of one spectrum from Na_2SO_4, the samples with the most similar spectra are sulfates, too. *Bottom*: Example of LIBS spectra comparison where a segment according to the Na cation becomes apparent.

Table 9.8: Model 1 identifications of the ions due to similarity of the LIBS and the Raman spectra, respectively. The values in brackets are the Pearson correlation coefficients between the spectrum and the five most similar spectra. Anions in bold denote correct assignments.

Sample	#	Most similar **LIBS**	Most similar **Raman**
$CaCl_2 \times 2H_2O$	1	**Ca** (0.97; 0.97; 0.97; 0.96; 0.96)	**chloride** (0.67; 0.67; 0.66; 0.52), perchlorate (0.51)
	2	**Ca** (0.95; 0.95; 0.94; 0.94; 0.94)	**chloride** (0.68; 0.68; 0.65; 0.59; 0.54)
	3	**Ca** (0.96; 0.96; 0.96; 0.96; 0.95)	**chloride** (0.68; 0.67; 0.63; 0.54; 0.50)
	4	**Ca** (0.96; 0.96; 0.95; 0.95; 0.95)	**chloride** (0.73; 0.73; 0.72; 0.58), perchlorate (0.53)
	5	**Ca** (0.95; 0.95; 0.94; 0.94; 0.94)	**chloride** (0.71; 0.71; 0.70; 0.60; 0.54)
$MgCO_3$	1	**Mg** (0.98; 0.98; 0.98; 0.98; 0.98)	sulfate (0.62; 0.62; 0.60), chloride (0.63; 0.60)
	2	**Mg** (0.99; 0.98; 0.98; 0.98; 0.98)	sulfate (0.66; 0.63; 0.65), chloride (0.65; 0.63)
	3	**Mg** (0.99; 0.99; 0.98; 0.98; 0.98)	sulfate (0.68; 0.64),chloride (0.65; 0.64; 0.63)
	4	**Mg** (0.98; 0.98; 0.98; 0.98; 0.98)	sulfate (0.66; 0.63; 0.61), chloride (0.64; 0.61)
	5	**Mg** (0.98; 0.98; 0.98; 0.97; 0.97)	sulfate (0.66), chloride (0.65; 0.64; 0.64; 0.63)
Na_2SO_4	1	**Na** (0.99; 0.99; 0.99; 0.99; 0.99)	**sulfate** (0.65; 0.64; 0.62; 0.64; 0.63)
	2	**Na** (0.99; 0.99; 0.99; 0.99; 0.99)	**sulfate** (0.64; 0.62; 0.61; 0.63; 0.62)
	3	**Na** (0.99; 0.99; 0.99; 0.99; 0.99)	**sulfate** (0.55, 0.49; 0.53; 0.53; 0.52)
	4	**Na** (0.99; 0.99; 0.99; 0.99; 0.99)	**sulfate** (0.67; 0.66; 0.64; 0.66; 0.65)
	5	**Na** (0.99; 0.99; 0.99; 0.99; 0.98)	**sulfate** (0.60; 0.55; 0.57; 0.56; 0.56)

the cation identification with the LIBS data is straightforward. On the contrary, the Raman data does not provide correct anion identification for all samples. This might be caused by the differences in the Raman spectra within one group of samples with the same anion. In other words, similarities between Raman spectra might not be ensured although the particular salts have the same anion. A larger set of samples for comparison could compensate for this as similarities between samples with the same anion would be more contrasted.

9.5 Summary and conclusion

Concepts of LIBS and Raman data fusion were evaluated by means of identification capabilities when using miniaturized instruments and multivariate data analysis methods. For this study, I investigated two sets of samples, sulfates and binary mixtures of them, and Mars relevant salts in a basaltic matrix. Mainly low-level data fusion was applied but also high-level data fusion approaches were tested. MVA techniques, namely PCA and PLS-DA, were employed for the analysis where clustering in the PCA models was assessed with distances and spreads.

In the PCA study of the binary sulfate mixtures, the objective was to test the capability of identifying mixtures, however, the outcomes show that also quantification is possible in some cases although the PCA models were built from data of only five pure sulfate samples. Regarding the clustering, distance and spread calculations demonstrated a good confinement and separation ratio of the pure sulfate clusters in all three models. In comparison of the Raman and LIBS only models with the combined model, the best cluster confinement based on the distance to spread ratio was given either by the Raman or the LIBS only model. The cluster spreads increased in the combined model compared to the Raman model indicating that the combined model is influenced by the larger fluctuations in the LIBS data. However, due to the distances between mixtures and pure sulfates clusters, identification of several mixtures was possible where the data fusion led to a moderate improved identification capability.

Both PCA and PLS-DA models from the salt/basalt mixtures showed that the major information in LIBS and Raman data indeed is about the cation and the anion of the salt, respectively. More differentiating information was provided by the Raman data which was then adapted by the combined model. As the three datasets are quite different, they were not best described by the same number of components in the MVA models. In order to be able to compare the classification capabilities of the models a fixed number of components had to be chosen. Fixing the models with six and ten PCs showed that the combined model has a better clustering in PCA based on the distance to spread ratio. In PLS-DA, smaller prediction errors were obtained from the combined model on average. When grouping based on the anion and the cation was used, the smallest RMSEs were provided by the Raman only and the LIBS only model, respectively. But these were closely followed by the values of the combined model indicating the capability of PLS-DA models to select the relevant features which best match the response variables. The approaches of high-level data fusion have further shown the LIBS and Raman capabilities for cation and anion identification, respectively. However, the Raman analysis led to a few incorrect identification which is most likely due to differences in the Raman spectra within groups of the same anion.

In summary, low-level data fusion of LIBS and Raman spectroscopy has shown improvements in comparison to the individual models. However, these improvements are not significant regarding the increased dataset due to the data fusion. Next to the size of the datasets, the complexity of the data is increased and MVA models for the combined data have to describe two physical phenomena in one model. In consequence, particular benefits of the single models do not contribute anymore to the combined model.

In high-level data fusion, the focus is on the actual capabilities of the single techniques which was in this study the identification of cations by LIBS and anions by Raman spectroscopy. The tested approaches are promising, although the anion identification with Raman data was not always correct. To improve this, larger sample sets for training of MVA models would be required.

10 Summary and outlook

The focus of this thesis is on data analysis techniques for LIBS and Raman spectroscopy for the in-situ exploration of extraterrestrial bodies. Most of the studies were done in the context of Mars exploration but also one study relevant for the exploration of bodies without an atmosphere, e.g., asteroids or moons was addressed. Different methods and data analysis techniques were evaluated, ranging from normalization approaches over MVA to data fusion techniques. For the studies, different setups were employed: (a) LIBS setup with an echelle spectrometer, covering a broad spectral range with high spectral resolution and the capability for time-resolved measurements with an ICCD and a confocal continuous wave Raman microscope – both are high-performance and with dimensions that are rather unrealistic for a space flight instrument; and (b) LIBS and Raman setups made of miniaturized components with dimensions suitable for space instruments and reduced but more realistic performance.

In total, four studies were presented which are in particular: (1) normalization of LIBS data by plasma parameters; (2) LIBS characteristics in low pressure environments; (3) identification and quantification of fluorine, chlorine, and phosphorus with the help of molecular emission; and (4) LIBS and Raman data fusion. In (3) and (4), MVA techniques were applied. The outcomes of these four studies are summarized in the following.

(1) For reliable comparison of LIBS data from different targets and for accurate quantification, normalization is necessary, especially, when the experimental conditions are not completely controllable like on robotic missions. There are many different normalization approaches but none of them has proven to be universally applicable. In terrestrial applications, it was shown that plasma parameters, in particular the temperature T and the electron density n_e, correlate with signal fluctuations and can be used for normalization [Panne et al., 1998]. This type of normalization was investigated and evaluated for a possible application to Martian LIBS data. The derivation of plasma parameters from spectral data is a widely investigated topic in the LIBS community [Hahn and Omenetto, 2012]. Most of the approaches rely on the assumption that the plasma is in LTE. In LTE, the Boltzmann relation for excitation and the Saha-Eggert equation for ionization are valid and can be used to derive the plasma temperature. This requires, however, time-resolved LIBS data with rather short integration times. The electron density n_e can be calculated from Stark broadening, i.e. the width of emission lines.

To evaluate if normalization with plasma parameters is useful for Martian LIBS data, three different scenarios were investigated: (i) measurement-to-measurement fluctuations at constant experimental parameters; (ii) normalization of emission lines contributing to linear calibration curves for which different sample matrices were used; (iii) varying experimental conditions, in particular, changing laser irradiance realized by changing the laser pulse energy. In all experiments, time-resolved LIBS spectra with integration time windows of 500 ns were measured starting 350 ns after plasma initiation. Iron and silicon are abundant on Mars and both elements appear in most of the Martian LIBS data. It was therefore decided to

test the iron and silicon emission lines (neutral and ionic) for their suitability to derive the plasma temperature for normalization. Moreover, the emission of magnesium, aluminum, and calcium was tested with the two-line method which also relies on LTE. Correlations between emission lines and plasma parameters, the linearity of calibration curves, and RSDs before and after normalization were analyzed. Different derivations of the plasma parameters from the spectral data were tested and compared, evaluating the accuracy, applicability to Martian data, and the complexity of the approach. For example, a different behavior of emission lines of different ionization stages was observed with varying laser energies. A correlation between ionic emission lines and the plasma temperature derived with Saha-Boltzmann plots was found with varying laser energies. However, this is not the case for the emission lines of neutrals.

In summary, for the LIBS data obtained in Martian atmospheric conditions it was found that temperatures derived from different elemental emission lines are correlated either weakly or not at all with emission lines of the particular element and also not with signals from other elements. The weak correlations were not sufficient to significantly reduce the RSD. One explanation is the complexity of the LIBS plasma and its short lifetime in Martian atmospheric conditions compared to the terrestrial atmosphere since these factors can impede exact estimates of the plasma parameters. Consequently, the assumption of LTE is most likely not fulfilled in these measurements. This study demonstrated that normalization with the derived T and n_e is not better suited than the usually applied normalization to total emission intensity. It was observed that the standard methods for plasma parameter derivation are critical for a correct description of the LIBS plasma in Martian atmospheric conditions. Besides the transient nature of the LIBS plasma, there are temperature and density gradients within the plasma. Thus, more detailed studies [Vogt et al., 2018a, Hansen et al., 2018, Schröder et al., 2019b] for better understanding the LIBS plasma in Martian atmospheric conditions are necessary in order to either identify parameters which are the most responsible for signal fluctuations or to develop appropriate computational approaches which can assist their derivation.

(2) LIBS instruments for space exploration missions to atmosphereless bodies like the Earth's moon or asteroids are proposed and motivated LIBS experiments in atmospheric conditions below 1 hPa. Experiments that reveal how the LIBS plasma changes in low pressure environments compared to Mars or ambient pressure were done with the LIBS setup equipped with the echelle spectrometer described in this work. Mars pressure is close to ideal for LIBS measurements and the plasma's lifetime and intensity decrease for lower pressures due to missing confinement by an atmospheric gas. Measurements were done with pressures ranging from 0.01 to 20 hPa and with delays from 0 to 300 ns with a fixed integration time of 1 ms to ensure that the whole plasma emission is captured in each measurement. Simple sample matrices like pure NaCl, Na_2SO_4, and iron were investigated to study the characteristics of the LIBS plasma and in particular of specific emission lines. In the LIBS data of sodium bearing samples it was observed that with decreasing pressure emission lines of higher ionized states appear, namely Na (III) emissions that were not observable for pressures above 10 hPa. This means that LIBS plasmas in low-pressure environments have a higher degree of ionization. An explanation is the lower particle density that reduces the probability of recombination. Such a higher ratio of ionization was supported with simulations that are based on solving the Saha-Eggert equation for low particle density plasmas ($n < 10^{22}\,m^{-3}$). LIBS instruments to bodies without an atmosphere can profit from additional emission lines at different wavelengths. However, it is not clear how robust these spectral features are and quantitative analysis might

be more complicated. Regarding the vacuum conditions on several bodies in the Solar System, one advantage of using LIBS for the exploration is the absence of atmospheric absorptions which allows the access of the UV spectral range (100-200 nm), e.g., [Kubitza et al., 2019a]. In this range, strong emission lines of, for example, sulfur or phosphorus can be observed. Thus, besides some challenges connected to vacuum conditions, LIBS has a great potential for the exploration of atmosphereless bodies and is versatile regarding the mission objectives.

(3) Elements like the halogens fluorine and chlorine, and also phosphorus are challenging to detect in LIBS measurements in the commonly used spectral range between 200 and 900 nm. Instead of using the rather weak elemental emission lines, fluorine and chlorine can be detected indirectly via molecular emission bands of simple CaF and CaCl molecules that form in the plasma [Gaft et al., 2014,Forni et al., 2015]. These molecular bands can, however, superimpose the best observable emission lines of phosphorus in the spectra. The analysis of these lines and bands require special and dedicated methods. In detailed analytical studies of our group [Vogt et al., 2018b, Vogt et al., 2020] it was shown that the use of molecular emission bands in univariate calibration models relying only on the concentrations of chlorine or fluorine can be misleading as the band intensities depend on the concentrations of both reactants. Thus, also the calcium concentration has to be considered in analytic calibration models using molecular emissions of CaCl and CaF.

Motivated by the detection of apatite ($Ca_5(PO_4)_3(F,Cl)$) in Martian LIBS data [Forni et al., 2015, Meslin et al., 2016], high-resolved LIBS data in simulated Martian atmospheric conditions were obtained in this study from different mixtures of $Ca_3(PO_4)_2$ with CaF_2 and $CaCl_2$ and also natural apatites. Suitable emission lines and molecular bands for qualitative and quantitative analysis were identified and MVAs were done testing the feasibility of LIBS to differentiate between the different samples. First, a PCA was conducted on spectral ranges with the molecular emissions of CaCl and CaF, and with elemental emission lines of fluorine, chlorine, and phosphorus. The outcomes show that it is possible to distinguish between chlor- and fluorapatite with PCA where the PCA loadings indicate that the molecular bands are most relevant for the identification. A second study focused on chlorine quantification with PLS-R investigated the usefulness of the CaCl molecular emission for the calibration of chlorine. Several sets of samples with varying chlorine and calcium concentrations, either correlated or anti-correlated were investigated in Martian atmospheric conditions (same data as acquired for [Vogt et al., 2018b]). The results show that the CaCl molecular emission can improve the PLS-R models for chlorine quantification. However, not all samples are well described by the same model. A better approach could be a prior classification of the sample and quantification with a sub-model dedicated to the particular matrix of the sample. This could be in particular an improved way of chlorine quantification with the ChemCam instrument. In this context, sample classes could relate to different types of rocks or distinct mineral phases.

(4) Three levels of data fusion are usually distinguished: low-, mid-, and high-level data fusion, where "low" refers to the fusion of the original data, i.e. spectral data for LIBS and Raman spectroscopy, and "high" refers to a combination of derived values such as the outcome of MVA. In this study, mostly low-level data fusion was applied for which the spectral data of both techniques was merged and analyzed afterwards but also high-level data fusion was performed and evaluated. All measurements for the LIBS and Raman data fusion study were done with miniaturized setups with samples relevant for Mars in-situ exploration (salts such as sulfates and carbonates in mixtures with Mars analogue soil) and in Martian atmospheric conditions. From the LIBS, the Raman, and their combined data, MVA models were com-

puted, respectively. Clustering in PCA space was analyzed by calculating the spreads and distances of the clusters. The analyses of both individual data and fused data allowed for a correct identification of the constituents and in some cases to semi-quantitatively infer the mixing ratio of binary mixtures. While with the fused data in general more semi-quantitative matches and also more correct assignments were achieved, some samples dropped out of the correct identification that was achieved with the individual models.

This comparative approach shows that each technique has advantages and the quality of the results must be balanced with the complexity of the analysis. Further investigations are necessary to specify and list the pros and cons of these different methods. For example, the combined model produced better clusters in the application described above, but in some cases analyzing only the Raman data would be sufficient. The combined model gives also the smallest prediction errors in a PLS-DA when considering all samples simultaneously. However, if the samples are split between anion and cation categories, individual Raman and LIBS models give better results, respectively. This type of work shall lead to recommendations for a specific method depending on the science goal: salt or specific ion identification, mixture ratio quantification, etc. In particular for the SuperCam instrument, the first combined LIBS and Raman instrument for space exploration, the findings in this study can give input for best suited data analysis strategies.

(1-4) To summarize the findings of this work, one tested data analysis method was not better suited than the established approach (total intensity normalization) while others revealed a great potential for improved analysis and therefore increasing the scientific return of LIBS space exploration instruments. The normalization with plasma parameters did not show an improvement compared to the total emission normalization. Better understanding the LIBS plasma in Martian atmospheric conditions with the help of plasma imaging or modeling could improve the accuracy of plasma parameter determination, however, it has to be evaluated if these methods would be applicable to Martian LIBS data. As a method with great potential, MVA methods were found to be useful for the identification and quantification of halogens by means of molecular emission. Further investigations with more samples, especially with geological samples could give more insight how these methods can be implemented in real mission scenarios. Also, evaluating the capabilities of other advanced data analysis techniques such as machine learning could be a further step in the analysis of Martian LIBS data analysis in general. Regarding the last evaluated method, data fusion of LIBS and Raman data can indeed improve the identification capabilities of each technique alone. Nevertheless, the improvement is small in comparison to the larger datasets due to low-level data fusion. Concepts of high-level data fusion were also evaluated indicating the potential of improved identification capabilities. In general, both spectroscopic techniques yield valuable information and it has to be evaluated how their data can be fused in the most efficient way for particular missions and their science objectives.

LIBS is a powerful technique for the robotic exploration of bodies in the Solar System: It is straightforward, fast, and needs only optical access to the sample. The ChemCam instrument on Mars has been successfully analyzing Martian rocks and soils since 2012 which led to the selection of its enhanced follow-up instrument SuperCam for the Mars 2020 mission and most likely inspired several other planned LIBS instruments for space exploration. The studies presented in this thesis emphasize how important the selection of dedicated data analysis strategies is in order to obtain the best possible scientific return. Although LIBS has some challenges mostly due to the low reproducibility, the present work has shown that there is

more potential when using optimized data analysis techniques. Future steps in the development of data analysis strategies can include, for example, input from LIBS plasma imaging, computational modeling of the LIBS plasma, or the use of advanced methods such as machine learning. Regarding the variety of fascinating worlds in the Solar System that could be studied with in-situ explorations, a wealth of potential targets for LIBS instruments are available. As the LIBS plasma is strongly affected by environmental conditions, specific studies for each possible destination are necessary. Understanding the origin and the evolution of bodies in the Solar System is of high interest for humankind and more robotic in-situ missions will be send to more destinations in the future. One potential standard technique belonging to the scientific payload of these missions can be LIBS with optimized and sophisticated data analysis techniques for precise qualitative and quantitative elemental analysis.

Bibliography

[Aguilera and Aragón, 2004] Aguilera, J. A. and Aragón, C. (2004). Characterization of a laser-induced plasma by spatially resolved spectroscopy of neutral atom and ion emissions. Comparison of local and spatially integrated measurements. *Spectrochimica Acta - Part B Atomic Spectroscopy*, 59(12):1861–1876.

[Aguilera and Aragón, 2007] Aguilera, J. A. and Aragón, C. (2007). Apparent excitation temperature in laser-induced plasmas. *Journal of Physics: Conference Series*, 59(1):210–217.

[Aguilera et al., 2003] Aguilera, J. A., Bengoechea, J., and Aragón, C. (2003). Curves of growth of spectral lines emitted by a laser-induced plasma: Influence of the temporal evolution and spatial inhomogeneity of the plasma. *Spectrochimica Acta - Part B Atomic Spectroscopy*, 58(2):221–237.

[Anderson et al., 2017] Anderson, D. E., Ehlmann, B. L., Forni, O., Clegg, S. M., Cousin, A., Thomas, N. H., Lasue, J., Delapp, D. M., McInroy, R. E., Gasnault, O., Dyar, M. D., Schröder, S., Maurice, S., and Wiens, R. C. (2017). Characterization of LIBS emission lines for the identification of chlorides, carbonates, and sulfates in salt/basalt mixtures for the application to MSL ChemCam data. *Journal of Geophysical Research: Planets*, 122(4):744–770.

[Angel et al., 2012] Angel, S. M., Gomer, N. R., Sharma, S. K., McKay, C., and Ames, N. (2012). Remote Raman spectroscopy for planetary exploration: A review. *Applied Spectroscopy*, 66(2):137–150.

[Aragón and Aguilera, 2008a] Aragón, C. and Aguilera, J. A. (2008a). Characterization of laser induced plasmas by optical emission spectroscopy: A review of experiments and methods. *Spectrochimica Acta - Part B Atomic Spectroscopy*, 63(9):893–916.

[Aragón and Aguilera, 2008b] Aragón, C. and Aguilera, J. A. (2008b). Spatial and temporal scaling and common apparent excitation temperature of laser-induced plasmas generated at constant irradiance with different pulse energies. *Journal of Applied Physics*, 103(1):013310.

[Aragón and Aguilera, 2015] Aragón, C. and Aguilera, J. A. (2015). Quantitative analysis by laser-induced breakdown spectroscopy based on generalized curves of growth. *Spectrochimica Acta Part B: Atomic Spectroscopy*, 110:124–133.

[Baker et al., 1991] Baker, V., Strom, R., Gulick, V., Kargel, J., Komatsu, G., and Kale, V. (1991). Ancient oceans, ice sheets and the hydrological cycle on Mars. *Nature*, 352(6336):589.

[Banerdt et al., 2019] Banerdt, W. B., Smrekar, S., Antonangeli, D., Asmar, S., Banfield, D., Beghein, C., Bowles, N., Bozdag, E., Chi, P., Christensen, U., Clinton, J., Collins, G., Daubar, I., Dehant, V., Fillingim, M., Folkner, W., Garcia, R., Garvin, J., Giardini, D., Golombek, M., Grant, J., Grott, M., Grygorczuk, J., Hudson, T., Irving, J., Johnson,

C., Kargl, G., Kawamura, T., Kedar, S., King, S., Knapmeyer-Endrun, B., Lemmon, M., Lognonné, P., Lorenz, R., Maki, J., Margerin, L., McLennan, S., Michaut, C., Mimoun, D., Mocquet, A., Morgan, P., Mueller, N., Nagihara, S., Newman, C., Nimmo, F., Panning, M., Pike, W. T., Plesa, A.-C., Rodriguez-Manfredi, J. A., Russell, C., Schmerr, N., Siegler, M., Spiga, A., Spohn, T., Stanley, S., Teanby, N., Tromp, J., Warner, N., Weber, R., and Wieczorek, M. (2019). Insight — The First Three Months on Mars. In *50th Lunar and Planetary Science Conference*, page Abstract #3109, Houston. Lunar and Planetary Institute.

[Barnett, 1968] Barnett, W. (1968). Theoretical principles of internal standardization in analytical emission spectroscopy. *Spectrochimica Acta Part B: Atomic Spectroscopy*, 23(10):643–664.

[Beck et al., 2006] Beck, P., Barrat, J. A., Gillet, P., Wadhwa, M., Franchi, I. A., Greenwood, R. C., Bohn, M., Cotten, J., van de Moortèle, B., and Reynard, B. (2006). Petrography and geochemistry of the chassignite Northwest Africa 2737 (NWA 2737). *Geochimica et Cosmochimica Acta*, 70(8):2127–2139.

[Beegle et al., 2015] Beegle, L., Bhartia, R., White, M., Deflores, L., Abbey, W., Wu, Y. H., Cameron, B., Moore, J., Fries, M., Burton, A., Edgett, K. S., Ravine, M. A., Hug, W., Reid, R., Nelson, T., Clegg, S., Wiens, R., Asher, S., and Sobron, P. (2015). SHERLOC: Scanning habitable environments with Raman & luminescence for organics & chemicals. *IEEE Aerospace Conference Proceedings*.

[Beyssac et al., 2019] Beyssac, O., Fau, A., Zanda, B., Gauthier, M., Pont, S., Sautter, V., Bernard, S., Boulliard, J. C., Hewins, R., Gasnault, O., and Maurice, S. (2019). Raman spectroscopy for Mars exploration: Insights from NWA7533 Martian breccia and terrestrial analogs for Jezero lithologies. In *9th International Conference on Mars*, page Abstract #6176, Pasadena, California, USA.

[Bibring et al., 2006] Bibring, J.-P., Langevin, Y., Mustard, J. F., Poulet, F., Arvidson, R., Gendrin, A., Gondet, B., Mangold, N., Pinet, P., Forget, F., Berthé, M., Bibring, J.-P., Gendrin, A., Gomez, C., Gondet, B., Jouglet, D., Poulet, F., Soufflot, A., Vincendon, M., Combes, M., Drossart, P., Encrenaz, T., Fouchet, T., Merchiorri, R., Belluci, G., Altieri, F., Formisano, V., Capaccioni, F., Cerroni, P., Coradini, A., Fonti, S., Korablev, O., Kottsov, V., Ignatiev, N., Moroz, V., Titov, D., Zasova, L., Loiseau, D., Mangold, N., Pinet, P., Douté, S., Schmitt, B., Sotin, C., Hauber, E., Hoffmann, H., Jaumann, R., Keller, U., Arvidson, R., Mustard, J. F., Duxbury, T., Forget, F., and Neukum, G. (2006). Global Mineralogical and Aqueous Mars History Derived from OMEGA/Mars Express Data. *Science*, 312(5772):400–404.

[Blank et al., 2015] Blank, J. G., Ollila, A. M., Lanza, N. L., Forni, O., Nachon, M., Mangold, N., Clegg, S. M., Yen, A., Maurice, S., and Wiens, R. C. (2015). Detection of Phosphorus by ChemCam in Gale Crater. In *46th Lunar and Planetary Science Conference*, page Abstract #2850, Houston. Lunar and Planetary Institute.

[Body and Chadwick, 2001] Body, D. and Chadwick, B. (2001). Optimization of the spectral data processing in a LIBS simultaneous elemental analysis system. *Spectrochimica Acta Part B: Atomic Spectroscopy*, 56(6):725–736.

[Borràs et al., 2015] Borràs, E., Ferré, J., Boqué, R., Mestres, M., Aceña, L., and Busto, O. (2015). Data fusion methodologies for food and beverage authentication and quality

assessment - A review. *Analytica Chimica Acta*, 891:1–14.

[Boström et al., 2007] Boström, H., Andler, S. F., Brohede, M., Johansson, R., Karlsson, A., Van Laere, J., Niklasson, L., Nilsson, M., Persson, A., and Ziemke, T. (2007). On the definition of information fusion as a field of research.

[Brass, 1980] Brass, G. W. (1980). Stability of brines on Mars. *Icarus*, 42(1):20–28.

[Brennetot et al., 2003] Brennetot, R., Lacour, J. L., Vors, E., Rivoallan, A., Vailhen, D., and Maurice, S. (2003). Mars Analysis by Laser-Induced breakdown Spectroscopy (MALIS): Influence of mars atmosphere on plasma emission and study of factors influencing plasma emission with the use of Doehlert designs. *Applied Spectroscopy*, 57(7):744–752.

[Carr, 2012] Carr, M. H. (2012). The fluvial history of Mars. *Philosophical Transactions of the Royal Society A: Mathematical, Physical and Engineering Sciences*, 370(1966):2193–2215.

[Chaleard et al., 1997] Chaleard, C., Mauchien, P., Andre, N., Uebbing, J., Lacour, J., and Geertsen, C. (1997). Correction of matrix effects in quantitative elemental analysis with laser ablation optical emission spectrometry. *Journal of Analytical Atomic Spectrometry*, 12(2):183–188.

[Choo-Smith et al., 2002] Choo-Smith, L.-P., Edwards, H. G. M., Endtz, H. P., Kros, J. M., Heule, F., Barr, H., Robinson Jr., J. S., Bruining, H. A., and Puppels, G. J. (2002). Medical applications of raman spectroscopy: From proof of principle to clinical implementation. *Biopolymers*, 67(1):1–9.

[Citron et al., 2018] Citron, R. I., Manga, M., and Hemingway, D. J. (2018). Timing of oceans on Mars from shoreline deformation. *Nature*, 555(7698):643–646.

[Clegg et al., 2014] Clegg, S. M., Wiens, R., Misra, A. K., Sharma, S. K., Lambert, J., Bender, S., Newell, R., Nowak-Lovato, K., Smrekar, S., Dyar, M. D., and Maurice, S. (2014). Planetary geochemical investigations using raman and laser-induced breakdown spectroscopy. *Applied Spectroscopy*, 68(9):925–936.

[Clegg et al., 2017] Clegg, S. M., Wiens, R. C., Anderson, R., Forni, O., Frydenvang, J., Lasue, J., Cousin, A., Payré, V., Boucher, T., Dyar, M. D., McLennan, S. M., Morris, R. V., Graff, T. G., Mertzman, S. A., Ehlmann, B. L., Belgacem, I., Newsom, H., Clark, B. C., Melikechi, N., Mezzacappa, A., McInroy, R. E., Martinez, R., Gasda, P., Gasnault, O., and Maurice, S. (2017). Recalibration of the Mars Science Laboratory ChemCam instrument with an expanded geochemical database. *Spectrochimica Acta - Part B Atomic Spectroscopy*, 129:64–85.

[Clifford et al., 2010] Clifford, S. M., Lasue, J., Heggy, E., Boisson, J., McGovern, P., and Max, M. D. (2010). Depth of the Martian cryosphere: Revised estimates and implications for the existence and detection of subpermafrost groundwater. *Journal of Geophysical Research: Planets*, 115(E7).

[Clifford and Parker, 2001] Clifford, S. M. and Parker, T. J. (2001). The Evolution of the Martian Hydrosphere: Implications for the Fate of a Primordial Ocean and the Current State of the Northern Plains. *Icarus*, 154(1):40 – 79.

[Colao et al., 2004a] Colao, F., Fantoni, R., Lazic, V., and Paolini, A. (2004a). LIBS application for analyses of martian crust analogues: Search for the optimal experimental parameters in air and CO2 atmosphere. *Applied Physics A: Materials Science and Processing*, 79(1):143–152.

[Colao et al., 2004b] Colao, F., Fantoni, R., Lazic, V., Paolini, A., Fabbri, F., Ori, G., Marinangeli, L., and Baliva, A. (2004b). Investigation of LIBS feasibility for in situ planetary exploration: An analysis on Martian rock analogues. *Planetary and Space Science*, 52(1-3):117–123.

[Colomban, 2012] Colomban, P. (2012). The on-site/remote Raman analysis with mobile instruments: a review of drawbacks and success in cultural heritage studies and other associated fields. *Journal of Raman Spectroscopy*, 43(11):1529–1535.

[Cotton, 2003] Cotton, F. A. (2003). *Chemical applications of group theory*. John Wiley & Sons.

[Cousin et al., 2015] Cousin, A., Forni, O., Schröder, S., Nachon, M., Gasnault, O., Maurice, S., and Wiens, R. C. (2015). Quantification of Chlorine on Mars using the ChemCam instrument. In *8th Euro-Mediterranean Symposium on Laser Induced Breakdown Spectroscopy*, page Abstract #37, Linz, Austria.

[Cousin et al., 2018] Cousin, A., Manrique, J., Maurice, S., Rull, F., Wiens, R., Fabre, C., Sautter, V., Montagnac, G., Beck, P., Drouet, C., Madariaga, J., Aramendia, J., Gomez-Nubla, L., Meslin, P.-Y., Dromart, G., Bernard, S., Beyssac, O., Gasnault, O., and Forni, O. (2018). SuperCam Calibration Targets for the Mars2020 NASA Rover. In *13th GeoRaman Conference*, page Abstract #154, Catania, Italy.

[Cremers, 2007] Cremers, D. A. (2007). Remote Analysis by LIBS: Application to Space Exploration. In Singh, J. P. and Thakur, S. N., editors, *Laser-Induced Breakdown Spectroscopy*, pages 353–379. Elsevier, Amsterdam.

[Cremers, 2014] Cremers, D. A. (2014). Space Applications of LIBS. In Musazzi, S. and Perini, U., editors, *Laser-Induced Breakdown Spectroscopy: Theory and Applications*, pages 257–291. Springer Berlin Heidelberg, Berlin, Heidelberg.

[Cremers and Radziemski, 2013] Cremers, D. A. and Radziemski, L. J. (2013). *Handbook of laser-induced breakdown spectroscopy*. Wiley, Chichester, 2. edition.

[Cristoforetti et al., 2010] Cristoforetti, G., De Giacomo, A., Dell'Aglio, M., Legnaioli, S., Tognoni, E., Palleschi, V., and Omenetto, N. (2010). Local Thermodynamic Equilibrium in Laser-Induced Breakdown Spectroscopy: Beyond the McWhirter criterion. *Spectrochimica Acta - Part B Atomic Spectroscopy*, 65(1):86–95.

[De Maesschalck et al., 2000] De Maesschalck, R., Jouan-Rimbaud, D., and Massart, D. L. (2000). The Mahalanobis distance. *Chemometrics and intelligent laboratory systems*, 50(1):1–18.

[Dehouck et al., 2019] Dehouck, E., Cousin, A., Mangold, N., Frydenvang, J., Gasnault, O., Fox, V., Bennett, K., Maurice, S., and Wiens, R. (2019). Geochemistry of the clay-bearing sedimentary rocks of Glen Torridon, Gale crater, Mars. In *13th European Planetary Science Congress*, page Abstract #979, Geneva, Switzerland.

[Douce et al., 2011] Douce, A. E. P., Roden, M. F., Chaumba, J., Fleisher, C., and Yogodzinski, G. (2011). Compositional variability of terrestrial mantle apatites, thermodynamic modeling of apatite volatile contents, and the halogen and water budgets of planetary mantles. *Chemical Geology*, 288(1-2):14–31.

[Dubessy et al., 2012] Dubessy, J., Caumon, M.-C., and Rull, F. (2012). *Raman spectroscopy applied to earth sciences and cultural heritage*, volume 12. The Mineralogical Society of

Great Britain and Ireland.

[Dundas et al., 2017] Dundas, C. M., McEwen, A. S., Chojnacki, M., Milazzo, M. P., Byrne, S., McElwaine, J. N., and Urso, A. (2017). Granular flows at recurring slope lineae on Mars indicate a limited role for liquid water. *Nature Geoscience*, 10(12):903.

[Edwards and Piqueux, 2019] Edwards, C. S. and Piqueux, S. (2019). The water content of recurring slope lineae on Mars. In *9th International Conference on Mars*, page Abstract #6299, Pasadena, California, USA.

[Effenberger and Scott, 2010] Effenberger, A. J. and Scott, J. R. (2010). Effect of atmospheric conditions on LIBS spectra. *Sensors*, 10(5):4907–4925.

[Ehlmann and Edwards, 2014] Ehlmann, B. L. and Edwards, C. S. (2014). Mineralogy of the Martian Surface. *Annual Review of Earth and Planetary Sciences*, 42(1):291–315.

[Eland et al., 2001] Eland, K. L., Stratis, D. N., Lai, T., Berg, M. A., Goode, S. R., and Angel, S. M. (2001). Some Comparisons of LIBS Measurements using Nanosecond and Picosecond Laser Pulses. *Appl. Spectrosc.*, 55(3):279–285.

[Elmenreich, 2002] Elmenreich, W. (2002). An introduction to sensor fusion. *Vienna University of Technology, Austria*, 502.

[Esbensen et al., 2010] Esbensen, K. H., Guyot, D., Westad, F., and Houmøller, L. P. (2010). *Multivariate Data Analysis - In Practice*. CAMO Software, 5. edition.

[Fabre et al., 2002] Fabre, C., Boiron, M.-C., Dubessy, J., Cathelineau, M., and Banks, D. A. (2002). Palaeofluid chemistry of a single fluid event: a bulk and in-situ multi-technique analysis (LIBS, Raman Spectroscopy) of an Alpine fluid (Mont-Blanc). *Chemical geology*, 182(2-4):249–264.

[Feng et al., 2010] Feng, J., Wang, Z., Li, Z., and Ni, W. (2010). Study to reduce laser-induced breakdown spectroscopy measurement uncertainty using plasma characteristic parameters. *Spectrochimica Acta - Part B Atomic Spectroscopy*, 65(7):549–556.

[Forni et al., 2015] Forni, O., Gaft, M., Toplis, M. J., Clegg, S. M., Maurice, S., Wiens, R. C., Mangold, N., Gasnault, O., Sautter, V., Le Mouélic, S., Meslin, P. Y., Nachon, M., McInroy, R. E., Ollila, A. M., Cousin, A., Bridges, J. C., Lanza, N. L., and Dyar, M. D. (2015). First detection of fluorine on Mars: Implications for Gale Crater's geochemistry. *Geophysical Research Letters*, 42(4):1020–1028.

[Forni et al., 2013] Forni, O., Maurice, S., Gasnault, O., Wiens, R. C., Cousin, A., Clegg, S. M., Sirven, J. B., and Lasue, J. (2013). Independent component analysis classification of laser induced breakdown spectroscopy spectra. *Spectrochimica Acta - Part B Atomic Spectroscopy*, 86:31–41.

[Fox et al., 2019] Fox, V. K., Bennett, K. A., Bristow, T., Ehlmann, B. L., House, C., Fairén, A. G., Horgan, B., Johnson, S., Salvatore, M., Stack, K., Wiens, R. C., and Williams, A. J. (2019). Exploring the Clay-Bearing Unit with the Curiosity Rover. In *50th Lunar and Planetary Science Conference*, page Abstract #2826, Houston. Lunar and Planetary Institute.

[Frydenvang et al., 2013] Frydenvang, J., Kinch, K. M., Husted, S., and Madsen, M. B. (2013). An optimized calibration procedure for determining elemental ratios using laser-induced breakdown spectroscopy. *Analytical Chemistry*, 85(3):1492–1500.

[Frydenvang et al., 2018] Frydenvang, J., Mangold, N., Wiens, R. C., Clark, B. C., Fraeman, A. A., Forni, O., Meslin, P.-Y., Ollila, A. M., Gasda, P. J., Payré, V., and Calef, F. (2018). Geochemical Variations Observed with the ChemCam Instrument on Vera Rubin Ridge in Gale Crater, Mars. In *49th Lunar and Planetary Science Conference*, page Abstract #2310, Houston. Lunar and Planetary Institute.

[Gaft et al., 2014] Gaft, M., Nagli, L., Eliezer, N., Groisman, Y., and Forni, O. (2014). Elemental analysis of halogens using molecular emission by laser-induced breakdown spectroscopy in air. *Spectrochimica Acta - Part B Atomic Spectroscopy*, 98:39–47.

[Gasda et al., 2017] Gasda, P. J., Haldeman, E. B., Wiens, R. C., Rapin, W., Bristow, T. F., Bridges, J. C., Schwenzer, S. P., Clark, B., Herkenhoff, K., Frydenvang, J., Lanza, N. L., Maurice, S., Clegg, S., Delapp, D. M., Sanford, V. L., Bodine, M. R., and McInroy, R. (2017). In situ detection of boron by ChemCam on Mars. *Geophysical Research Letters*, 44(17):8739–8748.

[Gornushkin et al., 1999] Gornushkin, I. B., King, L. A., Smith, B. W., Omenetto, N., and Winefordner, J. D. (1999). Line broadening mechanisms in the low pressure laser-induced plasma. *Spectrochimica acta, Part B: Atomic spectroscopy*, 54(8):1207–1217.

[Goudge et al., 2015] Goudge, T. A., Mustard, J. F., Head, J. W., Fassett, C. I., and Wiseman, S. M. (2015). Assessing the mineralogy of the watershed and fan deposits of the Jezero crater paleolake system, Mars. *Journal of Geophysical Research: Planets*, 120(4):775–808.

[Griem, 1964] Griem, H. R. (1964). *Plasma Spectroscopy*. McGraw-Hill.

[Griem, 1997] Griem, H. R. (1997). *Principles of Plasma Spectroscopy*. Cambridge University Press.

[Grotzinger et al., 2012] Grotzinger, J. P., Crisp, J., Vasavada, A. R., Anderson, R. C., Baker, C. J., Barry, R., Blake, D. F., Conrad, P., Edgett, K. S., Ferdowski, B., Gellert, R., Gilbert, J. B., Golombek, M., Gómez-Elvira, J., Hassler, D. M., Jandura, L., Litvak, M., Mahaffy, P., Maki, J., Meyer, M., Malin, M. C., Mitrofanov, I., Simmonds, J. J., Vaniman, D., Welch, R. V., and Wiens, R. C. (2012). Mars Science Laboratory Mission and Science Investigation. *Space Science Reviews*, 170(1):5–56.

[Grotzinger et al., 2015] Grotzinger, J. P., Crisp, J. A., Vasavada, A. R., and Team, M. S. (2015). Curiosity's mission of exploration at Gale Crater, Mars. *Elements*, 11(1):19–26.

[Grotzinger et al., 2014] Grotzinger, J. P., Sumner, D. Y., Kah, L., Stack, K., Gupta, S., Edgar, L., Rubin, D., Lewis, K., Schieber, J., Mangold, N., et al. (2014). A habitable fluvio-lacustrine environment at Yellowknife Bay, Gale Crater, Mars. *Science*, 343(6169):1242777.

[Haberle et al., 2017] Haberle, R. M., Catling, D. C., Carr, M. H., and Zahnle, K. J. (2017). The Early Mars Climate System. In Haberle, R. M., Clancy, R. T., Forget, F., Smith, M. D., and Zurek, R. W., editors, *The Atmosphere and Climate of Mars*, Cambridge Planetary Science, page 526–568. Cambridge University Press.

[Hagelschuer et al., 2019] Hagelschuer, T., Böttger, U., Buder, M., Cho, Y., Gensch, M., Hanke, F., Hübers, H.-W., Kameda, S., Kopp, E., Kubitza, S., Moral, A., Pertenais, M., Peter, G., Rammelkamp, K., Rodriguez, P., Rull, F., Ryan, C. Säuberlich, T., Schrandt, F., Schröder, S., Ulamec, S., and Vance, R. (2019). The Raman spectrometer onboard the MMX rover for Phobos. In *70th International Astronautical Congress*, Washington, D.C., USA.

[Hahn and Omenetto, 2012] Hahn, D. W. and Omenetto, N. (2012). Laser-induced breakdown spectroscopy (LIBS), part II: Review of instrumental and methodological approaches to material analysis and applications to different fields. 66(4):347–419.

[Hahn and Omenetto, 2010] Hahn, W. D. and Omenetto, N. (2010). Laser-Induced Breakdown Spectroscopy (LIBS), Part I: Review of Basic Diagnostics and Plasma-Particle Interactions: Still-Challenging Issues Within the Analytical Plasma Community. *Appl. Spectrosc.*, 64:335A–366A.

[Hall and Llinas, 1997] Hall, D. L. and Llinas, J. (1997). An introduction to multisensor data fusion. *Proceedings of the IEEE*, 85(1):6–23.

[Hanke et al., 2016] Hanke, F., Böttger, U., Pohl, A., Pavlov, S., and Hübers, H.-W. (2016). The differentiation of Raman spectra of salts using multivariate data analysis. In *12th GeoRaman Conference*, page Abstract #100, Novosibirsk, Russia.

[Hansen et al., 2018] Hansen, P. B., Vogt, D. S., Schröder, S., Rammelkamp, K., Kubitza, S., Frohmann, S., and Hübers, H.-W. (2018). Simple modelling of Plasma Parameters to Assist the Analysis of LIBS Spectra for Planetary Exploration. In *12th European Planetary Science Congress*, page Abstract #1027, Berlin, Germany.

[Haskin et al., 1997] Haskin, L. A., Wang, A., Rockow, K. M., Jolliff, B. L., Korotev, R. L., and Viskupic, K. M. (1997). Raman spectroscopy for mineral identification and quantification for in situ planetary surface analysis: A point count method. *Journal of Geophysical Research E: Planets*, 102(E8):19293–19306.

[Head et al., 2018] Head, J. W. I., Forget, F., Wordsworth, R., Turbet, M., Cassanelli, J., and Palumbo, A. (2018). Two Oceans on Mars?: History, Problems, and Prospects. In *49th Lunar and Planetary Science Conference*, page Abstract #2194, Houston. Lunar and Planetary Institute.

[Hecht et al., 2009] Hecht, M. H., Kounaves, S. P., Quinn, R. C., West, S. J., Young, S. M., Ming, D. W., Catling, D. C., Clark, B. C., Boynton, W. V., Hoffman, J., DeFlores, L. P., Gospodinova, K., Kapit, J., and Smith, P. H. (2009). Detection of perchlorate and the soluble chemistry of martian soil at the phoenix lander site. *Science*, 325(5936):64–67.

[Hermann et al., 1998] Hermann, J., Boulmer-Leborgne, C., and Hong, D. (1998). Diagnostics of the early phase of an ultraviolet laser induced plasma by spectral line analysis considering self-absorption. *Journal of Applied Physics*, 83(2):691–696.

[Hoehse et al., 2012] Hoehse, M., Paul, A., Gornushkin, I., and Panne, U. (2012). Multivariate classification of pigments and inks using combined Raman spectroscopy and LIBS. *Analytical and Bioanalytical Chemistry*, 402(4):1443–1450.

[Holtgreven, 1968] Holtgreven, W. L. (1968). *Plasma Diagnostics*. North-Holland, Amsterdam.

[Iida, 1990] Iida, Y. (1990). Effects of atmosphere on laser vaporization and excitation processes of solid samples. *Spectrochimica Acta Part B: Atomic Spectroscopy*, 45(12):1353–1367.

[Jakosky and Mellon, 2004] Jakosky, B. M. and Mellon, M. T. (2004). Water on Mars. *Physics Today*, 57(4):71–76.

[Jaumann et al., 2018] Jaumann, R., Köler, U., Pieth, S., Sohl, F., and Tirsch, D. (2018). *Expedition zu fremden Welten*. Springer, 1. edition.

[Johnson et al., 1991] Johnson, M. C., Rutherford, M. J., and Hess, P. C. (1991). Chassigny petrogenesis: Melt compositions, intensive parameters and water contents of Martian (?) magmas. *Geochimica et Cosmochimica Acta*, 55(1):349–366.

[Kessler, 2007] Kessler, W. (2007). *Multivariate Datenanalyse für die Pharma-, Bio- und Prozessanalytik*. Wiley.

[Khaleghi et al., 2013] Khaleghi, B., Khamis, A., Karray, F., and Razavi, S. (2013). Multisensor Data Fusion: A Review of the State-of-the-art. *Information Fusion - INFFUS*, 14.

[Knight et al., 2000] Knight, A. K., Scherbarth, N. L., Cremers, D. A., and Ferris, M. J. (2000). Characterization of laser-induced breakdown spectroscopy (LIBS) for application to space exploration. *Applied Spectroscopy*, 54(3):331–340.

[Kubitza et al., 2019a] Kubitza, S., Schröder, S., Frohmann, S., Dietz, E., Hansen, P. B., Rammelkamp, K., Vogt, D. S., and Hübers (2019a). VUV-LIBS for Volatile Detectionin Space Exploration. In *13th European Planetary Science Congress*, page Abstract #586, Geneva, Switzerland.

[Kubitza et al., 2019b] Kubitza, S., Schröder, S., Rammelkamp, K., Hagelschuer, T., Böttger, U., Hansen, P. B., Vogt, D. S., and Hübers, H.-W. (2019b). Evaluation of Close-Up Remote cw-Raman Spectroscopy for In-situ Planetary Exploration. In *50th Lunar and Planetary Science Conference*, page Abstract #2421, Houston, USA.

[Kubitza et al., 2018] Kubitza, S., Vogt, D. S., Rammelkamp, K., Böttger, U., Frohmann, S., Hansen, P. B., Schröder, S., and Hübers, H.-W. (2018). A miniaturized Raman/LIBS instrument for in-situ investigation of celestial bodies in pioneering missions. In *12th European Planetary Science Congress*, page Abstract #789, Berlin, Germany.

[Kurniawan et al., 2014] Kurniawan, K. H., Tjia, M. O., and Kagawa, K. (2014). Review of Laser-Induced Plasma, Its Mechanism, and Application to Quantitative Analysis of Hydrogen and Deuterium. *Applied Spectroscopy Reviews*, 49(5):323–434.

[Lasue et al., 2013] Lasue, J., Mangold, N., Hauber, E., Clifford, S., Feldman, W., Gasnault, O., Grima, C., Maurice, S., and Mousis, O. (2013). Quantitative assessments of the martian hydrosphere. *Space Science Reviews*, 174(1-4):155–212.

[Lasue et al., 2019] Lasue, J., Meslin, P. Y., Sautter, V., Maroger, I., Krämer Ruggiu, L., Bridges, J. C., Lewin, E., Wiens, R. C., Beck, P., Cousin, A., Forni, O., Gasnault, O., Goetz, W., Johnson, J. R., Le Mouélic, S., Nachon, M., Newsom, H., Maurice, S., and Wellington, D. F. (2019). Probable Chondritic Fragments Detected by ChemCam in Gale Crater. In *50th Lunar and Planetary Science Conference*, page Abstract #2274, Houston. Lunar and Planetary Institute.

[Lasue et al., 2012] Lasue, J., Wiens, R. C., Clegg, S. M., Vaniman, D. T., Joy, K. H., Humphries, S., Mezzacappa, A., Melikechi, N., McInroy, R. E., and Bender, S. (2012). Remote laser-induced breakdown spectroscopy (LIBS) for lunar exploration. *Journal of Geophysical Research E: Planets*, 117(1).

[Laxmiprasad et al., 2013] Laxmiprasad, A., Raja, V. S., Menon, S., Goswami, A., Rao, M., and Lohar, K. (2013). An in situ laser induced breakdown spectroscope (LIBS) for Chandrayaan-2 rover: Ablation kinetics and emissivity estimations. *Advances in Space Research*, 52(2):332 – 341.

[Lazic et al., 2004] Lazic, V., Fantoni, R., Colao, F., Santagata, A., Morone, A., and Spizzichino, V. (2004). Quantitative laser induced breakdown spectroscopy analysis of ancient marbles and corrections for the variability of plasma parameters and of ablation rate. *Journal of Analytical Atomic Spectrometry*, 19(4):429.

[Lieber and Mahadevan-Jansen, 2003] Lieber, C. A. and Mahadevan-Jansen, A. (2003). Automated Method for Subtraction of Fluorescence from Biological Raman Spectra. *Appl. Spectrosc.*, 57(11):1363–1367.

[Long, 1977] Long, D. A. (1977). *Raman spectroscopy*, volume 276. McGraw-Hill New York.

[Lopez-Reyes et al., 2014] Lopez-Reyes, G., Sobron, P., Lefebvre, C., and Rull, F. (2014). Application of Multivariate Analysis Techniques for the Identification of Sulfates From Raman Spectra. *Lecture Notes in Earth System Sciences*, pages 135–139.

[López-Díez et al., 2003] López-Díez, E. C., Bianchi, G., and Goodacre, R. (2003). Rapid Quantitative Assessment of the Adulteration of Virgin Olive Oils with Hazelnut Oils Using Raman Spectroscopy and Chemometrics. *Journal of Agricultural and Food Chemistry*, 51(21):6145–6150.

[Mabrouk et al., 2013] Mabrouk, B., Kawther, Kauffmann, T. H., Aroui, H., and Fontana, M. D. (2013). Raman study of cation effect on sulfate vibration modes in solid state and in aqueous solutions. *Journal of Raman Spectroscopy*, 44(11):1603–1608.

[Malin and Edgett, 2000] Malin, M. C. and Edgett, K. S. (2000). Evidence for recent groundwater seepage and surface runoff on Mars. *Science*, 288(5475):2330–2335.

[Mandic et al., 2005] Mandic, D. P., Obradovic, D., Kuh, A., Adali, T., Trutschell, U., Golz, M., De Wilde, P., Barria, J., Constantinides, A., and Chambers, J. (2005). Data fusion for modern engineering applications: An overview. In *International Conference on Artificial Neural Networks*, pages 715–721. Springer.

[Manrique et al., 2018] Manrique, J., Lopez-Reyes, G., Moral, A., Canora, C., Bozic, T., and Rull, F. (2018). Application of data fusion techniques for the Raman analysis of sulfates and chlorates brines relevant for the in-situ exploration of Europa. In *13th GeoRaman Conference*, page Abstract #185, Catania, Italy.

[Markl, 2014] Markl, G. (2014). *Minerale und Gesteine: Mineralogie - Petrologie - Geochemie*. Springer Berlin Heidelberg.

[Mauchien et al., 2014] Mauchien, P., Pailloux, A., and Vercouter, T. (2014). Applications of laser spectroscopy in nuclear research and industry. In Baudelet, M., editor, *Laser Spectroscopy for Sensing*, pages 522 – 543. Woodhead Publishing.

[Maurice et al., 2016] Maurice, S., Clegg, S. M., Wiens, R. C., Gasnault, O., Rapin, W., Forni, O., Cousin, A., Sautter, V., Mangold, N., Le Deit, L., Nachon, M., Anderson, R. B., Lanza, N. L., Fabre, C., Payré, V., Lasue, J., Meslin, P. Y., Léveillé, R. J., Barraclough, B. L., Beck, P., Bender, S. C., Berger, G., Bridges, J. C., Bridges, N. T., Dromart, G., Dyar, M. D., Francis, R., Frydenvang, J., Gondet, B., Ehlmann, B. L., Herkenhoff, K. E., Johnson, J. R., Langevin, Y., Madsen, M. B., Melikechi, N., Lacour, J. L., Le Mouélic, S., Lewin, E., Newsom, H. E., Ollila, A. M., Pinet, P., Schröder, S., Sirven, J. B., Tokar, R. L., Toplis, M. J., D'Uston, C., Vaniman, D. T., and Vasavada, A. R. (2016). ChemCam activities and discoveries during the nominal mission of the Mars Science Laboratory in Gale crater, Mars. *Journal of Analytical Atomic Spectrometry*, 31(4):863–889.

[Maurice et al., 2012] Maurice, S., Wiens, R. C., Saccoccio, M., Barraclough, B., Gasnault, O., Forni, O., Mangold, N., Baratoux, D., Bender, S., Berger, G., Bernardin, J., Berthé, M., Bridges, N., Blaney, D., Bouyé, M., Caïs, P., Clark, B., Clegg, S., Cousin, A., Cremers, D., Cros, A., Deflores, L., Derycke, C., Dingler, B., Dromart, G., Dubois, B., Dupieux, M., Durand, E., D'Uston, L., Fabre, C., Faure, B., Gaboriaud, A., Gharsa, T., Herkenhoff, K., Kan, E., Kirkland, L., Kouach, D., Lacour, J. L., Langevin, Y., Lasue, J., Le Mouélic, S., Lescure, M., Lewin, E., Limonadi, D., Manhès, G., Mauchien, P., McKay, C., Meslin, P. Y., Michel, Y., Miller, E., Newsom, H. E., Orttner, G., Paillet, A., Parès, L., Parot, Y., Pérez, R., Pinet, P., Poitrasson, F., Quertier, B., Sallé, B., Sotin, C., Sautter, V., Séran, H., Simmonds, J. J., Sirven, J. B., Stiglich, R., Striebig, N., Thocaven, J. J., Toplis, M. J., and Vaniman, D. (2012). The ChemCam instrument suite on the Mars Science Laboratory (MSL) rover: Science objectives and mast unit description. *Space Science Reviews*, 170(1-4):95–166.

[McCreery, 2000] McCreery, R. L. (2000). *Raman spectroscopy for chemical analysis*, volume 157. John Wiley & Sons.

[McCubbin et al., 2013] McCubbin, F. M., Jones, R. H., Shearer, C. K., Elardo, S. M., Agee, C. B., Santos, A. R., Burger, P. V., Bell, A. S., and Papike, J. J. (2013). The Volatile Chemistry of Apatite in Planetary Materials: Implications for the Behavior of Volatiles During Planetary Differentiation? In *44th Lunar and Planetary Science Conference*, page Abstract #2731, Houston. Lunar and Planetary Institute.

[McEwen et al., 2014] McEwen, A. S., Dundas, C. M., Mattson, S. S., Toigo, A. D., Ojha, L., Wray, J. J., Chojnacki, M., Byrne, S., Murchie, S. L., and Thomas, N. (2014). Recurring slope lineae in equatorial regions of Mars. *Nature geoscience*, 7(1):53.

[McEwen et al., 1998] McEwen, A. S., Keszthelyi, L., Spencer, J. R., Schubert, G., Matson, D. L., Lopes-Gautier, R., Klaasen, K. P., Johnson, T. V., Head, J. W., Geissler, P., Fagents, S., Davies, A. G., Carr, M. H., Breneman, H. H., and Belton, M. J. S. (1998). High-Temperature Silicate Volcanism on Jupiter's Moon Io. *Science*, 281(5373):87–90.

[McEwen et al., 2011] McEwen, A. S., Ojha, L., Dundas, C. M., Mattson, S. S., Byrne, S., Wray, J. J., Cull, S. C., Murchie, S. L., Thomas, N., and Gulick, V. C. (2011). Seasonal Flows on Warm Martian Slopes. *Science*, 333(6043):740–743.

[McSween Jr., 1994] McSween Jr., H. Y. (1994). What we have learned about Mars from SNC meteorites. *Meteoritics*, 29(6):757–779.

[Mercadier et al., 2013] Mercadier, L., Hermann, J., Grisolia, C., and Semerok, A. (2013). Diagnostics of nonuniform plasmas for elemental analysis via laser-induced breakdown spectroscopy: Demonstration on carbon-based materials. *Journal of Analytical Atomic Spectrometry*, 28(9):1446–1455.

[Meslin et al., 2016] Meslin, P. Y., Cicutto, L., Forni, O., Drouet, C., Rapin, W., Nachon, M., Cousin, A., Blank, J. G., McCubbin, F. M., Gasnault, O., Newsom, H., Mangold, N., Schröder, S., Sautter, V., Maurice, S., and Wiens, R. C. (2016). Calibration of the fluorine, chlorine and hydrogen content of apatites with the ChemCam LIBS instrument. In *47th Lunar and Planetary Science Conference*, page Abstract #1703, Houston, USA.

[Milliken et al., 2010] Milliken, R. E., Grotzinger, J. P., and Thomson, B. J. (2010). Paleoclimate of Mars as captured by the stratigraphic record in Gale crater. *Geophysical Research Letters*, 37(4):1–6.

[Milliken et al., 2019] Milliken, R. E., Grotzinger, J. P., Wiens, R. C., Gellert, R., Thompson, L. M., Sheppard, R., Vasavada, A., Bristow, T., and Mangold, N. (2019). The Chemistry and Mineralogy of an Ancient Lacustrine Sequence on Mars: Lessons Learned from Integrating Rover and Orbiter Datasets. In *9th International Conference on Mars*, page Abstract #6191, Pasadena, California, USA.

[Misra et al., 2011] Misra, A. K., Sharma, S. K., Acosta, T. E., and Bates, D. E. (2011). Compact remote Raman and LIBS system for detection of minerals, water, ices, and atmospheric gases for planetary exploration. In *Proc. SPIE 8032, Next-Generation Spectroscopic Technologies IV*, volume 8032, page 80320Q.

[Miziolek et al., 2006] Miziolek, A. W., Palleschi, V., and Schechter, I. (2006). *Laser-induced breakdown spectroscopy*. Cambridge university press.

[Moros et al., 2018] Moros, J., Elfaham, M. M., and Javier Laserna, J. (2018). Dual-Spectroscopy Platform for the Surveillance of Mars Mineralogy Using a Decisions Fusion Architecture on Simultaneous LIBS-Raman Data. *Analytical Chemistry*, 90(3):2079–2087.

[Moros and Javier Laserna, 2015] Moros, J. and Javier Laserna, J. (2015). Unveiling the identity of distant targets through advanced Raman-laser-induced breakdown spectroscopy data fusion strategies. *Talanta*, 134:627–639.

[Moros et al., 2011] Moros, J., Lorenzo, J. A., and Laserna, J. J. (2011). Standoff detection of explosives: Critical comparison for ensuing options on Raman spectroscopy-LIBS sensor fusion. *Analytical and Bioanalytical Chemistry*, 400(10):3353–3365.

[Murchie et al., 2009] Murchie, S. L., Mustard, J. F., Ehlmann, B. L., Milliken, R. E., Bishop, J. L., McKeown, N. K., Noe Dobrea, E. Z., Seelos, F. P., Buczkowski, D. L., Wiseman, S. M., et al. (2009). A synthesis of Martian aqueous mineralogy after 1 Mars year of observations from the Mars Reconnaissance Orbiter. *Journal of Geophysical Research: Planets*, 114(E2).

[Nachon et al., 2014] Nachon, M., Clegg, S. M., Mangold, N., Schröder, S., Kah, L. C., Dromart, G., Ollila, A., Johnson, J. R., Oehler, D. Z., Bridges, J. C., Le Mouélic, S., Forni, O., Wiens, R., Anderson, R. B., Blaney, D. L., Bell, J., Clark, B., Cousin, A., Dyar, M. D., Ehlmann, B., Fabre, C., Gasnault, O., Grotzinger, J., Lasue, J., Lewin, E., Léveillé, R., McLennan, S., Maurice, S., Meslin, P.-Y., Rapin, W., Rice, M., Squyres, S. W., Stack, K., Sumner, D. Y., Vaniman, D., and Wellington, D. (2014). Calcium sulfate veins characterized by ChemCam/Curiosity at Gale crater, Mars. *Journal of Geophysical Research: Planets*, 119(9):1991–2016.

[Nachon et al., 2017] Nachon, M., Mangold, N., Forni, O., Kah, L. C., Cousin, A., Wiens, R. C., Anderson, R., Blaney, D., Blank, J. G., Calef, F., et al. (2017). Chemistry of diagenetic features analyzed by ChemCam at Pahrump Hills, Gale crater, Mars. *Icarus*, 281:121–136.

[Neumaier et al., 2015] Neumaier, P. F. X., Schmalz, K., Borngräber, J., Wylde, R., and Hübers, H. W. (2015). Terahertz gas-phase spectroscopy: chemometrics for security and medical applications. *The Analyst*, 140(1):213–222.

[Niemax, 2001] Niemax, K. (2001). Laser ablation–reflections on a very complex technique for solid sampling. *Fresenius' journal of analytical chemistry*, 370(4):332–340.

[Niles, 2019] Niles, P. B. (2019). The mineralogical legacy of a cold wet early Mars. In *9th International Conference on Mars*, page Abstract #6415, Pasadena, California, USA.

[Ojha et al., 2015] Ojha, L., Wilhelm, M. B., Murchie, S. L., McEwen, A. S., Wray, J. J., Hanley, J., Massé, M., and Chojnacki, M. (2015). Spectral evidence for hydrated salts in recurring slope lineae on Mars. *Nature Geoscience*, 8(11):829.

[Orosei et al., 2018] Orosei, R., Lauro, S. E., Pettinelli, E., Cicchetti, A., Coradini, M., Cosciotti, B., Di Paolo, F., Flamini, E., Mattei, E., Pajola, M., Soldovieri, F., Cartacci, M., Cassenti, F., Frigeri, A., Giuppi, S., Martufi, R., Masdea, A., Mitri, G., Nenna, C., Noschese, R., Restano, M., and Seu, R. (2018). Radar evidence of subglacial liquid water on Mars. *Science*, 361(6401):490–493.

[Panne et al., 1998] Panne, U., Haisch, C., Clara, M., and Niessner, R. (1998). Analysis of glass and glass melts during the vitrification process of fly and bottom ashes by laser-induced plasma spectroscopy. Part I: Normalization and plasma diagnostics. *Spectrochimica acta, Part B: Atomic spectroscopy*, 53(14):1957–1968.

[Parente and Gemp, 2018] Parente, M. and Gemp, I. (2018). Raman/LIBS Data Fusion via Two-Way Variational Autoencoders. In *Planetary Science Informatics and Data Analytics Conference*, volume 2082, page Abstract #6064.

[Parker et al., 1989] Parker, T. J., Saunders, R. S., and Schneeberger, D. M. (1989). Transitional morphology in west Deuteronilus Mensae, Mars: Implications for modification of the lowland/upland boundary. *Icarus*, 82(1):111–145.

[Pavlov et al., 2012] Pavlov, S., Schröder, S., Rauschenbach, I., Jessberger, E., and Hübers, H.-W. (2012). Low-energy laser induced breakdown spectroscopy for in-situ space missions to solar system bodies without atmospheres. *Planetary and Space Science*, 71(1):57–63.

[Pohl and Van Genderen, 1998] Pohl, C. and Van Genderen, J. L. (1998). Review article Multisensor image fusion in remote sensing: Concepts, methods and applications. *International Journal of Remote Sensing*, 19(5):823–854.

[Ramirez and Craddock, 2019] Ramirez, R. M. and Craddock, R. A. (2019). The case for a warm and wet (semi-arid) early Mars. In *9th International Conference on Mars*, page Abstract #6001, Pasadena, California, USA.

[Rammelkamp et al., 2019] Rammelkamp, K., Schröder, S., Kubitza, S., Vogt, D. S., Frohmann, S., Hansen, P. B., Böttger, U., Hanke, F., and Hübers, H.-W. (2019). Low-level LIBS and Raman data fusion in the context of Martian exploration. pages 1–20.

[Rammelkamp et al., 2018] Rammelkamp, K., Vogt, D. S., Schröder, S., and Hubers, H.-W. (2018). Towards LIBS Chlorine Quantification Using the Cacl Molecular Emission in Martian Atmospheric Conditions. In *49th Lunar and Planetary Science Conference*, page Abstract #2083, Houston, USA.

[Ramos et al., 2008] Ramos, P. M., Ruisánchez, I., and Andrikopoulos, K. S. (2008). Micro-Raman and X-ray fluorescence spectroscopy data fusion for the classification of ochre pigments. *Talanta*, 75(4):926 – 936.

[Rapin et al., 2016] Rapin, W., Meslin, P.-Y., Maurice, S., Vaniman, D., Nachon, M., Mangold, N., Schröder, S., Gasnault, O., Forni, O., Wiens, R., Martínez, G., Cousin, A., Sautter, V., Lasue, J., Rampe, E., and Archer, D. (2016). Hydration state of calcium sulfates in Gale crater, Mars: Identification of bassanite veins. *Earth and Planetary Science Letters*, 452:197–205.

[Rapin et al., 2017] Rapin, W., Meslin, P. Y., Maurice, S., Wiens, R. C., Laporte, D., Chau-

viré, B., Gasnault, O., Schröder, S., Beck, P., Bender, S., Beyssac, O., Cousin, A., Dehouck, E., Drouet, C., Forni, O., Nachon, M., Melikechi, N., Rondeau, B., Mangold, N., and Thomas, N. H. (2017). Quantification of water content by laser induced breakdown spectroscopy on Mars. *Spectrochimica Acta - Part B Atomic Spectroscopy*, 130:82–100.

[Rauschenbach et al., 2010] Rauschenbach, I., Jessberger, E. K., Pavlov, S. G., and Hübers, H. W. (2010). Miniaturized Laser-Induced Breakdown Spectroscopy for the in-situ analysis of the Martian surface: Calibration and quantification. *Spectrochimica Acta - Part B Atomic Spectroscopy*, 65(8):758–768.

[Ren et al., 2018] Ren, X., Cai, T. N., Liu, D. W., Liu, J. J., Zhang, H. B., Fu, Q., Zhang, Z. B., and Xu, W. M. (2018). Preliminary Scientific Exploration Programs for Mars Surface Composition Detection Package of China's First Mars Exploration. In *12th European Planetary Science Congress*, page Abstract #759, Berlin, Germany.

[Root, 1989] Root, R. G. (1989). Modeling of post-breakdown phenomena. In Radziemski, L. J. and Cremers, D. A., editors, *Laser-induced plasmas and applications*, pages 69–103. Marcel Dekker New York.

[Rull et al., 2017] Rull, F., Maurice, S., Hutchinson, I., Moral, A., Perez, C., Diaz, C., Colombo, M., Belenguer, T., Lopez-Reyes, G., Sansano, A., Forni, O., Parot, Y., Striebig, N., Woodward, S., Howe, C., Tarcea, N., Rodriguez, P., Seoane, L., Santiago, A., Rodriguez-Prieto, J. A., Medina, J., Gallego, P., Canchal, R., Santamaría, P., Ramos, G., Vago, J. L., and on behalf of the RLS Team (2017). The Raman Laser Spectrometer for the ExoMars Rover Mission to Mars. *Astrobiology*, 17(6-7):627–654.

[Russo et al., 2007] Russo, R. E., Mao, X. L., Yoo, J. H., and Gonzalez, J. J. (2007). Laser Ablation. In Singh, J. P. and Thakur, S. N., editors, *Laser-Induced Breakdown Spectroscopy*, pages 49–79. Elsevier, Amsterdam.

[Ryder et al., 2000] Ryder, A. G., O'Connor, G. M., and Glynn, T. J. (2000). Quantitative analysis of cocaine in solid mixtures using Raman spectroscopy and chemometric methods. *Journal of Raman Spectroscopy*, 31(3):221–227.

[Sabsabi, 2007] Sabsabi, M. (2007). Femtosecond LIBS. In Singh, J. P. and Thakur, S. N., editors, *Laser-Induced Breakdown Spectroscopy*, pages 151–169. Elsevier, Amsterdam.

[Sallé et al., 2006] Sallé, B., Lacour, J. L., Mauchien, P., Fichet, P., Maurice, S., and Manhès, G. (2006). Comparative study of different methodologies for quantitative rock analysis by Laser-Induced Breakdown Spectroscopy in a simulated Martian atmosphere. *Spectrochimica Acta - Part B Atomic Spectroscopy*, 61(3):301–313.

[Sallé et al., 2004] Sallé, B., Lacour, J.-L., Vors, E., Fichet, P., Maurice, S., Cremers, D. A., and Wiens, R. C. (2004). Laser-Induced Breakdown Spectroscopy for Mars surface analysis: capabilities at stand-off distances and detection of chlorine and sulfur elements. *Spectrochimica Acta Part B: Atomic Spectroscopy*, 59(9):1413–1422.

[Schmidt et al., 2017] Schmidt, F., Andrieu, F., Costard, F., Kocifaj, M., and Meresescu, A. G. (2017). Formation of recurring slope lineae on Mars by rarefied gas-triggered granular flows. *Nature Geoscience*, 10(4):270.

[Schröder et al., 2019] Schröder, S., Rammelkamp, K., Hanke, F., Weber, I., Vogt, D. S., Frohmann, S., Kubitza, S., Böttger, U., and Hübers, H.-W. (2019). Effects of pulsed laser and plasma interaction on Fe, Ni, Ti, and their oxides for LIBS Raman analysis in

extraterrestrial environments. *Journal of Raman Spectroscopy*, pages 1–15.

[Schröder et al., 2018] Schröder, S., Wiens, R., Gasnault, O., Mangold, N., Johnson, J., L'Haridon, J., Frydenvang, J., Meslin, P.-Y., Cousin, A., Maurice, S., and the ChemCam Team. (2018). Overview of recent ChemCam Findings after 2000 sols at Gale Crater, Mars. In *12th European Planetary Science Congress*, page Abstract #260, Berlin, Germany.

[Schröder, 2012] Schröder, S. (2012). *PhD thesis: Laser-induced breakdown spectroscopy for planetary research: Analysis of salts and frozen salt solutions under Martian conditions.* Technical University Berlin.

[Schröder et al., 2015] Schröder, S., Meslin, P. Y., Gasnault, O., Maurice, S., Cousin, A., Wiens, R. C., Rapin, W., Dyar, M. D., Mangold, N., Forni, O., Nachon, M., Clegg, S., Johnson, J. R., Lasue, J., Le Mouélic, S., Ollila, A., Pinet, P., Sautter, V., and Vaniman, D. (2015). Hydrogen detection with ChemCam at Gale crater. *Icarus*, 249:43–61.

[Schröder et al., 2013] Schröder, S., Pavlov, S. G., Rauschenbach, I., Jessberger, E. K., and Hübers, H. W. (2013). Detection and identification of salts and frozen salt solutions combining laser-induced breakdown spectroscopy and multivariate analysis methods: A study for future martian exploration. *Icarus*, 223(1):61–73.

[Schröder et al., 2017] Schröder, S., Rammelkamp, K., Cousin, A., Vogt, D., Meslin, P.-Y., Maurice, S., and Hübers, H.-W. (2017). LIBS Analysis of Perchlorates and Chlorides in Soil in Mars-Like Conditions. In *48th Lunar and Planetary Science Conference*, page Abstract #2295, Houston. Lunar and Planetary Institute.

[Schröder et al., 2019a] Schröder, S., Rammelkamp, K., Vogt, D., Gasnault, O., and Hübers, H.-W. (2019a). Contribution of a martian atmosphere to laser-induced breakdown spectroscopy (LIBS) data and testing its emission characteristics for normalization applications. *Icarus*, 325:1–15.

[Schröder et al., 2019b] Schröder, S., Vogt, D. S., Rammelkamp, K., Hansen, P. B., Kubitza, S., Frohmann, S., and Hübers, H.-W. (2019b). Transient 2D and 3D LIBS Plasma Analysis for an Improved Understanding of LIBS Data Obtained on Mars. In *9th International Conference on Mars*, page Abstract #6223, Pasadena, California, USA.

[Scott et al., 2014] Scott, J. R., Effenberger, A. J., and Hatch, J. J. (2014). Influence of Atmospheric Pressure and Composition on LIBS. In Musazzi, S. and Perini, U., editors, *Laser-Induced Breakdown Spectroscopy: Theory and Applications*, pages 91–116. Springer Berlin Heidelberg, Berlin, Heidelberg.

[Senesi, 2014] Senesi, G. S. (2014). Laser-Induced Breakdown Spectroscopy (LIBS) applied to terrestrial and extraterrestrial analogue geomaterials with emphasis to minerals and rocks. *Earth-Science Reviews*, 139:231–267.

[Shaposhnikov et al., 2019] Shaposhnikov, D. S., Medvedev, A. S., Rodin, A. V., and Hartogh, P. (2019). Seasonal Water "Pump" in the Atmosphere of Mars: Vertical Transport to the Thermosphere. *Geophysical Research Letters*, 46(8):4161–4169.

[Sharma et al., 2007] Sharma, S., Misra, A., Lucey, P., Wiens, R., and Clegg, S. (2007). Combined remote LIBS and Raman spectroscopy at 8.6m of sulfur-containing minerals, and minerals coated with hematite or covered with basaltic dust. *Spectrochimica Acta Part A: Molecular and Biomolecular Spectroscopy*, 68(4):1036–1045.

[Sharma et al., 2003] Sharma, S. K., Lucey, P. G., Ghosh, M., Hubble, H. W., and Horton,

K. A. (2003). Stand-off Raman spectroscopic detection of minerals on planetary surfaces. *Spectrochimica Acta - Part A: Molecular and Biomolecular Spectroscopy*, 59(10):2391–2407.

[Singh and Thakur, 2007] Singh, J. P. and Thakur, S. N. (2007). *Laser-induced breakdown spectroscopy*. Elsevier.

[Sirven et al., 2006] Sirven, J. B., Bousquet, B., Canioni, L., and Sarger, L. (2006). Laser-induced breakdown spectroscopy of composite samples: Comparison of advanced chemometrics methods. *Analytical Chemistry*, 78(5):1462–1469.

[Sirven et al., 2008] Sirven, J. B., Mauchien, P., and Sallé, B. (2008). Analytical optimization of some parameters of a Laser-Induced Breakdown Spectroscopy experiment. *Spectrochimica Acta - Part B Atomic Spectroscopy*, 63(10):1077–1084.

[Sirven et al., 2007] Sirven, J. B., Sallé, B., Mauchien, P., Lacour, J. L., Maurice, S., and Manhès, G. (2007). Feasibility study of rock identification at the surface of Mars by remote laser-induced breakdown spectroscopy and three chemometric methods. *Journal of Analytical Atomic Spectrometry*, 22(12):1471–1480.

[Smith et al., 2009] Smith, P. H., Tamppari, L. K., Arvidson, R. E., Bass, D., Blaney, D., Boynton, W. V., Carswell, A., Catling, D. C., Clark, B. C., Duck, T., DeJong, E., Fisher, D., Goetz, W., Gunnlaugsson, H. P., Hecht, M. H., Hipkin, V., Hoffman, J., Hviid, S. F., Keller, H. U., Kounaves, S. P., Lange, C. F., Lemmon, M. T., Madsen, M. B., Markiewicz, W. J., Marshall, J., McKay, C. P., Mellon, M. T., Ming, D. W., Morris, R. V., Pike, W. T., Renno, N., Staufer, U., Stoker, C., Taylor, P., Whiteway, J. A., and Zent, A. P. (2009). H2O at the Phoenix Landing Site. *Science*, 325(5936):58–61.

[Sobron et al., 2014] Sobron, P., Lopez-Reyes, G., Sansano, A., Manrique, J. A., and Rull, F. (2014). Data Fusion in Planetary LIBS+Raman Spectroscopy. In *45th Lunar and Planetary Science Conference*, page Abstract #2875, Houston, USA.

[Sobron et al., 2012] Sobron, P., Wang, A., and Sobron, F. (2012). Extraction of compositional and hydration information of sulfates from laser-induced plasma spectra recorded under Mars atmospheric conditions - Implications for ChemCam investigations on Curiosity rover. *Spectrochimica Acta - Part B Atomic Spectroscopy*, 68:1–16.

[Soffen and Snyder, 1976] Soffen, G. A. and Snyder, C. W. (1976). The First Viking Mission to Mars. *Science*, 193(4255):759–766.

[Sohl et al., 2010] Sohl, F., Choukroun, M., Kargel, J., Kimura, J., Pappalardo, R., Vance, S., and Zolotov, M. (2010). Subsurface water oceans on icy satellites: Chemical composition and exchange processes. *Space Science Reviews*, 153(1-4):485–510.

[Stofan et al., 2007] Stofan, E. R., Elachi, C., Lunine, J. I., Lorenz, R. D., Stiles, B., Mitchell, K., Ostro, S., Soderblom, L., Wood, C., Zebker, H., et al. (2007). The lakes of Titan. *Nature*, 445(7123):61.

[Sundararajan, 2018] Sundararajan, V. (2018). Overview and Technical Architecture of India's Chandrayaan-2 Mission to the Moon. In *2018 AIAA Aerospace Sciences Meeting*, page 2178.

[Takahashi and Thornton, 2017] Takahashi, T. and Thornton, B. (2017). Quantitative methods for compensation of matrix effects and self-absorption in LIBS signals of solids. *Spectrochimica Acta - Part B Atomic Spectroscopy*, 138:31–42.

[Thakur, 2007] Thakur, S. (2007). Atomic Emission Spectroscopy. In Singh, J. P. and Thakur, S. N., editors, *Laser-Induced Breakdown Spectroscopy*, pages 23 – 48. Elsevier, Amsterdam.

[Thomas et al., 2018a] Thomas, N. H., Ehlmann, B. L., Anderson, D. E., Clegg, S. M., Forni, O., Schröder, S., Rapin, W., Meslin, P. Y., Lasue, J., Delapp, D. M., Dyar, M. D., Gasnault, O., Wiens, R. C., and Maurice, S. (2018a). Characterization of Hydrogen in Basaltic Materials With Laser-Induced Breakdown Spectroscopy (LIBS) for Application to MSL ChemCam Data. *Journal of Geophysical Research: Planets*, 123(8):1996–2021.

[Thomas et al., 2018b] Thomas, N. H., Ehlmann, B. L., Meslin, P.-Y., Cousin, A., Forni, O., Rapin, W., Anderson, D. D. E., Schröder, S., Mangold, N., Wiens, R. C., and Gasnault, O. (2018b). MSL ChemCam Observations of Chloride Salts in Gale Crater, Mars. In *49th Lunar and Planetary Science Conference*, page Abstract #2876, The Woodlands, Texas, USA.

[Thorne et al., 1999] Thorne, A., Litzén, U., and Johansson, S. (1999). *Spectrophysics: principles and applications*. Springer Science & Business Media.

[Titov, 2002] Titov, D. V. (2002). Water vapour in the atmosphere of Mars. *Advances in Space Research*, 29(2):183–191.

[Tognoni and Cristoforetti, 2016] Tognoni, E. and Cristoforetti, G. (2016). Signal and noise in Laser-Induced Breakdown Spectroscopy: An introductory review. *Optics and Laser Technology*, 79(May):164–172.

[Tognoni et al., 2010] Tognoni, E., Cristoforetti, G., Legnaioli, S., and Palleschi, V. (2010). Calibration-free laser-induced breakdown spectroscopy: state of the art. *Spectrochimica Acta Part B: Atomic Spectroscopy*, 65(1):1–14.

[Tognoni et al., 2006] Tognoni, E., Palleschi, V., Corsi, M., Cristoforetti, G., Omenetto, N., Gornushkin, I., Smith, B. W., and Winefordner, J. D. (2006). From sample to signal in laser-induced breakdown spectroscopy: a complex route to quantitative analysis. In Miziolek, A. W., Palleschi, V., and Schechter, I., editors, *Laser Induced Breakdown Spectroscopy*, page 122–170. Cambridge University Press.

[Toner et al., 2015] Toner, J. D., Catling, D. C., and Light, B. (2015). Modeling salt precipitation from brines on Mars: Evaporation versus freezing origin for soil salts. *Icarus*, 250:451–461.

[Treiman et al., 2016] Treiman, A. H., Bish, D. L., Vaniman, D. T., Chipera, S. J., Blake, D. F., Ming, D. W., Morris, R. V., Bristow, T. F., Morrison, S. M., Baker, M. B., Rampe, E. B., Downs, R. T., Filiberto, J., Glazner, A. F., Gellert, R., Thompson, L. M., Schmidt, M. E., Le Deit, L., Wiens, R. C., McAdam, A. C., Achilles, C. N., Edgett, K. S., Farmer, J. D., Fendrich, K. V., Grotzinger, J. P., Gupta, S., Morookian, J. M., Newcombe, M. E., Rice, M. S., Spray, J. G., Stolper, E. M., Sumner, D. Y., Vasavada, A. R., and Yen, A. S. (2016). Mineralogy, provenance, and diagenesis of a potassic basaltic sandstone on Mars: CheMin X-ray diffraction of the Windjana sample (Kimberley area, Gale Crater). *Journal of Geophysical Research: Planets*, 121(1):75–106.

[Treiman et al., 2000] Treiman, A. H., Gleason, J. D., and Bogard, D. D. (2000). The SNC meteorites are from Mars. *Planetary and Space Science*, 48(12):1213 – 1230.

[Tsuda et al., 2013] Tsuda, Y., Yoshikawa, M., Abe, M., Minamino, H., and Nakazawa, S. (2013). System design of the Hayabusa 2—Asteroid sample return mission to 1999 JU3.

Acta Astronautica, 91:356–362.

[Tuschel, 2014] Tuschel, D. (2014). Practical group theory and Raman spectroscopy, part i: Normal vibrational modes. *Spectroscopy*, 29(2):14.

[Vadillo and Laserna, 2004] Vadillo, J. M. and Laserna, J. J. (2004). Laser-induced plasma spectrometry: Truly a surface analytical tool. *Spectrochimica Acta - Part B Atomic Spectroscopy*, 59(2):147–161.

[Vasavada et al., 2014] Vasavada, A. R., Grotzinger, J. P., Arvidson, R. E., Calef, F. J., Crisp, J. A., Gupta, S., Hurowitz, J., Mangold, N., Maurice, S., Schmidt, M. E., Wiens, R. C., Williams, R. M. E., and Yingst, R. A. (2014). Overview of the Mars Science Laboratory mission: Bradbury Landing to Yellowknife Bay and beyond. *Journal of Geophysical Research: Planets*, 119(6):1134–1161.

[Vogt et al., 2020] Vogt, D., Schröder, S., Rammelkamp, K., Hansen, P., Kubitza, S., and Hübers, H.-W. (2020). CaCl and CaF emission in LIBS under simulated Martian conditions. *Icarus*, 335:113393.

[Vogt et al., 2018a] Vogt, D. S., Frohmann, S., Kubitza, S., Hansen, P. B., Rammelkamp, K., Schröder, S., and Hübers, H.-W. (2018a). Simple modelling of Plasma Parameters to Assist the Analysis of LIBS Spectra for Planetary Exploration. In *12th European Planetary Science Congress*, page Abstract #754, Berlin, Germany.

[Vogt et al., 2018b] Vogt, D. S., Rammelkamp, K., Schröder, S., and Hübers, H. W. (2018b). Molecular emission in laser-induced breakdown spectroscopy: An investigation of its suitability for chlorine quantification on Mars. *Icarus*, 302:470–482.

[Wang et al., 1995] Wang, A., Jolliff, B. L., and Haskin, L. A. (1995). Raman spectroscopy as a method for mineral identification on lunar robotic exploration missions. *Journal of Geophysical Research*, 100(E10):21189.

[Wei et al., 2015] Wei, D., Chen, S., and Liu, Q. (2015). Review of fluorescence suppression techniques in Raman spectroscopy. *Applied Spectroscopy Reviews*, 50(5):387–406.

[Westad and Marini, 2015] Westad, F. and Marini, F. (2015). Validation of chemometric models - A tutorial. *Analytica Chimica Acta*, 893:14–24.

[White, 1991] White, F. E. (1991). Data fusion lexicon. Technical report, Joint Directors of Labs Washington DC.

[Wiens et al., 2012] Wiens, R. C., Maurice, S., Barraclough, B., Saccoccio, M., Barkley, W. C., Bell, J. F., Bender, S., Bernardin, J., Blaney, D., Blank, J., Bouyé, M., Bridges, N., Bultman, N., Caïs, P., Clanton, R. C., Clark, B., Clegg, S., Cousin, A., Cremers, D., Cros, A., Deflores, L., Delapp, D., Dingler, R., D'Uston, C., Darby Dyar, M., Elliott, T., Enemark, D., Fabre, C., Flores, M., Forni, O., Gasnault, O., Hale, T., Hays, C., Herkenhoff, K., Kan, E., Kirkland, L., Kouach, D., Landis, D., Langevin, Y., Lanza, N., Larocca, F., Lasue, J., Latino, J., Limonadi, D., Lindensmith, C., Little, C., Mangold, N., Manhes, G., Mauchien, P., McKay, C., Miller, E., Mooney, J., Morris, R. V., Morrison, L., Nelson, T., Newsom, H., Ollila, A., Ott, M., Pares, L., Perez, R., Poitrasson, F., Provost, C., Reiter, J. W., Roberts, T., Romero, F., Sautter, V., Salazar, S., Simmonds, J. J., Stiglich, R., Storms, S., Striebig, N., Thocaven, J. J., Trujillo, T., Ulibarri, M., Vaniman, D., Warner, N., Waterbury, R., Whitaker, R., Witt, J., and Wong-Swanson, B. (2012). The ChemCam instrument suite on the Mars Science Laboratory (MSL) rover: Body unit and combined

system tests. *Space Science Reviews*, 170(1-4):167–227.

[Wiens et al., 2013] Wiens, R. C., Maurice, S., Lasue, J., Forni, O., Anderson, R. B., Clegg, S., Bender, S., Blaney, D., Barraclough, B. L., Cousin, A., Deflores, L., Delapp, D., Dyar, M. D., Fabre, C., Gasnault, O., Lanza, N., Mazoyer, J., Melikechi, N., Meslin, P. Y., Newsom, H., Ollila, A., Perez, R., Tokar, R. L., and Vaniman, D. (2013). Pre-flight calibration and initial data processing for the ChemCam laser-induced breakdown spectroscopy instrument on the Mars Science Laboratory rover. *Spectrochimica Acta - Part B Atomic Spectroscopy*, 82:1–27.

[Wiens et al., 2017] Wiens, R. C., Maurice, S., and Rull, F. (2017). The SuperCam Remote Sensing Instrument Suite for the Mars 2020 Rover: A Preview. *Spectroscopy*, 32(5):50–55.

[Wiens et al., 2005] Wiens, R. C., Sharma, S. K., Thompson, J., Misra, A., and Lucey, P. G. (2005). Joint analyses by laser-induced breakdown spectroscopy (LIBS) and Raman spectroscopy at stand-off distances. *Spectrochimica Acta - Part A: Molecular and Biomolecular Spectroscopy*, 61(10):2324–2334.

[Witze, 2014] Witze, A. (2014). NASA plans Mars sample-return rover. *Nature News*, 509(7500):272.

[Wordsworth et al., 2015] Wordsworth, R. D., Kerber, L., Pierrehumbert, R. T., Forget, F., and Head, J. W. (2015). Comparison of "warm and wet" and "cold and icy" scenarios for early Mars in a 3-D climate model. *Journal of Geophysical Research: Planets*, 120(6):1201–1219.

[Yalçin et al., 1999] Yalçin, c., Crosley, D. R., Smith, G. P., and Faris, G. W. (1999). Influence of ambient conditions on the laser air spark. *Applied Physics B: Lasers and Optics*, 68(1):121–130.

[Yokoya et al., 2017] Yokoya, N., Grohnfeldt, C., and Chanussot, J. (2017). Hyperspectral and Multispectral Data Fusion: A comparative review of the recent literature. *IEEE Geoscience and Remote Sensing Magazine*, 5(2):29–56.

[Zhang et al., 2018] Zhang, T., Tang, H., and Li, H. (2018). Chemometrics in laser-induced breakdown spectroscopy. *Journal of Chemometrics*, 32(11):1–18.

[Zorov et al., 2010] Zorov, N. B., Gorbatenko, A. A., Labutin, T. A., and Popov, A. M. (2010). A review of normalization techniques in analytical atomic spectrometry with laser sampling: From single to multivariate correction. *Spectrochimica Acta - Part B Atomic Spectroscopy*, 65(8):642–657.

List of Figures

List of Tables

List of Publications

Peer reviewed publications (first author)

- Rammelkamp, K., Schröder, S., Kubitza, S., Vogt, D. S., Frohmann, S., Hansen, P. B., Böttger, U., Hanke, F. and Hübers, H.-W. (2019). Low-level LIBS and Raman data fusion in the context of in situ Mars exploration. *Journal of Raman Spectroscopy*, 1– 20. *https://doi.org/10.1002/jrs.5615.*

Peer reviewed publications (co-author)

- Vogt, D. S., Rammelkamp, K., Schröder, S. and Hübers, H.-W. (2018). Molecular emission in laser-induced breakdown spectroscopy: An investigation of its suitability for chlorine quantification on Mars. *Icarus*, 302: 470-482. *https://doi.org/10.1016/j.icarus.2017.12.006.*
- Schröder, S., Rammelkamp, K., Vogt, D. S., Gasnault, O. and Hübers, H.-W. (2019). Contribution of a martian atmosphere to laser-induced breakdown spectroscopy (LIBS) data and testing its emission characteristics for normalization applications. *Icarus*, 325: 1-15. *https://doi.org/10.1016/j.icarus.2019.02.017.*
- Schröder, S., Rammelkamp, K., Hanke, F., Weber, I., Vogt, D. S., Frohmann, S., Kubitza, S., Böttger, U. and Hübers, H.-W. (2019). Effects of pulsed laser and plasma interaction on Fe, Ni, Ti, and their oxides for LIBS Raman analysis in extraterrestrial environments. *Journal of Raman Spectroscopy*, 1– 15. *https://doi.org/10.1002/jrs.5650.*
- Vogt, D. S., Schröder, S., Rammelkamp, K., Hansen, P. B., Kubitza, S. and Hübers, H.-W. (2020). CaCl and CaF emission in LIBS under simulated Martian conditions. *Icarus*, 335. *https://doi.org/10.1016/j.icarus.2019.113393.*

Oral presentations at conferences

- Rammelkamp, K., Vogt, D. S., Schröder, S. and Hübers, H.-W. (2017). Investigation of Normalization Methods using Plasma Parameters for Laser-Induced Breakdown Spectroscopy (LIBS) under simulated Martian Conditions. *EMSLIBS 2017*, Pisa, Italy.
- Rammelkamp, K., Schröder, S., Vogt, D. S., Kubitza, S., Frohmann, S., Hanke, F., Böttger, U. and Hübers, H.-W. (2018). Advantages of Combined LIBS and Raman Data for the Identification and Quantification of Hydrated Salts for in-situ Planetary Exploration. *GeoRaman 2018*, Catania, Italy.
- Rammelkamp, K., Schröder, S., Böttger, U., Frohmann, S., Hanke, F., Hansen, P. B., Kubitza, S., Vogt, D. S. and Hübers, H.-W. (2018), LIBS and Raman Spectroscopy for Planetary in-situ Exploration. *IPM 2018*, Berlin, Germany.
- Rammelkamp, K., Schröder, S., Kubitza, S., Vogt, D. S., Frohmann, S., Hansen, P. B., Böttger, U., Hanke, F., Hübers, H.- W. (2018). LIBS and Raman Data Fusion for in-situ Planetary Exploration, *EPSC 2018*, Berlin, Germany.

Poster presentations at conferences

- Rammelkamp, K., Schröder, S., Vogt, D. S., Meslin, P.-Y., Cousin, A., Forni, O., Drouet, C., Cicutto, L. and Hübers, H.-W. (2016). Investigation of halogen atomic and molecular emission in high resolved LIBS spectra under martian conditions. *LIBS 2016*, Chamonix, France.
- Rammelkamp, K., Vogt, D. S., Schröder, S. and Hübers, H.-W. (2017). Investigation of normalization methods using plasma parameters for laser-induced breakdown spectroscopy (LIBS) under simulated martian conditions. *48th LPSC 2017*, The Woodlands, USA.
- Rammelkamp, K., Schröder, S., Vogt, D. S. and Hübers, H.-W. (2017). Investigation of plasma parameter determination of LIBS plasmas in martian conditions. *EPSC 2017*, Riga, Latvia.
- Rammelkamp, K., Vogt, D. S., Schröder, S. and Hübers, H.-W. (2018), Towards LIBS chlorine quantification using the CaCl molecular emission in martian atmospheric conditions. *49th LPSC 2018*, The Woodlands, USA

Acknowledgments

At this position, I would like to use the space to thank many people who supported me during the course of this thesis. First, I would like to express my gratitude to Prof. Dr. Heinz-Wilhelm Hübers for giving me the possibility to do my research at the institute of optical sensor systems at DLR and for being the supervisor of this thesis.

Foremost, I want to thank Dr. Susanne Schröder for her guidance and support in the last three years. She gave me the possibility to be part of her Junior Research Group and her never ending enthusiasm for planetary exploration inspired me a lot. I could always ask her any kind of question and she always took the time to answer and to propose new ideas. She did not only care about my research in the group, moreover, she encouraged me finding my way and greatly supported my upcoming research project.

I also want to thank my colleagues David Sebastian Vogt, Simon Kubitza, Peder Bagge Hansen, and Sven Frohmann for their unlimited support including fruitful scientific discussions and technical assistance. Besides the support for my research, I also enjoyed the nice atmosphere in our office and the encouraging and sometimes very funny conversations. This made stressful moments quite easier.

Additionally, I want to thank the whole Terahertz and Laser Spectroscopy department for the nice working environment. I want to express special thanks to Ute Böttger, Franziska Hanke, Michael Greiner-Bär, and Sven Augustin for supporting my research but also for personal conversations.

Furthermore, I am deeply grateful to my family and my friends, especially to my parents, Suse, Fabia, Sanja, Fabian, and Diana for their support and understanding. Finally, I want to thank Matthias for always being there for me.

Statutory Declaration

I declare that I have completed the thesis independently using only the aids and tools specified. I have not applied for a doctor's degree in the doctoral subject elsewhere and do not hold a corresponding doctor's degree. I have taken due note of the Faculty of Mathematics and Natural Sciences PhD Regulations, published in the Official Gazette of Humboldt-Universität zu Berlin no. 42 on July 11 2018.

Berlin, September 2, 2019

Kristin Rammelkamp